CHAPTER V

RESULTS AND DISCUSSION

Chapter V demonstrates the experimental results and their discussion. The crystal structure and phase formation of NiO-based powders synthesized by a polymer pyrolysis method and their ceramics can be determined by using X-ray diffraction (XRD) results. The microstructure and ceramic surface morphologies of the powders and ceramics are revealed by scanning electron microscopy (SEM) images. The results of dielectric and electrical properties as functions of frequency and temperature of the NiO-based ceramics are demonstrated. The effect of doping concentrations on these experimental results (structural and dielectric properties) is briefly discussed; the influence of sintering temperature on the results is described as well. The origin of the giant dielectric properties of the NiO-based ceramics is discussed briefly and carefully based on the obtained experimental results. The influence of interfaces, between surfaces-bulk ceramic and grains-grain boundaries, on the dielectric properties of the NiO-based ceramics is certainly interpreted. To deepen the understanding of the origin of the giant dielectric properties, the effect post-annealing in argon atmosphere on the dielectric and electrical response in the NiO-based ceramics is shown and discussed. To understand the physical mechanism of the dielectric and electrical results, several dielectric and electrical models are suitably used to ascribe the dielectric relaxation behavior. Throughout this thesis, the associated data of XRD, SEM, and dielectric and related electrical properties are discussed together. Several microstructural models are proposed to separate each contribution that may have an effect on the total dielectric response. Throughout the chapter, the interesting results are observed and briefly discussed.

In the thesis, although NiO-based ceramics were synthesized from the powders prepared by using three different methods as described in the Chapter IV, the polymer pyrolysis method is selected as the main method used to fabricate various NiO-based ceramic systems. It is worth noting that the aims of the thesis do not focus on the influence of processing methods on properties of the NiO-based ceramics. The results of NiO-based ceramics present in sections 5.1-5.5 are the ceramics synthesized by using the polymer pyrolysis method. The results of properties of the NiO-based ceramics fabricated by the other two methods are illustrated in the sections 5.6 and 5.7 for the direct thermal decomposition and PVA solution methods, respectively. In the final section of this Chapter, the giant dielectric properties of the $Li_{0.05}Ti_{0.02}Ni_{0.93}O$ ceramic are compared to the dielectric properties of pure-CuO.

5.1 Li and Ti co-doped NiO system

5.1.1 Powder characterization: morphologies and crystal structure

Generally, the important characteristics of a powder can be divided into four groups: physical characteristics, chemical composition, phase composition, and surface characteristics (Rahaman, 2003). However, this thesis concentrates only on the phase composition and physical characteristics. The obtained (Li, Ti)-doped NiO ($Li_xTi_yNi_{1-x-y}O$, LTNO) powders with different concentrations of the Li and Ti doping ions were characterized by XRD and SEM techniques in order to identify and reveal the crystal structure and powder morphologies, respectively. The morphology of the NiO and LTNO powders calcined at 700 °C for 5 h are shown in figures 5.1(a)-5.1(o). As clearly seen in all SEM images, large agglomerates of the powders are observed; a high interconnection of the grains can be seen. The interconnection behaves as a solid bridge; as a result, *primary particles*[1] of the LTNO powders are chemically bonded together by the solid bridges. This agglomerate can be defined as *hard agglomerates*, which normally lead to the formation of micro-structural defects. Normally, the cluster of primary particles in the agglomerates can also hold together by surface force and by liquid. Therefore, it is believed that agglomerates are held together by such fairly weak surface forces, forming *soft agglomerates*. As revealed in figure 5.1, the particle sizes of the powders are found to be in the range of about 100 – 300 nm.

---

[1] A primary particle is a discrete, low-porosity unit that can be either a single crystal, a polycrystalline, or glass. It can not be broken down into smaller units by ultrasonic agitation in a liquid.

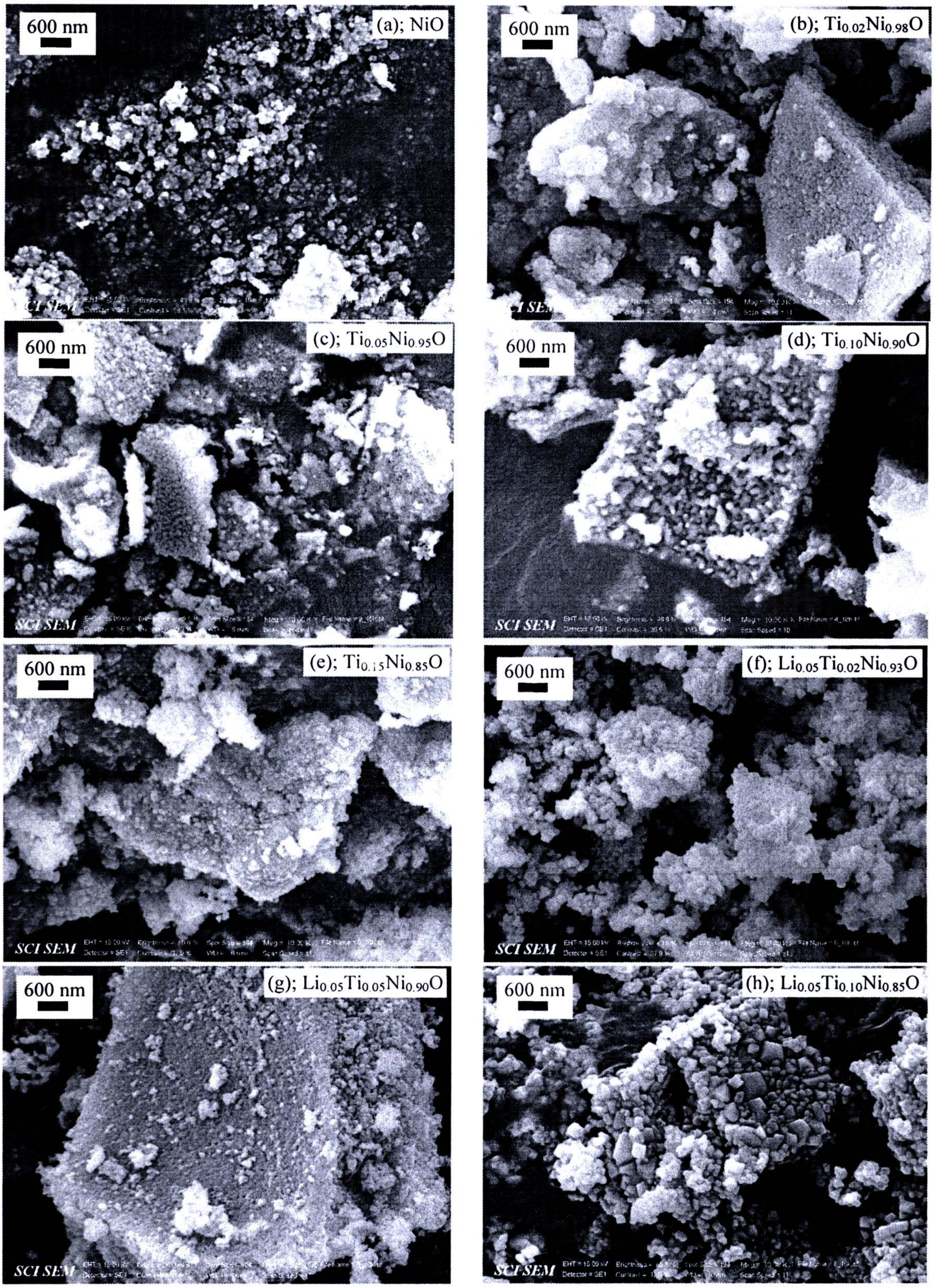

Figure 5.1 SEM images of NiO and $Li_xTi_yNi_{1-x-y}O$ powders with different concentrations of Li (x) and Ti (y) doping ions.

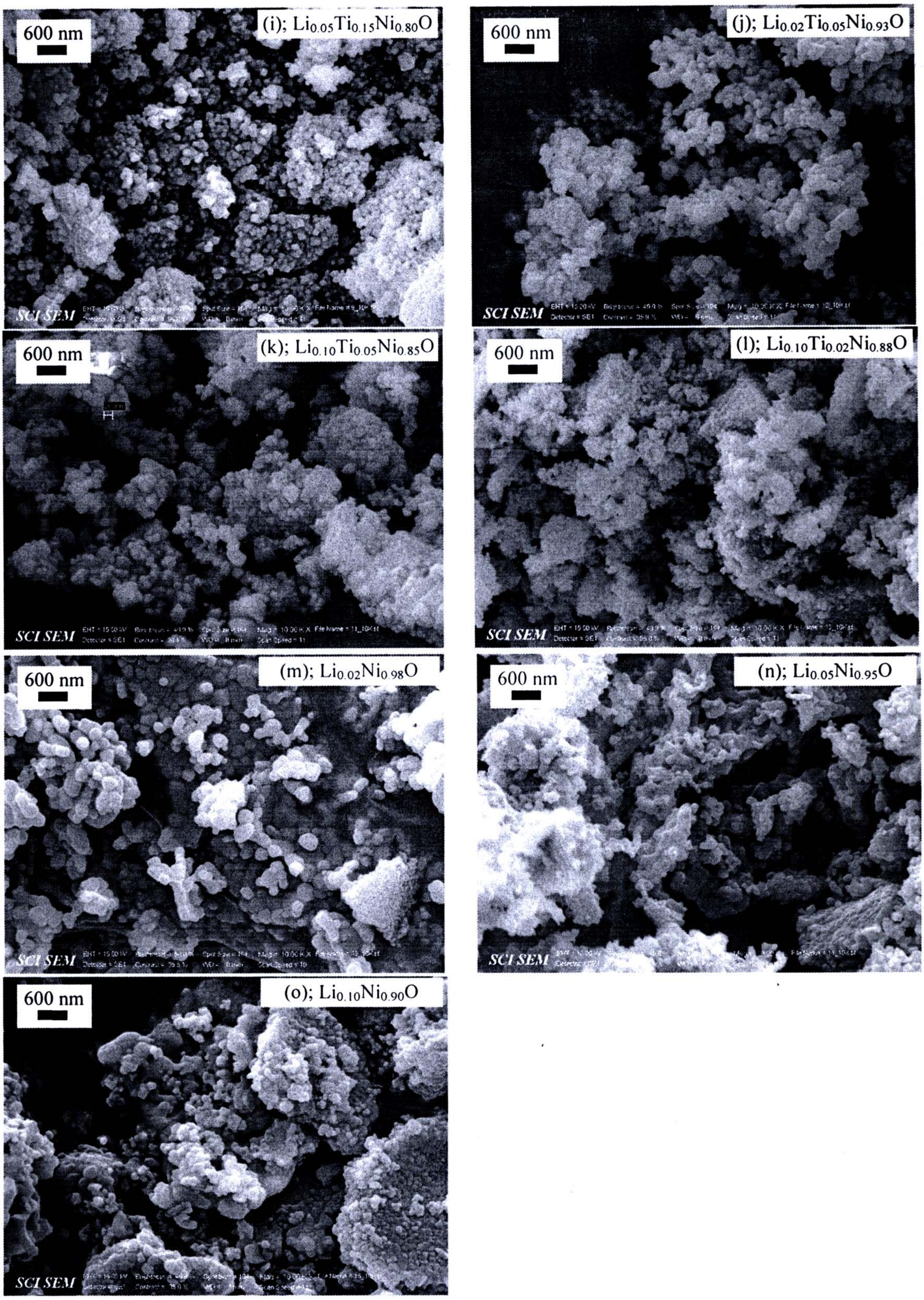

Figure 5.1 SEM images of NiO and $Li_xTi_yNi_{1-x-y}O$ powders with different concentrations of Li (x) and Ti (y) doping ions. (Cont.)

As well known, X-ray diffraction (XRD) in a crystal material can usually provide a wealth of information about the structure and chemical composition of crystalline materials. For structure analysis, a given crystalline material always exhibits a characteristic diffraction pattern. The crystal structure and phase composition of the prepared $Li_xTi_yNi_{1-x-y}O$ powders can be determined from their XRD patterns. For compositional analysis, the technique is unique in that it is the only analytic method capable of providing *qualitative*[2] and *quantitative*[3] information about the phases present in a crystalline solid. In this thesis, however, the qualitative analysis is only discussed.

To discuss the effect of Ti and Li doping concentrations on the crystal structure of NiO and phase composition of the prepared $Li_xTi_yNi_{1-x-y}O$ powders, the XRD results are divided into four groups as shown in figures 5.2-5.5. As revealed in figure 5.2, the first group, the XRD patterns of the NiO and Li-doped NiO powders, each powder sample exhibits a series of shape peaks (five peaks) within a 2θ angle range of 25°-85°. These five peaks locate on the 2θ angle of about 37.3°, 43.3°, 63.0°, 75.4°, and 79.4°. The observed series of peaks is due to the fact that the diffracted beams are arisen from different lattice planes. Consequently, it can be suggested that the prepared NiO and Li-doped NiO powders are crystalline materials. All of the main peaks are comparable to that of the powder diffraction pattern of NiO in Joint Committee of Powder Diffraction Standards (JCPDS) card no. 78-0429 and those reported in the literature for face-centered cubic NiO (Li Z et al., 2005). The observed five peaks in these XRD patterns from low- to high-angle of 2θ can be indexed as the (111), (200), (220), (311), and (222) planes of NiO, respectively. It can be observed from these planes that *h*, *k*, and *l* (Miller indices) are all even or all odd. This can be explained by using the structure factor, *F*, (Cullity, Stock, 2001; Mckelvey, 1993)

$$F = \sum_i f_i \exp[2\pi i(hu_i + kv_i + lw_i)], \tag{5.1}$$

---

[2] Qualitative analysis for a particular crystalline solid is accomplished by identification of the pattern of that crystalline solid.

[3] Quantitative analysis can be performed form the intensities of the diffraction peaks because the intensity due to one phase in a mixture depend on the proportion of that phase in the crystalline solid sample.

where *f* is the atomic scattering factor, *u*, *v*, and *w* are the atom position in the unit cell. The beam intensity diffracted by all the atoms in the unit cell in a given direction corresponding to Bragg's law is proportional to F^2. If $F^2 = 0$, there is no refection (Suryanarayana, Norton, 1998; Cullity, Stock, 2001). For a face-centered cubic structure, it can be proved that $F^2 \neq 0$ when *h*, *k*, and *l* are all even or all odd. As a result, the (100) and other mixed indices[4] can not be detected in the XRD patterns of the NiO and Li-doped NiO powders, as shown in figure 5.2, because these conditions can result in $F^2 = 0$.

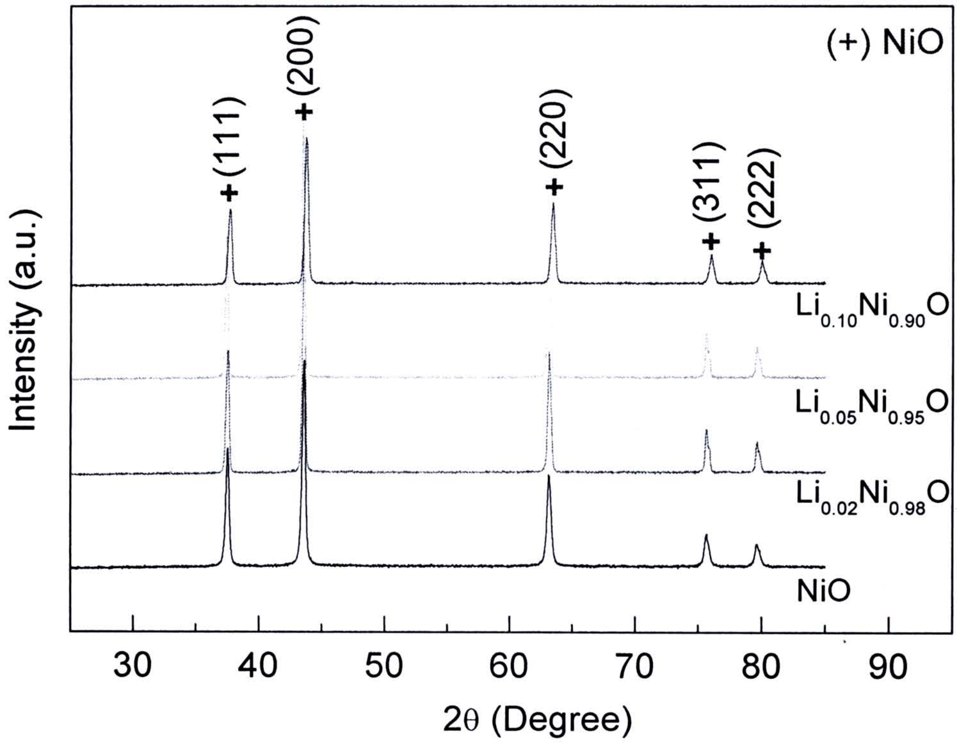

Figure 5.2 XRD patterns of the powders for NiO and Li-doped NiO with different concentrations of Li doping ions, Li = 2, 5, and 10 mol %.

---

[4] *Mixed indices* are defined that *h*, *k*, and *l* are mixed, i.e., some are odd and some are even. If *h*, *k*, and *l* are all odd and all even, these indices are therefore defined as "*unmixed indices*"

Besides the structure (crystalline or amorphous) and crystal structure analyses, the phase composition can usually be analyzed from the XRD patterns. As clearly seen in figure 5.2, the second phase or impurities phase can not be detected from the XRD patterns of all three Li-doped NiO powders, i.e., $Li_{0.02}Ni_{0.98}O$, $Li_{0.05}Ni_{0.95}O$, and $Li_{0.10}Ni_{0.90}O$. This may be due to the fact that all of Li^+ doping ions can completely substitute the Ni^{2+} ions sites in the NiO crystal lattice. The diffraction peaks of the $Li_xNi_{1-x}O$ powders shift to larger 2θ with x increases, especially for the $Li_{0.10}Ni_{0.90}O$ powder, indicating to the decrease in the lattice parameter. As revealed in Table 5.1, the lattice parameters calculated by using Cohen's least-squares method tend to decrease with increasing the concentration of Li doping ions. This result is consistent with the literatures (Antolini, 2003; Li Z et al., 2005).

It was reported that cubic structure of the $Li_xNi_{1-x}O$ system was maintained up to x~0.20-0.25; above this, it transferred to hexagonal structure (van Elp et al., 1992; Li Z et al., 2005). It was found from the preparation $Li_{0.21}Ni_{0.79}O$ powder prepared by thermal treatment of NiO/Li_2CO_3 powder mixture that the bulk diffusion of Li_2O in NiO occurred at a fast rate at temperature higher than 750 °C (Iida, 1960). This means that the solution of Li_2O in NiO is in competition with the evaporation of Li_2O at this temperature. As a result, the Li content of Li-doped NiO is always lower than the nominal composition. Antolini (2003), however, found that Li loss could be negligible for the $Li_xNi_{1-x}O$ system with $x < 0.28$ calcined at 745 °C for 48 h (prepared by a solid state reaction method). In this thesis, the $Li_xNi_{1-x}O$ and $Li_xTi_yNi_{1-x-y}O$ powders prepared by a polymer pyrolysis method were calcined at 700 °C for 5 h and the maximum of x is 0.10. Thus, it can suitably be deduced that Li^+ doping ions can completely substitute the Ni^{2+} ion sites in the NiO crystal lattice without the evaporation of Li ions during the firing process.

Table 5.1 Lattice parameter of NiO, Li-doped NiO, Ti-doped NiO, and (Li, Ti)-doped NiO powders with different concentrations of Li and Ti doping ions.

Sample	Lattice parameter (nm)
NiO (JCPDS no. 78-0429)	4.177
NiO	4.176±0.004
Group 1; Li-doped NiO	
$Li_{0.02}Ni_{0.98}O$	4.176±0.005
$Li_{0.05}Ni_{0.95}O$	4.171±0.001
$Li_{0.10}Ni_{0.90}O$	4.160±0.004
Group 2; Ti-doped NiO	
$Ti_{0.02}Ni_{0.98}O$	4.175±0.002
$Ti_{0.05}Ni_{0.95}O$	4.176±0.003
$Ti_{0.10}Ni_{0.90}O$	4.177±0.003
$Ti_{0.15}Ni_{0.85}O$	4.175±0.003
Group 3; (Li, Ti)-doped NiO	
$Li_{0.05}Ti_{0.02}Ni_{0.93}O$	4.176±0.002
$Li_{0.05}Ti_{0.05}Ni_{0.90}O$	4.173±0.003
$Li_{0.05}Ti_{0.10}Ni_{0.85}O$	4.174±0.002
$Li_{0.05}Ti_{0.15}Ni_{0.80}O$	4.175±0.003
Group 4; (Li, Ti)-doped NiO	
$Li_{0.10}Ti_{0.02}Ni_{0.88}O$	4.169±0.002
$Li_{0.10}Ti_{0.05}Ni_{0.85}O$	4.173±0.003
$Li_{0.02}Ti_{0.05}Ni_{0.93}O$	4.175±0.001

For the second group of the XRD patterns, as displayed in figure 5.3, the XRD patterns of Ti-doped NiO powders, the series of shape five peaks corresponding to the NiO phase with face-centered cubic structure (JCPDS card no. 78-0429) can be observed in all of the Ti-doped NiO ($Ti_yNi_{1-y}O$) powders. These XRD results demonstrate that the prepared $Ti_yNi_{1-y}O$ powders are crystalline materials just like the $Li_xNi_{1-x}O$ powders. The diffraction peaks corresponding to the NiO phase of the $Ti_yNi_{1-y}O$ powders do not shift to larger or lower 2θ with the change of y (concentration of Ti doping), suggesting that the Ti doping is most likely present in the microstructure either in the grain boundaries or as a second phase. With increasing the Ti doping up to 5 mol %, another series of diffraction peaks is clearly observed; furthermore, the intensity of these added peaks increases with increasing the concentration of Ti doping. This implies that there is an impurities phase exhibited in the $Ti_yNi_{1-y}O$ powders. This series of the diffraction peaks is comparable to those of the powder diffraction pattern of $NiTiO_3$ in JCPDS card no. 33-0960 for rhombohedral structure and reported in the literatures (Lin et al., 2006a; Lin et al., 2005b; Lopes et al., 2009). The lattice parameter of the $Ti_yNi_{1-y}O$ powders calculated by using Cohen's least-squares method does not change with the concentration of the Ti doping ions.

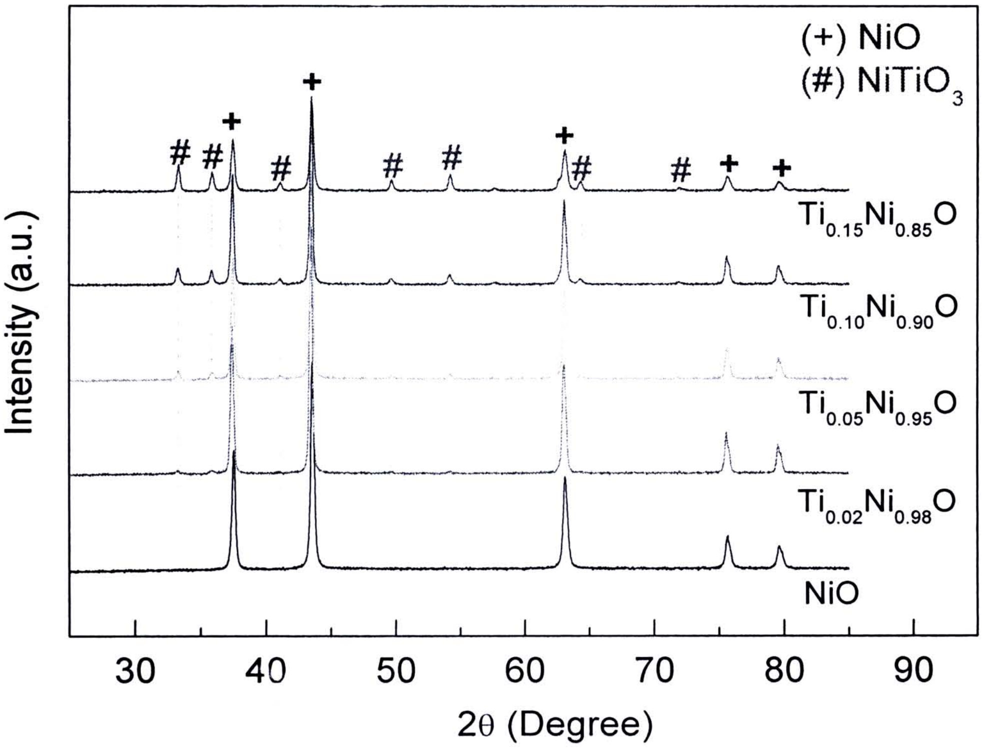

Figure 5.3 XRD patterns of NiO and Ti-doped NiO powders with different concentrations of Ti doping ions, Ti = 2, 5, 10, and 15 mol %.

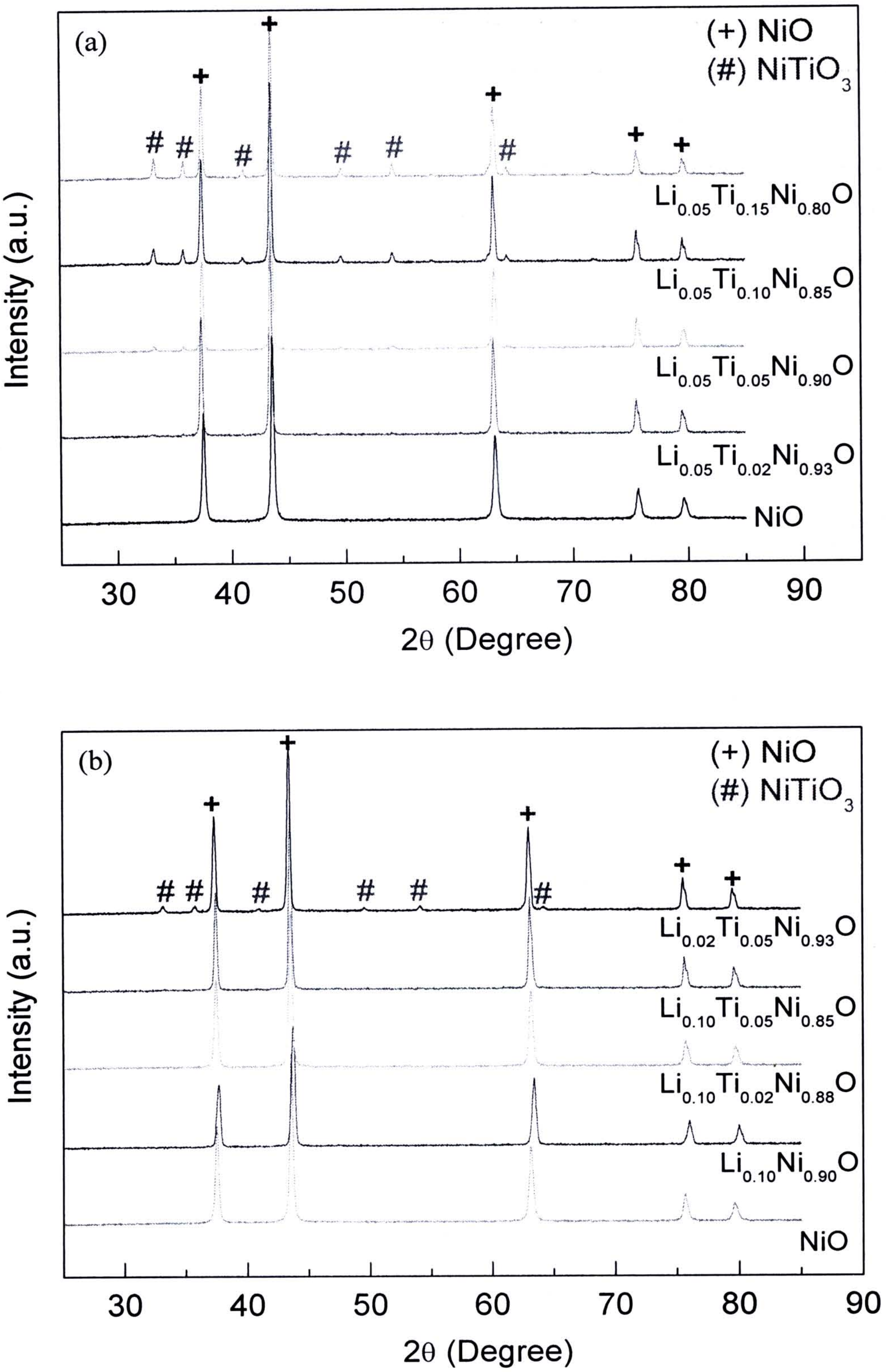

Figure 5.4 XRD patterns of $Li_xTi_yNi_{1-x-y}O$ powders with different concentrations of Li and Ti doping ions; (a) group 3 and (b) group 4.

For the other two groups of the XRD patterns, as illustrated in figures 5.4(a) and 5.4(b), the XRD patterns of the Li and Ti co-doped NiO powders ($Li_xTi_yNi_{1-x-y}O$), the series of the shape five peaks corresponding to the NiO phase with face-centered cubic structure (JCPDS card no. 78-0429) are certainly detected in all $Li_xTi_yNi_{1-x-y}O$ powders. The structural analysis suggests that the prepared $Li_xTi_yNi_{1-x-y}O$ powders are crystalline materials just as the $Li_xNi_{1-x}O$ and $Ti_yNi_{1-y}O$ powders are. As shown in figure 5.4(a), the XRD patterns of the $Li_{0.05}Ti_yNi_{0.95-y}O$ powders, where y = 0.02, 0.05, 0.10, and 0.15, it is found that the positions of the diffraction peaks of the $Li_{0.05}Ti_yNi_{0.95-y}O$ powders do not change significantly with y increases, comparing to that of the NiO powder diffraction peaks. With increasing the Ti doping concentration up to 5 mol %, another series of diffraction peaks is observed. Moreover, the intensity of these peaks increases with increasing the concentration of Ti doping. This series of the diffraction peaks is comparable to that of the powder diffraction pattern of $NiTiO_3$ in JCPDS card no. 83-0198 for rhombohedral structure and that reported in the literatures (Lin et al., 2006a; Lin et al., 2005b). The lattice parameter of the $Li_{0.05}Ti_yNi_{0.95-y}O$ powders calculated by using Cohen's least-squares method does not change with increasing the concentration of Ti doping ions. These results are similar to that observed in the XRD patterns of the $Ti_yNi_{1-y}O$ powders, as illustrated in figure 5.3.

As shown in figure 5.4(b), the XRD patterns of the $Li_xTi_yNi_{1-x-y}O$ powders with a variety of concentrations of Li (x) and Ti (y) doping ions, the overall diffraction patterns are similar to those of all the previous presents. The main phase of NiO and the second phase of $NiTiO_3$ can be observed. The lattice parameters of the $Li_xTi_yNi_{1-x-y}O$ powders are summarized in Table 5.1. A small difference in value of the lattice parameters can be seen. However, the important clue concerning about the solid solubility of the Li-Ti-Ni-O system is achieved from these XRD patterns. Considering the XRD patterns of the $Li_{0.10}Ti_{0.05}Ni_{0.85}O$ and $Li_{0.02}Ti_{0.05}Ni_{0.93}O$ powders, the series of diffraction peaks corresponding to the second phase of $NiTiO_3$ is only observed in the XRD pattern of the $Li_{0.02}Ti_{0.05}Ni_{0.93}O$ powder, while the concentration of Ti doping of both powders is equal. The lattice parameters of these two samples are nearly the same in value, as summarized in Table 5.1. This interesting result indicates that the solubility of the Ti ions in NiO for the Li-Ti-Ni-O system depends strongly on the concentration of Li doping. However, it is unsuitable now to suggest this result to be related to the Li doping effect, until there will be other supported data. The mechanism of this observation will be discussed in next sections.

5.1.2 Ceramic characterization: crystal structure and morphologies

To investigate the giant dielectric response and electrical properties of the $Li_xTi_yNi_{1-x-y}O$ (LTNO) ceramics, the obtained NiO and $Li_xTi_yNi_{1-x-y}O$ (LTNO) powders were pressed into the pallets, and then sintered at the temperature range of 1200-1280 °C for 4 h. Before the dielectric and electrical properties of these sintered ceramics were investigated, the crystal structure and morphologies of the sintered LTNO ceramics must be characterized by using the XRD and SEM techniques, respectively. The chemical elements comprising to the LTNO ceramics should be investigated at various regions in their microstructure as well.

5.1.2.1 Crystal structure and phase formation

As demonstrated in figures 5.5(a) and 5.5(b), the XRD patterns of the NiO and $Ti_yNi_{1-y}O$ (y = 0.02, 0.05, 0.10, and 0.15) ceramic samples sintered at 1200 and 1280 °C for 4 h, the series of the shape five peaks corresponding to the NiO phase with face-centered cubic structure (JCPDS card no. 78-0429) appears in all of the ceramic samples. The overall XRD patterns of these ceramic samples sintered at these two temperatures are alike in all ways. Certainly, these XRD results confirm that the sintered NiO and $Ti_yNi_{1-y}O$ ceramics are crystalline materials just as their powders are. No shifting of the diffraction peaks of the NiO phase in the XRD patterns of the $Ti_yNi_{1-y}O$ ceramics can be observed in all of the XRD patterns, suggesting that the Ti doping is most likely present in the microstructure either in the grain boundaries or as a second phase. With increasing the Ti doping up to 5 mol %, another series of diffraction peaks is clearly observed; furthermore, the intensity of these peaks increases with increasing the concentration of Ti doping. This series of the diffraction peaks is comparable to that of the powder diffraction pattern of $NiTiO_3$ in JCPDS card no. 83-0198 for rhombohedral structure and those reported in the literatures (Lin et al., 2006a; Lin et al., 2005b). The lattice parameter values of the ceramics calculated by using Cohen's least-squares method are summarized in Table 5.2. These values are independent on the concentration of the Ti content.

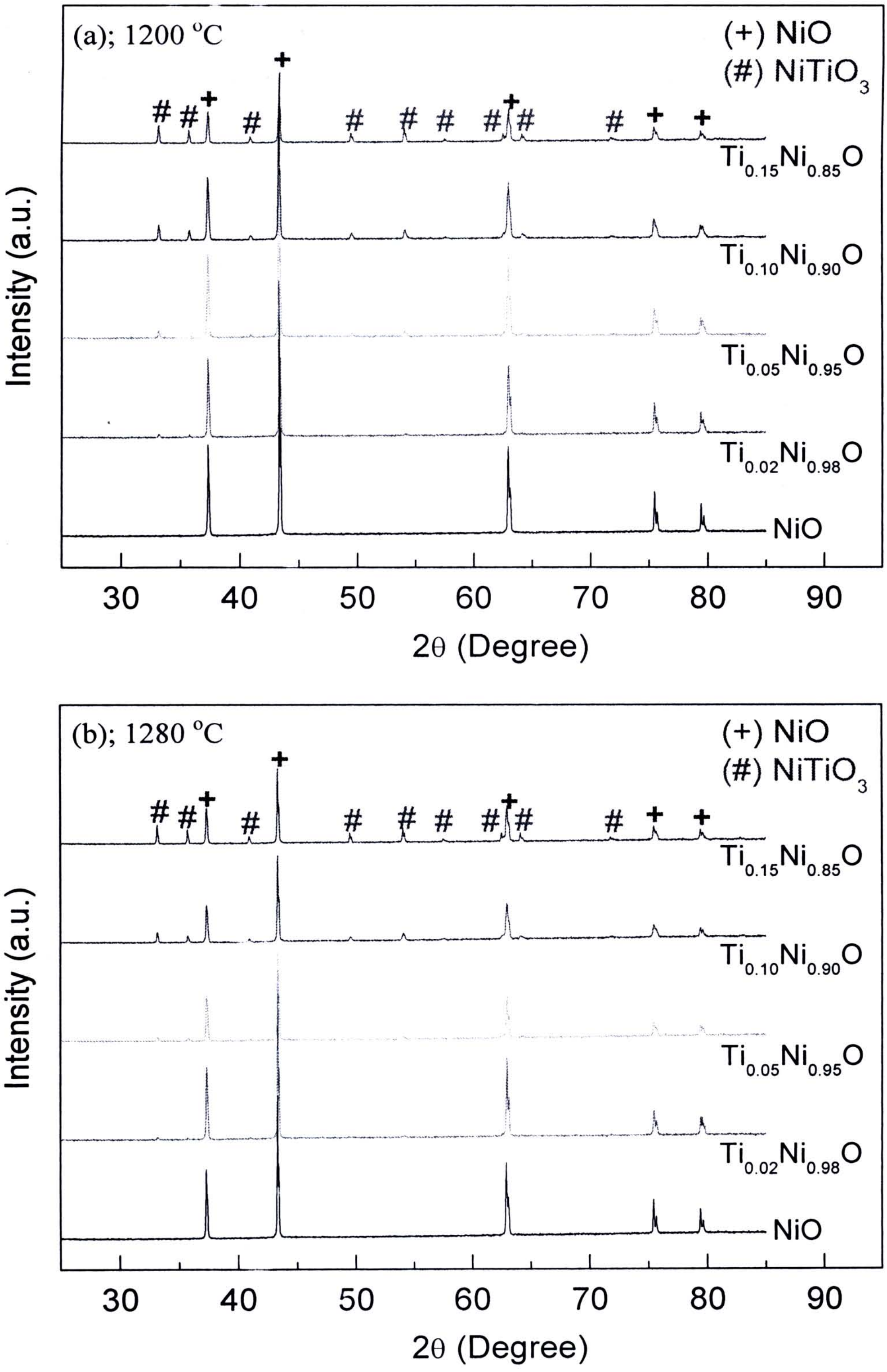

Figure 5.5 XRD patterns of NiO and $Ti_yNi_{1-y}O$ ceramics sintered at (a) 1200 °C and (b) 1280 °C.

Table 5.2 Lattice parameter of NiO, $Ti_yNi_{1-y}O$, and $Li_xTi_yNi_{1-x-y}O$ ceramics sintered at 1200 and 1280 °C for 4 h.

Sample	**Lattice parameter (nm)**	
	Sintered at 1200 °C	**Sintered at 1280 °C**
NiO	4.178±0.001	4.178±0.001
Ti-doped NiO		
$Ti_{0.02}Ni_{0.98}O$	4.178±0.001	4.178±0.002
$Ti_{0.05}Ni_{0.95}O$	4.178±0.002	4.179±0.002
$Ti_{0.10}Ni_{0.90}O$	4.179±0.002	4.178±0.001
$Ti_{0.15}Ni_{0.85}O$	4.178±0.001	4.178±0.001
(Li, Ti)-doped NiO		
$Li_{0.05}Ti_{0.02}Ni_{0.93}O$	4.176±0.001	4.176±0.001
$Li_{0.05}Ti_{0.05}Ni_{0.90}O$	4.175±0.001	4.175±0.001
$Li_{0.05}Ti_{0.10}Ni_{0.85}O$	4.171±0.001	4.175±0.001
$Li_{0.05}Ti_{0.15}Ni_{0.80}O$	4.172±0.001	4.176±0.001
$Li_{0.10}Ti_{0.02}Ni_{0.88}O$	4.173±0.001	4.175±0.001
$Li_{0.10}Ti_{0.05}Ni_{0.85}O$	4.173±0.002	4.173±0.001
$Li_{0.02}Ti_{0.05}Ni_{0.93}O$	4.177±0.001	4.177±0.002

Figure 5.6 demonstrates the XRD patterns of $Li_xTi_yNi_{1-x-y}O$ ceramics with different concentrations of Li (x) and Ti (y) doping ions sintered at 1200 (Figs. (a) and (b)) and 1280 °C (Figs. (c) and (d)) for 4 h. First of all, it is worth noting that the overall diffraction patterns of these LTNO ceramic samples sintered at 1200 °C are similar to those observed in the $Li_xTi_yNi_{1-x-y}O$ ceramics sintered at 1280 °C. Furthermore, the XRD patterns of each composition of the $Li_xTi_yNi_{1-x-y}O$ ceramics, which were sintered at the different temperatures, are similar to that observed in its XRD powder pattern. The series of the main peaks corresponding to the NiO phase with face-centered cubic structure (JCPDS card no. 78-0429) can be observed in all XRD patterns of the $Li_xTi_yNi_{1-x-y}O$ ceramic samples, as revealed in figures 5.6(a)-5.6(d). Certainly, all of the $Li_xTi_yNi_{1-x-y}O$ ceramics are suggested to be as a crystalline material. In spite of the variation of Li and Ti doping concentrations,

the positions of the diffraction peaks do not change significantly. This result is related to the unchanged lattice parameter of each $Li_xTi_yNi_{1-x-y}O$ ceramic, as summarized in Table 5.2. For the $Li_{0.05}Ti_yNi_{0.95-y}O$ ceramic samples, as shown in figures 5.6(a) and 5.6(c), the second phase of $NiTiO_3$ can be detected in the XRD patterns of the ceramic samples that contain the Ti ions with 5 mol % or over. Moreover, the peak intensity of this phase increases with increasing the concentration of Ti doping.

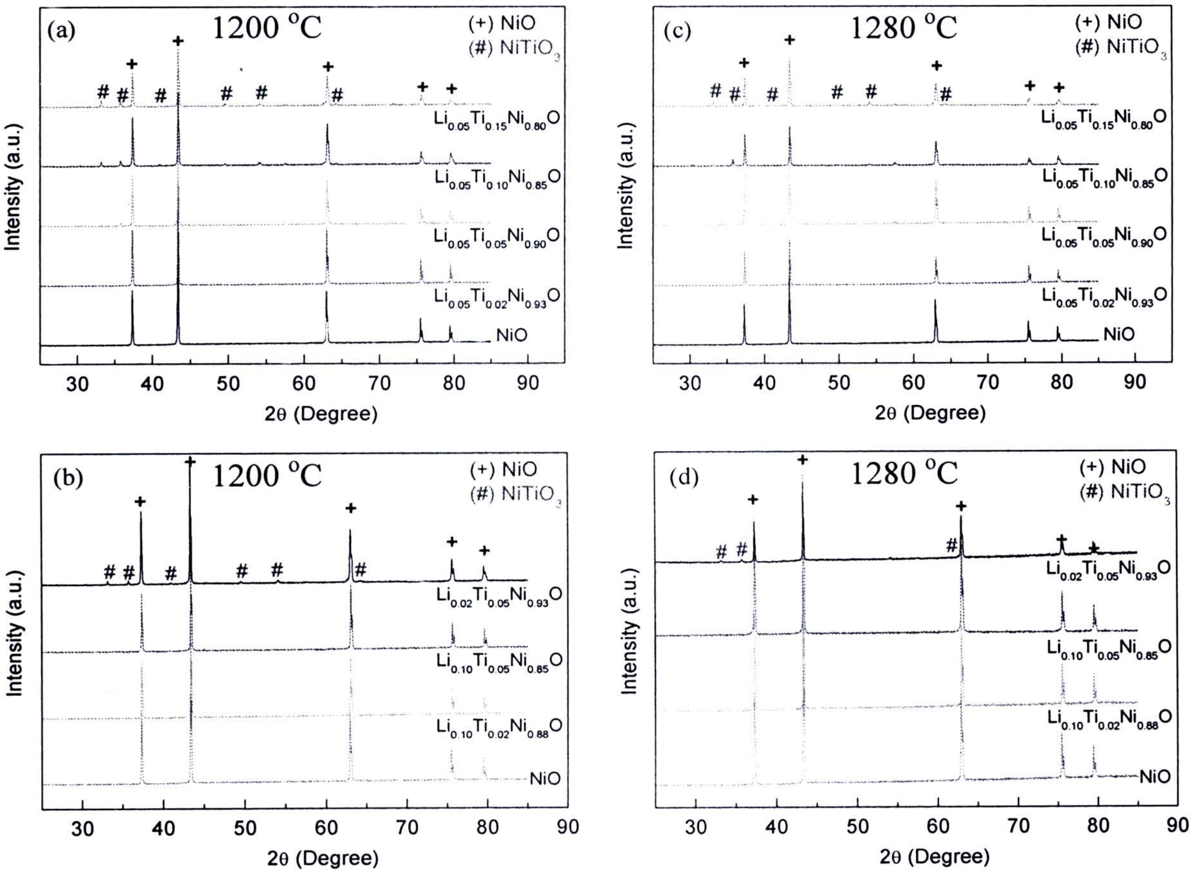

Figure 5.6 XRD patterns of $Li_xTi_yNi_{1-x-y}O$ ceramics sintered at 1200 °C [(a) and (b)] and 1280 °C [(c) and (d)].

Figures 5.6(b) and 5.6(d) show the XRD patterns of the $Li_xTi_yNi_{1-x-y}O$ powders with different concentrations of Li (x) and Ti (y) doping ions. The main phase of NiO appears in all XRD patterns, but the $NiTiO_3$ phase is only observed in the XRD pattern of the LTNO ceramics (both of sintered at 1200 and

1280 °C) with the nominal composition of $Li_{0.02}Ti_{0.05}Ni_{0.93}O$. This result is similar to that observed in the XRD patterns of their powders. Comparing the XRD pattern of the $Li_{0.02}Ti_{0.05}Ni_{0.93}O$ ceramic to that of the $Li_{0.10}Ti_{0.05}Ni_{0.85}O$ ceramic, it can be proved that the Li^+ doping has a remarkable influence on the solubility of the Ti ions in the NiO crystal lattice matrix for the Li-Ti-Ni-O system. The mechanism of this phase formation and the substitution of Ti ions will be interpreted together with the microstructural evolution of these $Li_xTi_yNi_{1-x-y}O$ ceramics, which will be discussed in the next section, microstructure and surface morphologies.

5.1.2.2 Microstructure and surface morphologies

The microstructure and surface morphologies of the $Li_xTi_yNi_{1-x-y}O$ (x = 0, 0.02, 0.05, 0.10 and y = 0, 0.02, 0.05, 0.10, 0.15) ceramics sintered at 1200 and 1280 °C are revealed in the SEM images, as shown in figures 5.7, 5.8, 5.10, 5.11, 5.12, 5.17, and 5.18. It is clearly seen in these figures that the Li and Ti doping ions have a great effect on the microstructural evolution of the NiO ceramic; the microstructure of the $Li_xTi_yNi_{1-x-y}O$ ceramics changes with the Li and Ti doping concentrations. Furthermore, the sintering temperature has also an impact on the microstructure, especially for a grain size—the estimated average grain size of all $Li_xTi_yNi_{1-x-y}O$ ceramics increases as the sintering temperature increases, as shown in Table 5.3. In general, few properties are completely independent of grain size; therefore, this change in the grain size may affect to the dielectric and electrical properties of the $Li_xTi_yNi_{1-x-y}O$ ceramics. The sintering mechanism related to the evolution of microstructure is briefly discussed as follows.

1) Effect of sintering temperature on the microstructure of NiO and $Li_xTi_yNi_{1-x-y}O$ ceramics

As revealed in Table 5.3 and figures 5.7, 5.8, 5.10, 5.11, 5.12, 5.17, and 5.18, the average grain size of a ceramic sintered at 1200 °C is smaller than that of a ceramic sintered at 1280 °C. The average grain size increases with increasing the sintering temperature. According to the fundamental concepts of sintering, for sintering to occur, there must be a reduction of the free energy of the system. To accomplish the process, however, it must also consider the kinetics of matter transport (Rahaman, 2003). As well known, matter transport in crystalline ceramics can occur by diffusion of atoms, ions, or other charged species. The rate of sintering depends on these diffusions. According to the Fick's first law, matter transport or diffusion can be viewed in term of the flux of atoms (J), which is proportional to the concentration gradient (dC/dx) of the diffusing species and diffusion coefficient or diffusivity (D). The diffusion coefficient is usually a strong function of temperature and is also a function of composition. For atomistic diffusion processes, it can be expressed that

$$D = D_0 \exp\left(\frac{-Q}{RT}\right), \tag{5.2}$$

where $-Q$ is the activation energy per mole, T is the absolute temperature, R is the gas constant, and D_0 is a constant value. Equation (5.2) indicates that the matter transport in ceramics increases with increasing the temperature. Accordingly, with increasing the sintering temperature of the $Li_xTi_yNi_{1-x-y}O$ ceramics from 1200 up to 1280 ^{o}C, the diffusion coefficient of O and Ni atoms in NiO should be enhanced. The diffusion coefficient of Ni atoms in NiO increased from ~10^{-11} to ~10^{-10} cm^2/s with increasing the temperature from 1200 to 1300 ^{o}C (at 1 atm). O atoms start to diffuse at the temperature of about 1300 ^{o}C (Chiang et al., 1997). As a result, the rate of diffusion of Ni in the NiO-based ceramics in this research increases with increasing the sintering temperature, which directly results in the increase in the rate of sintering. Consequently, the grain sizes of all ceramic compositions increase as the sintering temperature increases.

2) Effect of Ti doping on the microstructure of $Ti_yNi_{1-y}O$ ceramics

Comparing the microstructure of the NiO ceramic to the Ti-doped NiO ($Ti_yNi_{1-y}O$) ceramics sintered at 1200 and 1280 ^{o}C, as shown in figures 5.7[(a)-(e)] and 5.8[(a)-(e)], it is clear that the Ti doping has several effects on microstructure of the NiO ceramics; porosity, grain size and shape are varied with the Ti doping. As summarized in Table 5.3, the average grain sizes of the NiO ceramics (both of sintered at 1200 and 1280 ^{o}C) decrease when the NiO ceramics were doped with Ti ions. Moreover, the average grain sizes of the $Ti_yNi_{1-y}O$ ceramics decrease with increasing the concentration of Ti doping from 2 up to 10 mol %. However, it increases again when the concentration of Ti doping increases further from 10 to 15 mol %. For the porosity, as revealed in figures 5.7(a)-5.7(e), it is clear that the amount of pores observed in the microstructure of the NiO ceramic is less than that of observed in the $Ti_yNi_{1-y}O$ ceramic samples. However, the quantitative analysis of the amounts of such pores was not conducted in this thesis. It is important to note that the grain growth behavior as well as the evolution of the microstructure of the NiO and $Ti_yNi_{1-y}O$ samples sintered at 1280 °C shown in figures 5.8(a)-5.8(e) is similar to those observed in the samples sintered at 1200 °C. As revealed in the inset of figures 5.7(b)-5.7(e) and 5.8(b)-5.8(e) for the surface morphologies of the $Ti_yNi_{1-y}O$ ceramics with higher magnification, it is found that a set of small grains, as suggested by the yellow arrows, is exhibited in the microstructure. Most of them present in corners of regular grains, few exhibit in the regular grains. The grain sizes of these small grains are in the ranges of about 0.5-1.0 μm and 1.0-2.0 μm for the ceramics sintered at 1200 and 1280 °C, respectively. It is also found that both the grain size and the amounts of these small grains tend to increase with increasing the concentration of Ti doping. According to the XRD results as previously presented in the section 5.1.2.1, it is confirmed that the second phase of $NiTiO_3$ is exhibited in the $Ti_yNi_{1-y}O$ ceramic samples. Moreover, the intensity of the diffraction peaks corresponding to this second phase was found to increase when the Ti doping concentration increases. As a result, it is most likely that these small grains observed in the SEM images of the $Ti_yNi_{1-y}O$ samples may be the second phase of $NiTiO_3$, as detected in their XRD patterns.

To confirm this expectation, chemical compositions of these small grains and the regular grains were investigated by using SEM-EDS techniques. As shown in figure 5.9, SEM-EDS results of the $Ti_{0.02}Ni_{0.98}O$ ceramic sintered at 1280 °C, the chemical compositions of the ceramic were investigated at different four points in the microstructure. Points 1 and 4, as illustrated in figure 5.9(a), are in the small grains, which are expected to be the $NiTiO_3$ particles. Points 2 and 3 are in the different regular grains, which are expected to be the NiO grains. Figures 5.9(b)-5.9(e) show the EDS spectra corresponding to the testing points 1, 2, 3, and 4, respectively. Obviously, the peaks corresponding to the Ti atom can be observed in the EDS spectra of the testing points 1 and 4, but can not be observed at points 2 and 3. These results strongly indicate that the small grains observed in the $Ti_yNi_{1-y}O$ ceramics are specified as the $NiTiO_3$ particles. This implies that the Ti doping ions contained in the $Ti_yNi_{1-y}O$ mixture powders prefer to react with Ni ions forming the $NiTiO_3$ phase than to substitute into the Ni sites in the crystal lattice. It is important to note that the increase in the grain size observed in the $Ti_{0.15}Ni_{0.85}O$ ceramic is certainly due to the fact that the grain sizes of the $NiTiO_3$ particles are counted with the regular grain sizes. In this case, the grain size of only set of the regular grains can accurately be determined by using the SEM backscattered images; however, it is beyond the scope of this research. In spite of the low accuracy of the grain-sized measurement, it can be observed that the regular grain size of the NiO particles tends to decrease with increasing the concentration of Ti doping. Note that the peaks corresponding to Au observed in all EDS spectra are due to the gold sputtering on the surface of the sample for the SEM measurement. From this point of view, it is appropriate to suggest that Ti doping can affect to the microstructure of the NiO ceramics through the formation of the second phase of $NiTiO_3$. The large amounts of pores observed in the microstructure and the decrease in the grain size for the $Ti_yNi_{1-y}O$ samples can be described based on the *mechanisms of diffusion*[5]. Surface diffusion, lattice diffusion from the particle surfaces to the neck, and vapor transport, which lead to neck growth, may be suppressed by the $NiTiO_3$ phase. Furthermore, the movement of grain boundary under the *driving force*[6] of its curvature may also be held up by the $NiTiO_3$ particles. The grain growth of the ceramics is therefore obstructed by the second phase particles. This observed grain growth mechanism can be explained by the Zener model, which is the quantitative model that uses to ascribe particle inhibited grain growth, (Rahaman, 2003), as

$$G_L = \frac{2\alpha}{3}\left(\frac{r}{f}\right), \tag{5.3}$$

where G_L is the limiting grain size, f is the volume fraction of the including particles, r is the radius of the including particles, and α is a geometrical shape

---

[5] In general, solid-state diffusion can occur by several paths that define the mechanisms of diffusion.

[6] The driving force for grain growth is the decrease in free energy.

factor (e.g., =2 for a spherical grain). The Zener relationship, equation (5.3), indicates that a limiting grain size is inversely proportional to the volume fraction of including particles. Note that the Zener model have assumed that the including particles are nanosize, spherical, insoluble, immobile, and randomly distributed in the polycrystalline solid. Although the observed $NiTiO_3$ particles are not completely spherical and non-nanosize, the tendency of these experimental results is coincident with the model. This means that the grain growth behavior occurred in the $Ti_yNi_{1-y}O$ samples can qualitatively be described by the Zener model. Thus, the decrease in the grain size of the $Ti_xNi_{1-x}O$ samples should be attributed to the increase in volume fraction of $NiTiO_3$ phase.

Table 5.3 Average grain size of NiO, $Ti_yNi_{1-y}O$, $Li_xTi_{1-x}O$, and $Li_xTi_yNi_{1-x-y}O$ ceramics sintered at 1200 and 1280 °C for 4 h.

Sample	**Average grain size (μm)**	
	Sintered at 1200 °C	**Sintered at 1280 °C**
NiO	2.57	5.57
$Ti_{0.02}Ni_{0.98}O$	~2.12	~5.55
$Ti_{0.05}Ni_{0.95}O$	~2.16	~3.21
$Ti_{0.10}Ni_{0.90}O$	~1.81	~2.75
$Ti_{0.15}Ni_{0.85}O$	~1.94	~3.03
$Li_{0.05}Ti_{0.02}Ni_{0.93}O$	3.28	9.72
$Li_{0.05}Ti_{0.05}Ni_{0.90}O$	4.93	9.93
$Li_{0.05}Ti_{0.10}Ni_{0.85}O$	4.86	10.47
$Li_{0.05}Ti_{0.15}Ni_{0.80}O$	5.05	10.68
$Li_{0.10}Ti_{0.02}Ni_{0.88}O$	5.11	5.85
$Li_{0.10}Ti_{0.05}Ni_{0.85}O$	3.13	6.90
$Li_{0.02}Ti_{0.05}Ni_{0.93}O$	3.89	8.98
$Li_{0.02}Ni_{0.98}O$	-	4.25
$Li_{0.05}Ni_{0.95}O$	-	5.69
$Li_{0.10}Ni_{0.90}O$	-	6.68

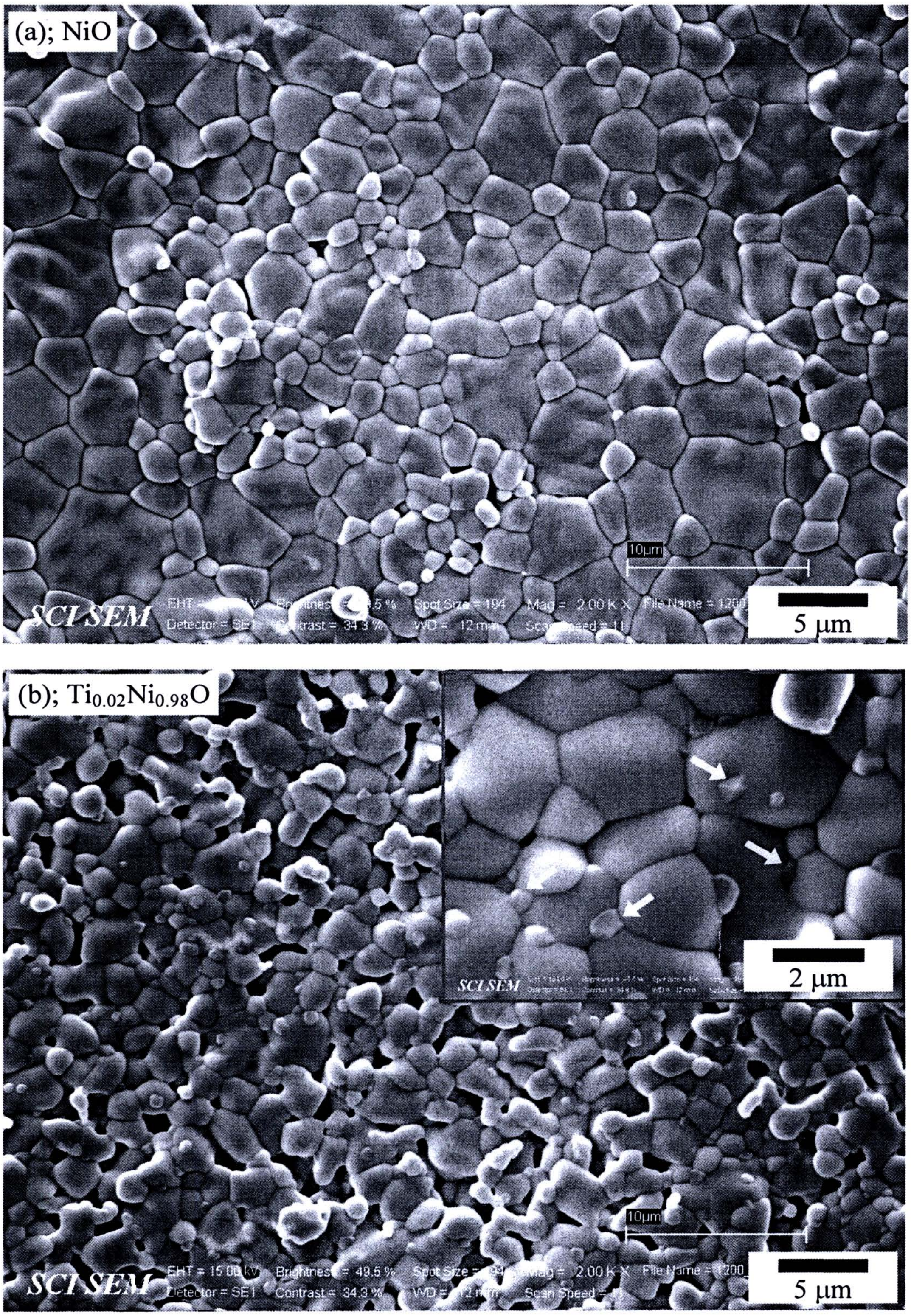

Figure 5.7 SEM images of $Ti_yNi_{1-y}O$ ceramics sintered at 1200 °C revealing the surface morphologies; inset is its higher magnification image.

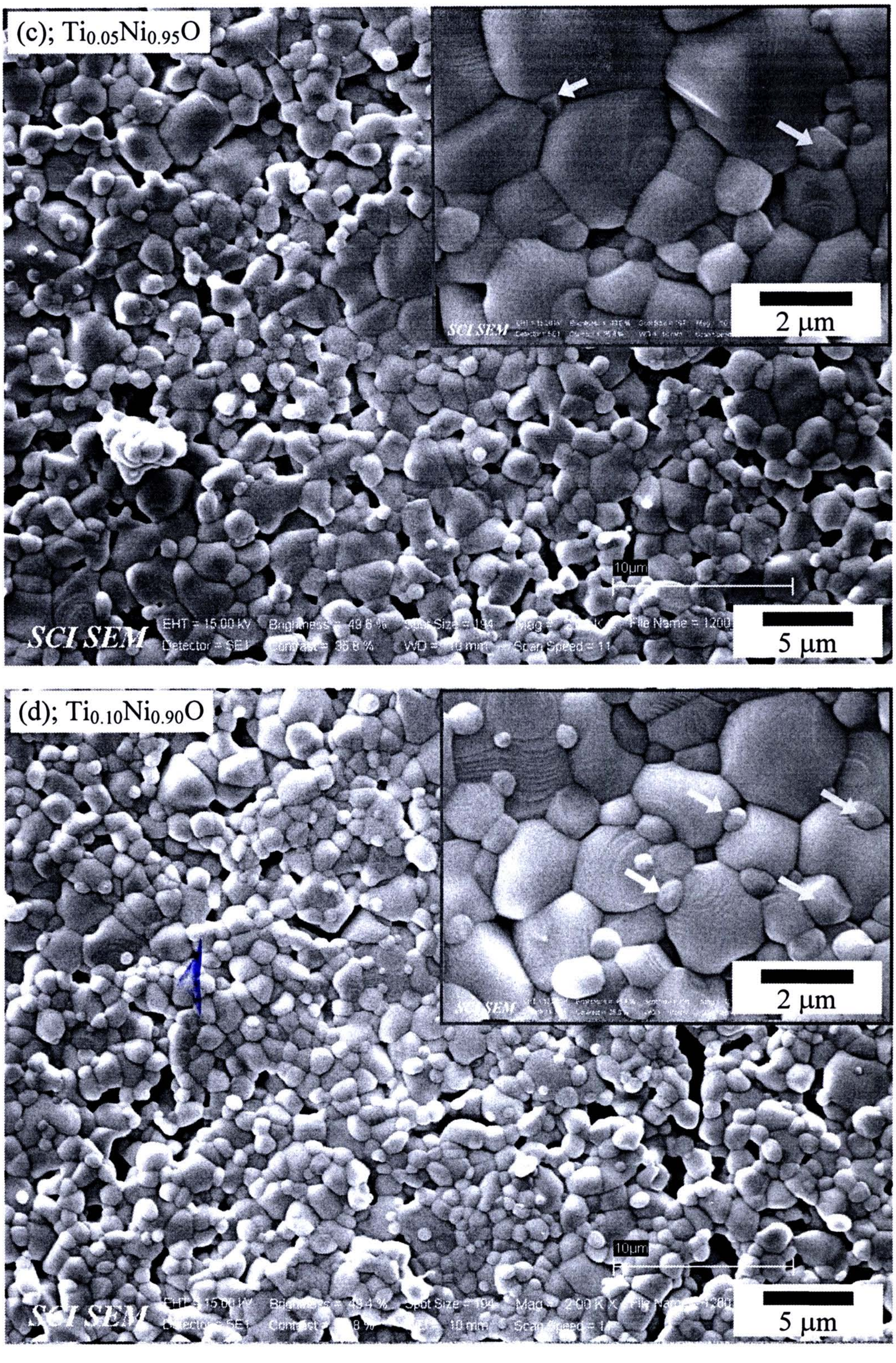

Figure 5.7 SEM images of $Ti_yNi_{1-y}O$ ceramics sintered at 1200 ^{o}C revealing the surface morphologies; inset is its higher magnification image. (Cont.)

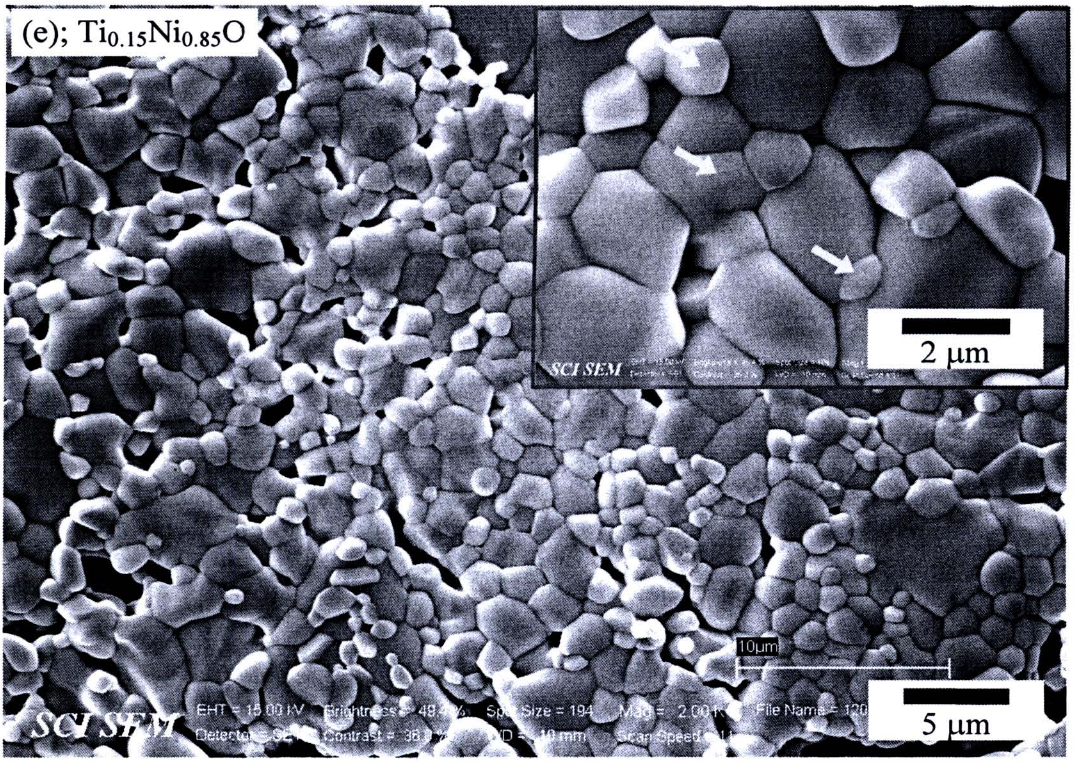

Figure 5.7 SEM images of $Ti_yNi_{1-y}O$ ceramics sintered at 1200 °C revealing the surface morphologies; inset is its higher magnification image. (Cont.)

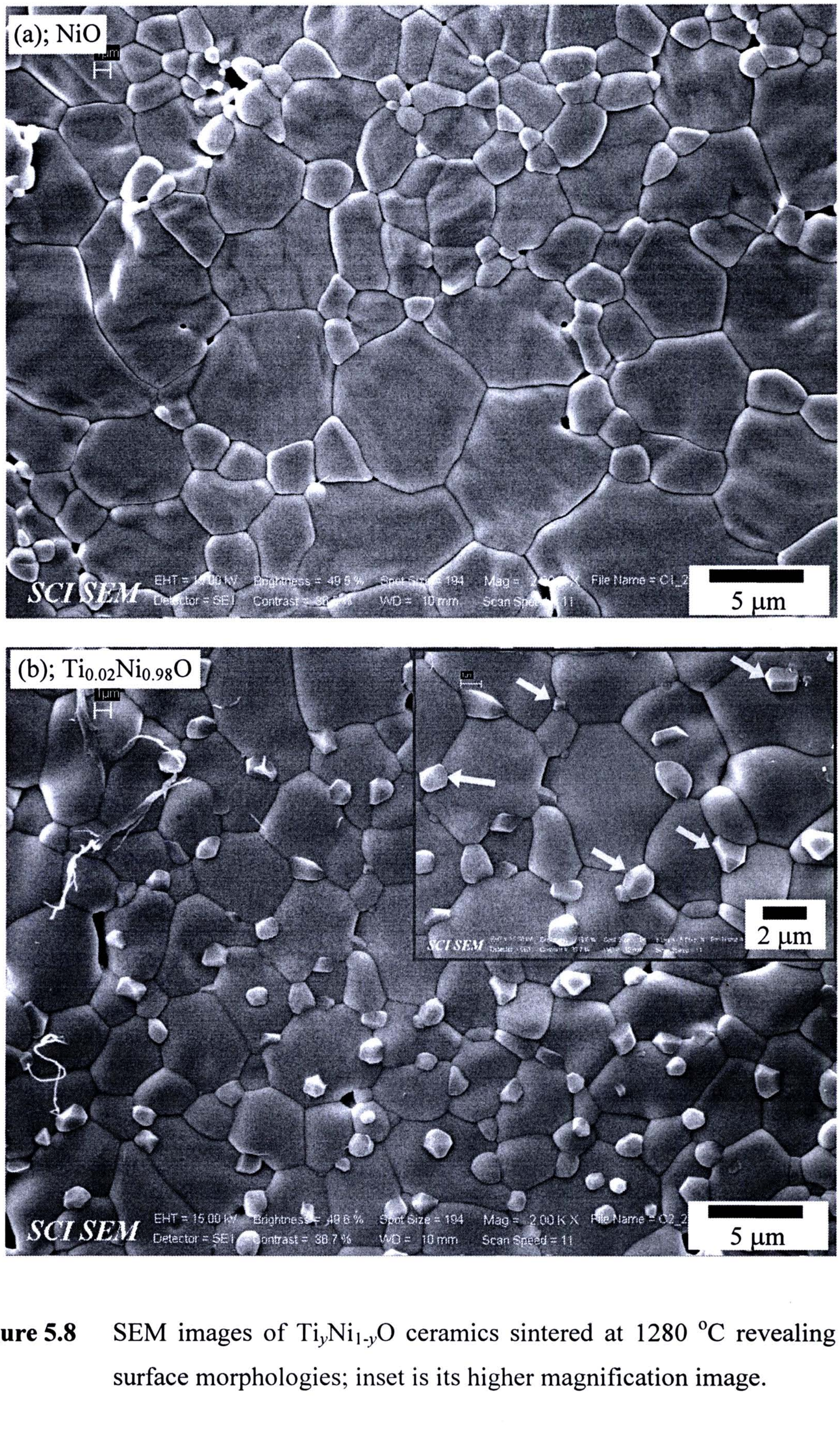

Figure 5.8 SEM images of $Ti_yNi_{1-y}O$ ceramics sintered at 1280 °C revealing the surface morphologies; inset is its higher magnification image.

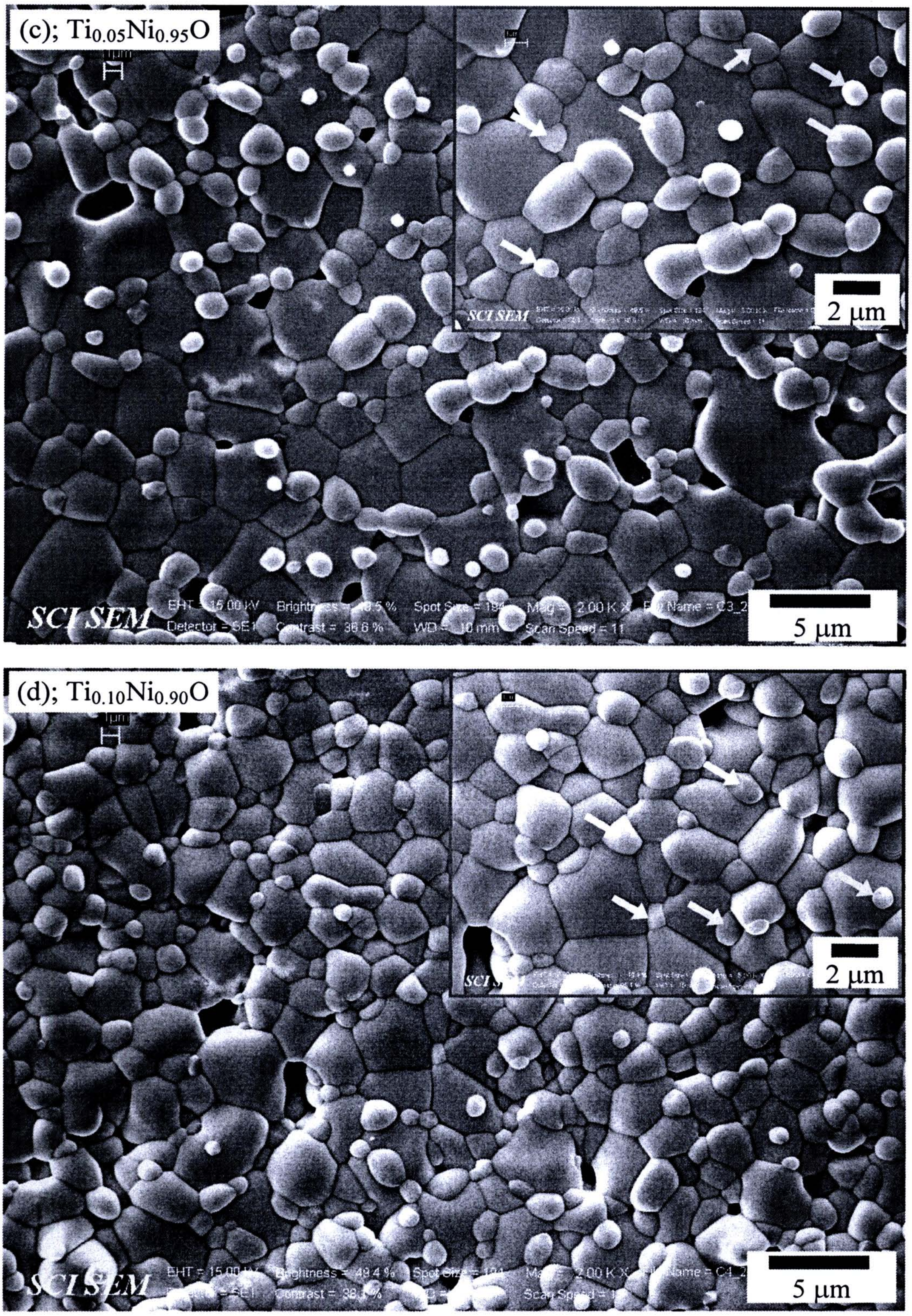

Figure 5.8 SEM images of $Ti_yNi_{1-y}O$ ceramics sintered at 1280 °C revealing the surface morphologies; inset is its higher magnification image. (Cont.)

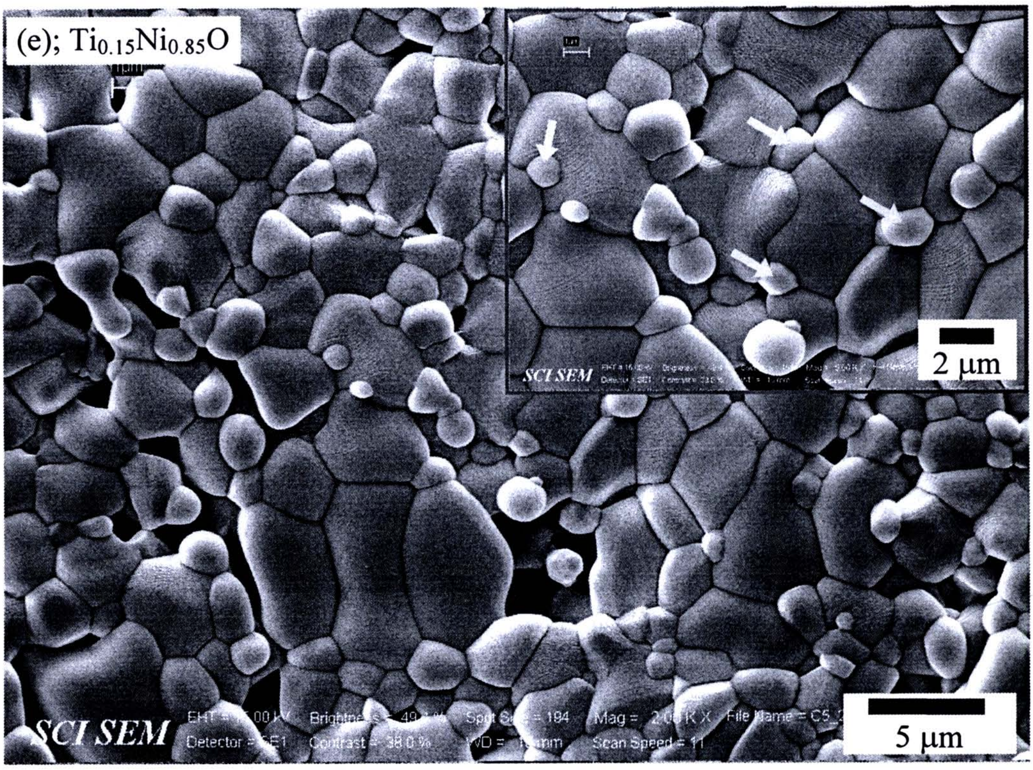

Figure 5.8 SEM images of $Ti_yNi_{1-y}O$ ceramics sintered at 1280 °C revealing the surface morphologies; inset is its higher magnification image. (Cont.)

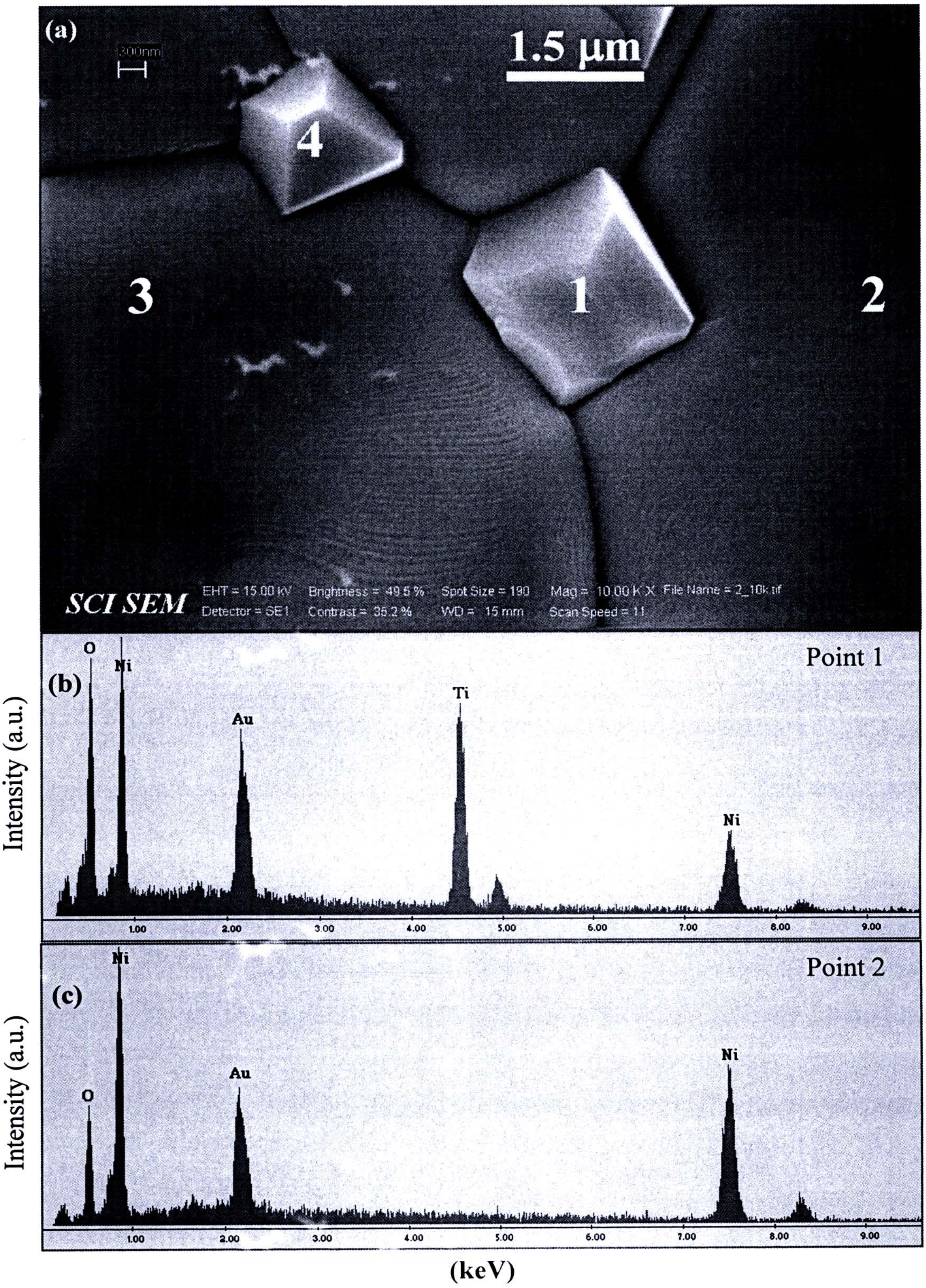

Figure 5.9 (a) SEM image and (b)-(e) EDS spectra of the testing points 1-4 for the $Ti_{0.02}Ni_{0.98}O$ ceramic sintered at 1280 ^{o}C.

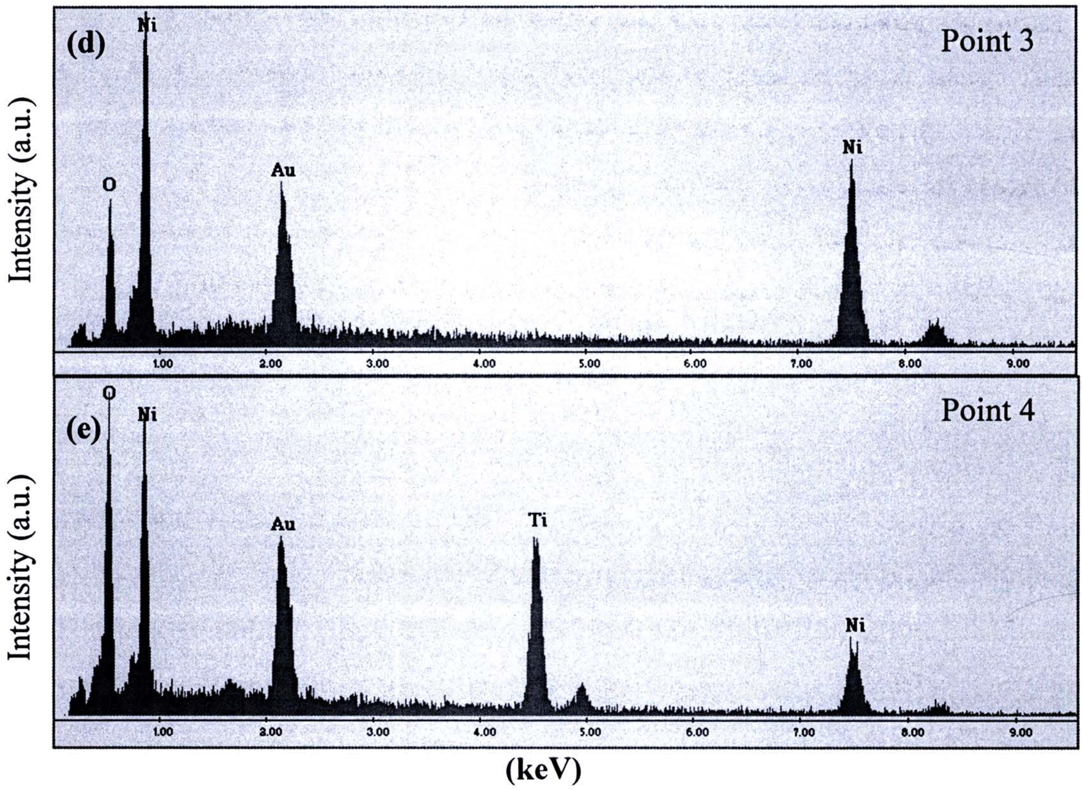

Figure 5.9 (a) SEM image and (b)-(e) EDS spectra of the testing points 1-4 for the $Ti_{0.02}Ni_{0.98}O$ ceramic sintered at 1280 °C. (Cont.)

3) Effect of Li doping on the microstructure of $Li_xNi_{1-x}O$ ceramics

To investigate the microstructure and understand the grain growth mechanism of the $Li_xTi_yNi_{1-x-y}O$ ceramics, it is important to study and characterize the microstructure of the $Ti_yNi_{1-y}O$ and $Li_xNi_{1-x}O$ ceramics comparing to the pure NiO ceramic. The surface morphology of the $Li_xNi_{1-x}O$ ceramics, where x = 0.02, 0.05, and 0.10, is shown in figures 5.10(a)-5.10(c), respectively. The average grain sizes of these three ceramic samples are summarized in Table 5.3. The average grain size of the $Li_xNi_{1-x}O$ ceramics increases with increasing the concentration of the Li doping ions. It can also be observed from the SEM images that the amounts of pores and the pore size of the $Li_xNi_{1-x}O$ ceramics enhance as the Li (x) increases. This result is similar to that observed in the literature (Antolini, 1990). All of the samples show the obvious grain and grain boundary structure. According to the XRD patterns of the $Li_xNi_{1-x}O$ powders (Fig. 5.2) and ceramics (do not show), only a series of diffraction peaks corresponding to the NiO phase can be observed in the XRD patterns. This may be due to the fact that the Li doping ions can substitute completely the Ni^{2+} sites (Antolini, 2003; Antolini, Ferretti, 1997; Lin SP et am., 2002; Li Z et al., 2005). When Ni sites in NiO crystal lattice are occupied by the Li doping ions, point defects are introduced and can be ascribed by the Kroger-Vink notation, as

$$Li_2O \xrightarrow{NiO} 2Li'_{Ni} + V_O^{\bullet\bullet} + O_O^x . \qquad (5.4)$$

According to equation (5.4) and assuming that the Li_2O is completely incorporated into the NiO ceramic, the electroneutrality condition becomes,

$$[Li'_{Ni}] = 2[V_O^{\bullet\bullet}] = [Li] . \qquad (5.5)$$

Equation (5.5) means that the concentration of oxygen vacancy ($[V_O^{\bullet\bullet}]$) is depended on the total atomic concentration of the Li ($[Li]$) doping. Therefore, the concentration of oxygen vacancies in the $Li_xNi_{1-x}O$ particles increases with increasing the Li doping. Generally, it is widely accepted that the rate of sintering is related linearly to the rate of diffusion, which depends on the type and concentration of defects (Rahaman, 2003). Thus, the observed enhancement of the average grain size of the $Li_xNi_{1-x}O$ ceramics might be associated with the increase in the concentration of the point defects, i.e., oxygen vacancies ($[V_O^{\bullet\bullet}]$), which is due to the increase in the Li doping. However, this change in the grain size is certainly related to other factors because the sintering of ceramics is usually the complication process. Furthermore, it is very complex because of the several transport paths and different ionic species.

It was suggested that $LiNiO_2$ particles were firstly formed in the firing process of the Li-Ni-O system, and then they melted and diffused into the interior of NiO particles (Li Z et al., 2005). It is possible that the melting $LiNiO_2$ phase can result in a change of the surface diffusion and lattice diffusion from the particle surfaces to the neck. These two diffusion mechanisms lead to the neck growth without densification (Rahaman, 2003). Thus, the pore size will be increased with increasing the Li content, corresponding to the experimental result. It can roughly be suggested that the Ti doping ions can not enter into the NiO crystal lattice, but the Li doping can. The different mechanism of these two types of substitution might be described based on the melting point of the $NiTiO_3$ and $LiNiO_2$ phases for the Ti-Ni-O and Li-Ni-O ceramic systems, respectively. With adding the Ti and Li ions into NiO, they prefer to form with the Ni and O atoms to produce the $NiTiO_3$ and $LiNiO_2$ phases, respectively. Unfortunately, the melting point of the $NiTiO_3$ ceramic phase is very high (>1200 °C); as a result, it is usually used in high temperature applications (Murugan et al., 2006; Dharmaraj et al., 2004). Thus, the $NiTiO_3$ and NiO particles can not diffuse into each other. Unlikely, the melting point of the $LiNiO_2$ phase is about 730 °C (Li Z et al., 2005); hence, it can diffuse easily into the NiO particles during the sintering process at temperature about 1200-1280 °C or during the calcinations process.

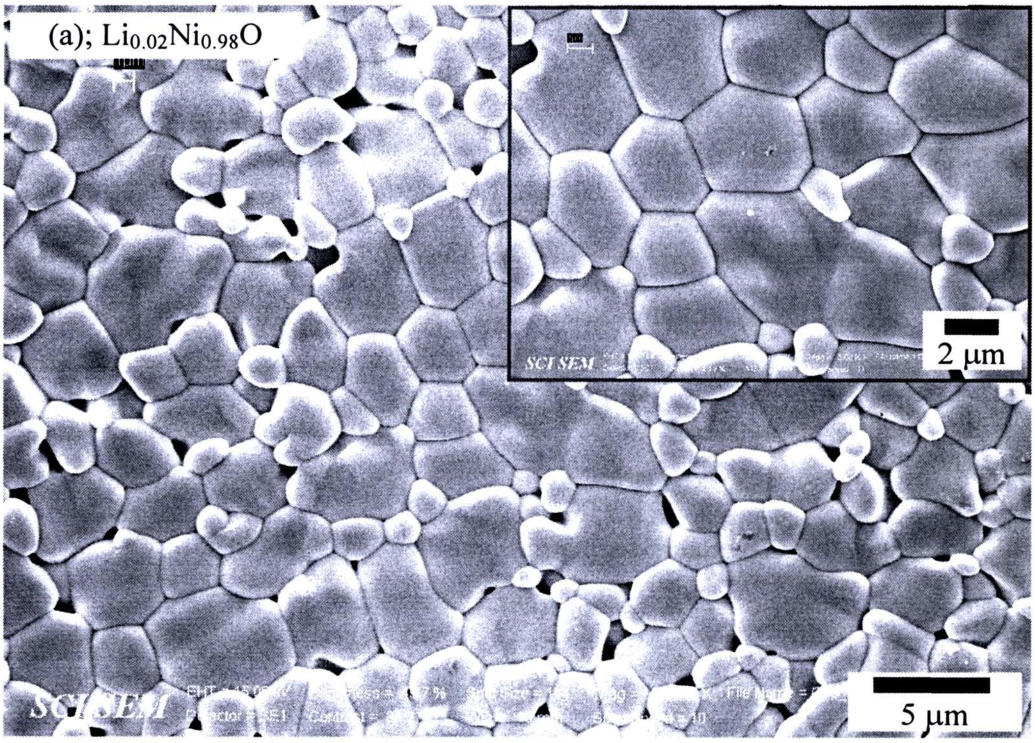

Figure 5.10 SEM images of $Li_xNi_{1-x}O$ ceramics sintered at 1280 °C revealing the surface morphologies; inset is its higher magnification image.

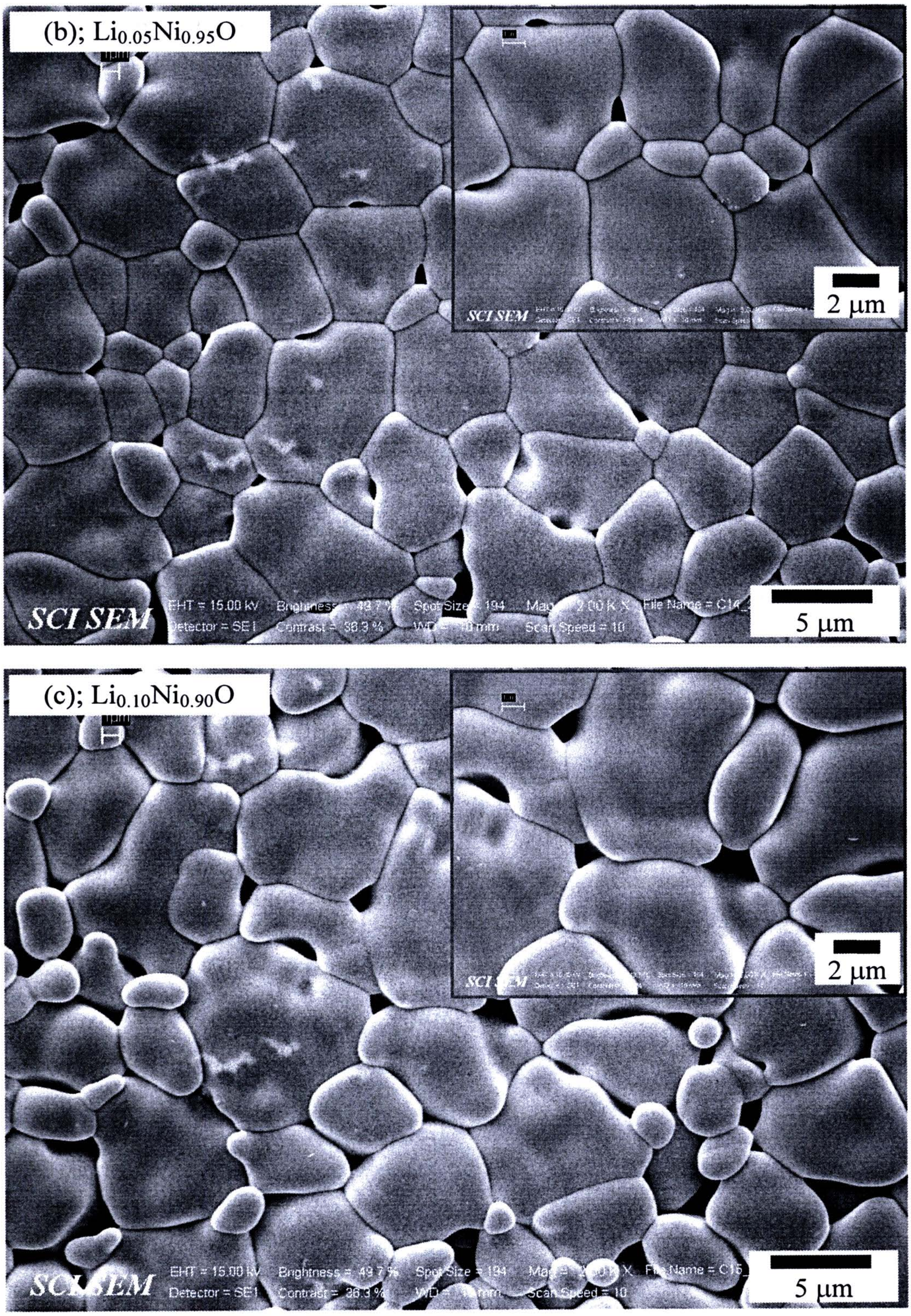

Figure 5.10 SEM images of $Li_xNi_{1-x}O$ ceramics sintered at 1280 °C revealing the surface morphologies; inset is its higher magnification image. (Cont.)

4) Effect of Li doping added into $Ti_yNi_{1-y}O$ for the $Li_{0.05}Ti_yNi_{0.95-y}O$ ceramics

According to the phase formation and the microstructure analyses as well as the investigation of chemical compositions for the $Ti_yNi_{1-y}O$ ceramics, it is strongly suggested that the Ti doping ions tend to bond with the Ni and O ions forming a second phase of $NiTiO_3$. Most of the $NiTiO_3$ particles are found to be at the grain boundaries, especially at the corners of the grains. However, it is possible that few parts of the Ti doping ions might substitute the Ni^{2+} sites in the NiO crystal lattice. The XRD patterns of the $Li_{0.05}Ti_yNi_{0.95-y}O$ ceramics, as shown in figures 5.6(a) and 5.6(c), demonstrate that the $NiTiO_3$ phase can clearly be observed when the Ti doping concentration increases up to 5 mol % ($y \geq 0.05$) similar to the XRD patterns of the $Ti_yNi_{1-y}O$ ceramics. Indeed, the $NiTiO_3$ phase can be exhibited in the $Ti_{0.02}Ni_{0.98}O$ powder and ceramics. However, it is not clearly observed because the intensity is relatively low. With doping 5 mol % of Li, the $NiTiO_3$ phase can not be observed, as revealed in the XRD pattern of the $Li_{0.05}Ti_{0.02}Ni_{0.93}O$ ceramic. This observed mechanism of the phase formation of the doped-ceramic system of the $Ti_yNi_{1-y}O$ and $Li_{0.05}Ti_yNi_{0.95-y}O$ ceramics indicates that the phase formation of the $Li_xTi_yNi_{1-x-y}O$ ceramic system might be associated with the Li doping. Moreover, it is demonstrated from the SEM images that the Li doping has a great impact on the microstructure of the $Li_xTi_yNi_{1-x-y}O$ ceramics, as shown in figures 5.11 and 5.12.

The SEM images showing surface morphologies of the $Li_{0.05}Ti_yNi_{0.95-y}O$ ceramics sintered at 1200 and 1280 °C are respectively revealed in figures 5.11 and 5.12. It is clear that the Li doping has an remarkable influence on the microstructure of the $Li_{0.05}Ti_yNi_{0.95-y}O$ ceramics. Those $Li_{0.05}Ti_yNi_{0.95-y}O$ ceramics are denser than the $Ti_yNi_{1-y}O$ ceramics (Figs. 5.7 and 5.8) for each composition of the Ti doping (y). The average grain size of a $Li_{0.05}Ti_yNi_{0.95-y}O$ ceramic is found to be larger than that of an initial $Ti_yNi_{1-y}O$ ceramic, as summarized in Table 5.3. This means that the Li doping can cause a change in grain size and shape of the $Ti_yNi_{1-y}O$ ceramics. The features of grains and grain boundaries are considered to be the major difference between the $Ti_yNi_{1-y}O$ and $Li_{0.05}Ti_yNi_{0.95-y}O$ microstructures. For examples, the small *grains of the $NiTiO_3$ particles observed in the $Ti_{0.02}Ni_{0.98}O$ ceramic (Fig. 5.8(b)) are fully erased by doping Li ions, as shown in figure 5.12*(a). *These $NiTiO_3$ particles can* not be observed in the SEM image of the $Li_{0.05}Ti_{0.02}Ni_{0.93}O$ ceramic (Fig. 5.12(a)). Looking carefully at the grain boundaries of the $Li_{0.05}Ti_{0.02}Ni_{0.93}O$ ceramic as demonstrated in the inset, it is found that there is something accumulated along the grain boundaries. On the other hand, there is nothing accumulated along the grain boundaries of the $Ti_{0.02}Ni_{0.98}O$ ceramic (the inset of Fig. 5.8(b)). These results are an important clue concerning about the effect of Li doping on the solubility of the Ti ions into the crystal lattice of the Li-Ti-Ni-O system. The brief discussion on the influence of Li doping on the crystal structure of the $Li_xTi_yNi_{1-x-y}O$ ceramic system will be represented in the next two sections for the effects of Li doping on the solubility and microstructure of the $Li_xTi_yNi_{1-x-y}O$ ceramics. Note that the small particles of $NiTiO_3$ present in the microstructure of all $Ti_yNi_{1-y}O$ samples can be erased by doping Li ions. These particles of the second phase of $NiTiO_3$ disappear on the microstructure of the $Li_xTi_yNi_{1-x-y}O$ ceramics. The microstructural evolution of the $Li_xTi_yNi_{1-x-y}O$ ceramics is affected by the Li doping.

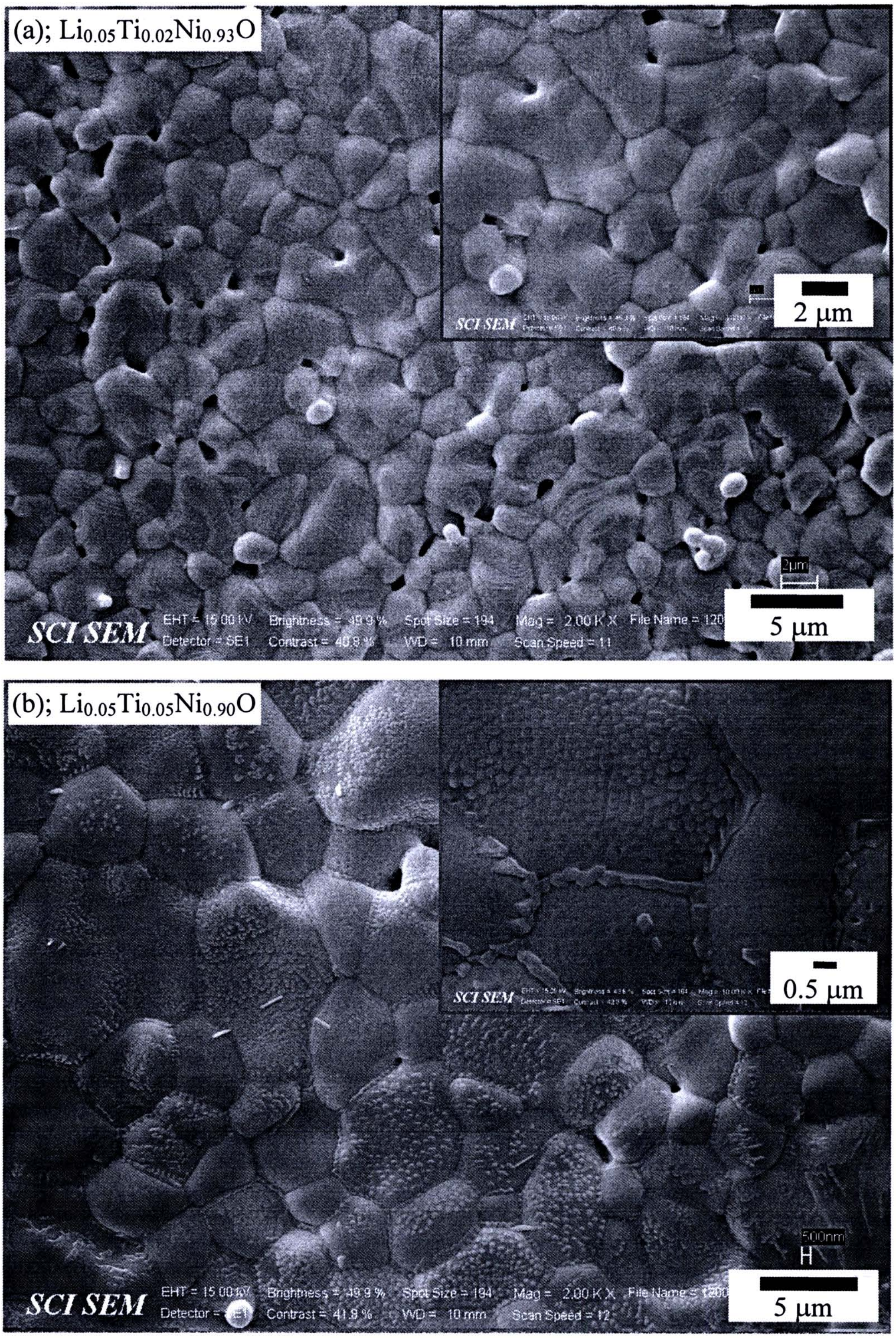

Figure 5.11 SEM images of $Li_{0.05}Ti_yNi_{0.95-y}O$ ceramics sintered at 1200 °C; inset shows its higher magnification image.

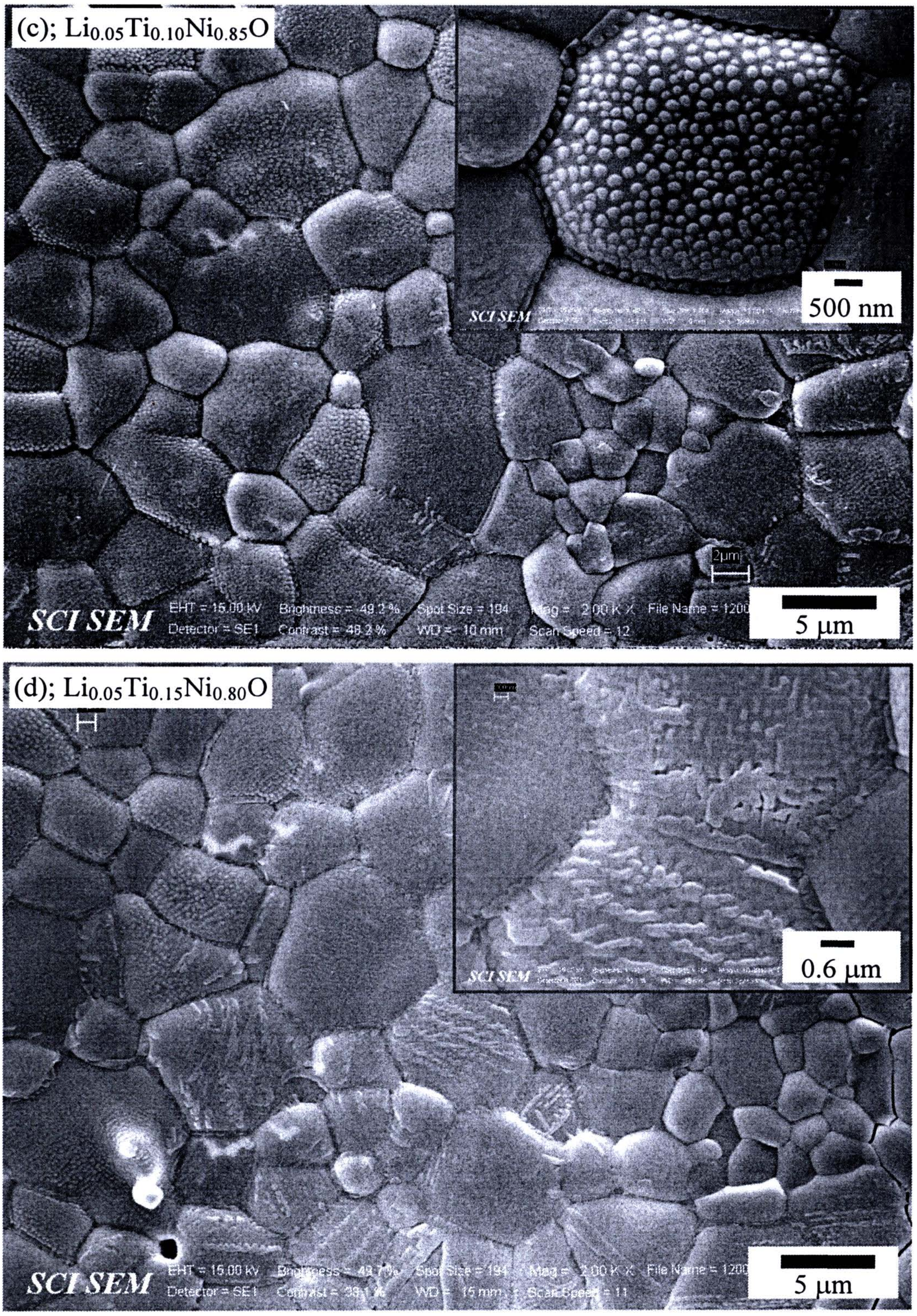

Figure 5.11 SEM images of $Li_{0.05}Ti_yNi_{0.95-y}O$ ceramics sintered at 1200 °C; inset shows its higher magnification image. (Cont.)

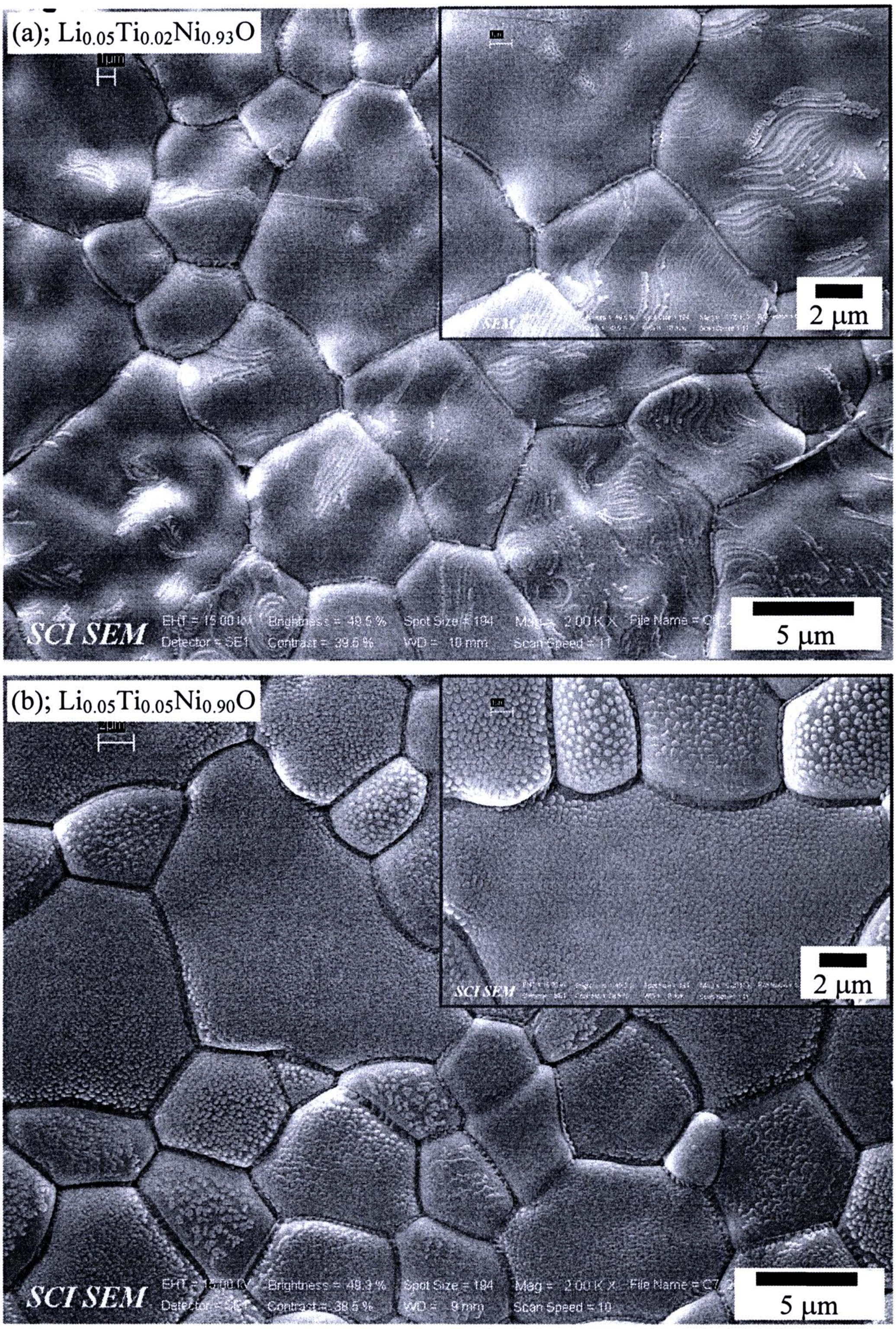

Figure 5.12 SEM images of $Li_{0.05}Ti_yNi_{0.95-y}O$ ceramics (sintered at 1280 °C; inset shows its higher magnification image.

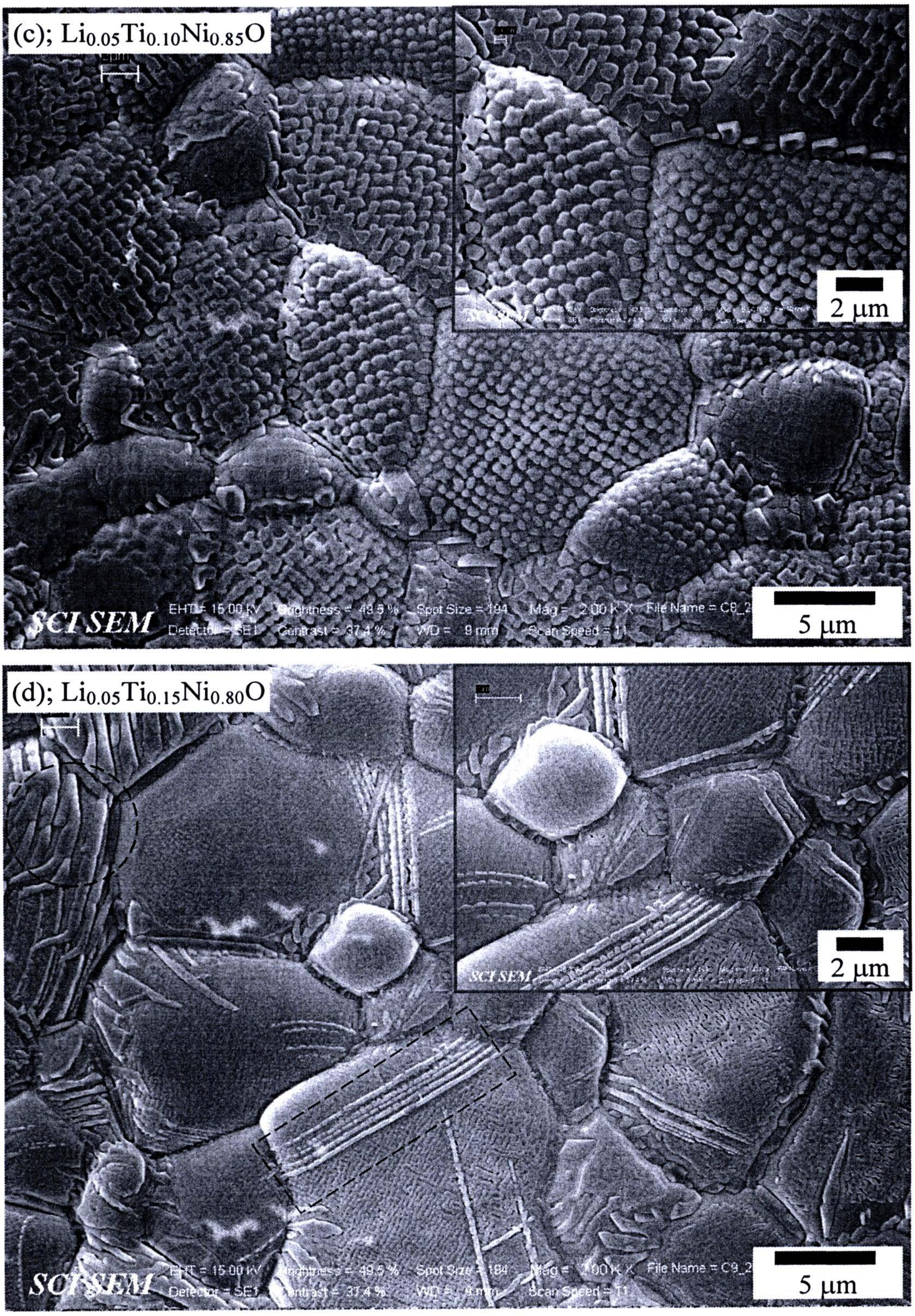

Figure 5.12 SEM images of $Li_{0.05}Ti_yNi_{0.95-y}O$ ceramics sintered at 1280 °C; inset shows its higher magnification image (Cont.)

5) Effect of Ti doping concentration on the microstructural evolution of the $Li_{0.05}Ti_yNi_{0.95-y}O$ ceramics

By focusing on the $Li_{0.05}Ti_yNi_{0.95-y}O$ ceramics where y = 0.02, 0.05, 0.10, and 0.15, it can be observed that the concentration of the Ti doping cause a change in the feature of microstructure. As discussed early, the $NiTiO_3$ particles can not be observed in the SEM images of all $Li_{0.05}Ti_yNi_{0.95-y}O$ ceramics. However, the significant different features of the microstructure among these four samples are occurred. As demonstrated in Table 5.3, although the average grain sizes of the $Li_{0.05}Ti_yNi_{0.95-y}O$ samples are insignificantly dependent on the Ti doping, the average grain size of the samples tends to increase gradually with increasing the Ti doping. To brief, only the set of the samples sintered at 1280 °C [Figs. 5.12(a)-5.12(d)] is selected as the subject for the discussion in order to elucidate the effect of Ti doping on the evolution of microstructure.

The surface morphology of the $Li_{0.05}Ti_{0.02}Ni_{0.93}O$ (y = 0.02) ceramic (Fig. 5.12(a)) shows clearly smooth grains; in addition, there is something accumulated along the grain boundaries. The overall microstructure of the $Li_{0.05}Ti_{0.02}Ni_{0.93}O$ ceramic is totally different from that observed in the $Ti_{0.02}Ni_{0.98}O$ ceramic (Fig. 5.8(b)). The surprising result is found in the SEM image of the $Li_{0.05}Ti_{0.05}Ni_{0.90}O$ (y = 0.05) ceramic (Fig. 5.12(b)). This surprising result is exhibited by increasing the Ti doping concentration from 2 up to 5 mol %, whereas the Li content remains constant. As revealed in the inset of figure 5.12(b), very small grains (~0.1-0.3 μm) are observed on the surface of the $Li_{0.05}Ti_{0.05}Ni_{0.95}O$ ceramic. In addition, something that accumulates along the grain boundaries is more evident. As a result, it is possible that these very small grains, sub-micron grains, which cover over on the top surface of the $Li_{0.05}Ti_{0.05}Ni_{0.90}O$ ceramic, may be associated with such something observed along the grain boundaries. More interesting, a size of these sub-micron grains that cover on the top surfaces are enlarged by increasing the Ti doping concentration up to 10 mol %, as demonstrated in figure 5.12(c) for the SEM image of the $Li_{0.05}Ti_{0.10}Ni_{0.85}O$ ceramic (y = 0.10). Certainly, these sub-micron grains and such something accumulated along the grain boundaries are as the same thing. A careful inspection reveals that these sub-micron grains are growing; as a result, some grains have become to connect with the adjacent grains, as observed in the inset of figure

5.12(c). Every a doubt is opened from the SEM image of the $Li_{0.05}Ti_{0.15}Ni_{0.85}O$ ceramic, as shown in figure 5.12(d). The sub-micron grains are rarely observed on the top surface of the sample because they have almost connected completely to each other, forming a layer-like covered the top surface of the $Li_{0.05}Ti_{0.15}Ni_{0.85}O$ ceramic. Unlike the clearly smooth surface of the $Li_{0.05}Ti_{0.02}Ni_{0.93}O$, the rough surface of the $Li_{0.05}Ti_{0.15}Ni_{0.85}O$ ceramic is dominant. Moreover, it is also found from the microstructure of the $Li_{0.05}Ti_{0.15}Ni_{0.85}O$ ceramic (the sample with highest concentration of Ti doping) that some sub-micron grains are in the form of line shape. These lines are remarked inside the dashed-rectangle area in the figure 5.12(d). The bigger lines can also be observed in some area of the SEM image as remarked by the dashed-circular area. It is worth noting that the effect of the Ti doping concentration on the microstructure for the $Li_{0.05}Ti_{y}Ni_{0.95-y}O$ ceramics sintered at 1200 °C is quite similar to those observed in the $Li_{0.05}Ti_{y}Ni_{0.95-y}O$ ceramics sintered at 1280 °C.

To clarify and understand the microstructural evolution of the $Li_{0.05}Ti_{y}Ni_{0.95-y}O$ ceramics, the chemical compositions of the grains and grain boundaries on the top surface of samples should be known. The SEM-EDS results are shown in figures 5.13-5.16. For the SEM-EDS results of the $Li_{0.05}Ti_{0.02}Ni_{0.93}O$ ceramic, as demonstrated in figure 13, the peak intensities corresponding to the Ti atom (remarked by the blue arrows) at the testing points 1 and 2, which are respectively on the top surface at a smooth grain and coarse grain boundary, are slight different. The amount of the Ti atom detected at points 1 and 2 are 1.05 and 2.64 at%, respectively. For the $Li_{0.05}Ti_{0.05}Ni_{0.90}O$ ceramic, as shown in figure 14, two specific areas are selected: a clean and smooth grain (point 1) and a dirty grain (point 2) that is covered by the sub-micron grain. The EDS results [Figs. 14(b) and 14(c)] show that the Ti peaks are nearly the same in intensity. The amount of the Ti atom detected at points 1 and 2 are 3.02 and 2.53 at. %, respectively. The EDS data obtained from these two samples are still not sufficient and not enough for the microstructure characterization.

The SEM-EDS results of the $Li_{0.05}Ti_{0.10}Ni_{0.85}O$ and $Li_{0.05}Ti_{0.15}Ni_{0.80}O$ ceramics are illustrated figures 15 and 16, respectively. The interesting results are achieved by analysis of these two ceramic samples. It is found that the Ti atom is more detected at the corner of grains. For the $Li_{0.05}Ti_{0.10}Ni_{0.85}O$

ceramic, the amount of the Ti atom detected at points 1 and 2 are 4.44 and 6.90 at %, respectively. It is important to note that the relative intensity of Ti atom detected at point 1′ and 1″ are respectively 4.18 and 3.84 at %, which are nearly the same in intensity detected at point 1. At point 2′, the detected value is 6.41 at %, which is the same as value detected at point 2. The difference of the detected Ti atom at the grain boundaries (especially at the corner of the grains) and in the grains is clearly observed in the SEM-EDS results of the $Li_{0.05}Ti_{0.15}Ni_{0.80}O$ ceramic. At corners of the grain, the amounts of Ti atom detected at the testing points 2, 2′, and 2″ are found to be 11.40, 11.96, and 11.36 at %, respectively. At the surfaces on the grains, it is found to be 5.80, 2.97, and 4.97 at % for the testing points 1, 1′, and 1″, respectively.

The high accumulation of the Ti atom observed at the corners of the grains may be associated with the $NiTiO_3$ particles observed in the microstructure of the $Ti_yNi_{1-y}O$ ceramics. As shown in the XRD patterns of the $Li_{0.05}Ti_yNi_{0.95-y}O$ ceramics [Figs. 5.6(a) and 5.6(c)], it can be suggested that the $NiTiO_3$ phase is exhibited in the surface of the $Li_{0.05}Ti_yNi_{0.95-y}O$ ceramics with $y \geq 0.05$. This observation of the phase formation relates to the SEM images. Both of the $NiTiO_3$ phase and the sub-micron grains are observed when the Ti doping concentration increased up to 5 mol %. As a result, the sub-micron grains may be a new form of the change in the $NiTiO_3$ phase. Based on this suggestion, the important questions concerning about the microstructure of the $NiTiO_3$ particles occur. First, why did the $NiTiO_3$ particles morphologies present in the $Ti_yNi_{1-y}O$ ceramics differ from that observed in the $Li_xTi_yNi_{1-x-y}O$ ceramics? Second, how does the Li doping influence on the surface morphology of the $Li_xTi_yNi_{1-x-y}O$ ceramics ceramics? Third, can Ti doping ions substitute the Ni^{2+} sites in crystal lattice? To answer these questions, the effect of Li doping ions concentration on the ability of Ti substitution and microstructural evolution of the $Li_xTi_yNi_{1-x-y}O$ ceramics must be investigated. The detail of the microstructure and phase formation analyses related to these matters will be briefly discussed in the next two sections.

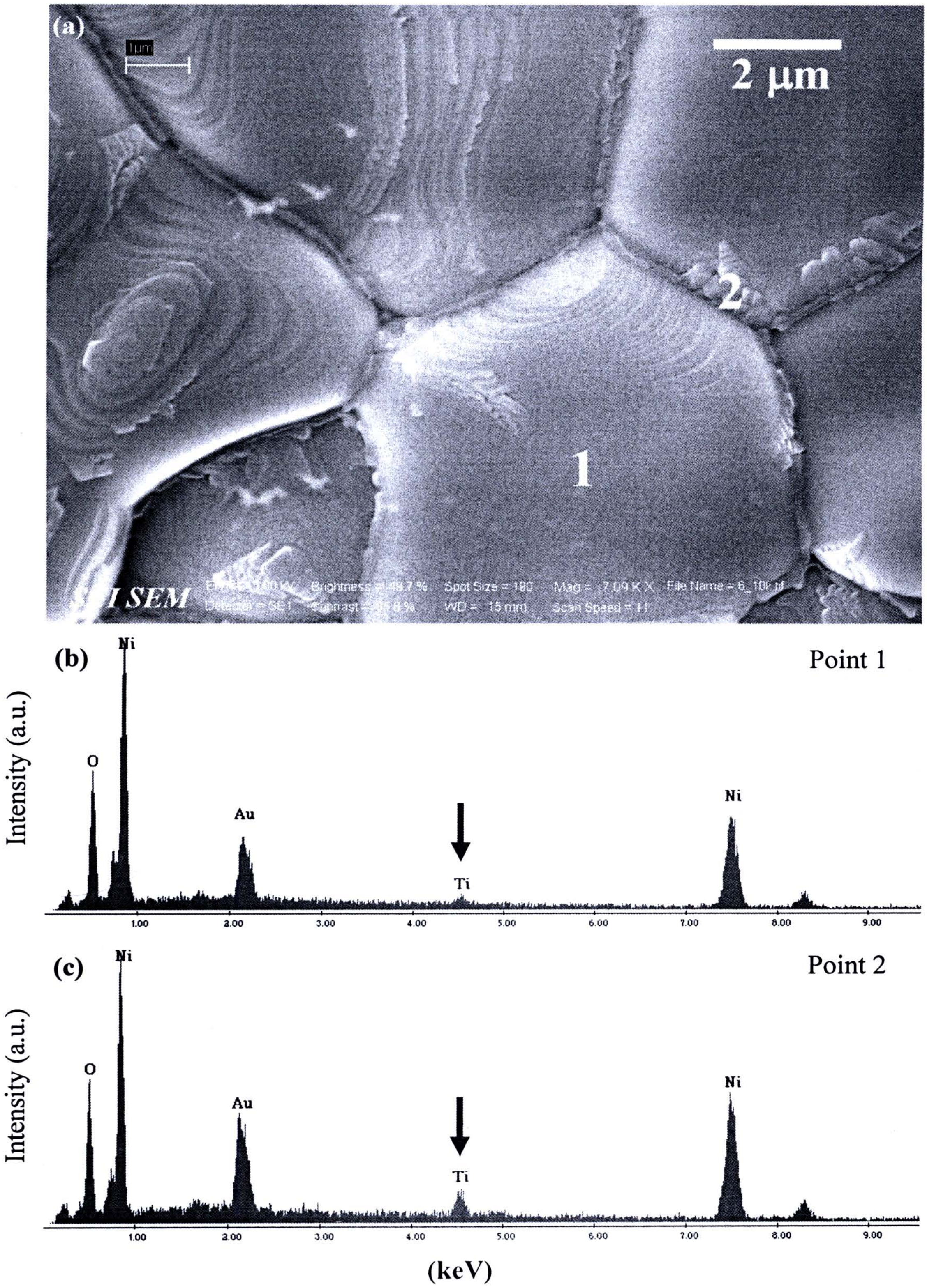

Figure 5.13 (a) SEM image and (b)-(c) EDS spectra of the testing points 1 and 2 for the $Li_{0.05}Ti_{0.02}Ni_{0.93}O$ ceramic sintered at 1280 °C.

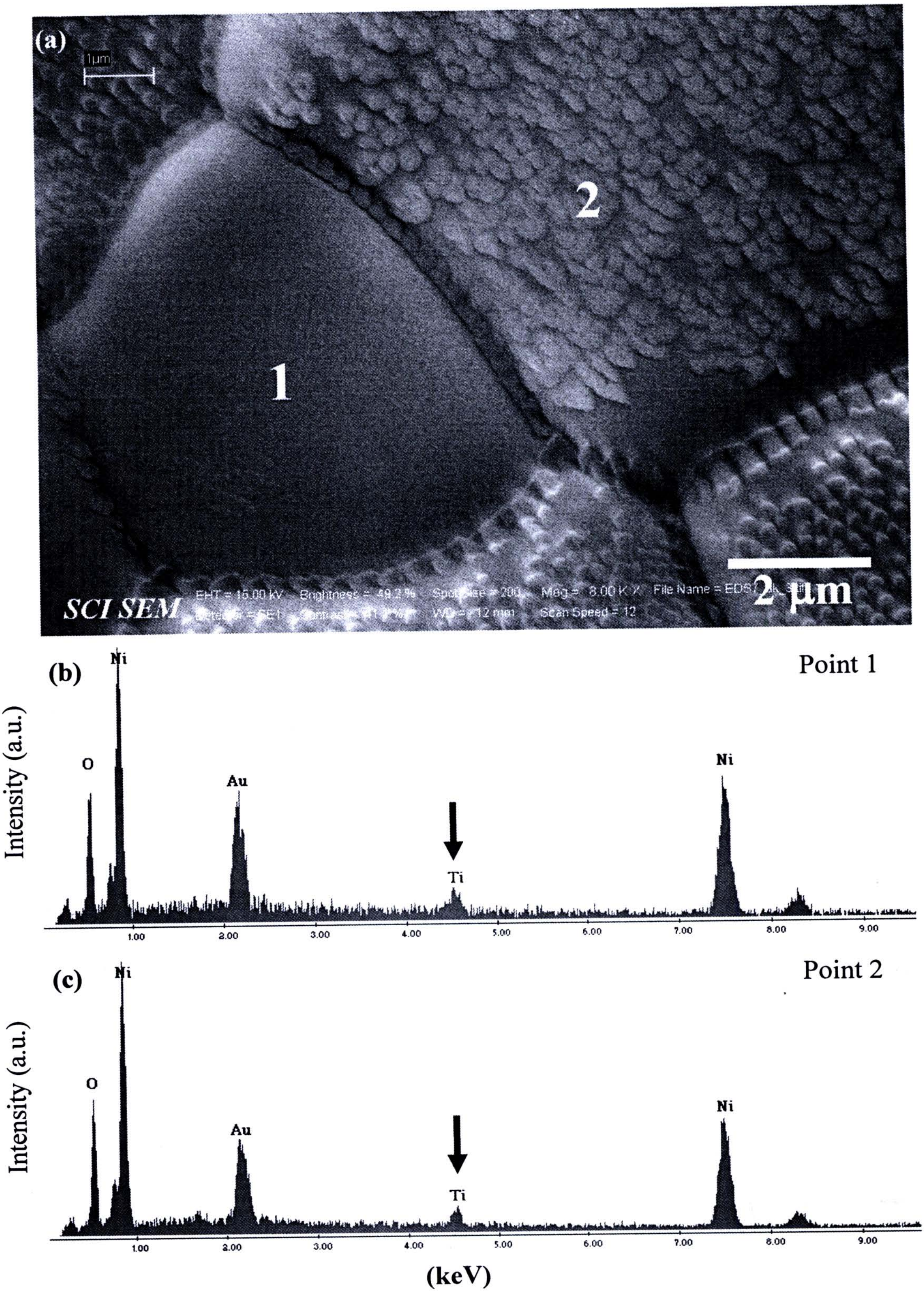

Figure 5.14 (a) SEM image and (b)-(c) EDS spectra of the testing points 1 and 2 for the $Li_{0.05}Ti_{0.05}Ni_{0.90}O$ ceramic sintered at 1280 °C.

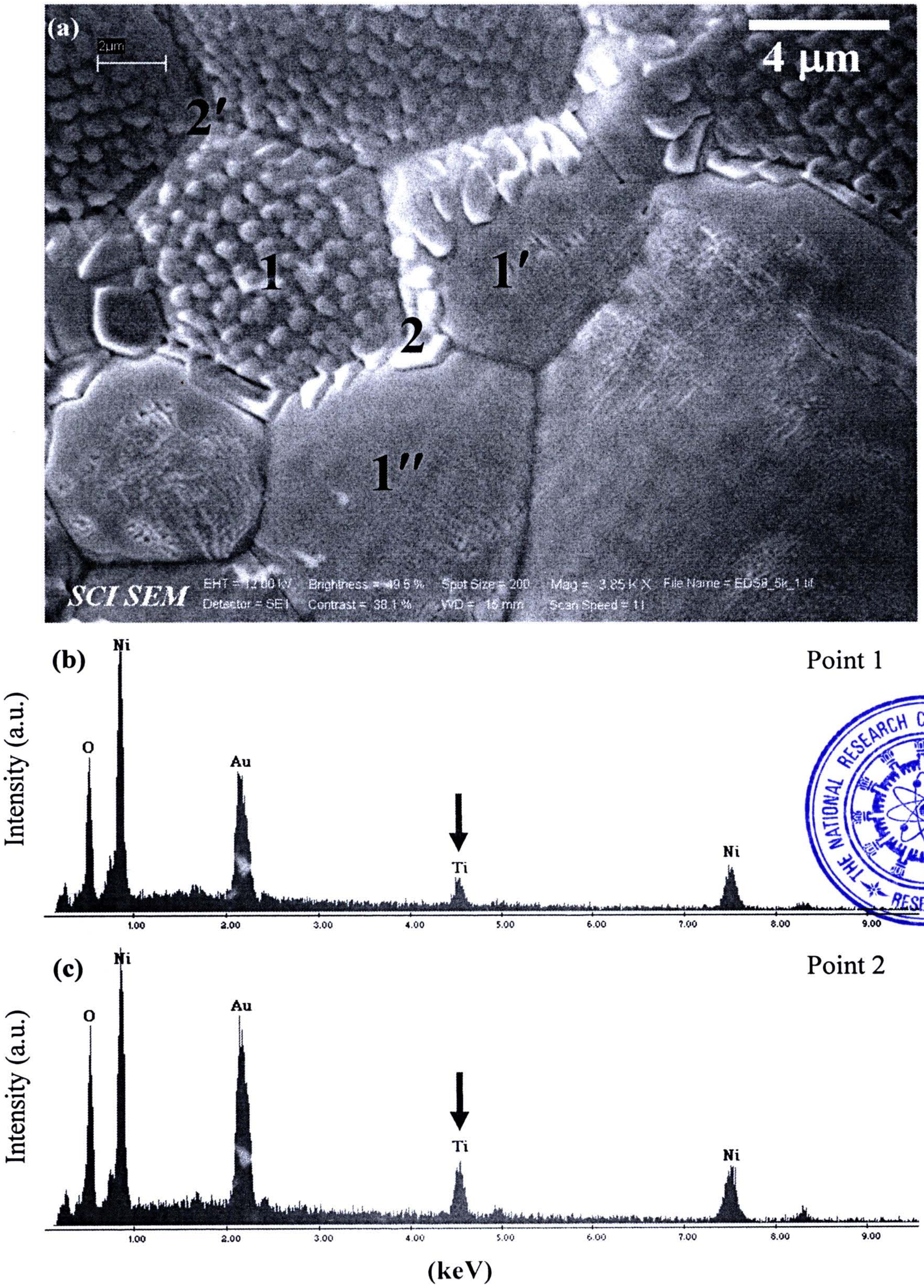

Figure 5.15 (a) SEM image and (b)-(c) EDS spectra of the testing points 1 and 2 for the $Li_{0.05}Ti_{0.10}Ni_{0.85}O$ ceramic sintered at 1280 °C.

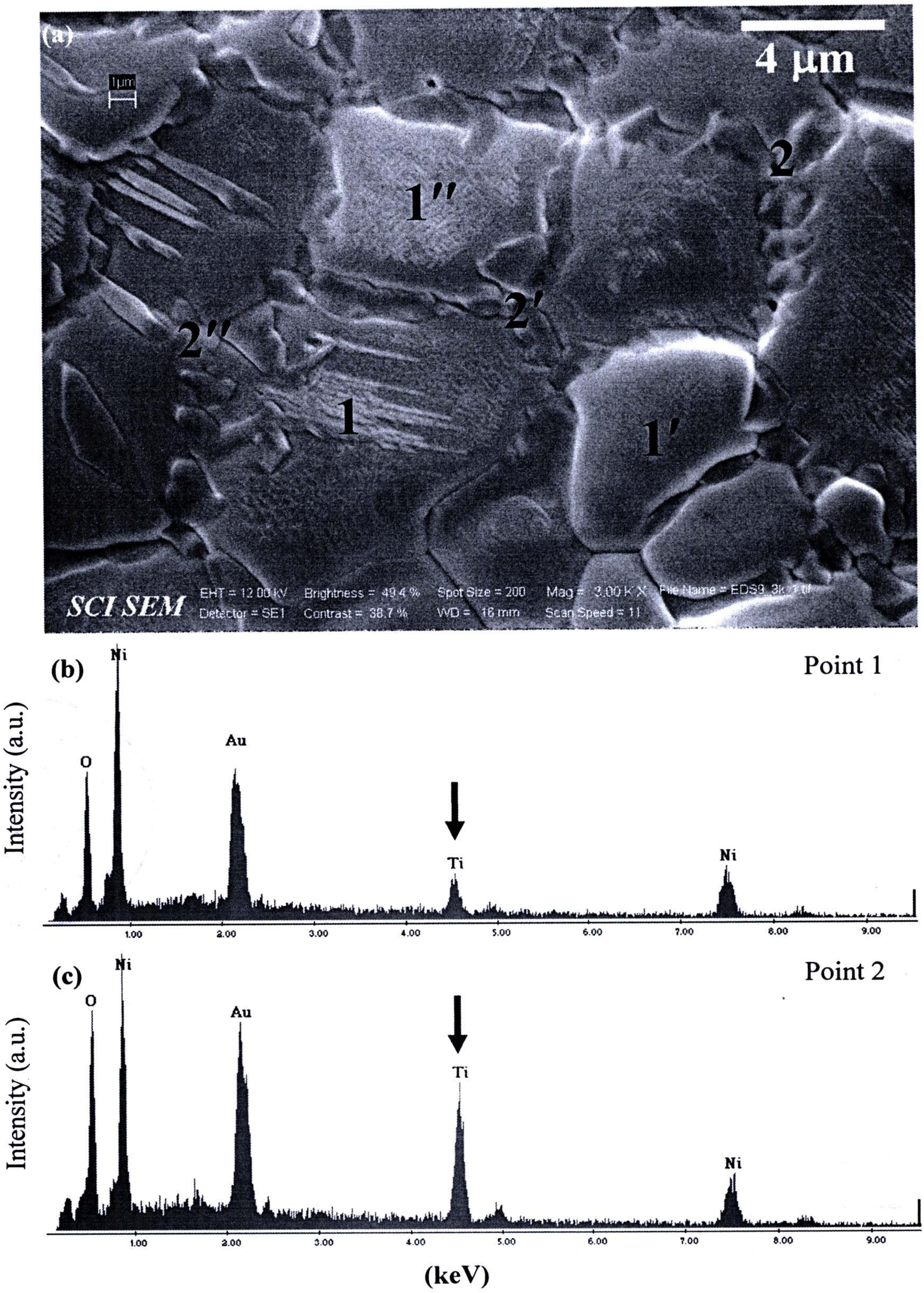

Figure 5.16 (a) SEM image and (b)-(c) EDS spectra of the testing points 1 and 2 for the $Li_{0.05}Ti_{0.15}Ni_{0.80}O$ ceramic sintered at 1280 °C.

6) Effects of Li doping concentration on the ability of Ti substitution and microstructure of $Li_xTi_yNi_{1-x-y}O$ ceramics

As previous results and discussion, it is found that both of Li and Ti doping ions have remarkable influences on both of the phase formation and microstructure of the NiO-based ceramics. Looking carefully at the XRD patterns of the $Li_{0.02}Ti_{0.05}Ni_{0.93}O$, $Li_{0.05}Ti_{0.05}Ni_{0.90}O$, and $Li_{0.10}Ti_{0.05}Ni_{0.85}O$ ceramics (Fig. 5.6), the important result can be observed. The $NiTiO_3$ phase, which relates linearly to the Ti doping concentration, can be observed from the XRD patterns of the $Li_{0.02}Ti_{0.05}Ni_{0.93}O$ and $Li_{0.05}Ti_{0.05}Ni_{0.90}O$ ceramics, but can not for the $Li_{0.10}Ti_{0.05}Ni_{0.85}O$ ceramic. These mean that the Li doping has not only the effect on the microstructure of the NiO, but may also on the ability and/or solubility of the Ti ions in the $Li_xTi_yNi_{1-x-y}O$ ceramics. Figures 5.17 and 5.18 show the surface morphologies of the $Li_xTi_{0.05}Ni_{0.95}O$ ceramics with different concentrations of the Li doping ions comparing to the $Li_{0.10}Ti_{0.02}Ni_{0.88}O$ ceramics sintered at 1200 and 1280 °C, respectively. To brief, the microstructural evolution of the ceramics sintered at 1280 °C is only discussed. It is clearly seen in figures 5.18(a)-5.18(d), the microstructure can be changed by tuning the ratio of Li to Ti doping concentrations. Figure 5.18(a) shows the SEM image of the $Li_{0.02}Ti_{0.05}Ni_{0.93}O$ ceramic. The large accumulation along the grain boundaries, which is expected to be the related-Ti phase, is observed. The sub-micron grains can also be observed in some grains. Some parts of such phase accumulated along the grain boundaries, which the thickness is about ~1 μm, reach into the grains. With increasing the Li doping concentration up to 5 mol %, the $Li_{0.05}Ti_{0.05}Ni_{0.90}O$ ceramic (Fig. 5.18(b)), the thick grain boundaries (~1 μm) are reduced to about 0.2-0.3 μm. Moreover, the surface of the grains is covered by the homogeneous sub-micron grains. Surprisingly, these homogeneous sub-micron grains are completely removed by increasing the Li doping concentration up to 10 mol %, for the $Li_{0.10}Ti_{0.05}Ni_{0.85}O$ ceramic (Fig. 5.18(c)). Both of the grains and grain boundaries of this ceramic are smooth again; however, the pores start to appear just like in the $Li_xTi_{1-x}O$ ceramics. With decreasing the Ti doping concentration to 2 mol %, i.e., the $Li_{0.10}Ti_{0.02}Ni_{0.88}O$ ceramic (Fig. 5.18(d)), the microstructure do not change, and the grains and grain boundaries are still clear and claer. The discussion is represented in the next section.

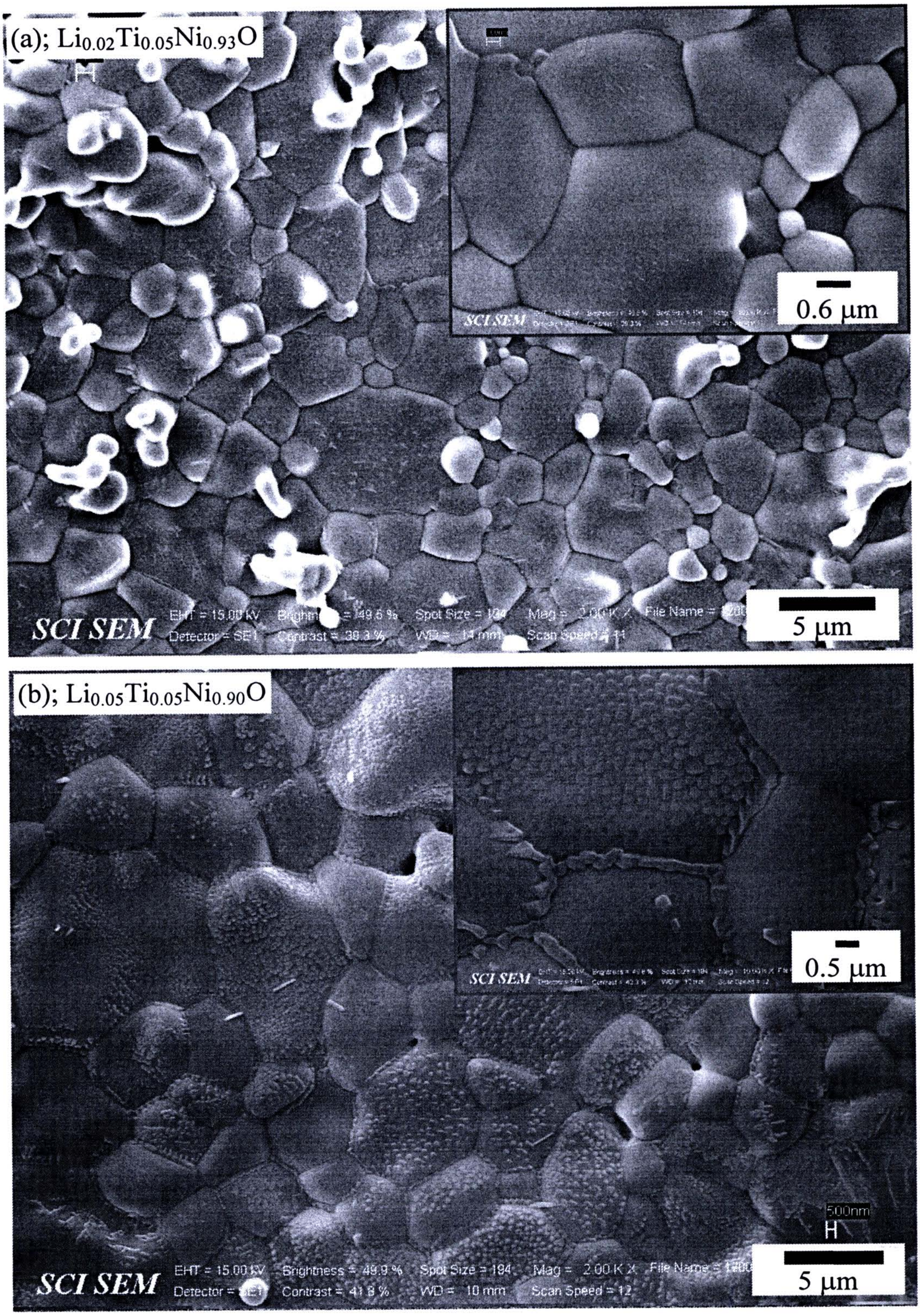

Figure 5.17 SEM images of $Li_xTi_{0.05}Ni_{0.95-x}O$ (x = 0.02, 0.05, and 0.10) and $Li_{0.10}Ti_{0.02}Ni_{0.88}O$ ceramics sintered at 1200 °C; inset shows its higher magnification image.

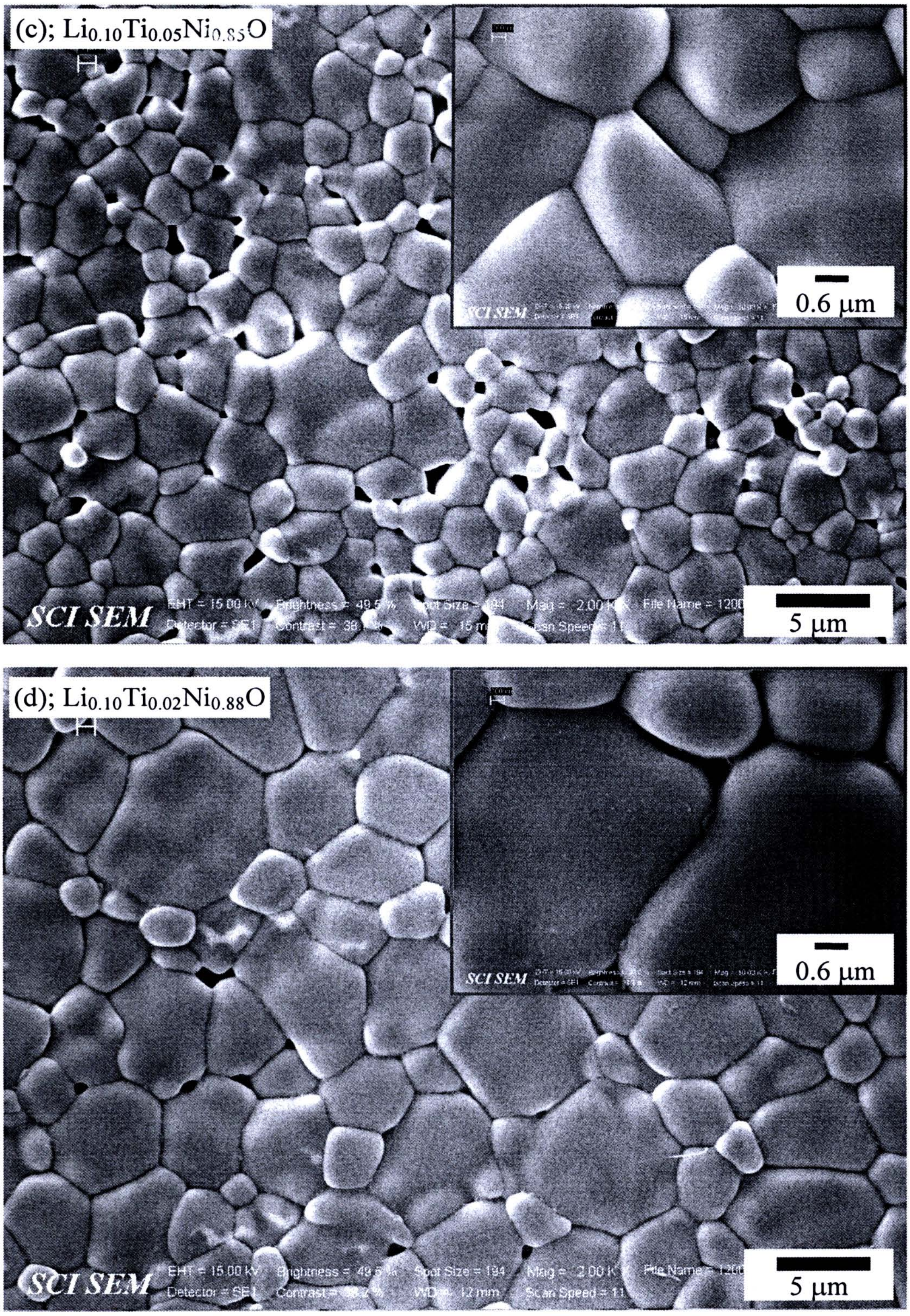

Figure 5.17 SEM images of $Li_xTi_{0.05}Ni_{0.95-x}O$ (x = 0.02, 0.05, and 0.10) and $Li_{0.10}Ti_{0.02}Ni_{0.88}O$ ceramics sintered at 1200 °C; inset shows its higher magnification image. (Cont.)

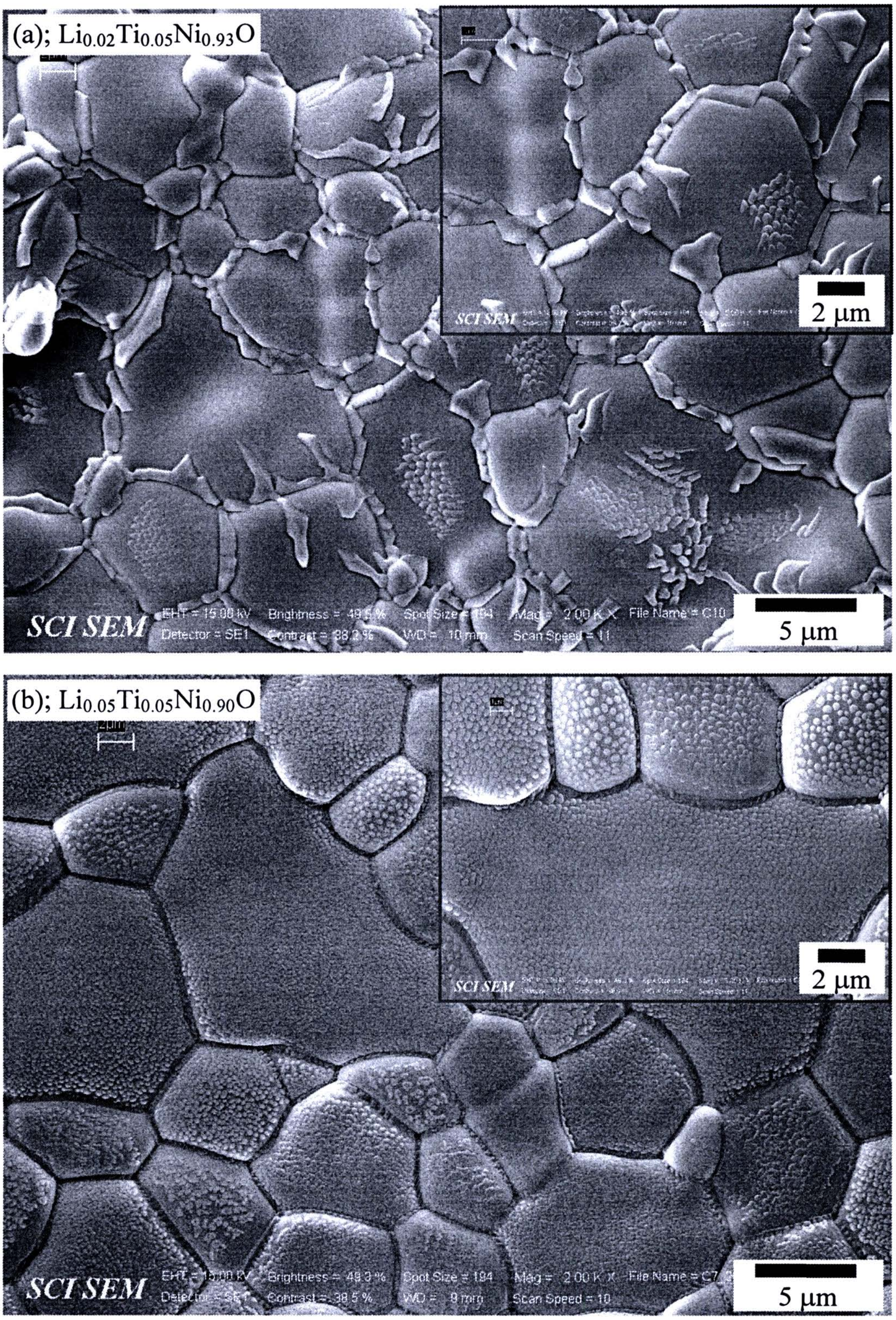

Figure 5.18 SEM images of $Li_xTi_{0.05}Ni_{0.95-x}O$ (x = 0.02, 0.05, and 0.10) and $Li_{0.10}Ti_{0.02}Ni_{0.88}O$ ceramics sintered at 1280 °C; inset shows its higher magnification image.

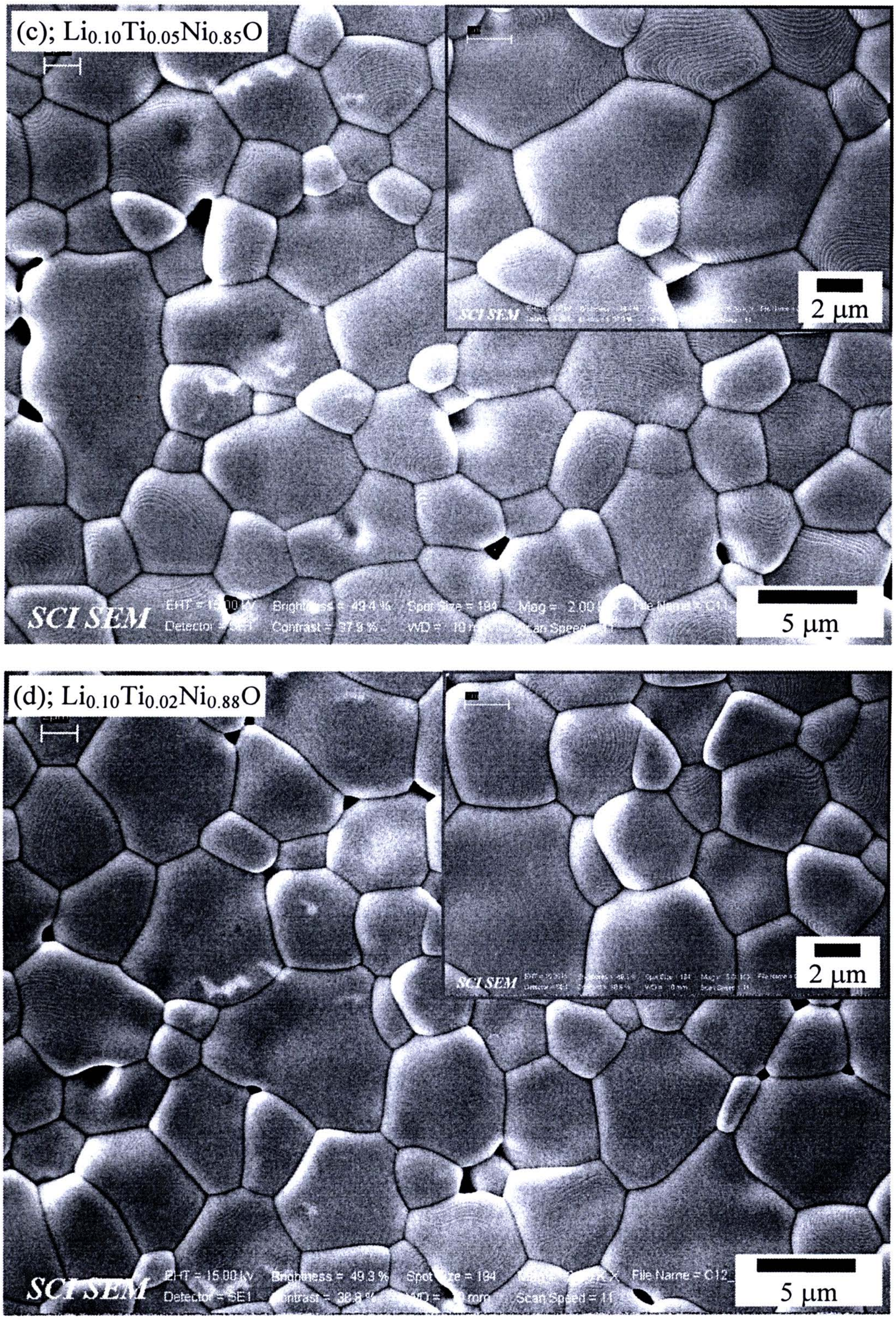

Figure 5.18 SEM images of $Li_xTi_{0.05}Ni_{0.95-x}O$ (x = 0.02, 0.05, and 0.10) and $Li_{0.10}Ti_{0.02}Ni_{0.88}O$ ceramics sintered at 1280 °C; inset shows its higher magnification image. (Cont.)

7) Possible mechanism(s) of the phase formation and the microstructural evolution of the $Li_xTi_yNi_{1-x-y}O$ ceramics

First of all, the chemical compositions of any surface-regions of the ceramics, especially for the $Li_{0.02}Ti_{0.05}Ni_{0.93}O$ ceramic as demonstrated in figure 5.18(a), should be known. Figure 5.19 shows the SEM-EDS results of the $Li_{0.02}Ti_{0.05}Ni_{0.93}O$ ceramic sintered at 1280 °C. It is interesting that the peak of the EDS spectra corresponding to the Ti atom can only be observed in the EDS spectrum of the testing point 2, as shown in figure 5.19(c). However, it can not be observed in the EDS spectrum of the testing point 1, as shown in figure 5.19(b). It is also found that at the testing points 1′, 1″, and 1‴, the peak related to the Ti atom is not detected (do not shown). Furthermore, at the testing points 2′, 2″, and 2‴, the peak related to the Ti atom is certainly detected (do not shown). According to the XRD result of the $Li_{0.02}Ti_{0.05}Ni_{0.93}O$ ceramic, the existence of the $NiTiO_3$ phase on the surface sample was proved as well as the NiO phase. Therefore, it can suitably be suggested that the phase that precipitates along the grain boundaries of the $Li_{0.02}Ti_{0.05}Ni_{0.93}O$ ceramic is the $NiTiO_3$ phase, which relates to the Ti doping. More interesting, the EDS spectrum of the testing point 3 (the inset of Fig. 5.19(b)), which is in the grain that there are the sub-micron grains inside, demonstrates that the cluster of these grains are the $NiTiO_3$ particles. Form the EDS results of the $Li_{0.10}Ti_{0.05}Ni_{0.85}O$ ceramic as shown in figures 5.20(a) and 5.20(b), it is revealed that the Ti atom can be observed in both of the grain and grain boundary regions. The observed small intensities of the Ti peaks at various testing points are not different from each other. According to the XRD pattern of the $Li_{0.10}Ti_{0.05}Ni_{0.85}O$ ceramic, the $NiTiO_3$ phase can not be observed in the diffraction pattern. There are at least two possible mechanisms that are responsible for the observation. First, the Ti doping ions can substitute the Ni^{2+} sites in the crystal lattice; thus, just small parts or none of the Ti doping have formed the $NiTiO_3$ phase. Second, the second phase of $NiTiO_3$ is indigent on the outer surface layer of the $Li_{0.10}Ti_{0.05}Ni_{0.85}O$ ceramic due to the evaporation. With decreasing the Ti doping concentration down to 2 mol %, the Ti peak can not be detected from the EDS spectra of the grain and grain boundary, as shown in figures 5.20(c) and 5.20(d).

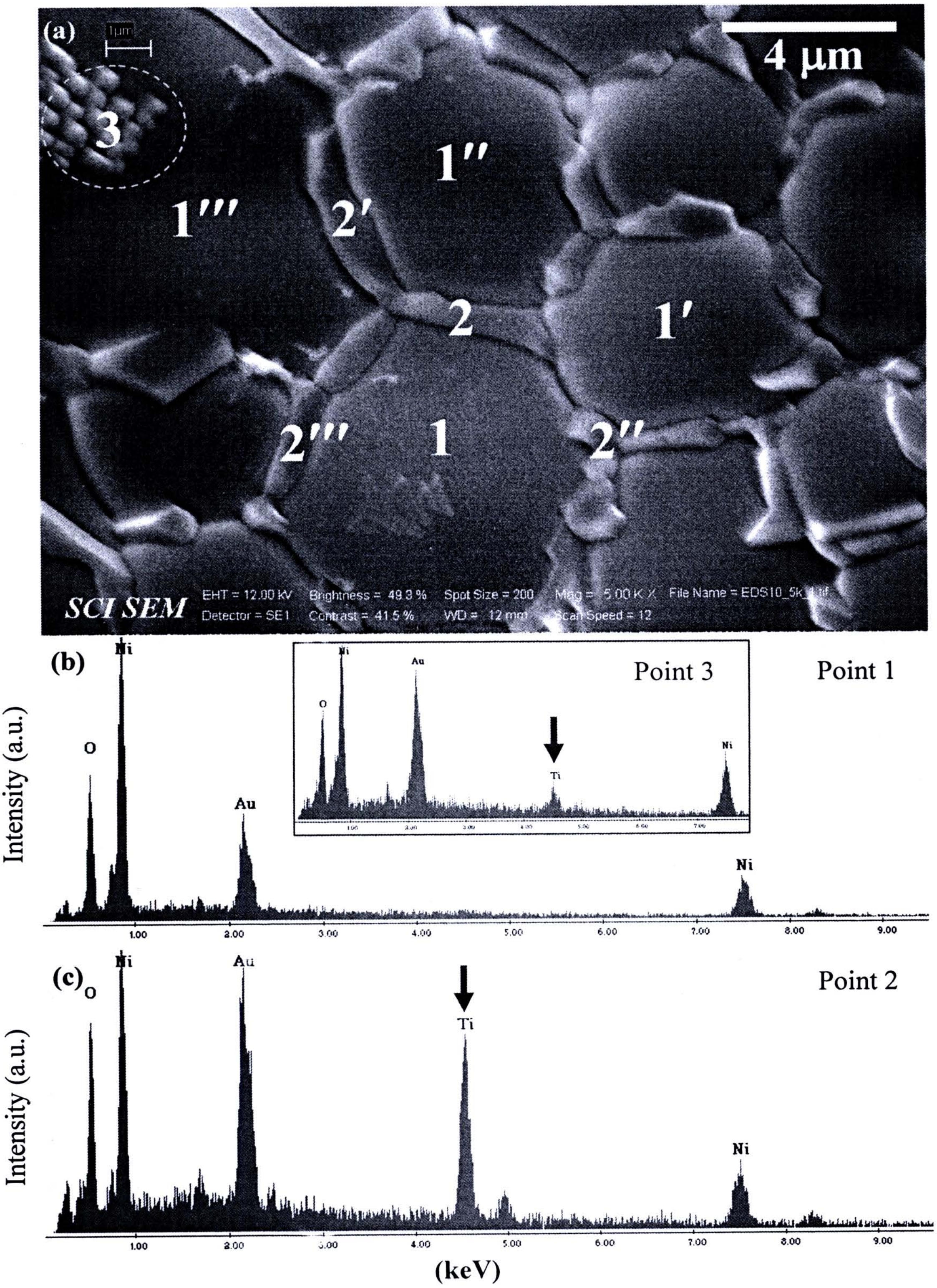

Figure 5.19 (a) SEM image and (b)-(c) EDS spectra of the testing points 1 and 2 for the $Li_{0.02}Ti_{0.05}Ni_{0.93}O$ ceramic sintered at 1280 °C; inset is in (b) shows the EDS spectrum of the testing point 3.

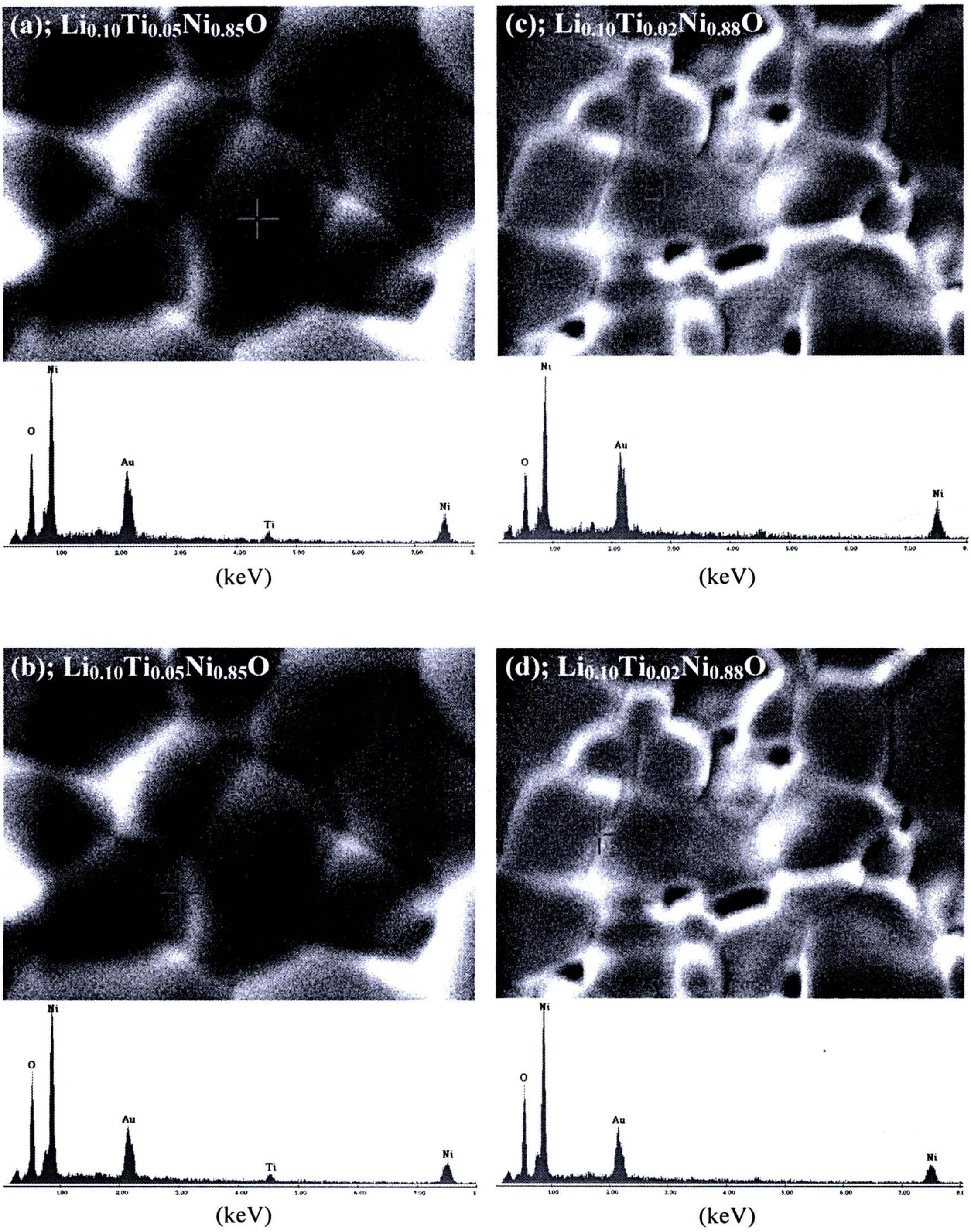

Figure 5.20 SEM-EDS results of the testing points at a grain and grain boundary for (a), (b) $Li_{0.10}Ti_{0.05}Ni_{0.85}O$ and (c), (d) $Li_{0.10}Ti_{0.02}Ni_{0.98}O$ ceramics sintered at 1280 °C.

According to the XRD, SEM, and EDS results, the major points that give the important clues concerning about mechanism(s) of phase formation and microstructural evolution can be concluded as the following steps. (1) The $NiTiO_3$ particles observed in the grain boundaries (especially at corners of the grains) of the $Ti_yNi_{1-y}O$ ceramics are erased by doping with 5 mol % of Li ions ($Li_{0.05}Ti_yNi_{0.95-y}O$). (2) On the surfaces of the $Li_{0.05}Ti_yNi_{0.95-y}O$ ceramics, the relative large size of the $NiTiO_3$ particles disappears, but the clusters of sub-micron grains (~0.1-0.3 μm) are found. The surfaces of the regular grains and grain boundaries are covered by the sub-micron grains. The $NiTiO_3$ phase is still detected in the XRD patterns of the $Li_{0.05}Ti_yNi_{0.95-y}O$ ceramics ($y \geq 0.05$) just like the $Ti_yNi_{1-y}O$ ceramics. As a result, these sub-micron grains are suggested to be the $NiTiO_3$ phase. (3) With increasing the Ti doping concentration, the size of these $NiTiO_3$ sub-micron grains tends to increase and to connect with the adjacent small grains. The accumulation of these sub-micron grains at the grain boundaries is found to be more evident. (4) Eventually, if the Ti is sufficient large (15 mol %), the sub-micron grains connected together completely, forming the plated layer-like of $NiTiO_3$. (5) Turning to see the $Li_xTi_{0.05}Ni_{0.95-x}O$ ceramics (fixed $y = 0.05$), with $x = 0$, the $NiTiO_3$ particles are observed in the microstructure of the $Ti_{0.05}Ni_{0.95}O$ sample. (6) By doping with 2 mol % of Li ions ($x = 0.02$), the relative large size of the $NiTiO_3$ particles disappears; however, these $NiTiO_3$ particles connect together and enclose the particle grains. Some parts of the connected $NiTiO_3$ particles reach into grain regions. (7) With increasing the Li doping concentration up to 5 mol % ($x = 0.05$), the thickness of grain boundary is reduced; whereas, the clusters of the sub-micron grains are observed. At this stage, the $NiTiO_3$ phase is still detected in the XRD patterns of the $Ti_{0.05}Ni_{0.95}O$, $Li_{0.02}Ti_{0.05}Ni_{0.93}O$, and $Li_{0.05}Ti_{0.05}Ni_{0.90}O$ ceramic samples (samples that were described in steps (5), (6), and (7). (8) The surprising result is observed on the surface of the $Li_xTi_{0.05}Ni_{0.95-x}O$ ceramic when $x = 0.10$, the $Li_{0.10}Ti_{0.05}Ni_{0.85}O$ ceramic. The large amount of the clusters of sub-micron grains that cover the grain surfaces and grain boundaries are totally cleaned, they disappear on the surface. (9) With decreasing the Ti doping concentration down to 2 mol % (fixed $x = 0.10$), the microstructure does not change, it is still clear and smooth.

As outlined above, it is strongly suggested that the Li doping concentration can cause a change in both of the feature and distribution of the $NiTiO_3$ particles on the surface of the $Li_xTi_yNi_{1-x-y}O$ ceramics. The evolution of microstructure of the $Li_xTi_yNi_{1-x-y}O$ ceramics might be related to the ratio of the Ti to Li doping ions. With doping the Li ions (5 mol %) into the $Ti_yNi_{1-y}O$ ceramics ($y = 0.02, 0.05, 0.10$, and 0.15), the particle sizes of $NiTiO_3$ observed on the surface of the $Ti_yNi_{1-y}O$ ceramics are significantly reduced from the range of 1-2 μm to the sub-micron range of ~0.1-0.3 μm. The $NiTiO_3$ particles are dispersed homogeneously on the surface. Moreover, the regular grain size is enhanced by doping with the Li ions. As results, it is likely that during the sintering process, the solid state of the $NiTiO_3$ particles as presented in the $Ti_yNi_{1-y}O$ ceramics might be changed to the liquid state by the effect of Li doping ions, as demonstrated in the $Li_xTi_yNi_{1-x-y}O$ ceramics. Without the Li doping, during the sintering process, the $NiTiO_3$ particles are in the solid state. With doping Li ions, in contrast, during the sintering process the $NiTiO_3$ particles might be in the liquid state. On the other way, they might be dispersed in some liquid. This expectation is due to the fact that the shape of some clusters of sub-micron grains observed on the surfaces of the $Li_xTi_yNi_{1-x-y}O$ ceramics, especially for the $Li_{0.05}Ti_{0.15}Ni_{0.90}O$ sample, is in the shape of lines. These lines like the sudden freeze of some liquid during flow.

From these points of view, the *liquid-phase sintering*[7] and/or the related process, activated sintering, may be related to this observed microstructural evolution. For the activated sintering, the minor amounts of additives that segregate strongly to the grain boundaries can significantly increase mass transport rates along the grain boundary (Rahaman, 2003). Compared to solid-state sintering (e.g., as occurred in the $Ti_yNi_{1-y}O$ ceramic system), the presence of the liquid phase leads to increase in the densification of the $Li_xTi_yNi_{1-x-y}O$ ceramics. Although

---

[7] The formation of a liquid phase is commonly used to assist in the sintering process and evolution of microstructure. Usually, the objective of this sintering is to obtained accelerated grain growth, enhance densification rates, or produce specific grain boundaries properties. Commonly, the amount of liquid formed during sintering is small, typically less that a few volume percent. This sintering is more important when the use of solid-state sintering is quite expensive or requires high temperature for the fabrication. However, a disadvantage of the liquid-phase sintering can also occurred—the liquid used in a process usually remains as glassy intergranular phase, which can degrade high temperature mechanical properties (Rahaman, 2003).

there is no clear difference in principles between these two sintering processes, i.e., liquid-phase sintering and activated sintering, it is believed that both of sintering processes can give a great contribution to the sintering of the $Li_xTi_yNi_{1-x-y}O$ ceramics. Because there are two types of the doping ions (Li and Ti ions), the understanding of the sintering process of the $Li_xTi_yNi_{1-x-y}O$ ceramics seems to be very difficult. Moreover, the chemical reaction or interaction between the Li and Ti doping ions might also be produced during the sintering process. There are at least two cases of these sintering processes. (1) It is likely that the Li doping ions may act as the activation of the sintering. While the $NiTiO_3$ particles, which have been activated by the Li doping, might be transformed to the liquid phase. (2) All of or either of the Li or Ti doping can act as the liquid phase(s). In the latter case, the Ti doping ions may be dissolved and dispersed in the liquid phase that relates to the Li doping. When the liquid spreads over the solid surfaces of the NiO particles; certainly, the Ti doping ions spread over the surfaces.

The condition of a small Ti doping concentration such as in the $Li_{0.05}Ti_{0.02}Ni_{0.93}O$ ceramic, which leads to a small ratio of Ti to Li doping ions (Ti/Li = 0.4), is firstly considered. During the sintering process, the $NiTiO_3$ liquid phase and/or the $NiTiO_3$ particles dispersed in the liquid phase of Li doping assist to this sintering process. The enhanced rearrangement of the NiO particulate solid due to the influence of capillary stress gradients and *the enhanced matter transport*[8] through the liquid are exhibited. As a result, the $Li_{0.05}Ti_{0.02}Ni_{0.93}O$ ceramic is highly dense (considering from the surface morphology) and its grain size increases (compared to the $Ti_{0.02}Ni_{0.98}O$). On the cooling process, the $NiTiO_3$ particles, which are dispersed homogeneous, segregate to the grain boundaries. Therefore, it more accumulates along the grain boundaries and is hardly detected on the surface in the grain region; consequently, the grains of this sample are quite smooth.

With increasing the Ti doping concentration up to 5, 10, and 15 mol %, the ratio of Ti to Li doping ions increases, Ti/Li = 1.0, 2.0, and 3.0,

---

[8] The enhanced matter transport is occurred due to two main reasons. (1) Diffusion through a liquid is certainly much faster than in solids; therefore, the liquid provides a path for enhanced matter transport. (2) According to the definition of the grain boundary diffusion, which is the product of the grain boundary diffusion coefficient (D) and the grain boundary thickness (δ), it is clear that δ in the liquid-phase sintering is many times thicker than that of the solid-state sintering. Therefore, the grain boundary diffusion in the liquid-phase sintering is larger.

respectively. As a result, the liquid might be sufficient large (in the case of $NiTiO_3$, it is considered as liquid phase) or more $NiTiO_3$ particles are dispersed in the liquid of Li doping. The accumulation of the liquid phase(s) at the grain boundaries near the surfaces is therefore over limitation, and then the remained liquid phase can spread into the solid surfaces of the $Li_xTi_yNi_{1-x-y}O$ samples by the liquid flow. On the cooling process, the viscosity of the liquid tends to increase; as a result, the surface stress of the liquid should be enhanced. The thin film of the liquid, which is under the stress, is transformed to the clusters of sub-micron grains covered the surfaces of the ceramic samples. With increasing the Ti doping concentration, the thickness of the liquid film will be enhanced. The surface stress of the thicker film is certainly smaller than that of the thinner film. With the lower stress and higher concentration of Ti ions of the thicker liquid film, on the cooling process, the sub-micron grains are formed as the plate layer-like of $NiTiO_3$ phase. It is important to suggest that the possible one can also be produced based on the presence of the liquid phase of the Li doping.

Tuning to see the influence of the Li doping on the sintering to reach to the most possibility of the sintering mechanism, the $Li_{0.02}Ti_{0.05}Ni_{0.93}O$ ceramic (Ti/Li = 2.5) is firstly considered. This high-ratio value is closely to the ratios of 2.0 and 3.0 for the $Li_{0.05}Ti_{0.10}Ni_{0.85}O$ and $Li_{0.05}Ti_{0.15}Ni_{0.80}O$ ceramics, respectively. Unlikely, the grains of the $Li_{0.02}Ti_{0.05}Ni_{0.93}O$ ceramic are quite smooth although there are few clusters of sub-micron grains exhibited in some grains. Moreover, it is found that the $NiTiO_3$ phase segregates strongly along the grain boundaries, as shown in figure 5.19. This result is totally different from those observed in the $Li_{0.05}Ti_{0.10}Ni_{0.85}O$ and $Li_{0.05}Ti_{0.15}Ni_{0.80}O$ ceramics, whereas the Ti/Li ratio values of these three samples are close. Consequently, it is suggested that the Ti/Li ratio is not directly related to the microstructural evolution. With increasing the Li doping up to 5 mol %, the relative large particles of the $NiTiO_3$ that enclose the grains are reduced and dispersed over the surface, suggesting that the Li doping may act as the liquid during the sintering process.

Interestingly, these sub-micron grains are removed completely by increasing the Li doping up to 10 mol %, for the $Li_{0.10}Ti_{0.05}Ni_{0.85}O$ ceramic. It is very important to note that there are a small number of systems that the liquid phase presents in the sintering process, but then disappears. Three possible mechanisms related to this process are suggested (Rahaman, 2003): (1) the liquid phase can incorporate into the solid phase to produce a solid solution, (2) there exist of the crystallization of the liquid, and (3) it is evaporated. Therefore, the presence of no phase related to the Li and Ti doping ions (observed from the XRD pattern) in the $Li_{0.10}Ti_{0.05}Ni_{0.85}O$ ceramic may be associated with one or more of these three mechanisms, especially for the first suggestion. Both of the Li^{+} and Ti^{4+} ions may substitute the Ni^{2+} sites in the crystal lattice. Generally, Li^{+} is easily incorporated in the NiO crystal structure and can substitute the Ni^{2+} sites (Antolini, 2003; Li Z et al., 2005; Antolini, Ferretti, 1997). According to the XRD and SEM-EDS results, it is suggested that the Ti doping ions are hardly incorporated into the NiO crystal structure; in contrast, it prefers to form a second phase of $NiTiO_3$. The observed crystal structure and microstructure in the $Li_{0.10}Ti_{0.05}Ni_{0.85}O$ ceramic are certainly suggested to the suitable condition for the sintering to obtain an exactly doped-ceramic system for the $Li_xTi_yNi_{1-x-y}O$ ceramics. As outlined earlier, the liquid phase presented in the microstructure during sintering can assist and contribute to the matter transport. Therefore, 10 mol % of the Li doping may be high enough to produce the liquid that its driving force is sufficient to assist the diffusion of Ti ions during the firing process. As the explanation above, it also indicates that the ability of the substitution of Ti ions in the matrix of the NiO particles is depended on the Li doping concentration. Thus, the concentration of the Ti ions that can diffuse into the matrix of NiO crystal lattice can be assigned by the Li doping concentration. As a result, it is suggested that the amounts of the Ti ions that can substitute the Ni^{2+} sites for the $Li_{0.05}Ti_{0.02}Ni_{0.93}O$, $Li_{0.05}Ti_{0.05}Ni_{0.90}O$, $Li_{0.05}Ti_{0.10}Ni_{0.85}O$, and $Li_{0.05}Ti_{0.15}Ni_{0.80}O$ ceramics might not be significantly different. This is because of the same concentration of the Li doping ions.

In conclusion of the microstructure analysis, it is found from the experimental results that both of the Ti and Li doping ions have remarkable influences on the microstructural evolution of the $Li_xTi_yNi_{1-x-y}O$ ceramics. The Ti doping prefers to form the second phase of $NiTiO_3$. In contrast, the Li doping ions can easily substitute the Ni^{2+} sites in the crystal lattice. However, the ability of the substitute of the Ti doping ions can be enhanced by increasing the concentration of the Li doping. It is also found that the morphology of the $NiTiO_3$ particles is changed by the Li doping ions. The explanation of the microstructural evolution might be described by the liquid-phase sintering. However, the role of the dopants, i.e., Ti and Li ions, is still not understood very well. This is owing to the fact that both the Ti and Li doping ions can often display a variety of functions, which makes understanding of the dopants role difficult. Certainly, the microstructural evolution is expected to associate with the dielectric and electrical properties of these ceramics, which will be discussed in next sections.

5.1.3 Temperature and frequency dependence of dielectric properties

5.1.3.1 Temperature dependence of dielectric properties of the $Li_xTi_yNi_{1-x-y}O$ ceramics

Figures 5.21(a)-5.21(f) show the temperature dependence of the dielectric constant (ε') and loss tangent ($\tan\delta$) at the frequency range of 10^2-10^6 Hz for the $Ti_{0.10}Ni_{0.90}O$, $Li_{0.05}Ti_{0.02}Ni_{0.93}O$, $Li_{0.05}Ti_{0.05}Ni_{0.90}O$, $Li_{0.05}Ti_{0.10}Ni_{0.85}O$, $Li_{0.05}Ti_{0.15}Ni_{0.80}O$, and $Li_{0.02}Ti_{0.05}Ni_{0.93}O$ ceramics sintered at 1200 °C for 4 h. For the $Ti_{0.15}Ni_{0.85}O$ ceramic as shown in figure 5.21(a), at the frequency of 10^2 Hz, the dielectric constant tends to increase with increasing temperature. This increase in the dielectric constant relates to the increase in the loss tangent, which increases with increasing the temperature. By considering at any fixed temperature, for example at 100 °C, the dielectric constant and the loss tangent decrease with increasing the frequency. This dielectric behavior is affected by the dc conductivity, which is usually depended on temperature (Wu J et al., 2002). The interesting result can also be observed in the dielectric constant spectra at high frequencies and at low temperature. The dielectric constant decreases rapidly at the frequency of 100 kHz and temperature below -40 °C. With increasing the frequency up to 1 MHz, the rapid drop of the dielectric constant is occurred at higher temperature. At this frequency, the peak of the loss tangent appears at a lower temperature range corresponding to the sudden drop of the dielectric constant. These dielectric behaviors, i.e., the appearance of sudden drop and the loss tangent peak, are suggested to be the dielectric relaxation behavior (Wu J et al., 2002; Liu et al., 2004, 2005; Homes et al., 2001; Ikeda et al., 2005; Wang, Zhang., 2006; Wang et al., 2006, 2007; Zhang et al., 2005). According to figures 5.21(a)-5.21(f), it is found that the dielectric relaxation peak (loss tangent peak) shifts to higher temperature with increasing frequency. The deep mechanism of this observed dielectric behavior will be described in section 5.1.3.2.

The temperature dependence of the dielectric properties of the $Li_xTi_yNi_{1-x-y}O$ ceramics with different concentrations of Li and Ti doping ions is revealed in figures 5.21(b)-5.21(f). It is clear that all of these ceramics exhibit the giant dielectric constant values of about 10^3-10^4 at low frequencies. As a result, the $Li_xTi_yNi_{1-x-y}O$ ceramics can be classified as the *giant dielectric material.* At the frequency range of 10 Hz-10 kHz, the dielectric constants of all these ceramics are nearly independent of temperature over the measuring temperature range. With increasing the frequency up to 100 kHz, the sudden drop of the dielectric constant is observed at a low temperature range. Moreover, this drop shifts to higher temperature with increasing the frequency up to 1 MHz. Certainly, the peak of the loss tangent can be observed at the low temperature range just like in the case of the $Ti_{0.10}Ni_{0.90}O$ ceramic. The loss tangent due to the effect of the dc conduction is also observed at the frequency below 10 kHz. It is important to note that the values of the loss tangent at the room temperature and 1 kHz of all $Li_xTi_yNi_{1-x-y}O$ ceramics are over 0.5. The suitable values of the loss tangent for capacitor applications must be lower than 0.05 (Moulson, Herbert, 2003). Therefore, the high values of the loss tangent observed in all ceramics are undesirable for the capacitor applications. However, the origin of the observed giant dielectric response in (Li, Ti)-doped NiO ceramics is still unclear now. The investigation of NiO-based ceramics to understand the origin of the giant dielectric response is therefore needed. In recent years, several researches have devoted to the investigation of the giant dielectric behavior observed in the NiO-based ceramics to elucidate the origin of this observation as well as this thesis. Note that, the temperature dependence of the dielectric properties of the ceramics sintered at 1200 °C is similar to that observed in the ceramics sintered at 1280 °C.

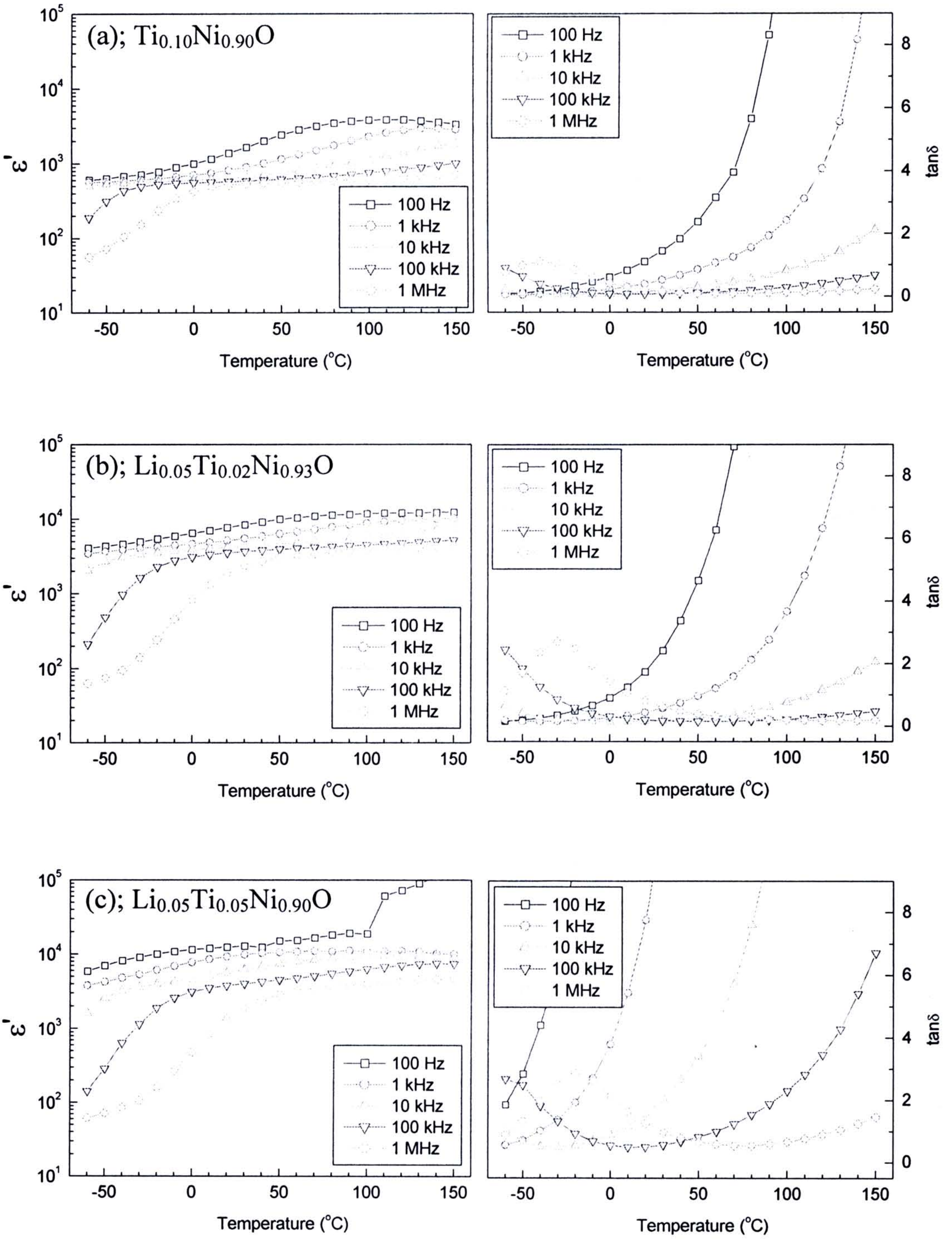

Figure 5.21 Temperature dependence of dielectric constant (ε') and loss tangent ($\tan\delta$) at the frequency range of 10^2-10^6 Hz for $Li_xTi_yNi_{1-x-y}O$ ceramics sintered at 1200 °C.

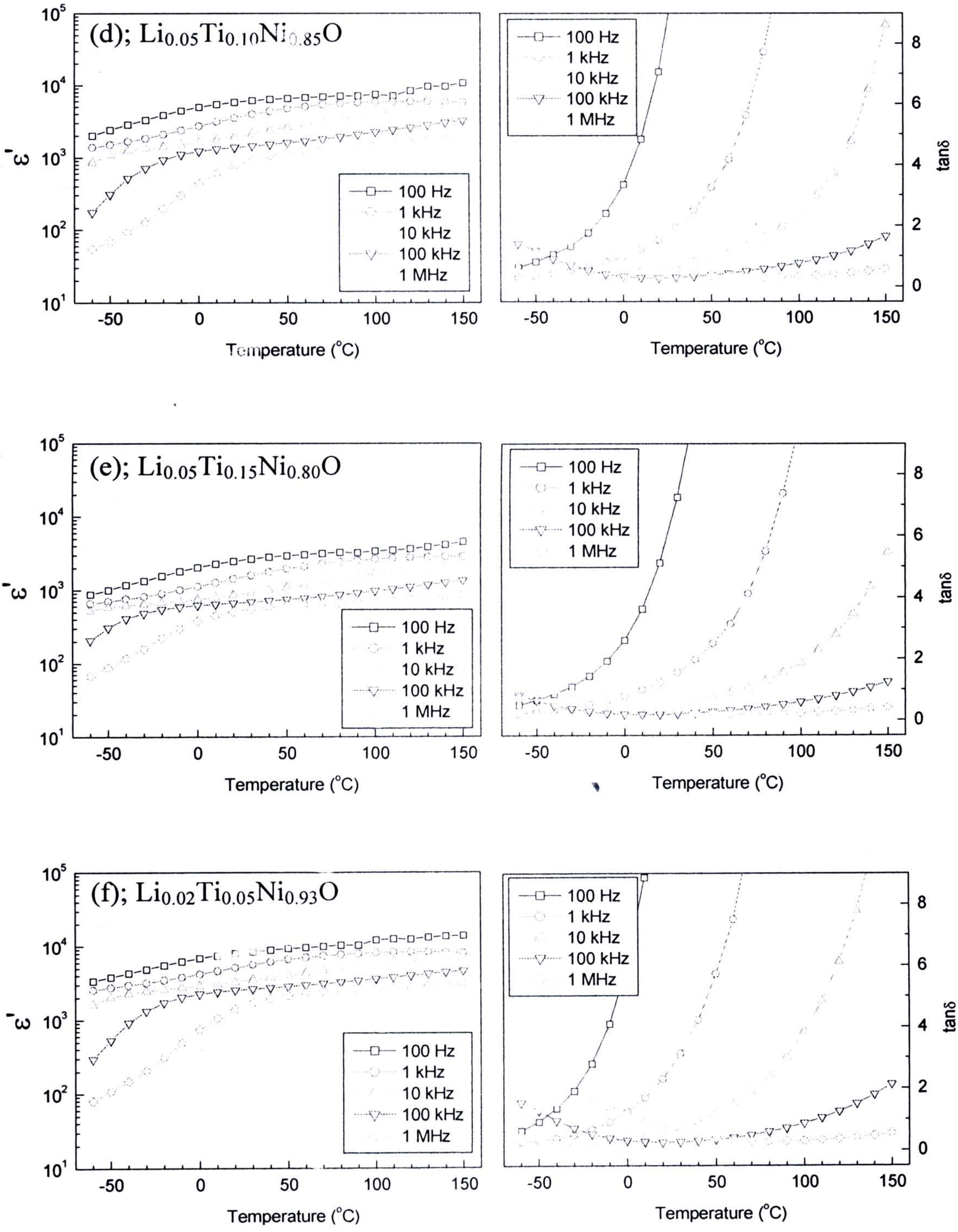

Figure 5.21 Temperature dependence of dielectric constant (ε') and loss tangent ($\tan\delta$) at the frequency range of 10^2-10^6 Hz for $Li_xTi_yNi_{1-x-y}O$ ceramics sintered at 1200 °C. (Cont.)

5.1.3.2 Frequency dependence of the dielectric properties of the $Li_xTi_yNi_{1-x-y}O$ ceramics

According to the temperature dependence of the dielectric properties of the $Li_xTi_yNi_{1-x-y}O$ ceramics as previously presented in section 5.1.3.1, the understanding of the mechanism related to the dielectric relaxation is difficult to ascribe. Alternatively, the mechanism of the dielectric relaxation can be well understood by considering the frequency dependence of the dielectric properties (Ahmad, Yamada, 2007; Liu et al., 2004). Figures 5.22(a)-5.22(g) demonstrate the frequency dependence of the dielectric constant (ε'), loss tangent ($\tan\delta$), and dielectric loss (ε'') at the selected temperatures of -60, -30, 0, 30, and 60 °C for the $Li_xTi_yNi_{1-x-y}O$ ceramics sintered at 1200 °C for 4 h. All of the samples show the dielectric relaxation behavior, as described in Chapter II. Note that the dielectric spectra of all samples are similar in every way. The overall dielectric relaxation behavior of these $Li_xTi_yNi_{1-x-y}O$ ceramics can be ascribed as the following steps. (1) The dielectric spectrum at the temperature of -60 °C is firstly considered. A plateau of dielectric constant (ε') can be observed at frequencies below 10^4 Hz. This dielectric constant region is highest. (2) At this temperature, with increasing the frequency, the dielectric constant decreases rapidly to a low value. (3) Another plateau of the low dielectric constant can be observed at a high frequency range, ~10^5-10^6 Hz, especially for the $Li_{0.05}Ti_{0.02}Ni_{0.93}O$ and $Li_{0.05}Ti_{0.05}Ni_{0.90}O$ ceramics. (4) The observed rapid decrease in the dielectric constant is found to associate with the appearance of the peaks of the loss tangent ($\tan\delta$) and the dielectric loss (ε'). (5) It is interesting that the sudden drop and the related peaks of loss tangent and dielectric loss move to higher frequencies with increasing the temperature. Additionally, the plateau of the high dielectric constant extends to the higher frequencies as well. (6) If the temperature is sufficient high, the dielectric loss and the loss tangent peaks shift out of the measuring frequency range. This dielectric relaxation behavior is suggested to the thermally activated mechanism. The energy required for these relaxation processes can also be calculated form the dielectric relaxation behavior, which will be expressed in the section 5.1.4 for the effect of sintering temperature on structural and dielectric properties. The overall dielectric relaxation of the $Li_xTi_yNi_{1-x-y}O$ ceramics observed in figures 5.22(a)-5.22(g) is typical for the Debye-like relaxation model.

These steps of the dielectric relaxation behavior observed in the $Li_xTi_yNi_{1-x-y}O$ ceramics can be ascribed based on the orientational polarization. At a fixed temperature, dipoles that are produced in the samples require a time to produce the polarization. This means that the dipole can not immediately be rotated with respect to the direction of an applied electric field after the samples is applied by the field. On the other hand, the orientation of the dipoles from the initial position to the same direction of the applied field must use a time. This time is called to be a *dielectric relaxation time* (τ), which is constant at any temperature. At a low-frequency range, all of the dipoles in the samples can rotate with respect to the direction of the applied alternating electric field. As a result, the polarization can fully be introduced. Consequently, the dielectric constant of the $Li_xTi_yNi_{1-x-y}O$ ceramics is found to be highest at the low-frequency range. The reversion of the alternating electric field at a high-frequency range is faster than that of a low-frequency range. When the frequency is sufficiently high, the reversion of the alternating electric field at this frequency will be faster than that of the reversion of the dipoles. In this case, the direction of the alternating electric field reversed before the dipoles can be responsed; therefore, the polarization can not fully be produced. Consequently, the dielectric constant is found to decrease rapidly. At the sudden drop frequency range, the loss tangent and the dielectric loss are found to be maximum values. The dielectric behavior can be explained based on the fact that at this frequency range, the frequency of the applied electric field is very close to the natural frequency of the dipoles. The oscillating charge dipoles are coupled directly with the oscillating field; as a result, a maximum in electrical energy is absorbed.

At a fixed temperature, the frequency at a peak position of the loss tangent ($\tan\delta$) is found to be higher than that of the dielectric loss (ε''). As suggested in Chapter II by equations (2.63) and (2.64), the peak positions of the loss tangent and the dielectric loss are located at the frequencies of $\sqrt{\varepsilon'_s/\varepsilon'_\infty}/2\pi\tau$ and $1/2\pi\tau$, respectively. All of the cases, term $\sqrt{\varepsilon'_s/\varepsilon'_\infty}$ is higher than unity; consequently, the peak position of the loss tangent would be higher than that of the dielectric loss by

$$\Delta f_p = \frac{1}{2\pi\tau}\left(\sqrt{\frac{\varepsilon'_s}{\varepsilon'_\infty}} - 1\right), \tag{5.6}$$

where $\Delta f_p = f_{p(\delta)} - f_{p(\varepsilon'')}$, $f_{p(\delta)}$ and $f_{p(\varepsilon'')}$ are the frequencies at the peak position of the loss tangent and the dielectric loss, respectively. It is worth noting that the values of the dielectric loss and the loss tangent at low frequencies are relatively high compared to the loss due to the relaxation process. This high value is due to the influence of the dc conduction produced in the ceramics (Wu J et al., 2002). The effect of the dc conduction will briefly be discussed in the section 5.1.5 for the effect of dc conductivity on dielectric relaxation behavior.

The another interesting result can be observed from the dielectric relaxation behavior of the $Ti_{0.10}Ni_{0.90}O$ and $Ti_{0.15}Ni_{0.85}O$ ceramics, as shown respectively in figures 5.22(a) and 5.22(b). In general, it is widely accepted that the dielectric relaxation behavior of the $Li_xTi_yNi_{1-x-y}O$ ceramics is closely related to the Maxwell-Wagner polarization or the interfacial polarization. The observed giant dielectric constant in this material is therefore attributed to the Maxwell-Wagner polarization (Wu J et al., 2002, 2003; Lin et al., 2006a; Maensiri et al., 2007). Under an applied electric field, free charge carriers, which are produced by the Li doping, are restricted and accumulated at insulating grain boundaries due to the accumulation of the $NiTiO_3$ phase. However, these two ceramic samples are not doped with the Li doping. Hence, this observed dielectric relaxation should not be related to the Maxwell-Wagner polarization as suggested in the literatures. Moreover, it was suggested from the XRD and SEM results as discussed in the first two sections that the most of Ti doping ions can not substitute the Ni^{2+} sites in the NiO crystal lattice. Thus, the dielectric relaxation behavior of the $Ti_{0.10}Ni_{0.90}O$ and $Ti_{0.15}Ni_{0.85}O$ ceramics is not certainly associated with the defect dipoles that are produced by the substitution of the Ti ions. The dielectric relaxation of these two samples might be related to the intrinsic defects that can be occurred in ceramics during the sintering process such as Schottky or Frenkel defects as well as oxygen vacacies. The detail of this subject will be discussed in section 5.1.4.2 for the effect of the sintering temperature on dielectric relaxation behavior of the $Li_xTi_yNi_{1-x-y}O$ ceramics.

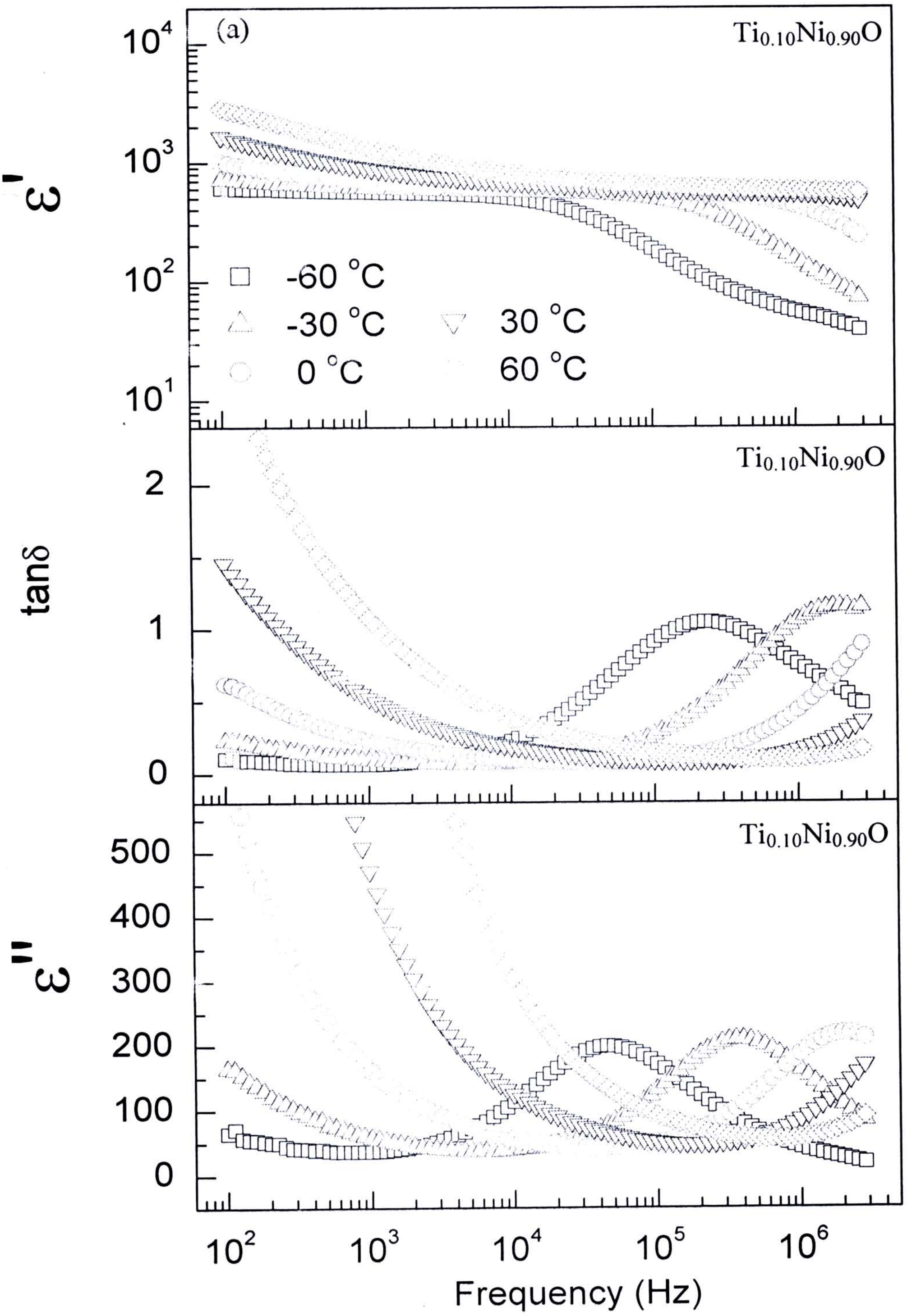

Figure 5.22 Frequency dependence of dielectric properties (dielectric constant (ε′), loss tangent (tanδ), and dielectric loss (ε″)) at the temperature range of -60 to 60 °C for $Li_xTi_yNi_{1-x-y}O$ ceramics sintered at 1200 °C.

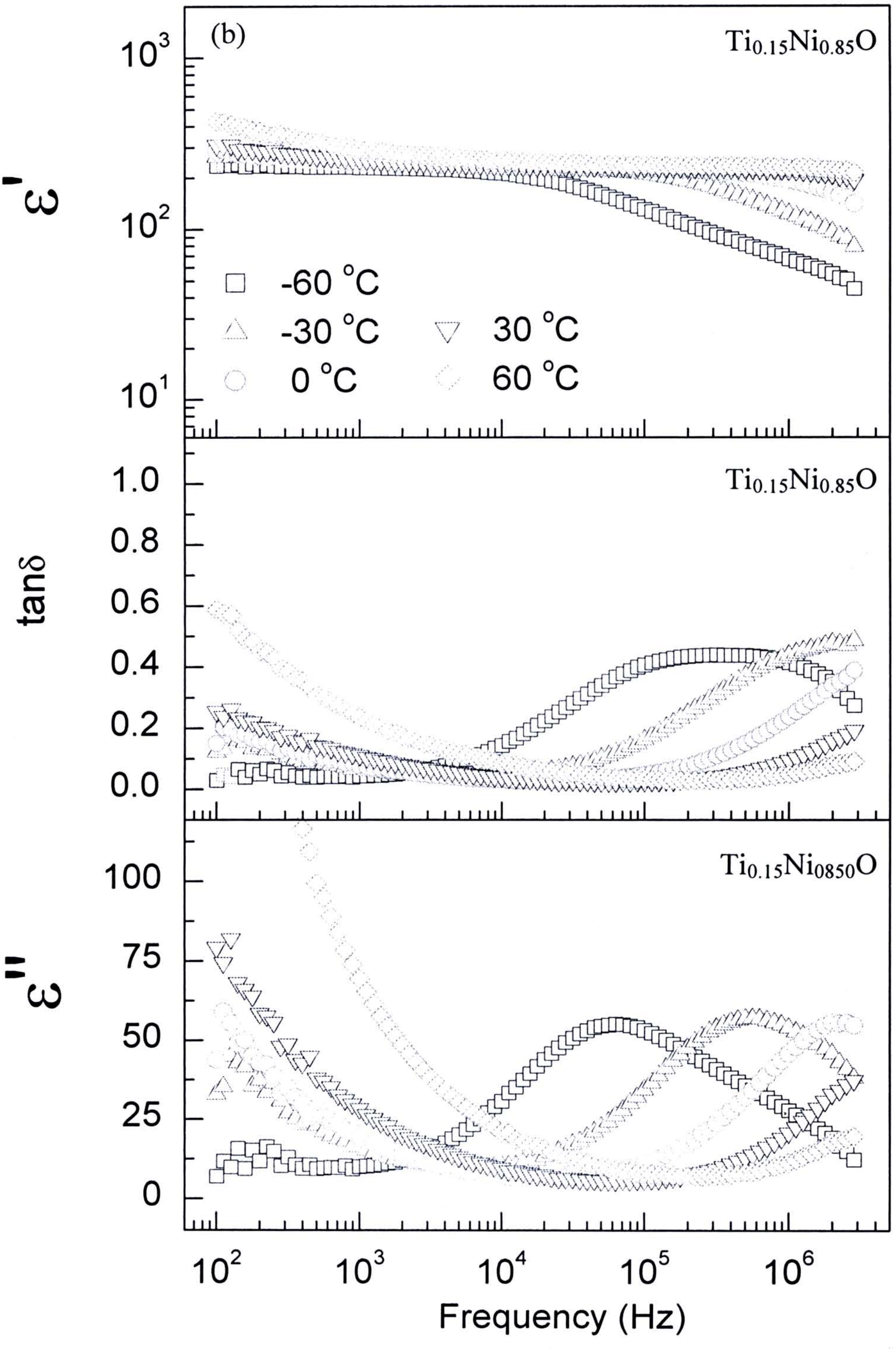

Figure 5.22 Frequency dependence of dielectric properties (dielectric constant (ε'), loss tangent (tanδ), and dielectric loss (ε'')) at the temperature range of -60 to 60 °C for $Li_xTi_yNi_{1-x-y}O$ ceramics sintered at 1200 °C. (Cont.)

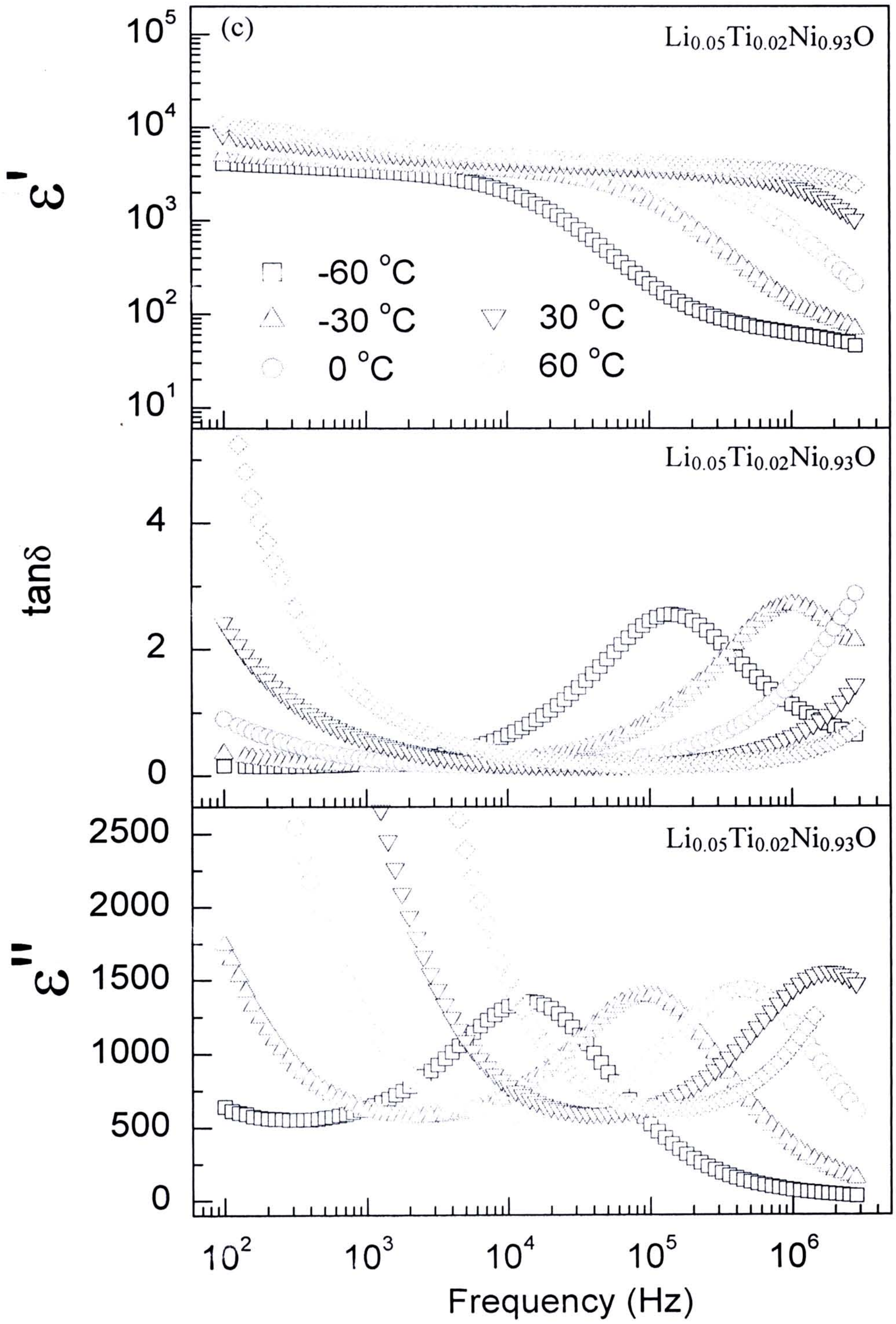

Figure 5.22 Frequency dependence of dielectric properties (dielectric constant (ε′), loss tangent (tanδ), and dielectric loss (ε″)) at the temperature range of -60 to 60 °C for $Li_xTi_yNi_{1-x-y}O$ ceramics sintered at 1200 °C. (Cont.)

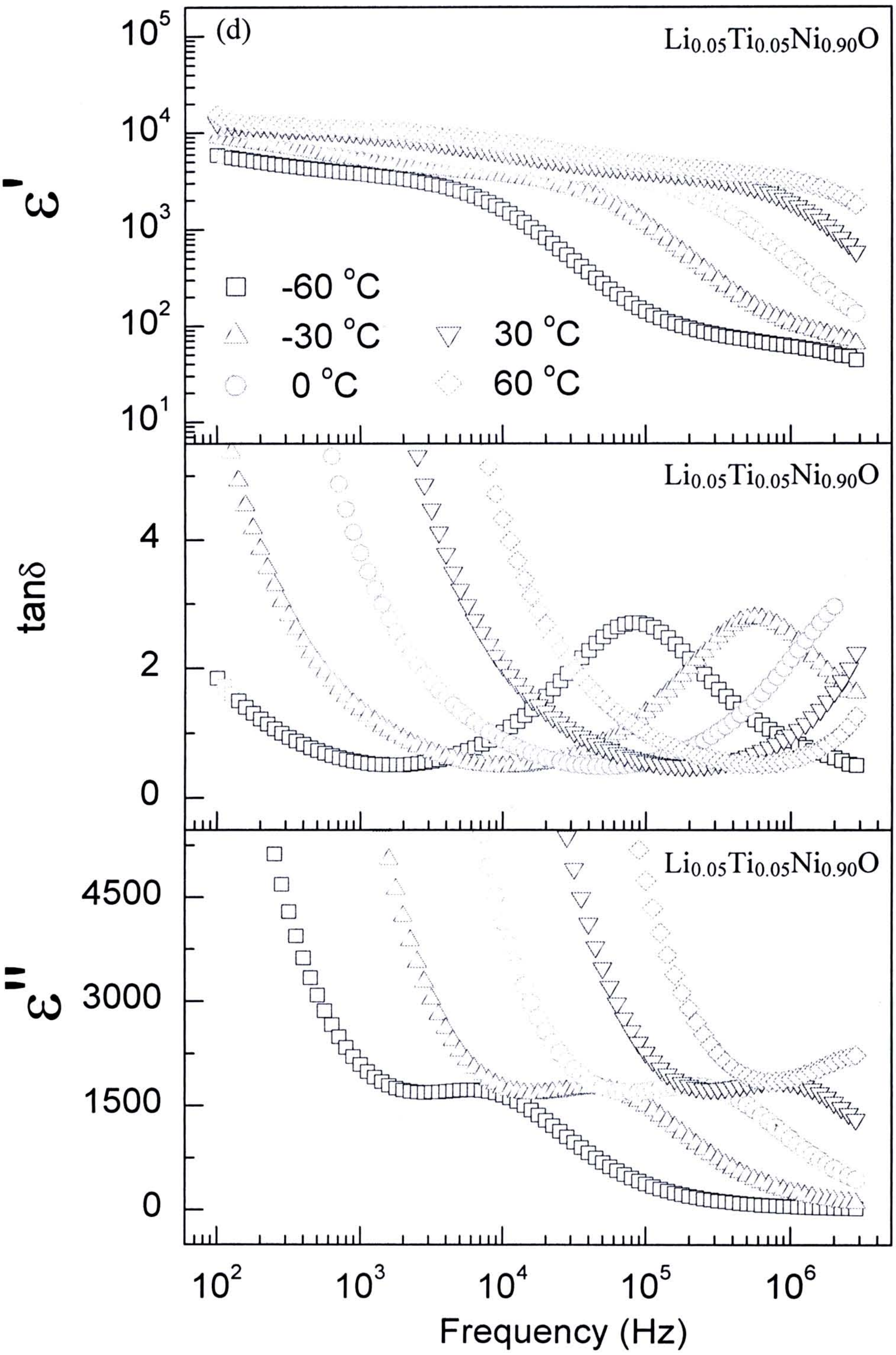

Figure 5.22 Frequency dependence of dielectric properties (dielectric constant (ε′), loss tangent (tanδ), and dielectric loss (ε″)) at the temperature range of -60 to 60 °C for $Li_xTi_yNi_{1-x-y}O$ ceramics sintered at 1200 °C. (Cont.)

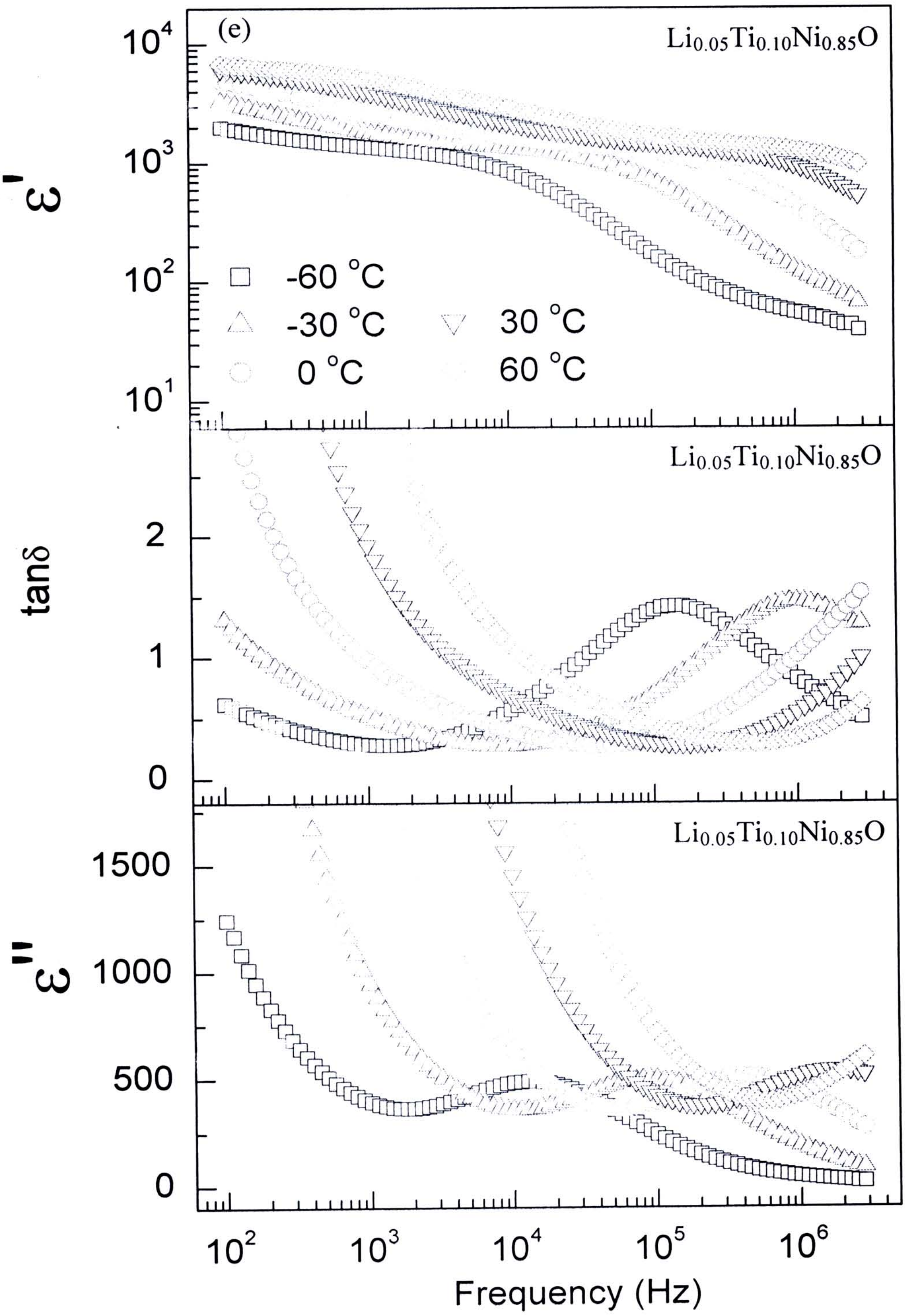

Figure 5.22 Frequency dependence of dielectric properties (dielectric constant (ε′), loss tangent (tanδ), and dielectric loss (ε″)) at the temperature range of -60 to 60 °C for $Li_xTi_yNi_{1-x-y}O$ ceramics sintered at 1200 °C. (Cont.)

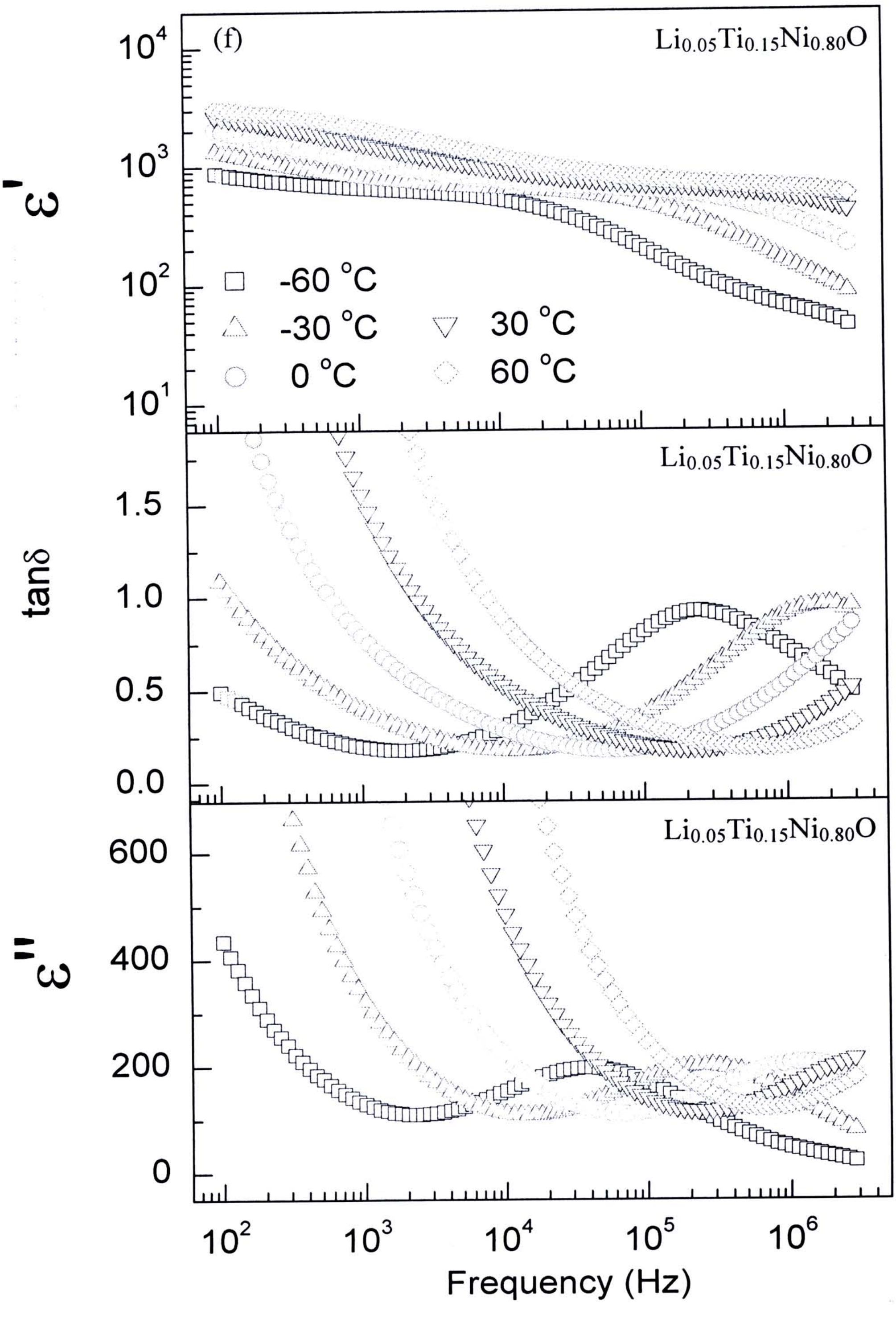

Figure 5.22 Frequency dependence of dielectric properties (dielectric constant (ε′), loss tangent (tanδ), and dielectric loss (ε″)) at the temperature range of -60 to 60 °C for $Li_xTi_yNi_{1-x-y}O$ ceramics sintered at 1200 °C. (Cont.)

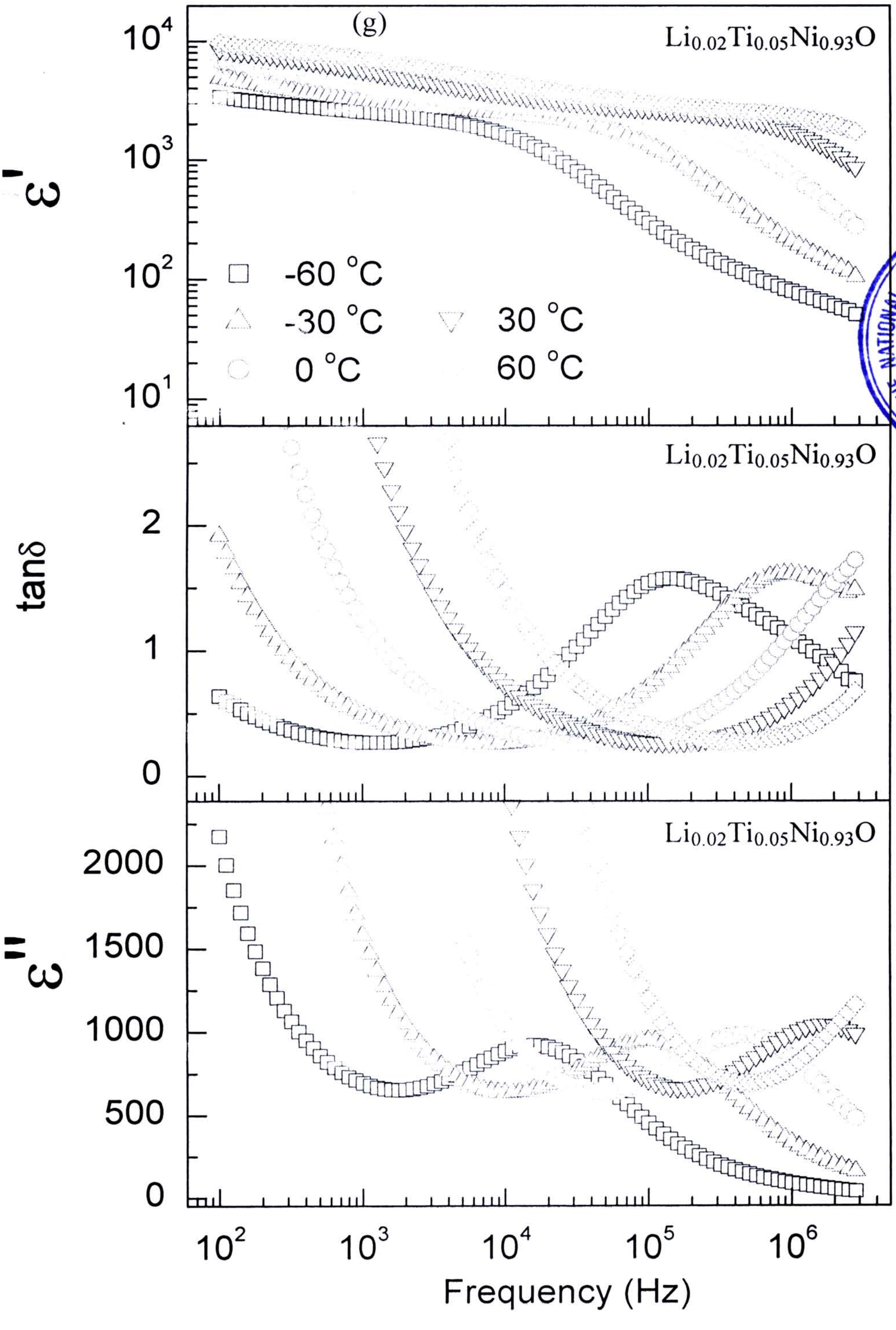

Figure 5.22 Frequency dependence of dielectric properties (dielectric constant (ε′), loss tangent (tanδ), and dielectric loss (ε″)) at the temperature range of -60 to 60 °C for $Li_xTi_yNi_{1-x-y}O$ ceramics sintered at 1200 °C. (Cont.)

5.1.4 Effect of sintering temperature on dielectric properties

5.1.4.1 Effect of the sintering temperature on the dielectric constant and dielectric loss of the $Li_xTi_yNi_{1-x-y}O$ ceramics

It is well known that the microstructure of ceramics relates closely with their properties. Therefore the variation in the microstructure can result in the change of the properties. In general, sintering conditions can be used to control the microstructure of materials. According to the SEM results, the grain sizes of the $Li_xTi_yNi_{1-x-y}O$ ceramics sintered at 1280 °C are found to be higher than those of the samples sintered at 1200 °C. The change in the microstructure due to the sintering temperature can affect to the dielectric properties of the $Li_xTi_yNi_{1-x-y}O$ ceramics, as shown in figure 5.23. Figures 5.23(a)-5.23(d) demonstrate the effect of sintering temperature on the dielectric constant of the $Li_{0.05}Ti_yNi_{0.95-y}O$ ceramics with different concentration of the Ti doping. It is clearly seen from these figures that the dielectric constant of all $Li_{0.05}Ti_yNi_{0.95-y}O$ ceramics increases with increasing the sintering temperature. This result may be related to the increase in the grain size of the ceramics or other changes in the microstructure or defects.

As suggested in the section of the microstructure analysis, the observed increase in the grain size due to the increase in the sintering temperature is attributed to the enhancement of the diffusion coefficient. The diffusion rate of ceramics is depended on the type and concentration of defects (Rahaman, 2003). It is possible that the concentration of the defects, especially for oxygen vacancies, may increase with increasing the sintering temperature during the sintering process (Sinclair et al., 2002). The oxygen vacancies produced in the ceramics sintered at 1280 °C should therefore be higher than those of the ceramics sintered at 1200 °C. As a result, the grain size of the ceramics increases by this way. Generally, in ceramics, the defects can be electrically charged; moreover, the composition of the ceramics may become nonstoichiometric by annealing in a suitable gaseous atmosphere. Therefore, defects in the $Li_{0.05}Ti_yNi_{0.95-y}O$ ceramics may become defect dipoles when the samples are applied by the electric field. These defect dipoles can rotate with respect to the applied field, producing the orientational polarization. Furthermore, the presence of domain boundaries in the ceramics sintered at 1280 °C, which have the larger grain size, is more possible compared to the small grain size

(Shao et al., 2006; Fang, Liu, 2005; Chung et al., 2004; Zhao et al., 2007). Under an applied electric field, some charge carriers can be accumulated at these boundaries, generating the interfacial polarization at the domain boundaries. Thus, the total polarization produced in the ceramics is enhanced; the dielectric constant of the ceramics sintered at 1280 °C is therefore enhanced.

As shown in figures 5.23(e)-5.23(h), the dielectric loss of all $Li_{0.05}Ti_yNi_{0.95-y}O$ ceramics increases as the sintering temperature increases. This observation corresponds to the observed increase in their dielectric constant. As outlined earlier, the enhancement of the dielectric constant is suggested to the increase in the oxygen vacancies, which can be considered as charge carriers. Certainly, more charge carriers can cause in a change of the dielectric loss. With increasing the sintering temperature, the concentration of the charge carriers increases; as a result, the possibility that charges can surmount barriers in the ceramics is certainly enhanced. Consequently, the dc conduction, which relates to the motion of free charges, must rise. It is worth noting that the difference in the dielectric constant of the $Li_{0.05}Ti_yNi_{0.95-y}O$ ceramics sintered at these two temperatures might be attributed to the porosity in the ceramics. However, the raise in the dielectric constant is most likely due to the enhancement of the oxygen vacancies because it corresponds to the observed increase in the dielectric loss.

Figures 5.24(a)-5.24(e) show the frequency dependence of the dielectric properties at various temperatures for the $Li_xTi_yNi_{1-x-y}O$ ceramics with different concentrations of Li and Ti doping sintered at 1280 °C for 4 h in air. Although the values of the dielectric constant and dielectric loss of the $Li_xTi_yNi_{1-x-y}O$ ceramics sintered at 1200 and 1280 °C are completely different, the frequency dependence of the dielectric properties of these two sets of the ceramics sintered at 1200 and 1280 °C is very similar. The dielectric relaxation behavior can be observed and it is related to the thermally activated mechanism. From these points of view, it is important to note that both of the temperature and frequency dependence of the dielectric properties of the $Li_xTi_yNi_{1-x-y}O$ ceramics are similar to those observed in $CaCu_3Ti_4O_{12}$ (Liu et al., 2005; Krohns et al., 2008; Adams et al., 2002; Ramirez et al., 2000; Thongbai et al., 2007), $BaTi_{0.9}(Ni_{1/2}W_{1/2})_{0.1}O_3$ (Zhao et al., 2007), and CuO (Sarkar et al., 2006, 2008a,b) ceramics.

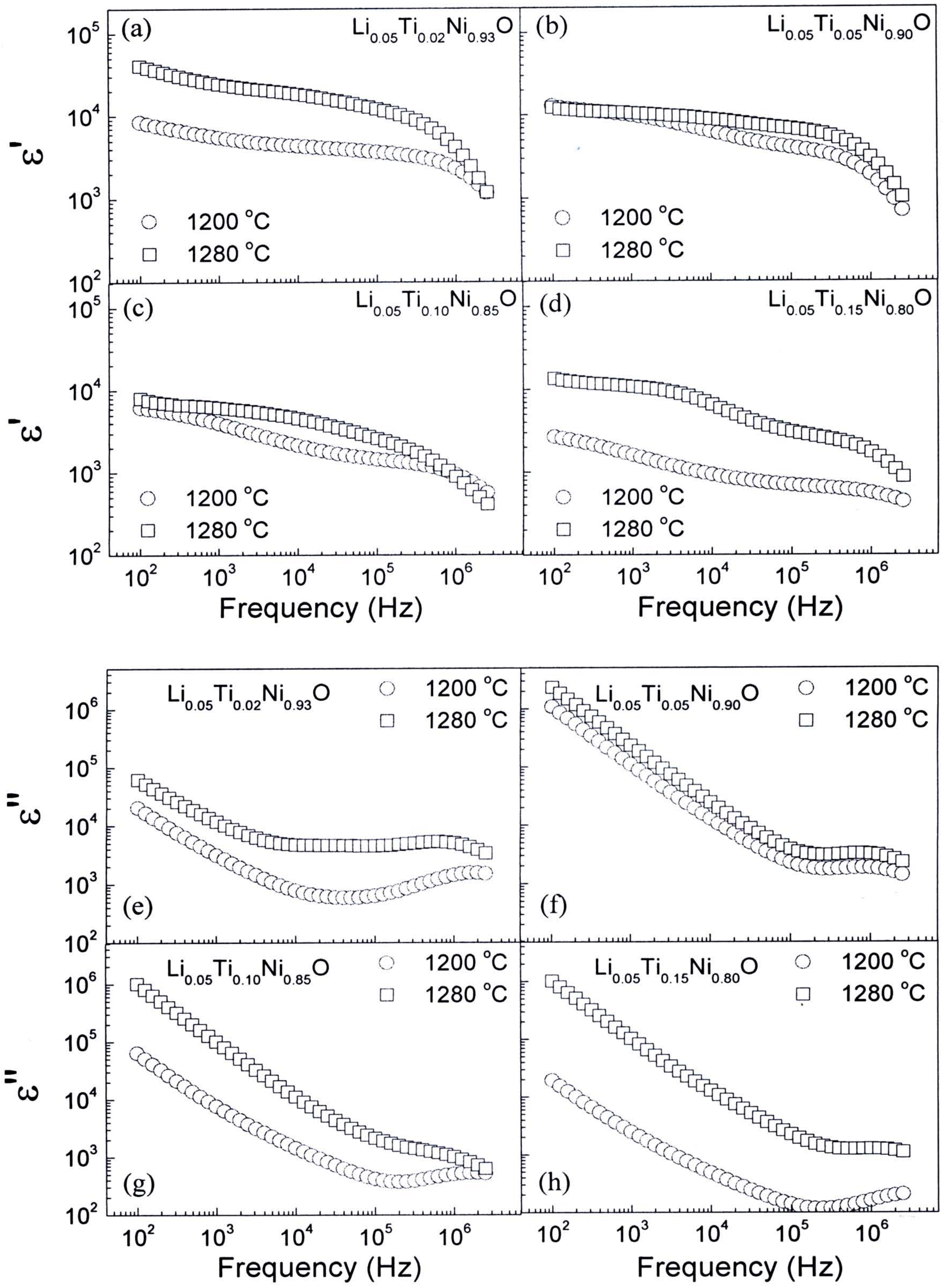

Figure 5.23 (a)-(d) Dielectric constant (ε') and (e)-(h) dielectric loss (ε'') of the $Li_{0.05}Ti_yNi_{0.95-y}O$ ceramics sintered at 1200 and 1280 °C

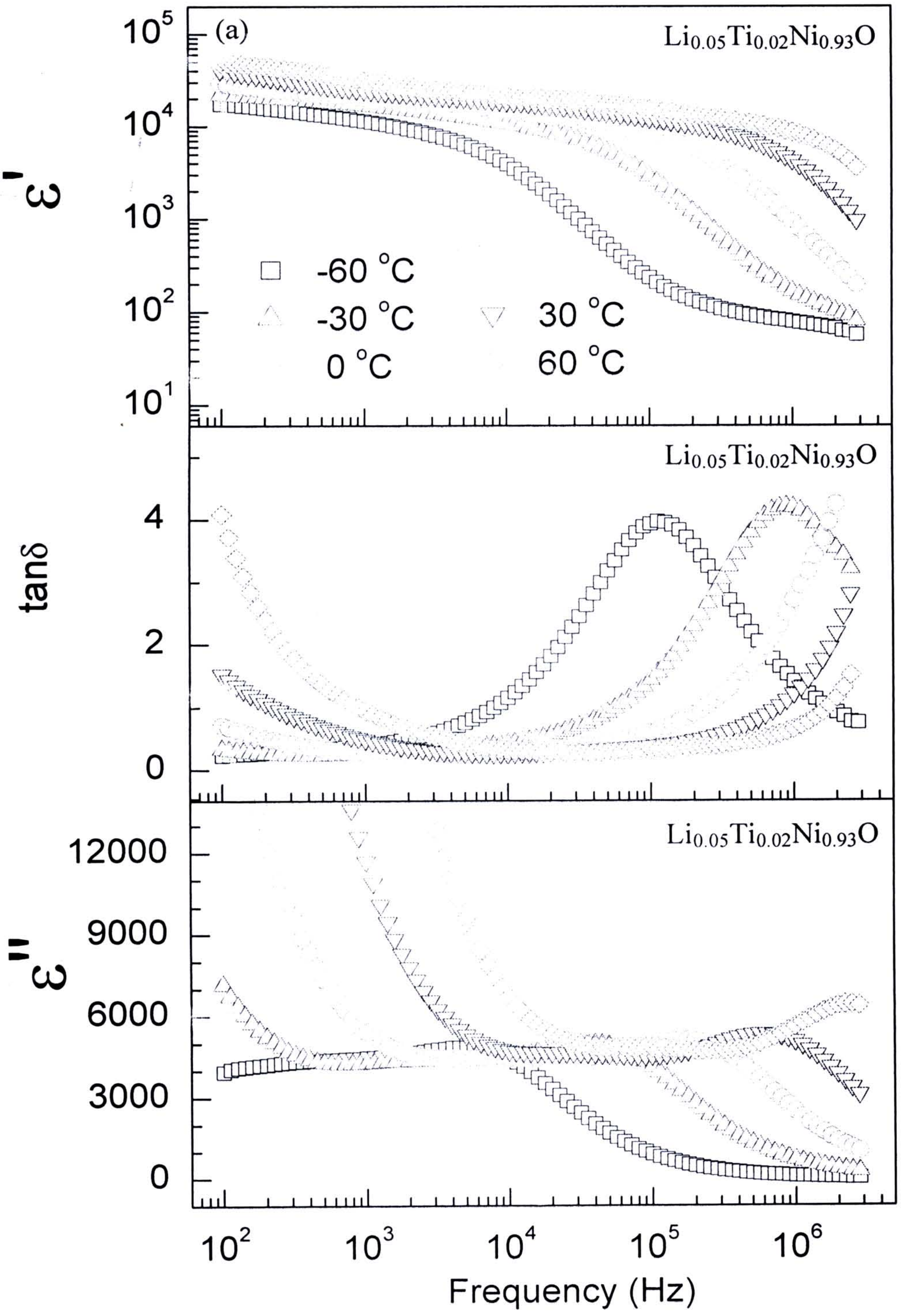

Figure 5.24 Frequency dependence of dielectric properties (dielectric constant (ε′), loss tangent (tanδ), and dielectric loss (ε″)) at the temperature range of -60 to 60 °C for $Li_xTi_yNi_{1-x-y}O$ ceramics sintered at 1280 °C.

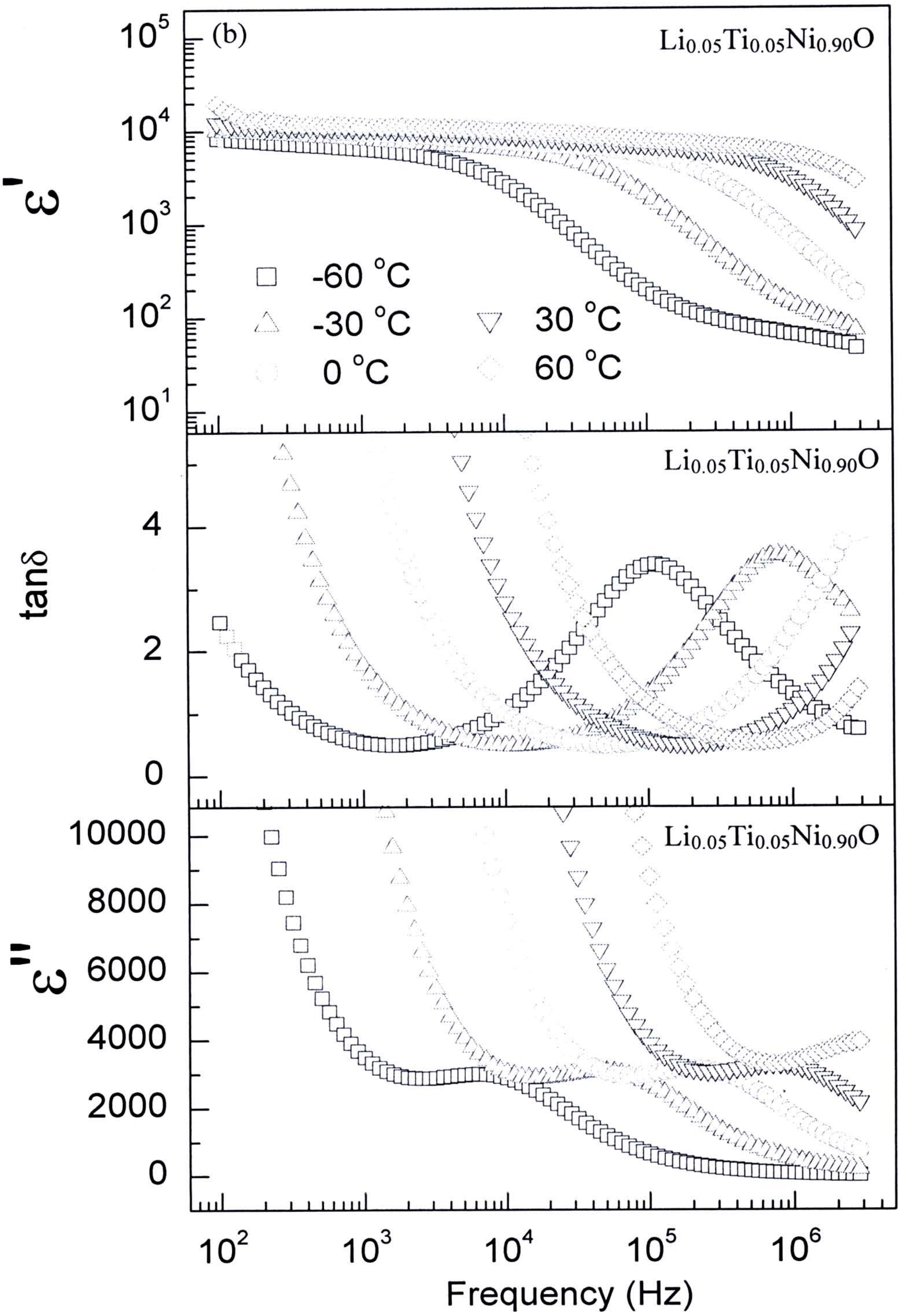

Figure 5.24 Frequency dependence of dielectric properties (dielectric constant (ε'), loss tangent (tanδ), and dielectric loss (ε'')) at the temperature range of -60 to 60 °C for $Li_xTi_yNi_{1-x-y}O$ ceramics sintered at 1280 °C. (Cont.)

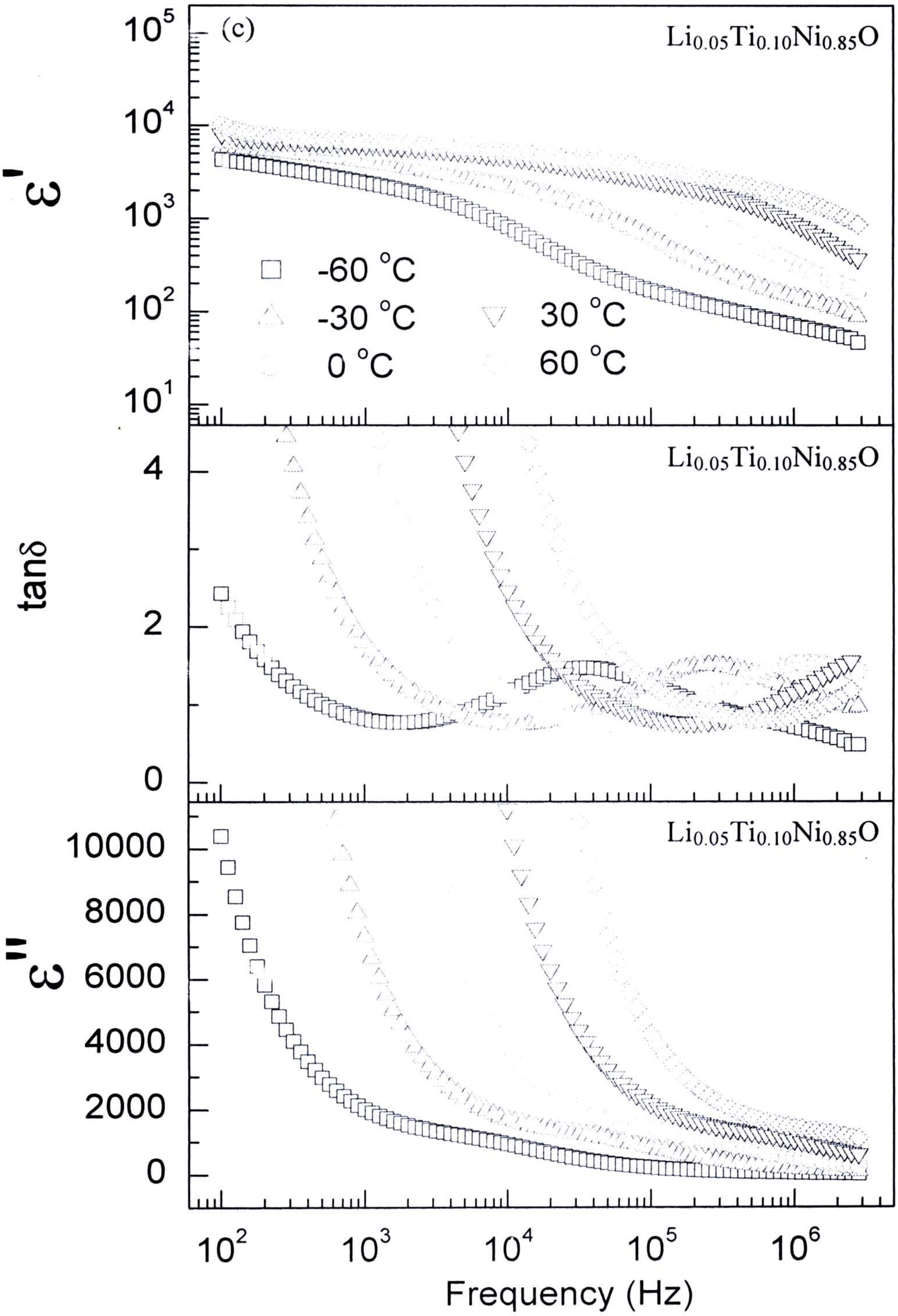

Figure 5.24 Frequency dependence of dielectric properties (dielectric constant (ε′), loss tangent (tanδ), and dielectric loss (ε″)) at the temperature range of -60 to 60 °C for $Li_xTi_yNi_{1-x-y}O$ ceramics sintered at 1280 °C. (Cont.)

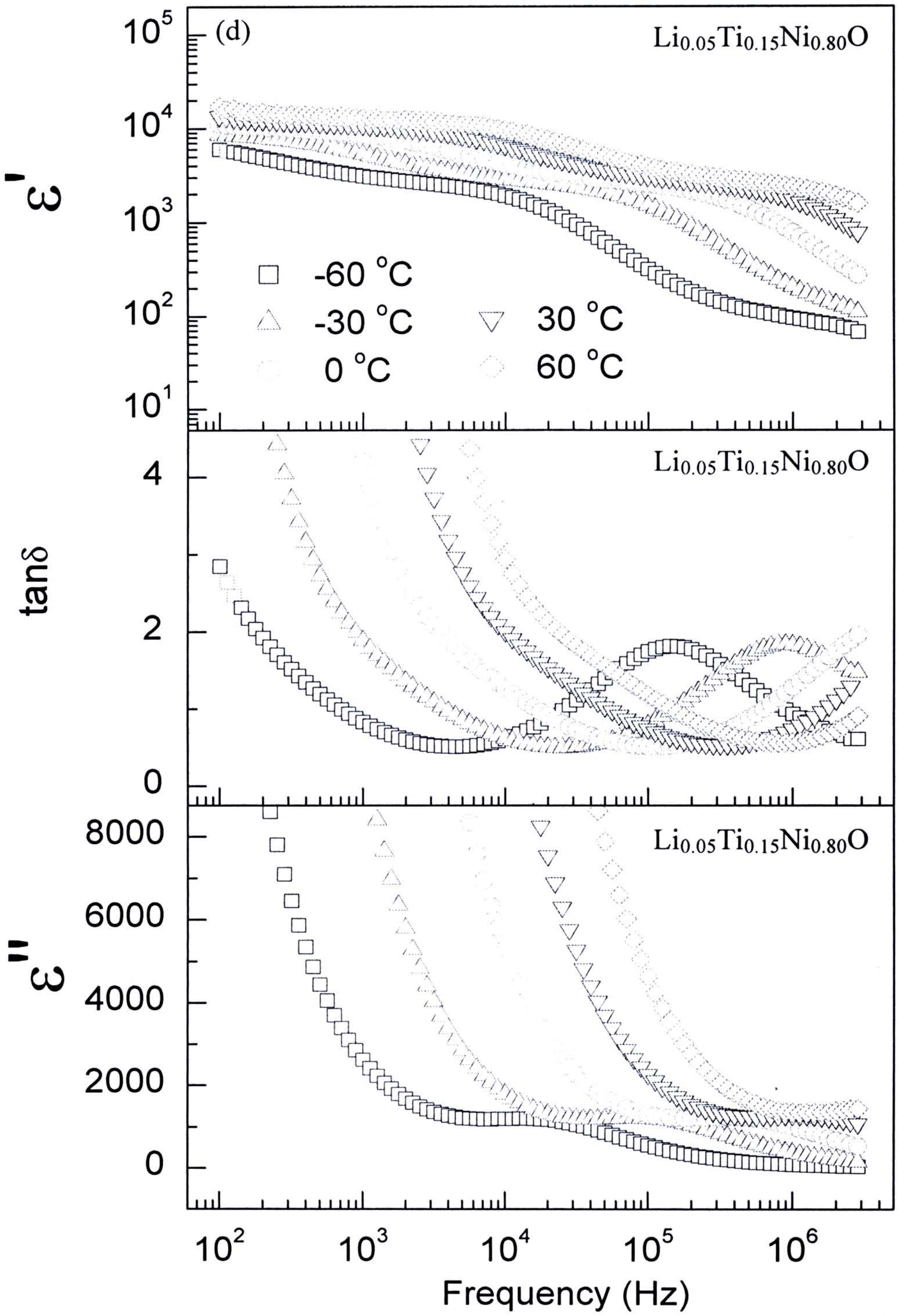

Figure 5.24 Frequency dependence of dielectric properties (dielectric constant (ε′), loss tangent (tanδ), and dielectric loss (ε″)) at the temperature range of -60 to 60 °C for $Li_xTi_yNi_{1-x-y}O$ ceramics sintered at 1280 °C. (Cont.)

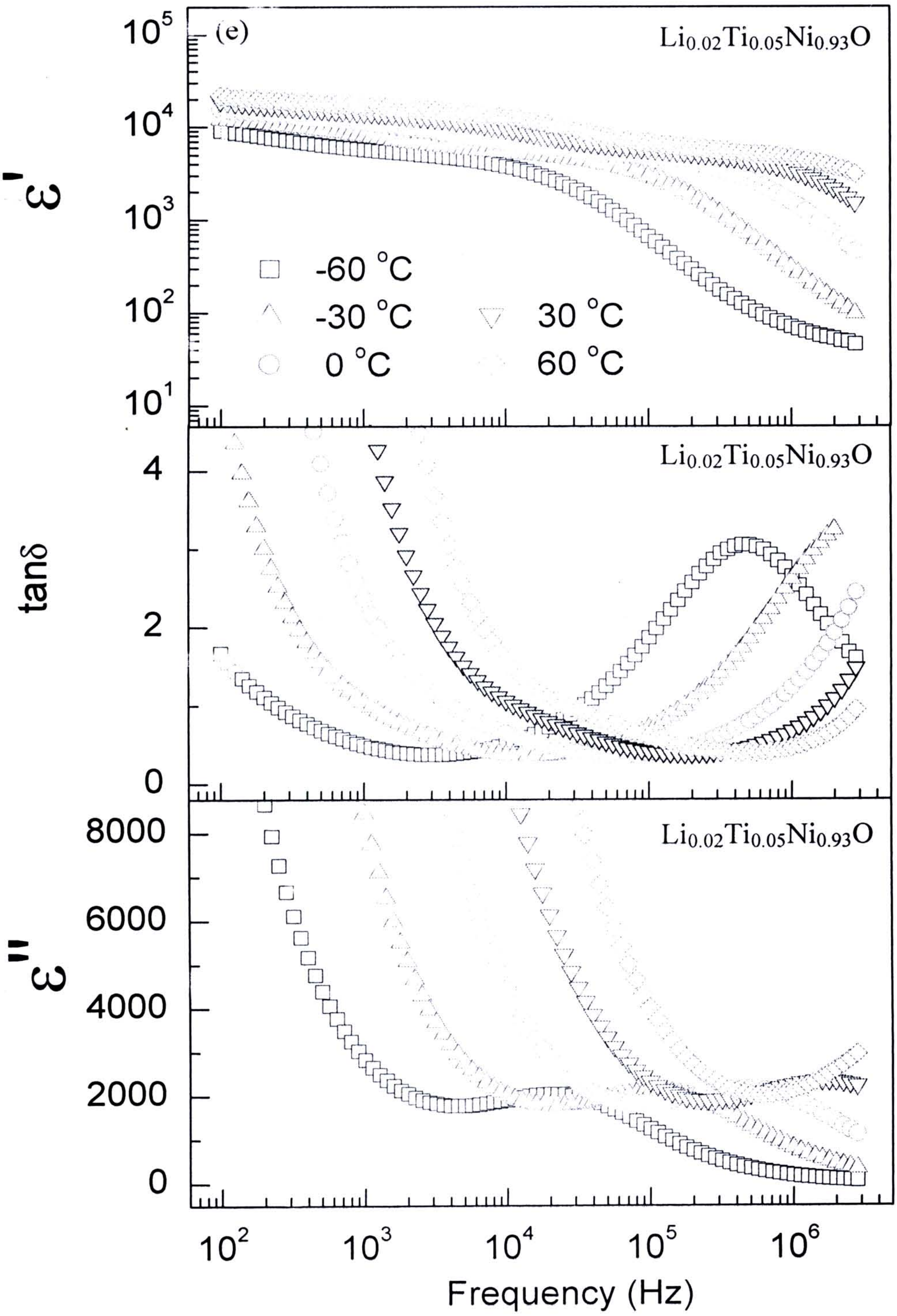

Figure 5.24 Frequency dependence of dielectric properties (dielectric constant (ε′), loss tangent (tanδ), and dielectric loss (ε″)) at the temperature range of -60 to 60 °C for $Li_xTi_yNi_{1-x-y}O$ ceramics sintered at 1280 °C. (Cont.)

5.1.4.2 Effect of the sintering temperature on the dielectric relaxation behavior of the $Li_xTi_yNi_{1-x-y}O$ ceramics

The interesting result can be observed from the dielectric spectra of the $Li_{0.05}Ti_{0.10}Ni_{0.85}O$, $Li_{0.05}Ti_{0.15}Ni_{0.80}O$, and $Li_{0.02}Ti_{0.05}Ni_{0.93}O$ ceramics, as revealed in figures 5.24(c)-5.24(e), respectively. Two steps of the rapid decrease in the dielectric constant are observed at low- and high-frequency ranges, suggesting that there exist two sets of thermally activated dielectric relaxations in these three ceramics. The existence of two sets of the dielectric relaxations indicates that there are at least two sources of polarizations contributed to the total dielectric constant of these three samples. The low-frequency relaxation will be discussed in section 5.7.1.2. As previous section, the frequency dependence of the dielectric properties of the $Li_xTi_yNi_{1-x-y}O$ ceramics, the high-frequency relaxation behavior can be observed in all of these ceramics. The dielectric relaxation can be exhibited in the ceramics both of those sintered at 1200 and 1280 ^{o}C. The relaxation peak and the related rapid decrease in the dielectric constant move to higher frequency with increasing the measuring temperature. Certainly, this movement of both needs energy to drive the mechanism. This energy is usually referred to the *activation energy*, which requires for the thermally activated dielectric relaxation process. This relaxation activation energy can be calculated by following the Arrhenius law,

$$\tau = \tau_0 \exp\left(\frac{E_a}{k_B T}\right), \qquad (5.7)$$

where τ is the relaxation time, τ_0 is a constant time, E_a is the activation energy required for the relaxation process. As proved in Chapter II, the value of τ can be achieved using the relation,

$$\tau = \frac{1}{\omega_p} = \frac{1}{2\pi f_p}, \qquad (5.8)$$

where f_p is the frequency at the dielectric loss (ε'') peak. Thus, the values of τ at various temperatures that are observed the dielectric loss peak are obtained from the experimental results. Because τ_0 can not be obtained from the experimental result, the activation energy can not therefore be achieved at a certain temperature. However, it can be calculated from the slope of the graph that expresses the relationship between $\ln(\tau)$ and $1/T$. It can be proved from equation (5.7) that

$$\ln(\tau) = \frac{1}{T}\left(\frac{E_a}{k_B}\right) + \ln(\tau_0). \tag{5.9}$$

If the relaxation times are linearly depended on the inversely temperature, the activation energy can suitably be calculated. Therefore, the slope of the graph following to equation (5.9) is equal to E_a / k_B.

Figures 5.25(a) and 5.25(b) demonstrate the temperature dependence of the relaxation time of all $Li_xTi_yNi_{1-x-y}O$ ceramics sintered at 1200 and 1280 °C respectively. It is evident that the temperature dependence of the relaxation time follows to the Arrhenius law. In this condition, the relaxation activation energy (E_a) of the $Li_xTi_yNi_{1-x-y}O$ ceramics can suitably be calculated as summarized in Table 5.4. Moreover, the constant parameter τ_0 is also obtained from this calculation. As revealed in figures 5.25(a) and 5.25(b), the relaxation time of all samples decreases with increasing the temperature, suggesting to the faster rate of polarization at high temperature. At a relative high temperature, the oscillating charges or dipoles are in the higher state of energy. Thus, the changed state of these dipoles from the equilibrium state to the excited state can be activated in a shorter time comparing to a relative low temperature. As a result, the value of τ is reduced by increasing the temperature. According to the relationship of $\omega_p \tau = 1$, it is clear that ω_p can be driven to higher frequency by increasing the temperature. Consequently, the relaxation process can extend to a higher frequency range.

As revealed in Table 5.4, for the $Li_xTi_yNi_{1-x-y}O$ ceramics, the sintering temperature has an influence on the relaxation activation energy, except for the $Li_{0.05}Ti_{0.02}Ni_{0.93}O$ ceramic. With increasing the sintering temperature, the activation energy of the $Li_{0.05}Ti_{0.02}Ni_{0.93}O$ ceramic is found to be constant. On the other hand, the activation energies of the $Li_{0.05}Ti_{0.05}Ni_{0.90}O$, $Li_{0.05}Ti_{0.15}Ni_{0.80}O$, and $Li_{0.02}Ti_{0.05}Ni_{0.93}O$ ceramics are respectively found to decrease by 2.30, 6.94, and 7.61 %. The observed decrease in the activation energy may be related to the difference in oxygen vacancy concentration between the samples sintered at 1200 and 1280 ^{o}C. As suggested in the previous section, the dielectric constant of all $Li_xTi_yNi_{1-x-y}O$ ceramics is found to increase with increasing the sintering temperature. The variation in the oxygen vacancy concentration is suggested to be the most one of the possible mechanisms that may be responsible for this observation. The increase in the dielectric constant might be associated with the decrease in the activation energy (Lin et al., 2006a; Cheng et al., 2008).

The activation energies required for the relaxation process of the $Ti_yNi_{1-y}O$ ceramics are found to be higher than those of the $Li_xTi_yNi_{1-x-y}O$ ceramics. Moreover, it is found that the values of τ_0 of the $Ti_yNi_{1-y}O$ ceramics are two orders of magnitude lower than those of the $Li_xTi_yNi_{1-x-y}O$ ceramics. Usually, the value of τ_0 that is in the range of 10^{-13}-10^{-14} s can be suggestive that the ionic polarization is dominant. The value of τ_0 that is higher than this range may be suggestive that the dielectric response in a material relates to the interracial polarization such as the Maxwell-Wagner polarization (Hence, West, 1990). This is an important clue to describe the giant dielectric response in the $Li_xTi_yNi_{1-x-y}O$ ceramics. However, it is not enough to associate this observation with the origin of the giant dielectric response in NiO-based ceramics. Although almost researches have suggested that the giant dielectric properties of the $Li_xTi_yNi_{1-x-y}O$ ceramics are attributed to the Maxwell-Wagner polarization at the grain boundaries (Wu J et al., 2002, 2003; Maensiri et al., 2007; Lin et al., 2006a), the strong experimental data to support this model are still missing. Note that the values of τ_0 of the $Ti_yNi_{1-y}O$ ceramics are suggested to be the ionic polarization. Therefore, it is possible that the relaxation of the $Ti_yNi_{1-y}O$ ceramics might be due to the presence of defects, which are produced during the sintering process.

Table 5.4 Activation energy required for relaxation process (E_a) and the relaxation time at the upper limited temperature (τ_0) for the $Li_xTi_yNi_{1-x-y}O$ ceramics sintered at 1200 and 1280 °C for 4 h.

Sample	**Sintered at 1200 °C**		**Sintered at 1280 °C**	
	E_a (eV)	**τ_0 (s)**	**E_a (eV)**	**τ_0 (s)**
Ti-doped NiO				
$Ti_{0.05}Ni_{0.95}O$	0.348	7.41×10^{-14}	0.364	0.13×10^{-14}
$Ti_{0.10}Ni_{0.90}O$	0.317	0.11×10^{-14}	-	-
$Ti_{0.15}Ni_{0.85}O$	-	-	0.347	2.68×10^{-14}
(Li, Ti)-doped NiO				
$Li_{0.05}Ti_{0.02}Ni_{0.93}O$	0.298	1.09×10^{-12}	0.299	1.91×10^{-12}
$Li_{0.05}Ti_{0.05}Ni_{0.90}O$	0.305	1.72×10^{-12}	0.298	2.38×10^{-12}
$Li_{0.05}Ti_{0.10}Ni_{0.85}O$	0.300	1.03×10^{-12}	-	-
$Li_{0.05}Ti_{0.15}Ni_{0.80}O$	0.288	0.65×10^{-12}	0.268	5.49×10^{-12}
$Li_{0.10}Ti_{0.02}Ni_{0.88}O$	-	-	-	-
$Li_{0.10}Ti_{0.05}Ni_{0.85}O$	-	-	0.315	3.23×10^{-12}
$Li_{0.02}Ti_{0.05}Ni_{0.93}O$	0.289	1.60×10^{-12}	0.267	4.02×10^{-12}

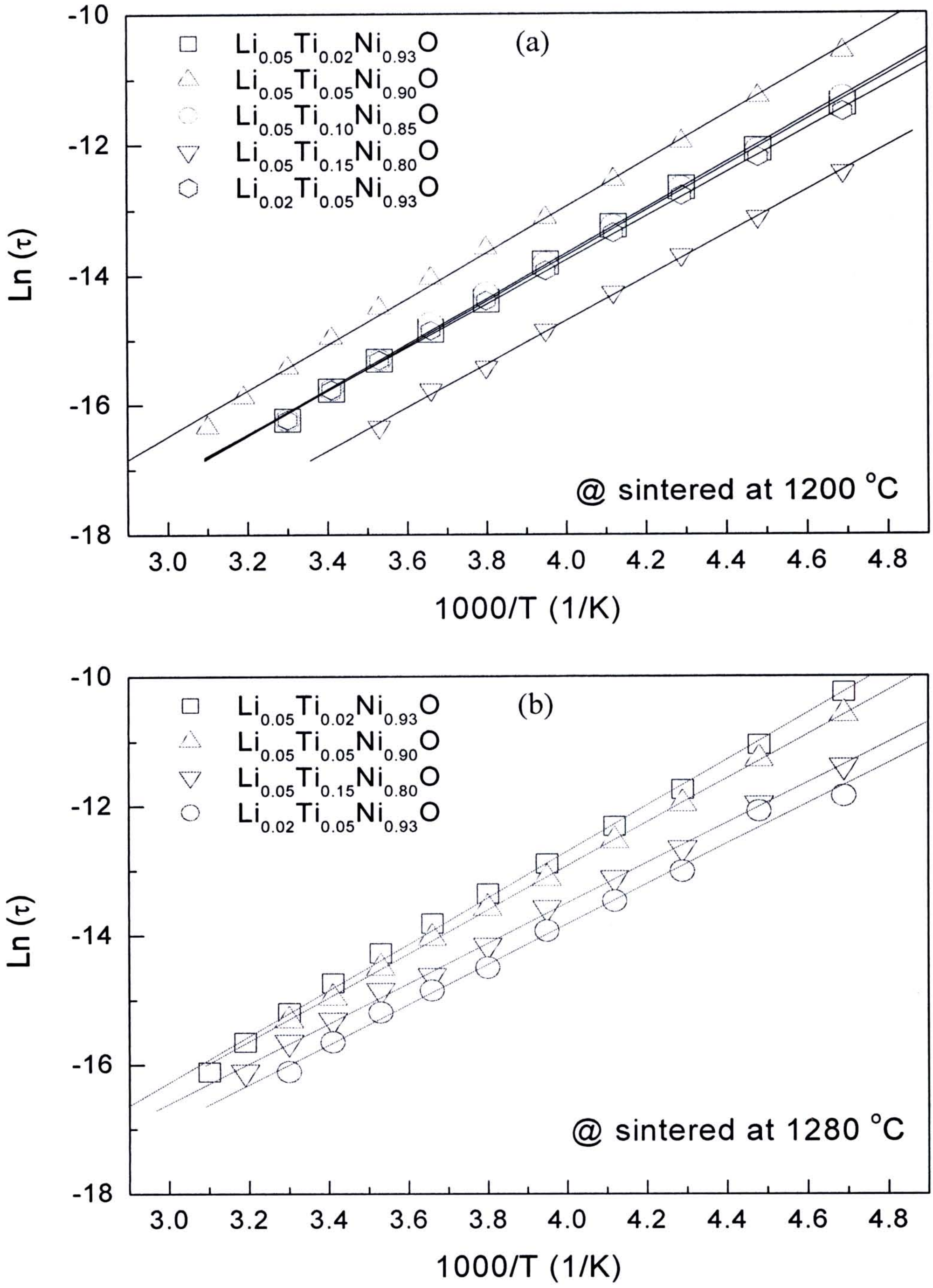

Figure 5.25 Temperature dependence of relaxation time of $Li_xTi_yNi_{1-x-y}O$ ceramics sintered at (a) 1200 and (b) 1280 °C; the solid lines are the data fitted by an Arrhenius law.

5.1.5 Effect of dc conductivity on dielectric relaxation behavior

As explained in Chapter II for the effect of dc conductivity on the dielectric properties of dielectric materials, it was expressed that the dc conductivity can result to the total of dielectric loss of a material. The evolution of each contribution to the total dielectric loss was clearly demonstrated in figure 2.10. According to previous sections, it is found that the frequency dependence of the dielectric loss, the dielectric loss behavior, of all the samples is very similar. At a low-frequency range, the exponential-like decrease is observed; it decreases exponentially to a low value at higher frequency. If the frequency is sufficiently high, the loss due to the relaxation process is dominant, the peak of the dielectric loss can be observed. Although a dielectric material is an insulator, these results indicate that the dc conductivity has an effect on the total dielectric properties of the $Li_xTi_yNi_{1-x-y}O$ ceramics. Consequently, the dielectric properties of the $Li_xTi_yNi_{1-x-y}O$ ceramics may be ascribed by the Cole-Cole relaxation model combined with the term of dc conductivity (σ_{dc}), as

$$\varepsilon^* = \varepsilon' - j\left(\varepsilon'' + \frac{\sigma_{dc}}{\omega\varepsilon_0}\right) = \varepsilon'_\infty + \frac{\varepsilon'_s - \varepsilon'_\infty}{1 + j\omega\tau^\alpha} - j\frac{\sigma_{dc}}{\omega\varepsilon_0}. \tag{5.10}$$

The fitted results of the experimental data are shown in figure 5.26, the symbols are as the experimental data, and the solid lines are obtained using equation (5.10) fitting to the experimental data. It is clearly seen from the fitted results that this relaxation model (Eq. (5.10)) can be well used to fit to the experimental data of the dielectric constant at only a high-frequency range. This is the frequency range of the rapid decrease in the dielectric constant and the appearance of the relaxation peak. At a low-frequency range, the dielectric constants deviate from the spectra fitting by the model. The deviation is more evident in the $Li_{0.05}Ti_{0.15}Ni_{0.80}O$ and $Li_{0.02}Ti_{0.05}Ni_{0.93}O$ ceramics at the frequency below 10^4 Hz.

There are two possibilities that may be related to these observed deviations. First, the deviation is affected by the influence of the dc conduction due to the transport of charged species. Second, it is due to the effect of another source of polarization that can exhibit the dielectric relaxation process. In the later case, the dielectric loss peak corresponding to the step decrease in the dielectric constant at the low-frequency range must be presented in the dielectric loss spectra. Unfortunately, this expected peak can not be observed from the dielectric loss spectra, as revealed in the inset of figure 5.26. The blue solid lines in the insets are expressed as fitted results. Unlike the dielectric constant, the relaxation model as expressed in equation (5.10) can be well used to describe the frequency dependence of the dielectric loss over the measuring frequency range. The dielectric loss due to the effect of the dc conductivity can contribute to the total dielectric loss at a low-frequency range. On the other hand, the loss related to the relaxation process is dominant at a relative-high frequency range. As a result, the first assumption, effect of dc conductivity concerning about the deviation of the dielectric constant data from the model is likely possible. However, the second assumption related to another source of polarization may be still possible. It is possible that the relaxation peak corresponding to the step decrease in the dielectric constant at the low-frequency range may be exhibited, but it is concealed by the great contribution of the dc conductivity. According the dielectric spectra of the $Li_{0.05}Ti_{0.10}Ni_{0.85}O$ ceramic, as revealed in the inset, the peak of the dielectric loss can not be observed from the experimental data. However, it can be observed from the fitted results, suggesting that the dc conduction can conceal the peak of the dielectric loss. If the later case is true, the dc conduction can only contribute to the dielectric loss, but does not to the dielectric constant. The characterization of the second relaxation, the part of dielectric spectra that deviate from the fitted data at the low-frequency range, will be briefly discussed and investigated in the section 5.1.7, influence of interfaces on dielectric and electrical properties. It is more important to impress that the observed second relaxation in the dielectric properties of the $Li_xTi_yNi_{1-x-y}O$ ceramics has never been reported. Therefore, this observation may give an important data to support the discussion of the giant dielectric response in the NiO-based ceramics.

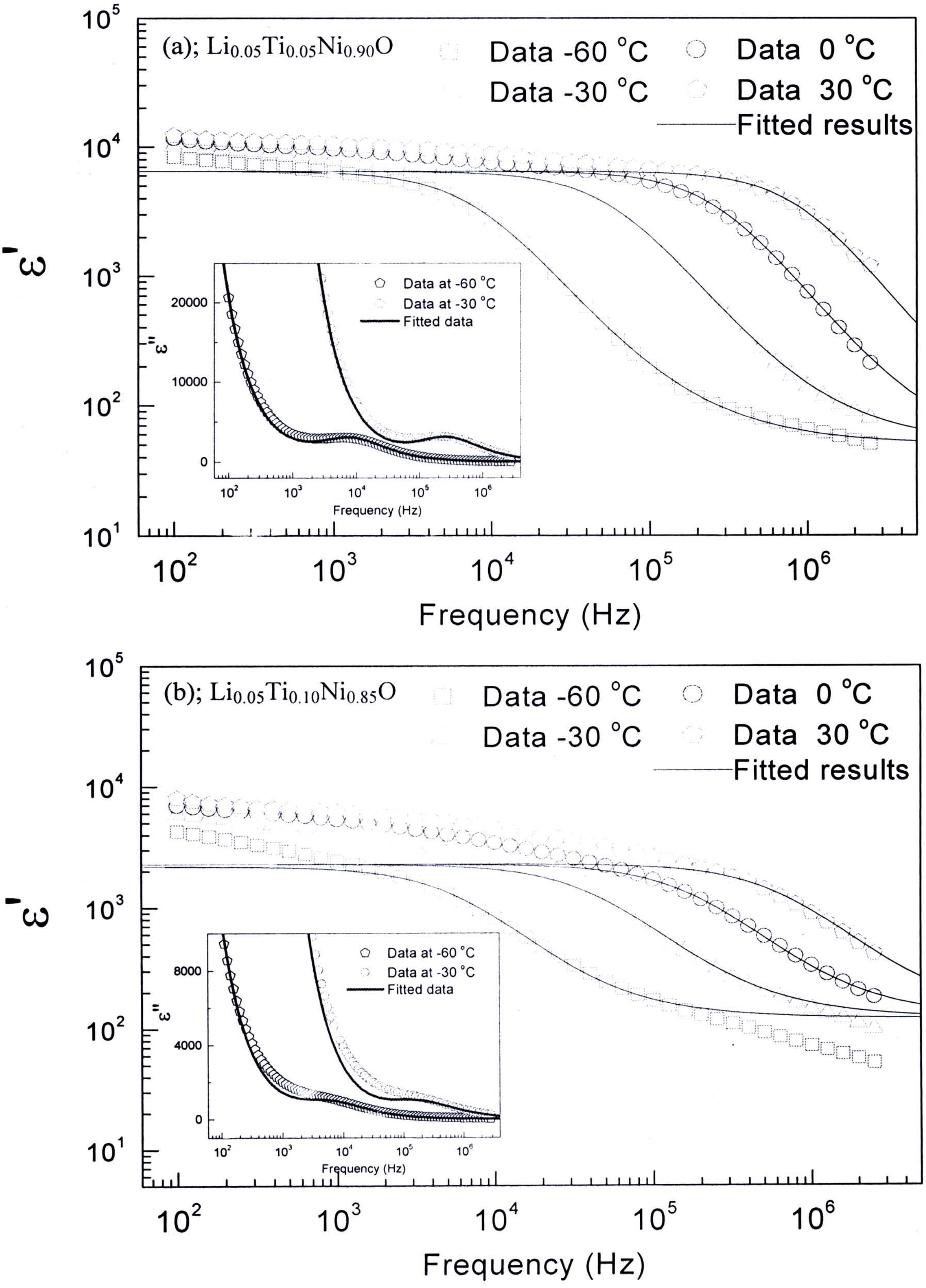

Figure 5.26 Dielectric spectra of $Li_xTi_yNi_{1-x-y}O$ ceramics sintered at 1280 °C fitting to equation (5.10); inset shows dielectric loss and fitted results.

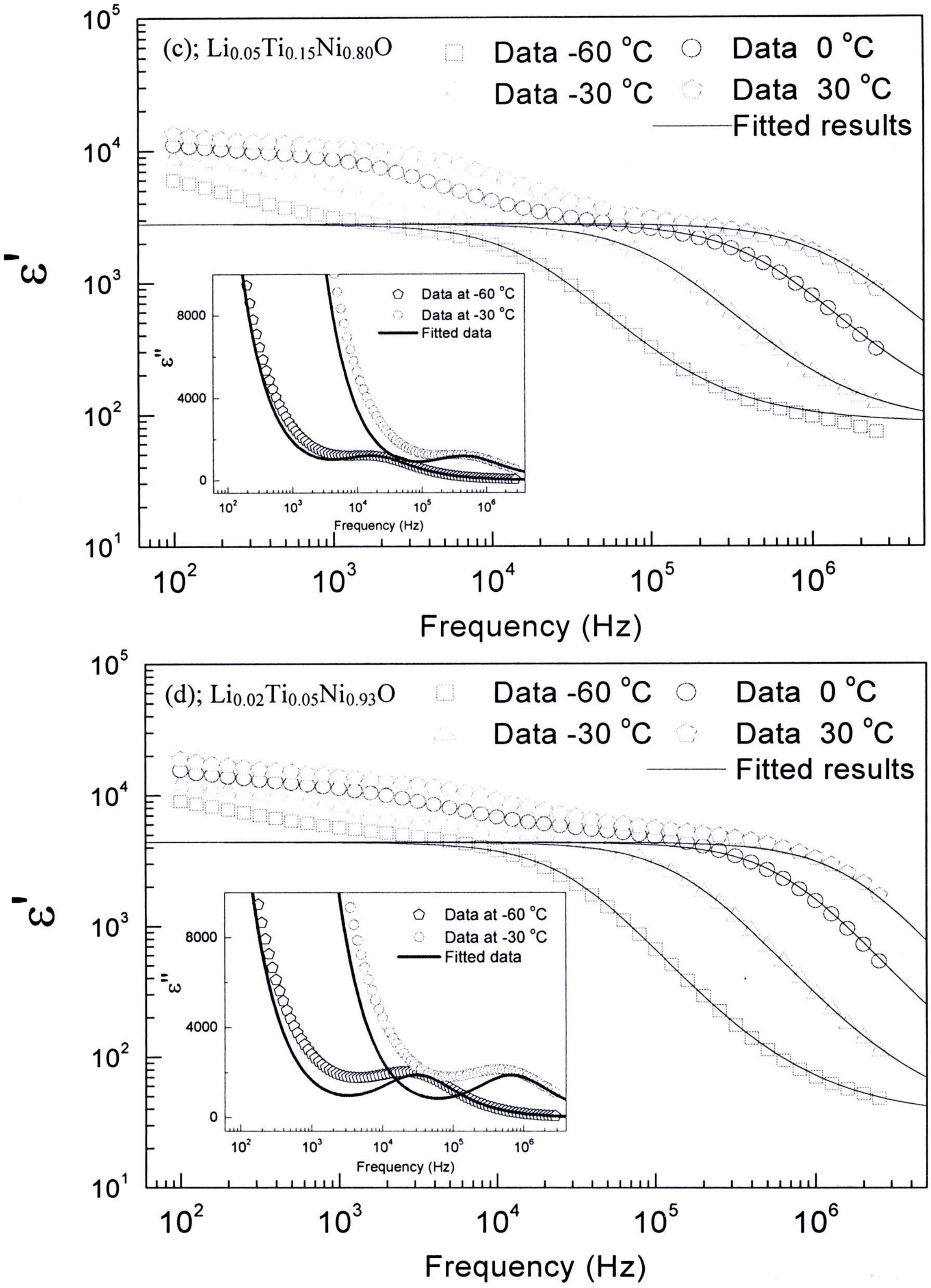

Figure 5.26 Dielectric spectra of $Li_xTi_yNi_{1-x-y}O$ ceramics sintered at 1280 °C fitting to equation (5.10); inset shows dielectric loss and fitted results. (Cont.)

5.1.6 Electrical property: Impedance spectroscopy

Since the discovery of the giant dielectric response in the (Li, Ti)-doped NiO ($Li_xTi_yNi_{1-x-y}O$) ceramics (Wu J et al., 2002), much attention has been paid to investigate the origin of the observed giant dielectric response (Lin et al., 2005b, 2006; Maensiri et al., 2007; Jana et al., 2008; Wu P et al., 2009). Most investigations have suggested that the giant dielectric properties exhibited in the $Li_xTi_yNi_{1-x-y}O$ ceramics may be attributed to the Maxwell-Wagner polarization, the interfacial polarization at the grain boundaries. As well known, the interfacial polarization can be introduced in inhomogeneous materials, consisting of semiconducting grains and insulating grain boundaries. It was suggested that the Li doping can transform the insulating properties of NiO bulk to semiconductor; whereas, the Ti doping accumulated at the grain boundaries acts as the insulator. Thus, under an applied electric field, charge carriers inside the semiconducting grains of the Li-doped NiO particles are restricted at the insulating grain boundaries. These accumulated charges can produce the Maxwell-Wagner polarization at the interface between grain and grain boundary. This is responsible for the observed giant dielectric properties of the $Li_xTi_yNi_{1-x-y}O$ ceramics.

To prove the presence of the inhomogeneous microstructure exhibited in the $Li_xTi_yNi_{1-x-y}O$ ceramics in this thesis, the electrical properties of grains and grain boundaries are investigated using impedance spectroscopy. This is a powerful tool technique to characterize the electrical properties of materials (Li M et al., 2009a; Liu et al., 2004; Sinclair et al., 1989, 2002; Morrison et al., 2001; Adams et al., 2002; Irvine et al., 1990). Normally, the complex impedance, Z^*, can be calculated from the complex dielectric permittivity, ε^*, as

$$Z^* = Z' - jZ'' = \frac{1}{j\omega C_0 \varepsilon^*}, \tag{5.11}$$

where Z' and Z'' are the real part and imaginary part of the complex impedance. Z' and Z'' are associated with the resistance and capacitance of a material, respectively.

Figures 5.27(a)-5.27(f) show the complex impedance plane plot at two temperature ranges—low- and relative high-temperature ranges—of the $Li_xTi_yNi_{1-x-y}O$

ceramics sintered at 1200 °C. Note that the impedance spectra of the $Li_xTi_yNi_{1-x-y}O$ ceramics sintered at 1280 °C are similar to those observed in these figures. First of all, the impedance spectra of the $Ti_{0.05}Ni_{0.95}O$ ceramic (Fig. 5.27(a)) are used as the example to describe the general feature of the impedance spectra to instead of all samples. As shown in figure 5.27(a), the impedance spectra look like a semicircle. In addition, the diameter of the large semicircle increases with decreasing the measuring temperature, suggesting to the increase in the resistance with decreasing the temperature. If the measuring temperature is sufficient low, a semicircle-like and its tail are observed at the high-frequency range, as revealed in the inset of figure 5.27(a). The observed tail in the inset is the high-frequencies part of the large semicircle at the temperature of -60 °C. Moreover, it is found from the impedance spectra of the $Li_xTi_yNi_{1-x-y}O$ ceramics [Figs. 5.27(c)-5.27(f)] that the diameter of the small semicircle increases with decreasing the measuring temperature just as the large semicircle does.

According to the brick-layer model for a polycrystalline material (Macdonald, 2005; Irvine et al., 1990; Waser, Hagenbeck, 2000) as demonstrated in figure 2.15 in Chapter II, the microstructure that consists of semiconducting grains and insulating grain boundaries can be modeled as ideal equivalent circuit. The circuit consists of a series array of two subcircuits—one representing grain effects (R_g, C_g) and the other representing grain boundaries (R_{gb}, C_{gb}). Each sub-circuit is composed of a resistor and capacitor joined in parallel, as shown in figure 2.14 in Chapter II. This complex impedance of the circuit can be expressed as,

$$Z^* = Z' - jZ'' = \frac{1}{R_g^{-1} + j\omega C_g} + \frac{1}{R_{gb}^{-1} + j\omega C_{gb}}, \tag{5.12}$$

$$Z' = \frac{R_g}{1+(\omega R_g C_g)^2} + \frac{R_{gb}}{1+(\omega R_{gb} C_{gb})^2}, \tag{5.13}$$

$$Z'' = R_g\left[\frac{\omega R_g C_g}{1+(\omega R_g C_g)^2}\right] + R_{gb}\left[\frac{\omega R_{gb} C_{gb}}{1+(\omega R_{gb} C_{gb})^2}\right]. \tag{5.14}$$

The complex impedance plan plot, $-Z''$ vs. Z', obtained from equations (5.12) to (5.14) can be almost used to fit the experimental data. Usually, $-Z''$ vs. Z' is better ascribed by using the Cole-Cole equation, as

$$Z^* = Z' - jZ'' = \frac{1}{R_g^{-1} + (j\omega C_g)^\alpha} + \frac{1}{R_{gb}^{-1} + (j\omega C_{gb})^\beta}, \tag{5.15}$$

where α and β are constant values and $0 < \alpha, \beta \leq 1$. As clearly seen in figure 5.28, equation (5.15) can be well used to explain the experimental results both of a small and high semicircles. The values of α and β are achieved from the fitted results to be 0.860 and 0.835, respectively. However, this thesis is not interested in this model because it does not offer any physical underlying mechanism. The aim of the illustrated-fitting model is to prove that the impedance spectra of all $Li_xTi_yNi_{1-x-y}O$ ceramics follow to the expressed-equivalent circuit model. This implies that the microstructure of the $Li_xTi_yNi_{1-x-y}O$ ceramics is electrically heterogeneous consisting of a relative high-conductivity grains and a relative low-conductivity grain boundaries. Therefore, the giant dielectric properties of the $Li_xTi_yNi_{1-x-y}O$ ceramics might be attributed to the Maxwell-Wagner polarization at the grain boundaries, the interfacial polarization at the grain boundaries. Although this heterogeneous structure is exhibited in the $Li_xTi_yNi_{1-x-y}O$ ceramics, on the other ways, it might not be related to this matter. It is exhibited, but there may be no relationship to the giant dielectric response. Other possible mechanism may also relate to this giant dielectric response such as the effect of defect dipoles or a small polaron hopping inside the grains. Hence, it is unsuitable now to suggest that the Maxwell-Wagner polarization is the origin of the observed giant dielectric constant. If this explanation is true, however, there may also be other possible mechanisms that have a great effect on the total dielectric response in the $Li_xTi_yNi_{1-x-y}O$ ceramics such as the electrode effect and the surface-layer effect. The final decision to specify the most possibility mechanism based on the experimental results in this thesis will be briefly discussed in section 5.1.9.

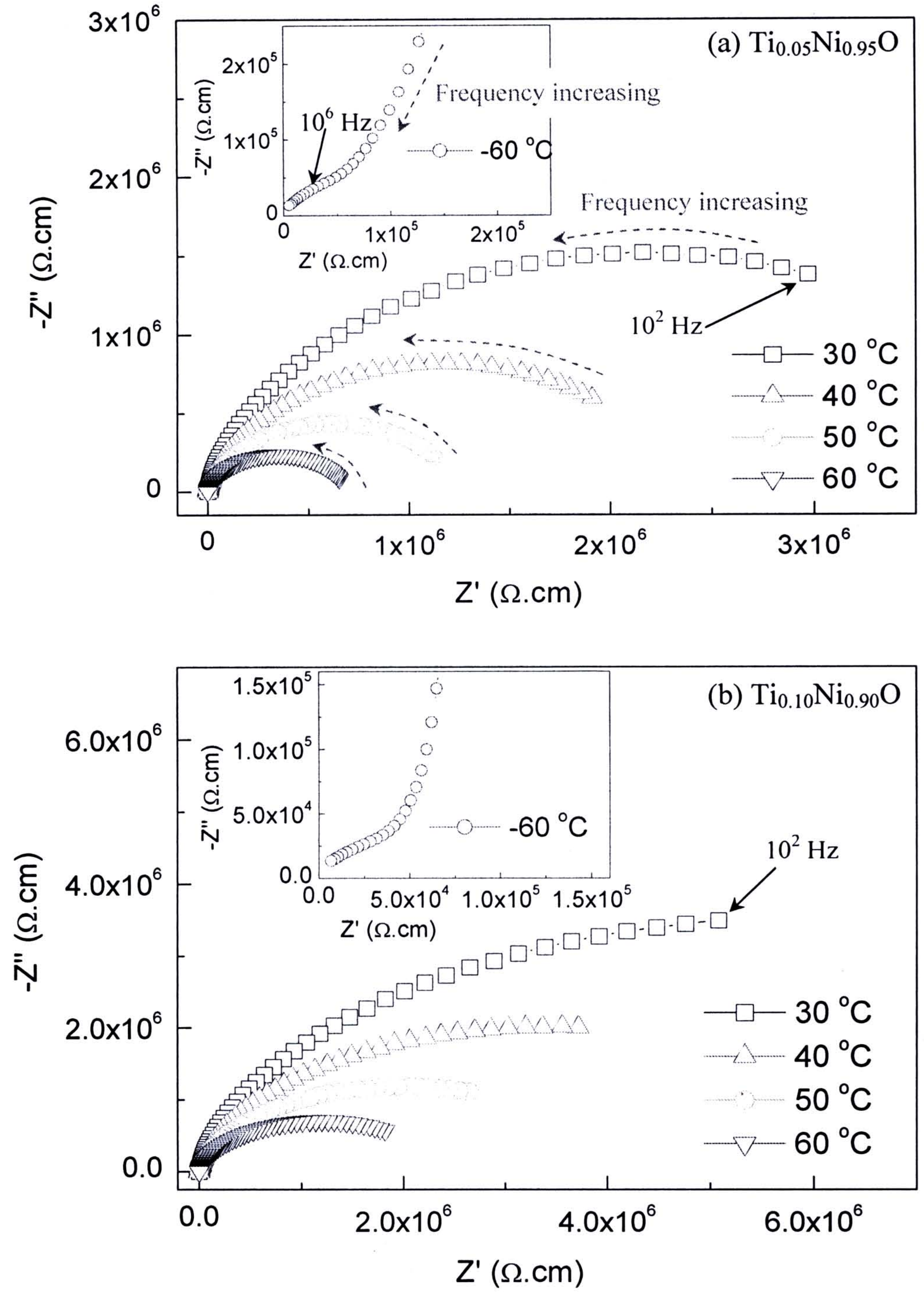

Figure 5.27 Impedance spectra of $Ti_yNi_{1-y}O$ and $Li_xTi_yNi_{1-x-y}O$ ceramics sintered at 1200 °C at various temperatures; inset shows its impedance spectrum at -60 °C.

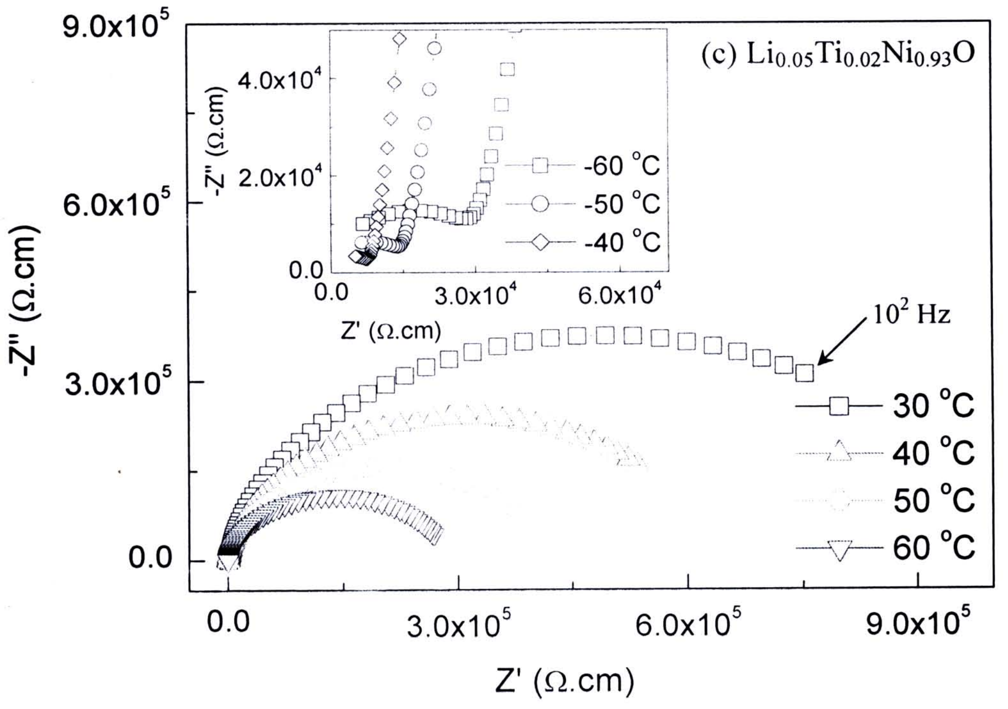

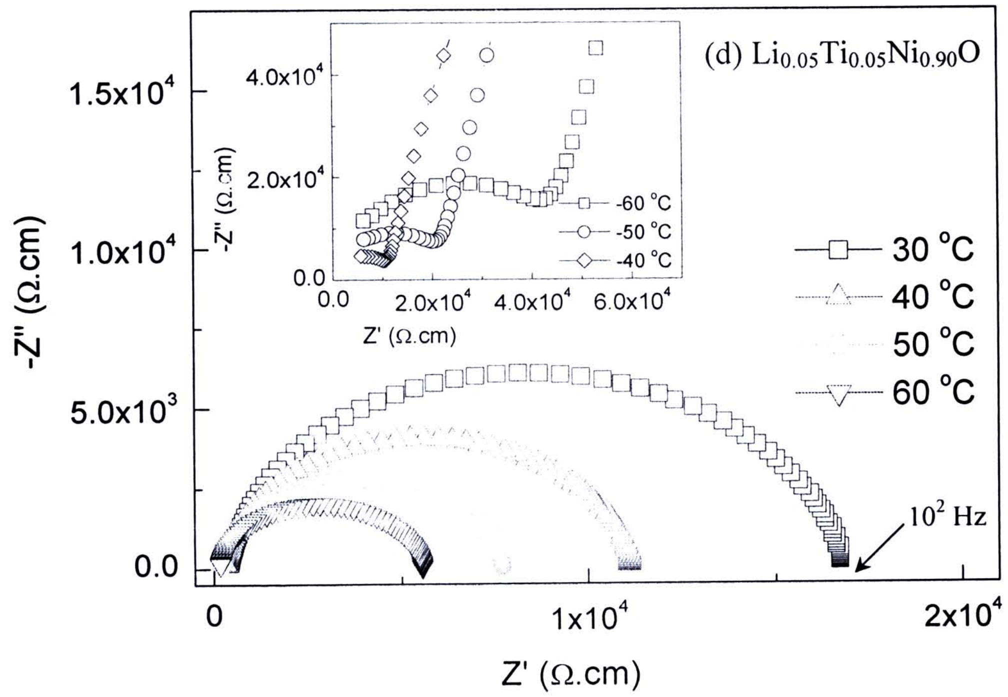

Figure 5.27 Impedance spectra of $Ti_yNi_{1-y}O$ and $Li_xTi_yNi_{1-x-y}O$ ceramics sintered at 1200 °C at various temperatures; inset shows its impedance spectra at a low temperature range. (Cont.)

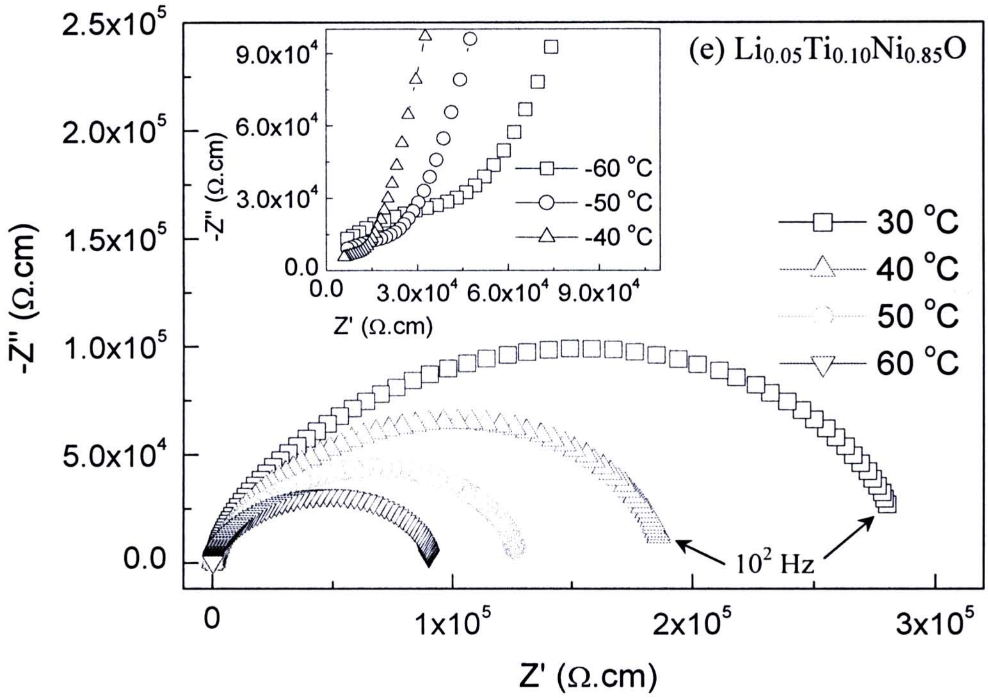

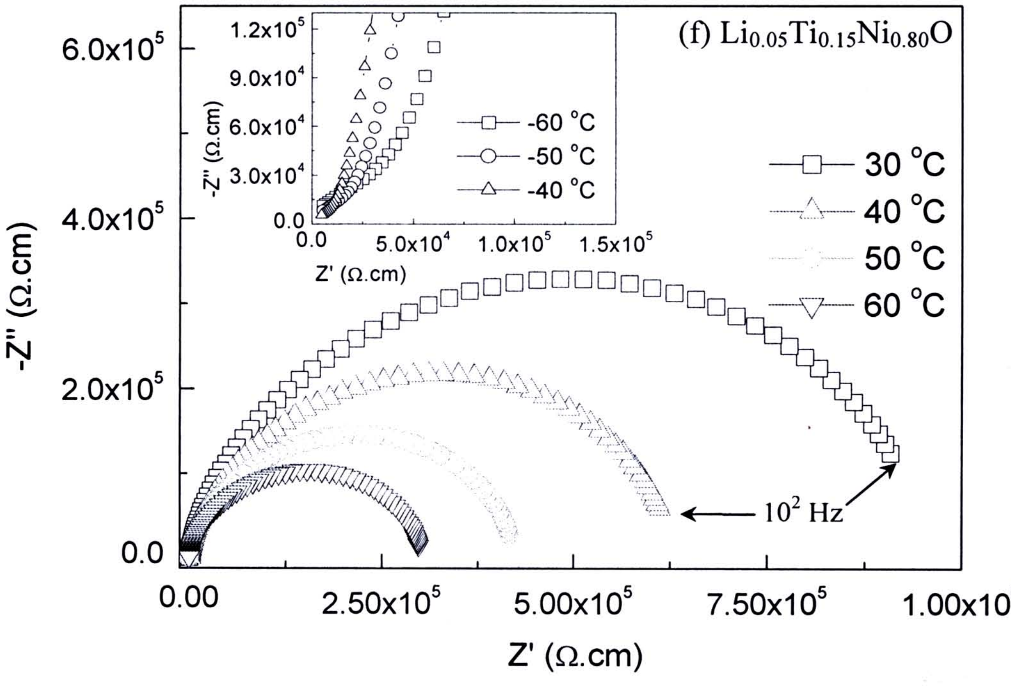

Figure 5.27 Impedance spectra of $Ti_yNi_{1-y}O$ and $Li_xTi_yNi_{1-x-y}O$ ceramics sintered at 1200 °C at various temperatures; inset shows its impedance spectra at a low temperature range. (Cont.)

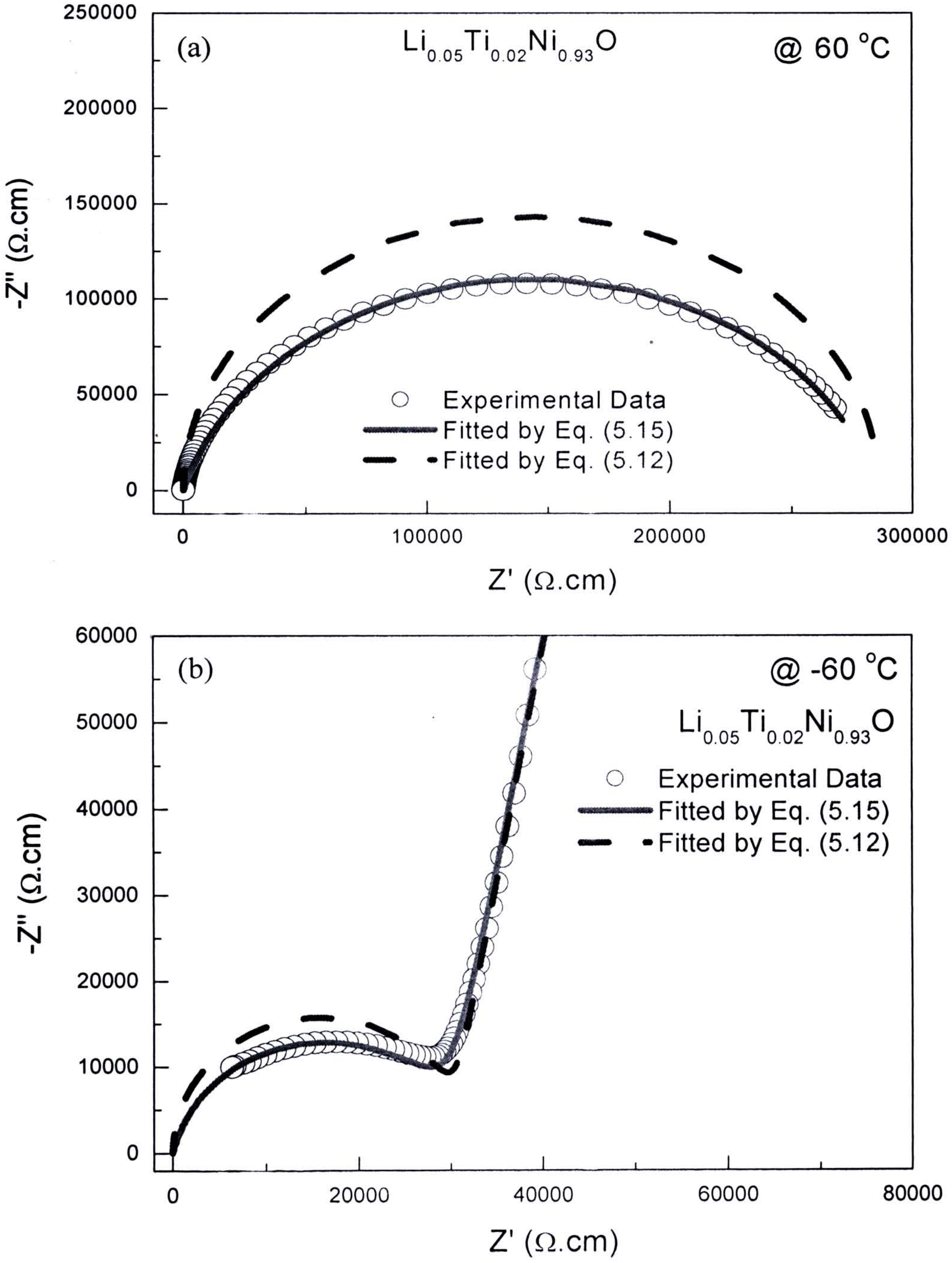

Figure 5.28 Impedance spectra of $Li_{0.05}Ti_{0.02}Ni_{0.93}O$ ceramic sintered at 1200 °C at temperatures of (a) 60 °C and (b) -60 °C fitted by equations (5.12) and (5.15).

5.1.7 Influence of interfaces on dielectric and electrical properties

Although the origin of the observed giant dielectric response in the $Li_xTi_yNi_{1-x-y}O$ ceramics as all previous discussion is still unclear, the interesting result that may reach to the most possible solution of this subject is observed. Such result is the appearance of the second relaxation at a low-frequency range, as shown in figures 5.26(b)-5.26(d)—the dielectric constant at the low-frequency range was found to deviate from the relaxation model. As previously suggested, this deviation of the dielectric constant is associated with either of the dc conductivity effect or polarization relaxation. In general, as added dielectric relaxation can be observed in the dielectric spectra of $CaCu_3Ti_4O_{12}$ ceramics. Either of the outmost surface-layer effect (Wang, Zhang, 2006) and the electrode effect (Li M et al., 2009b) may be the origin of the exhibited second relaxation. Due to the limitation of the experiment, the effect of surface layer, polarization at the interface between the surfaces and the inner part, is only investigated. Moreover, the polarization at the interface between the semiconducting grains and insulating grain boundaries is also discussed. These two interfaces may contribute to the total dielectric response in the $Li_xTi_yNi_{1-x-y}O$ ceramics.

5.1.7.1 Surface-layer effect in dielectric properties of $Li_xTi_yNi_{1-x-y}O$ ceramics

The experimental method of the study of the surface-layer effect is shortly described. Usually, before the dielectric properties of a sample are conducted, surfaces of the sample must be polished to remove the outmost surface layers. Then, the sample is electroded by metallic electrode such as silver paint. The dielectric results of the $Li_xTi_yNi_{1-x-y}O$ ceramics, as expressed previously in sections 5.1.3-5.1.6, are obtained by this way. In this section of the thesis, however, to investigate the surface-layer effect, the $Li_xTi_yNi_{1-x-y}O$ ceramic samples sintered at 1280 °C for 4 h without the polishing process were electroded by silver paint. These $Li_xTi_yNi_{1-x-y}O$ ceramic samples, which their surfaces were not removed, were denoted as *as-samples*. After the dielectric properties of the as-samples were conducted as functions of frequency and temperature, the initial electrodes and some parts of the surfaces were polished to remove the outmost surface layers from both sides of the pellet samples. The removed-surface samples were electroded again by silver paint, and then the dielectric properties of these samples were conducted again. These removed-surface samples were denoted as *polished-samples*.

1) The variation of the dielectric constant

The dielectric properties—dielectric constant (ε') and loss tangent ($\tan\delta$)—at the temperature of 30 °C for the as- and polished-samples of the $Li_xTi_yNi_{1-x-y}O$ ceramics are illustrated in figures 5.29(a)-5.29(g). Certainly, the outmost surface layer of the $Li_xTi_yNi_{1-x-y}O$ ceramics has a remarkable influence on their dielectric properties. After the surfaces of the $Li_xTi_yNi_{1-x-y}O$ ceramics are removed from both sides of the pellet samples, the variation of the dielectric properties of the polished-samples is observed. This change in the dielectric properties can roughly be divided into three groups: group-I for the $Li_{0.05}Ti_{0.02}Ni_{0.93}O$ and $Li_{0.10}Ti_{0.02}Ni_{0.88}O$ ceramics, group-II for the $Li_{0.02}Ti_{0.05}Ni_{0.93}O$ and $Li_{0.10}Ti_{0.05}Ni_{0.85}O$ ceramics, and group-III for the $Li_{0.05}Ti_{0.05}Ni_{0.90}O$, $Li_{0.05}Ti_{0.10}Ni_{0.85}O$, and $Li_{0.05}Ti_{0.15}Ni_{0.80}O$ ceramics. For group-I, with removing the outmost surface layers, the dielectric constant increases; whereas, in group-II, the dielectric constant slightly decreases over a measuring frequency range. It is found that the loss tangent ($\tan\delta$) of the $Li_{0.05}Ti_{0.02}Ni_{0.93}O$ (group-I) and $Li_{0.10}Ti_{0.05}Ni_{0.85}O$ and $Li_{0.02}Ti_{0.05}Ni_{0.93}O$ (group-II) ceramics does not change (over the measured frequency range) with removing the surface layers. Unlikely, the loss tangent of the $Li_{0.10}Ti_{0.02}Ni_{0.88}O$ (group-I) is found to decrease after the surface layers are polished. An interesting result can be observed in the inset figures 5.29(a), 5.29(g), 5.29(f) for the $Li_{0.05}Ti_{0.02}Ni_{0.93}O$, $Li_{0.10}Ti_{0.02}Ni_{0.88}O$, and $Li_{0.10}Ti_{0.05}Ni_{0.85}O$ ceramics, respectively. These insets demonstrate the dielectric properties of these three ceramic compositions both of as- and polished-samples at the temperature of -40 °C. The dielectric relaxation characteristics, the rapid decrease in the dielectric constant and the observed loss tangent peak, of the as- and polished-samples are similar in every way. Both of the dielectric constant and loss tangent spectra of the as-samples coincide exactly with the spectra of the polished-samples. As a result, it is strongly suggested that the high-frequency relaxation, which is linearly related to giant dielectric response, is not due to an external effects such as an electrode effect just like a giant-permittivity CuO ceramic (Li M et al., 2009).

In the special case, for group-III, with removing the surface layers, the dielectric constant decreases at the low-frequency range ($< 10^4$

Hz); whereas it is nearly constant at the high-frequency range (> 10^4 Hz). As displayed in figures 5.29(b)-5.29(d), two step-like decreases (sudden drops) in the dielectric constant can be observed in the dielectric spectra of the as-samples. Note that these two step-like decreases can also be observed in the sample of $Li_{0.02}Ti_{0.05}Ni_{0.93}O$ ceramic of group-II. Moreover, these two step-like decreases shift to higher frequency with increasing the measuring temperature. This observation indicates that there may exist two sets of thermally activated relaxations in these ceramics (Wang et al., 2007)—low-frequency relaxation (LFR) and high-frequency relaxation (HFR). Importantly, the LFR of the polished-sample of the $Li_{0.05}Ti_{0.05}Ni_{0.90}O$ ceramic disappears. It is completely erased by removing the surfaces. Although the dielectric constant at the low-frequency range of the other polished-samples is reduced, the LFR of the polished-samples is still observed. This result implies that the low-frequency dielectric constant of the $Li_xTi_yNi_{1-x-y}O$ ceramics relates to the surface-layer effect. Furthermore, it is likely that the LFR may not relate to the surface-layer effect of the $NiTiO_3$ phase. However, it is strongly believed that the plated layer-like structure of the $NiTiO_3$ sub-micron grains that covered the surface can result in the value of the dielectric constant.

2) Classification of surface morphologies

To understand the effect of surface layer on the dielectric properties of the $Li_xTi_yNi_{1-x-y}O$ ceramics classified in the three groups, the surface morphologies of the as- and polished-samples of the $Li_xTi_yNi_{1-x-y}O$ ceramics are classified into these three groups of the $Li_xTi_yNi_{1-x-y}O$ ceramics. As revealed in figures 5.30-5.32, the surface morphologies of the $Li_xTi_yNi_{1-x-y}O$ as- and polished-samples are classified following to the variation of the dielectric properties. The surface morphologies of the as-samples classified in group-I and group-II are quite smooth and clear. For group-III, the surface morphologies of the as-samples are covered with the sub-micron grains of the $NiTiO_3$ phase. Interestingly, the classification of surface morphologies with the variation of dielectric properties may give an important clue. The smooth surface is related to the increase and slight decrease in the dielectric constant of the ceramic samples that are classified in group-I and group-II, respectively. These results are difficult to explain now because there is no data supported. However, all of the possible mechanisms related to these observations will be suggested at the end of this section. On the other hand, it can be expected that the decrease in the dielectric constant of the polished-samples being in group-III may be associated with the presence of the sub-micron grains of the $NiTiO_3$ that cover the surfaces of the as-samples. As suggested in literatures (Wu J et al., 2002; Lin et al., 2006a), the accumulation of the second phase of $NiTiO_3$ at grain boundaries in the microstructure of $Li_xTi_yNi_{1-x-y}O$ ceramics can act as the insulating layer. This insulating boundary can block the motion of charge carriers, producing the interfacial polarization at the insulating grain boundaries. This mechanism was suggested to be responsible for the observed giant dielectric constant in (Li, Ti)-doped NiO ceramics. Therefore, in this research, the sub-micron grains of the $NiTiO_3$ may act as the insulating (or less relative conducting) thin-layer, which covers the surfaces of the as-samples.

3) The variation of the loss tangent

To deepen the understanding of the assumption above, the loss tangent ($\tan\delta$) at the same measuring temperature as the dielectric constant measurement, 30 °C, should be considered. The loss tangent data, the closest relationship of the dielectric constant, usually provide an important clue about sources of energy losses (Hence, West, 1990). The exponential-like increase in the loss tangent with decreasing frequency to the lower-frequency range can be suggested as the effect of dc conductivity (Hence, West, 1990; Wang et al., 2007; Wu J et al., 2002; Maensiri et al., 2007; Kao, 2004; Gross, 1941). Turning to see the loss tangent of the samples of group-I and group-II, both of low- and high-frequency loss tangents of the polished-samples are similar to the as-samples, except for the $Li_{0.10}Ti_{0.02}Ni_{0.88}O$ ceramic sample. This means that total dc conductivity of these ceramic compositions does not associate with the outmost surface-layer effect. The chemical compositions or defects chemistry of the smooth surfaces and the inner part may be similar, leading to the same electrical properties. The unchanged dc conductivity is clearly seen in the loss tangent spectra of the as- and polished-samples of the $Li_{0.02}Ti_{0.05}Ni_{0.93}O$ ceramic observed at the low-frequency range. In the case of the samples of group-III, as illustrated in figures 5.29(b.2)-5.29(d.2), at the high-frequency range (>10^4 Hz), the loss tangent of all as-samples coincides exactly with the polished-samples. This corresponds to the unchanged dielectric constant in the same frequency range.

However, at the low-frequency range of 10^2-10^4 Hz, the range that the dielectric constant is found to be changed, the loss tangent of the polished-samples is much larger than those of the as-samples. After the surfaces of the as-samples are removed, abnormally, the variations of dielectric constant and the loss tangent occur in different tendencies—the dielectric constant decreases, but the loss tangent increases. These changes in the dielectric properties of the polished-samples of the $Li_xTi_yNi_{1-x-y}O$ ceramics are evidently seen in the dielectric spectra at the low measuring temperature of -40 °C. As shown in the inset of figures 5.29(b)-5.29(d), it is found that the high-frequency relaxation (HFR) does not change—both of the relaxation peaks (loss tangent peak) and the corresponding rapid decrease in the dielectric constant of the as- and polished-samples are coincident. Clearly, the main relaxation, HFR, is attributed to the effect of the inner part of the samples such a grain boundary effect or a small polaron hopping. Although the measuring temperature is sufficiently low, the dc conduction in the samples is still dominant. The loss tangent due to the influence of the dc conduction of the polished-samples is larger than those of the as-samples.

The change in the loss tangent due to the removing surface can be used to support the assumption that is created by the variation in dielectric constant. This assumption is expected that the sub-micron grains of $NiTiO_3$ exhibited on the surface layer behave as an insulating layer. This is due to the fact that this insulating surface layer can block the movement of charge carriers, which are forced by an applied electric field. The accumulated charges can produce the interfacial polarization at this type of interface; as a result, the total polarization increases resulting to the increase in a total dielectric constant. The decrease in the low-frequency dielectric constant of the polished-samples of group-III is attributed to the disappearance of the interfacial polarization at the insulating surface layers. When the insulating surfaces are removed (the polished-samples), the accumulated charges disappear. These accumulated charges transform to free charges, resulting to the increase in the total free charge carriers. Consequently, the loss tangent should be enhanced by polishing the insulating surface layers. Although this discussion is based on a good reason, it should be recognized that an experimental result supporting to the insulating properties of the surface layer is still not proved. The supporting data and their characterization will be expressed in the next section.

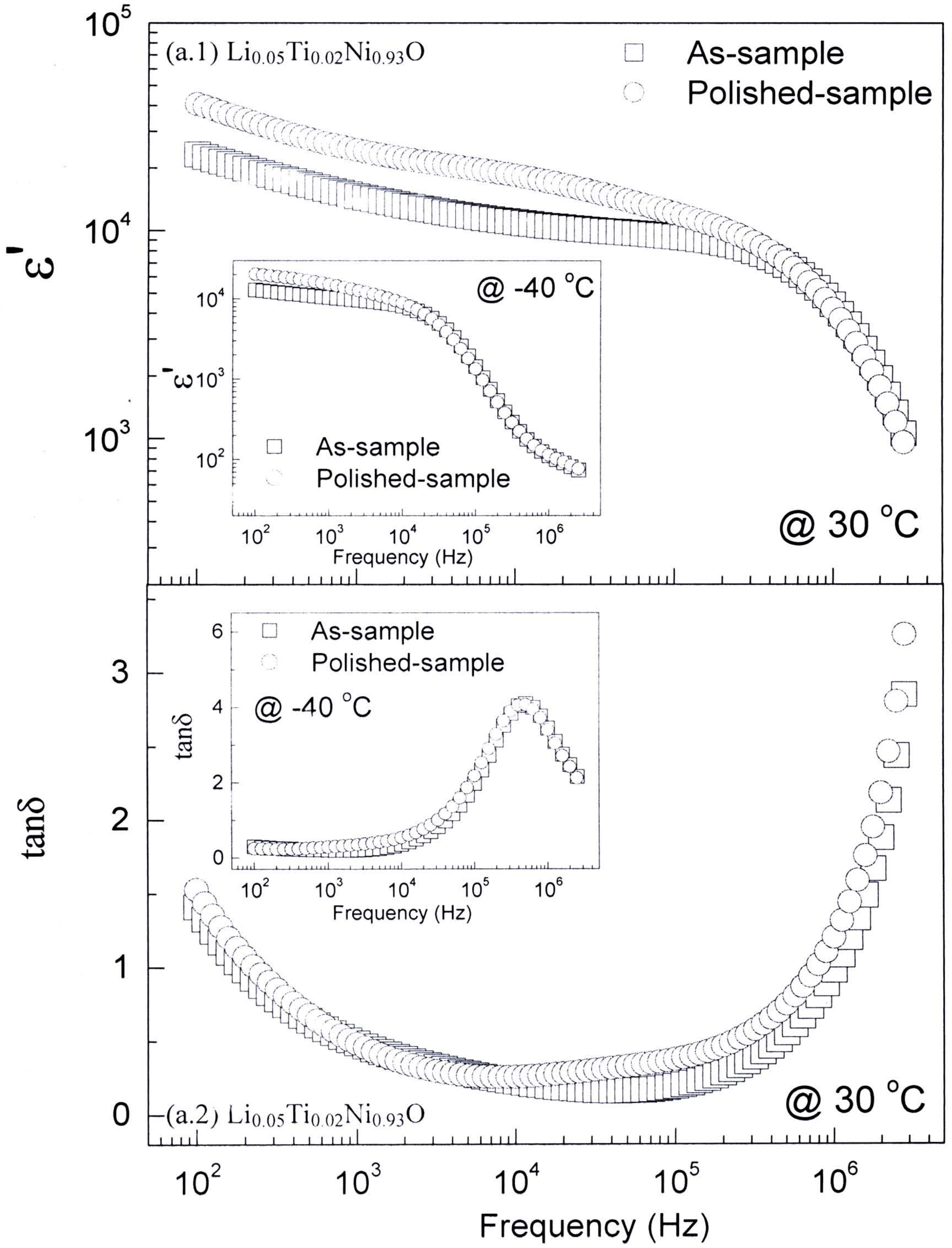

Figure 5.29 Dielectric constant (ε′) and loss tangent (tanδ) at 30 °C of $Li_xTi_yNi_{1-x-y}O$ ceramics sintered at 1280 °C for non- (as-) and polished-samples; inset is the dielectric properties at -40 °C.

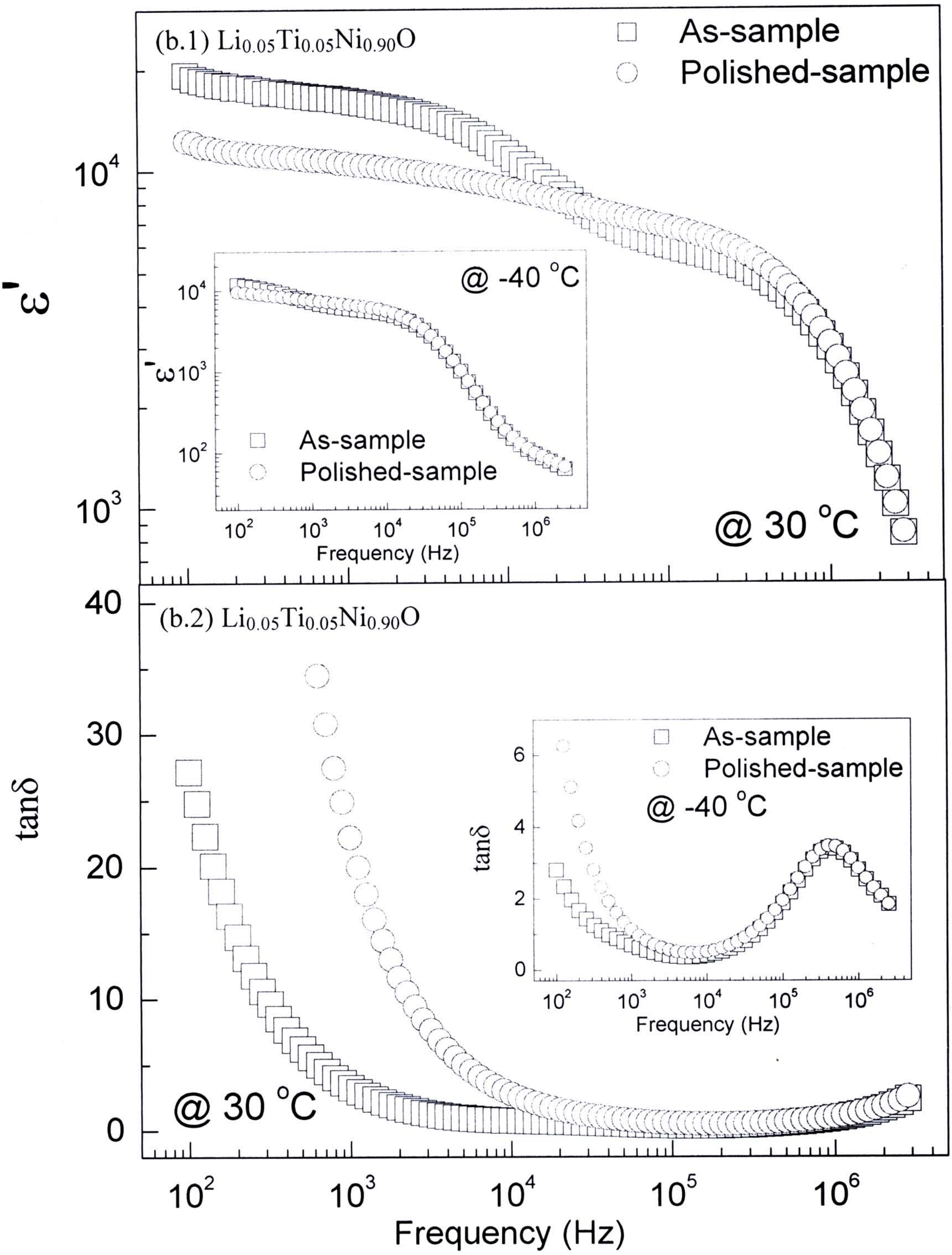

Figure 5.29 Dielectric constant (ε′) and loss tangent (tanδ) at 30 °C of $Li_xTi_yNi_{1-x-y}O$ ceramics sintered at 1280 °C for non- (as-) and polished-samples; inset is the dielectric properties at -40 °C. (Cont.)

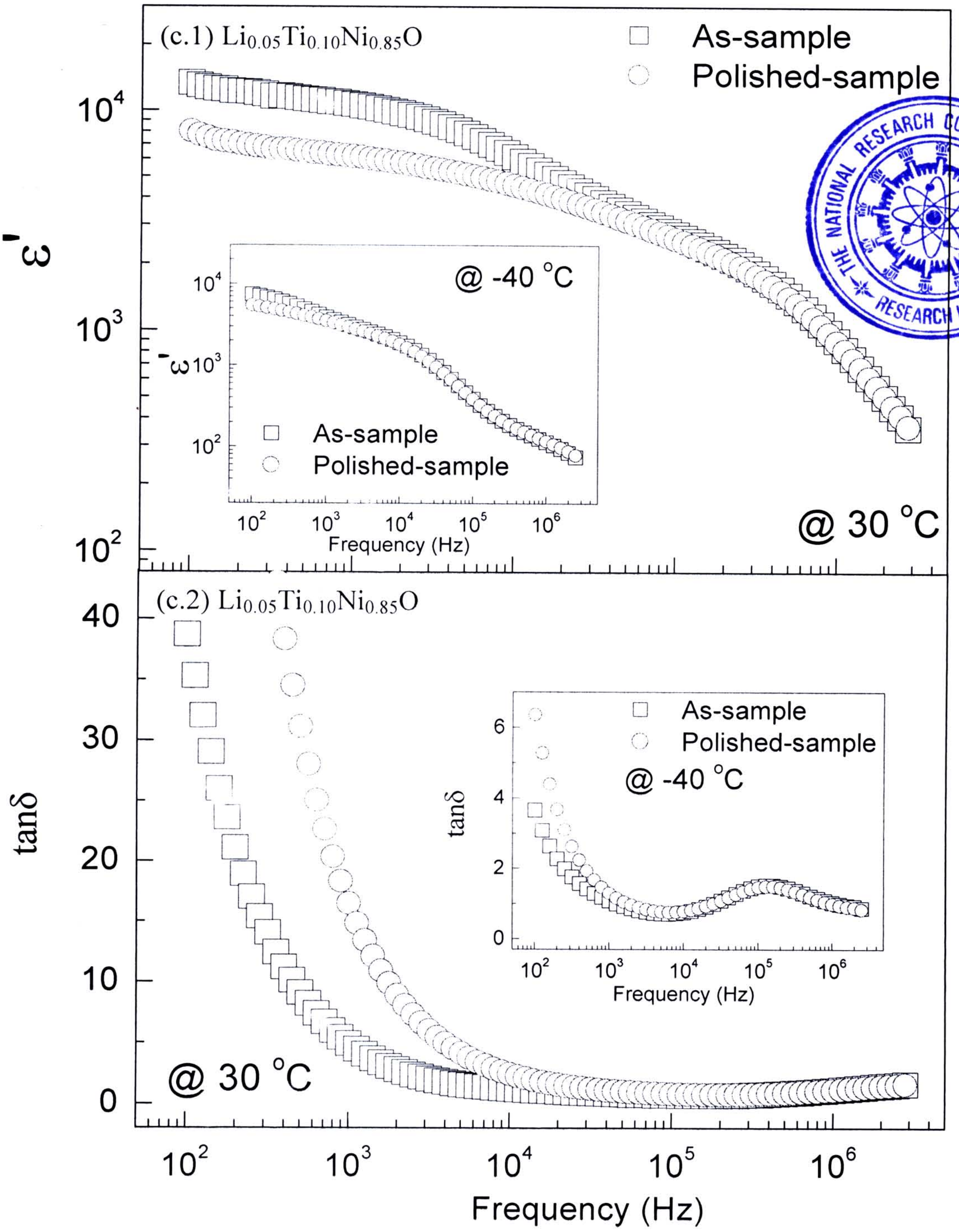

Figure 5.29 Dielectric constant (ε′) and loss tangent (tanδ) at 30 °C of $Li_xTi_yNi_{1-x-y}O$ ceramics sintered at 1280 °C for non- (as-) and polished-samples; inset is the dielectric properties at -40 °C. (Cont.)

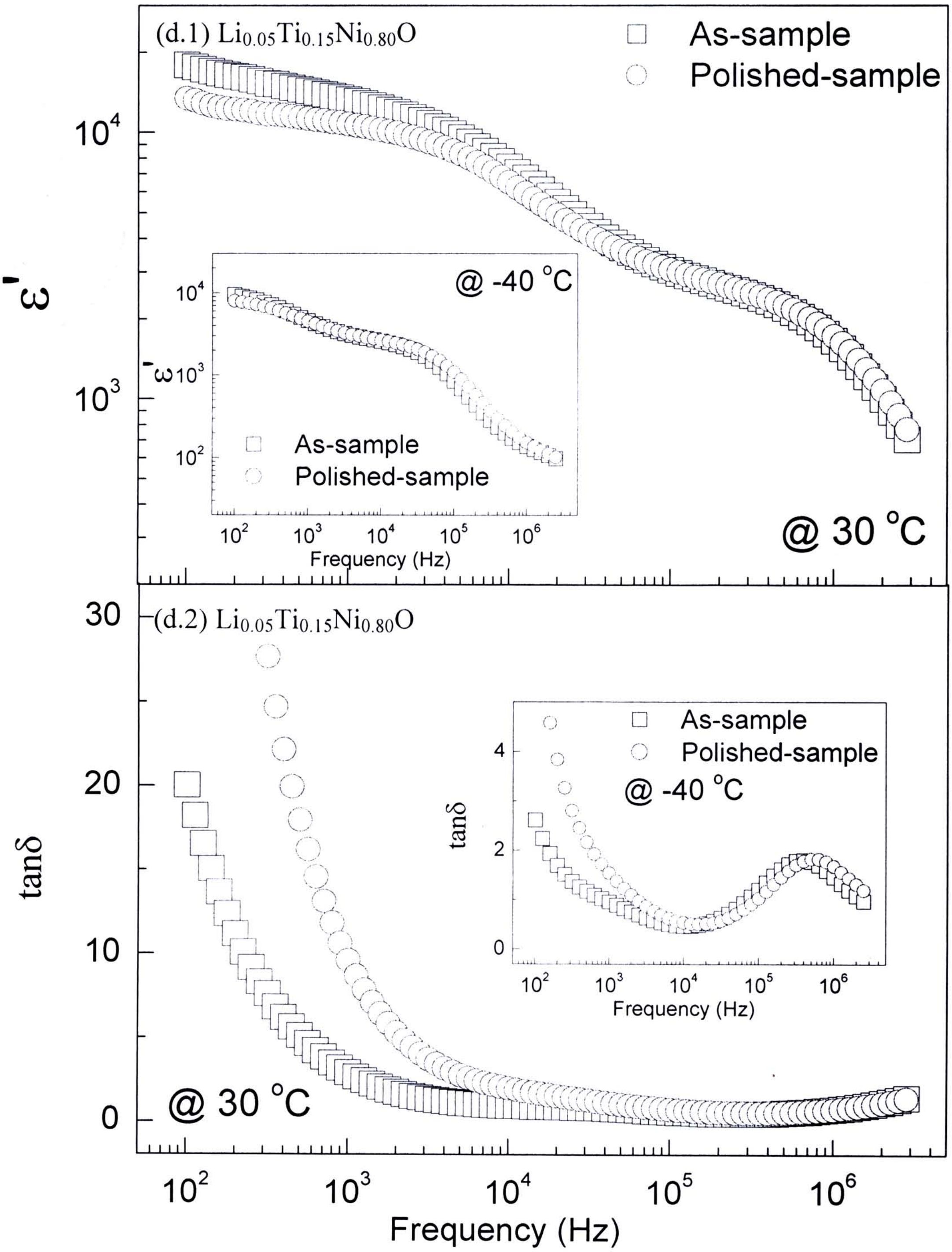

Figure 5.29 Dielectric constant (ε′) and loss tangent (tanδ) at 30 °C of $Li_xTi_yNi_{1-x-y}O$ ceramics sintered at 1280 °C for non- (as-) and polished-samples; inset is the dielectric properties at -40 °C. (Cont.)

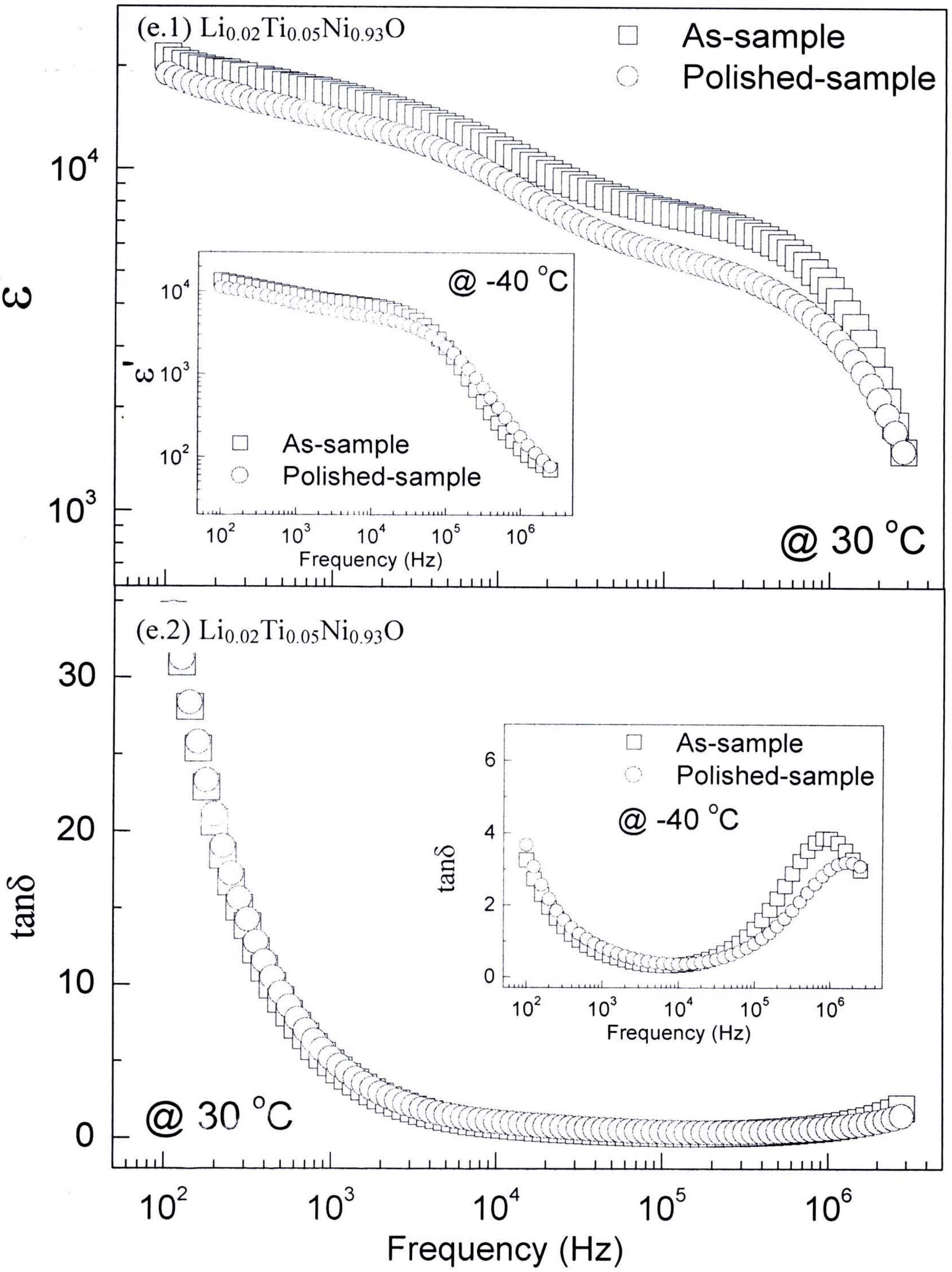

Figure 5.29 Dielectric constant (ε′) and loss tangent (tanδ) at 30 °C of $Li_xTi_yNi_{1-x-y}O$ ceramics sintered at 1280 °C for non- (as-) and polished-samples; inset is the dielectric properties at -40 °C. (Cont.)

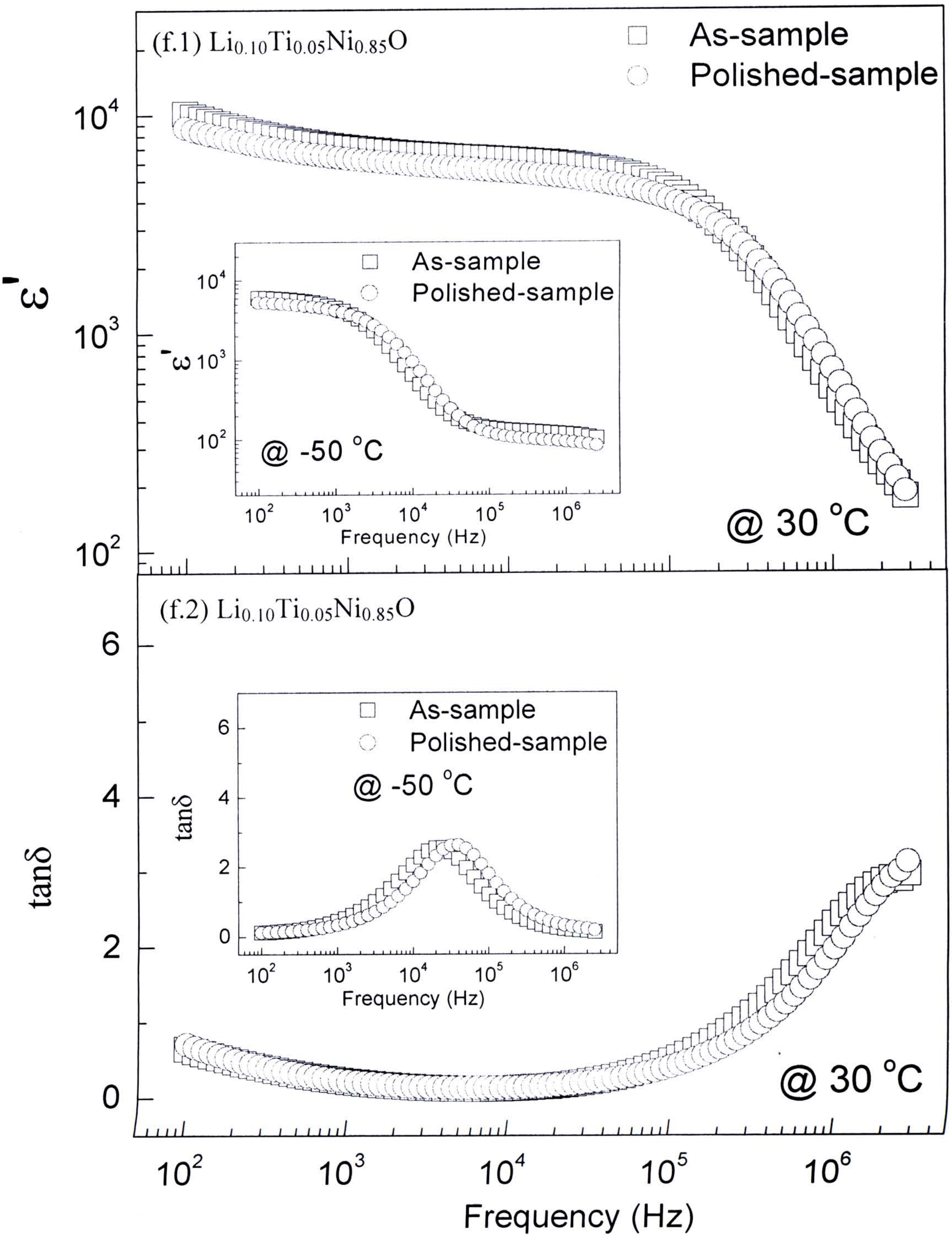

Figure 5.29 Dielectric constant (ε′) and loss tangent (tanδ) at 30 °C of $Li_xTi_yNi_{1-x-y}O$ ceramics sintered at 1280 °C for non- (as-) and polished-samples; inset is the dielectric properties at -40 °C. (Cont.)

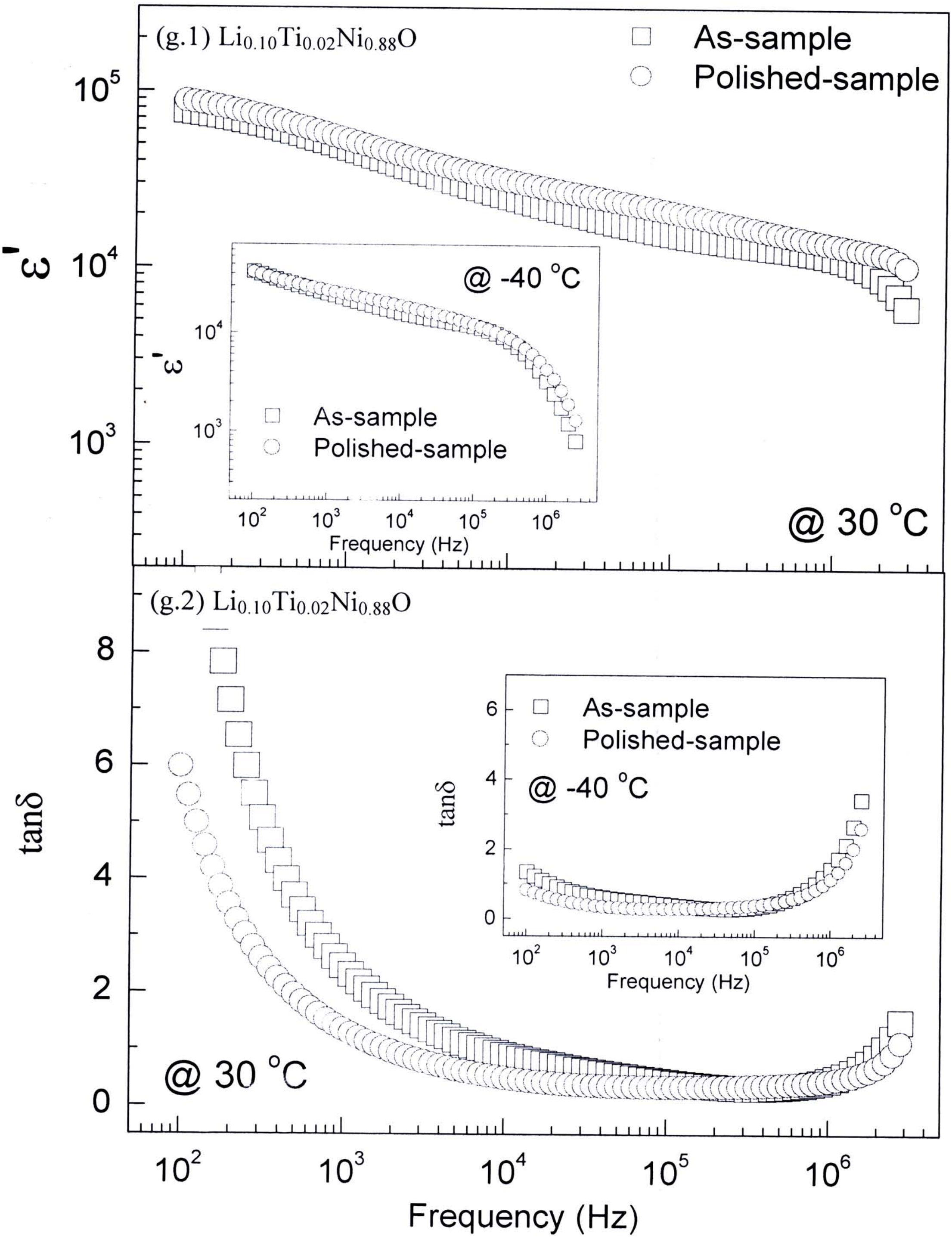

Figure 5.29 Dielectric constant (ε′) and loss tangent (tanδ) at 30 °C of $Li_xTi_yNi_{1-x-y}O$ ceramics sintered at 1280 °C for non- (as-) and polished-samples; inset is the dielectric properties at -40 °C. (Cont.)

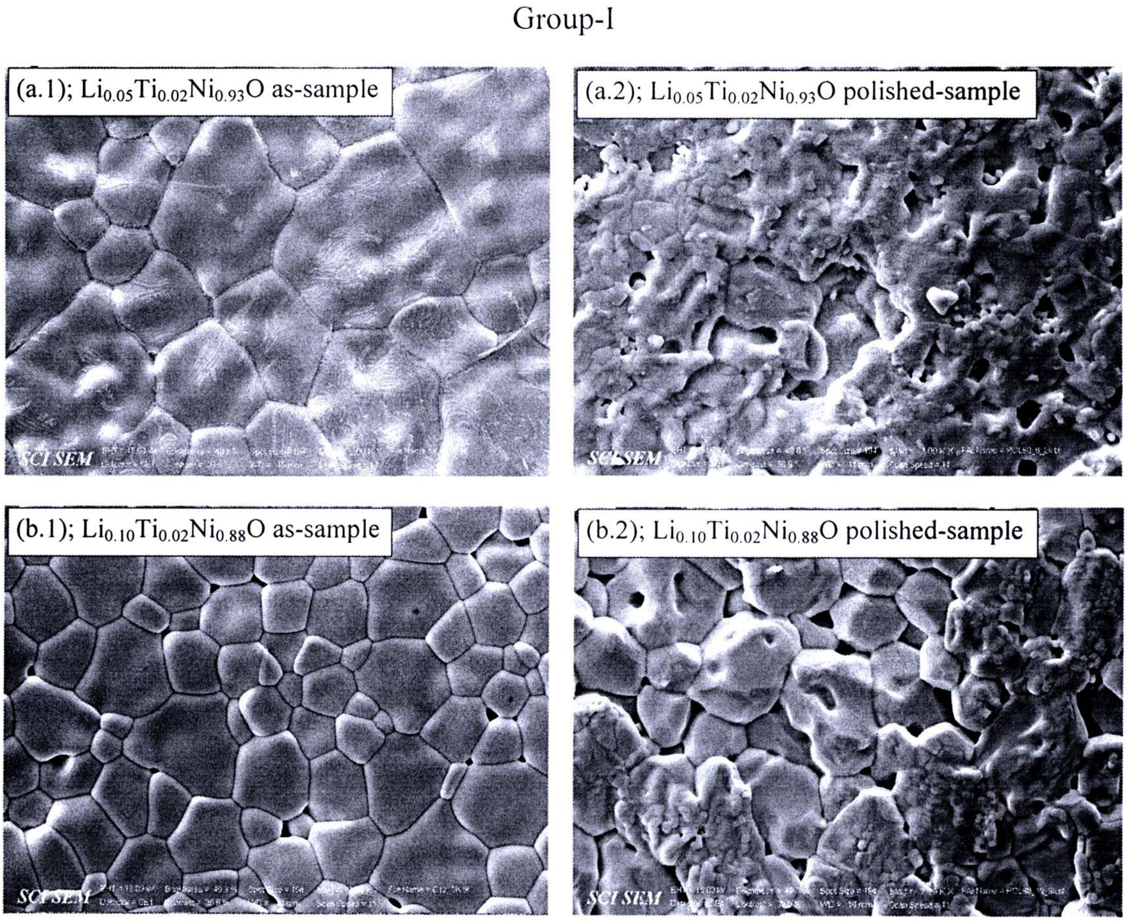

Figure 5.30 SEM images of surface morphologies of $Li_xTi_yNi_{1-x-y}O$ as- and polished-samples sintered at 1280 °C for group-I.

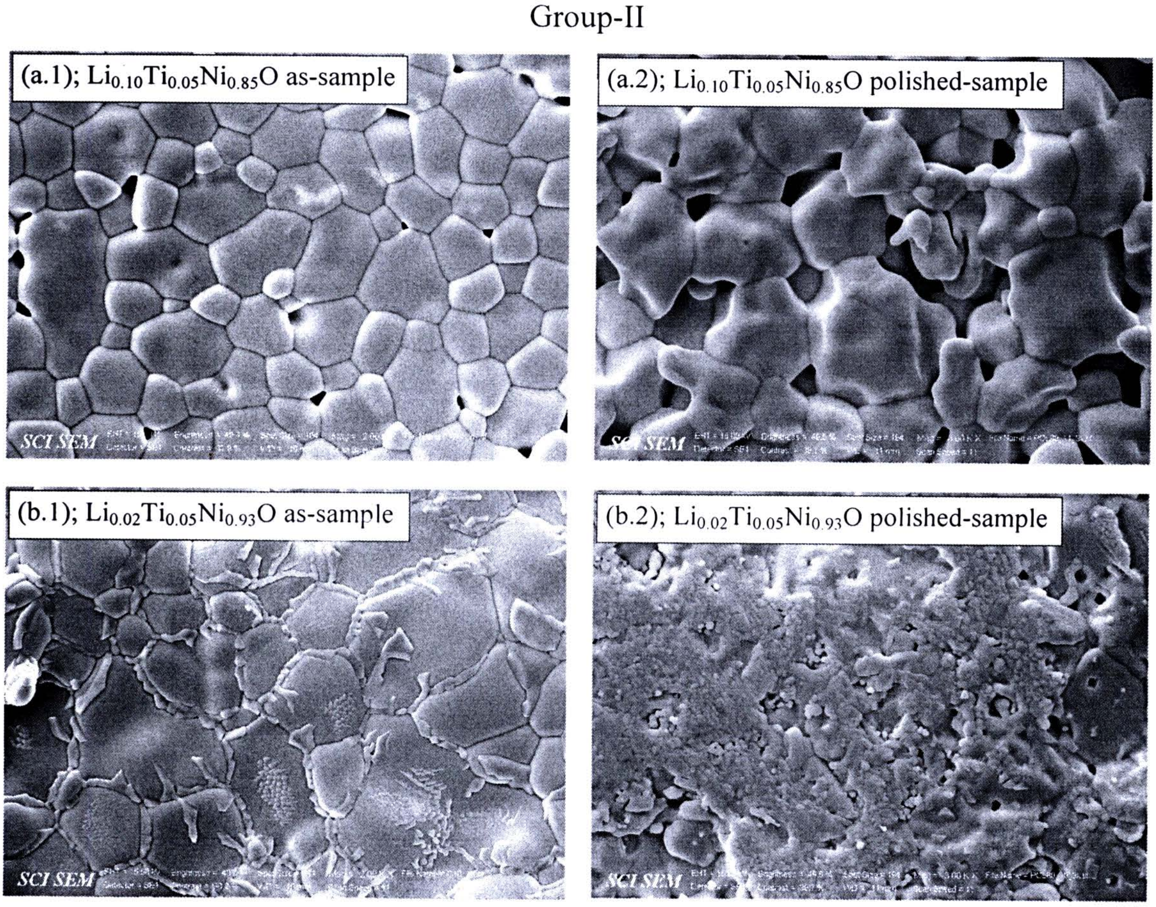

Figure 5.31 SEM images of surface morphologies of $Li_xTi_yNi_{1-x-y}O$ as- and polished-samples sintered at 1280 °C for group-II.

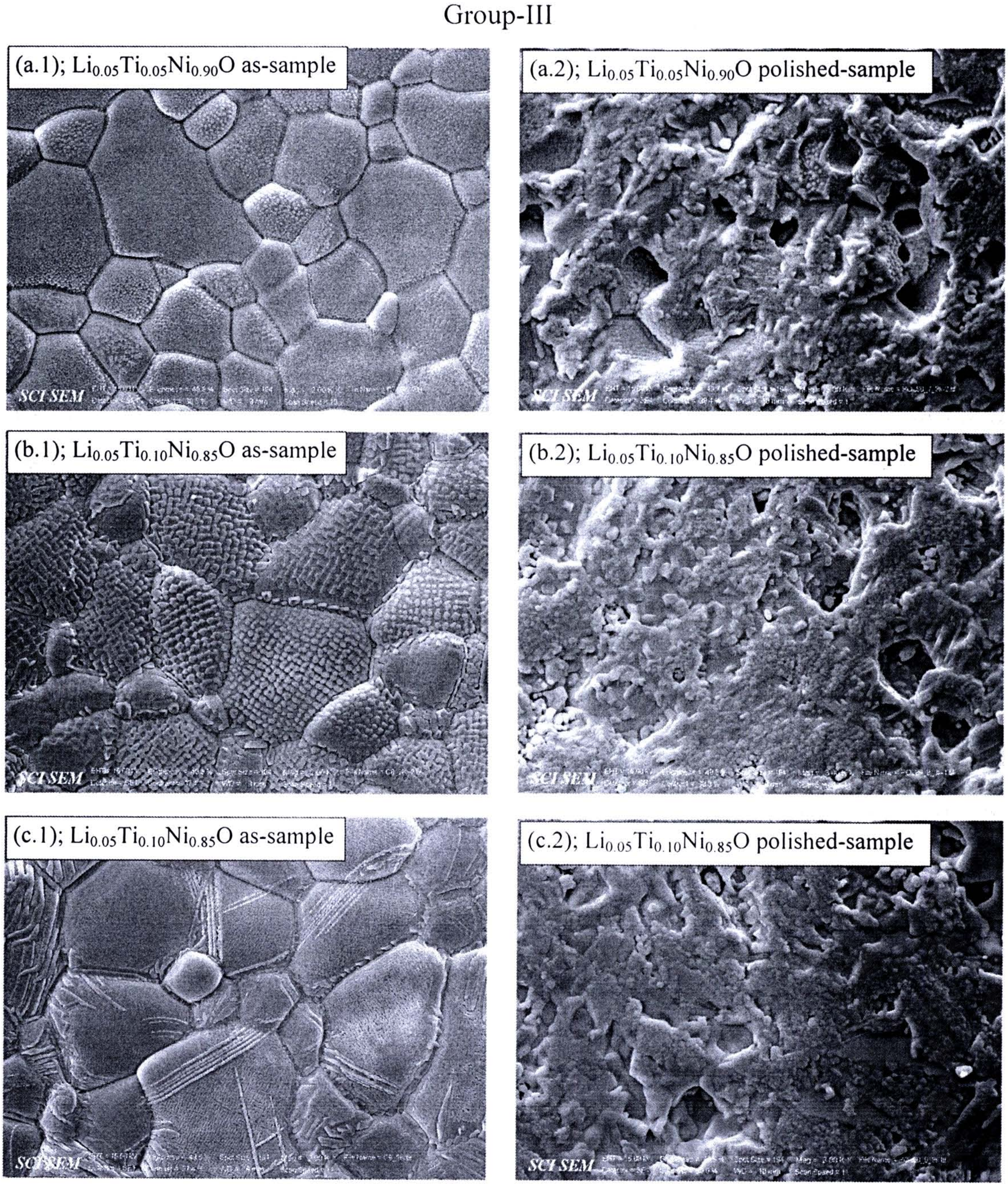

Figure 5.32 SEM images of surface morphologies of $Li_xTi_yNi_{1-x-y}O$ as- and polished-samples sintered at 1280 °C for group-III.

5.1.7.2 Characterization of electrical properties of the outmost surface layer of the $Li_xTi_yNi_{1-x-y}O$ ceramics

As previously discussed in the section 5.1.6, the electrical properties of the $Li_xTi_yNi_{1-x-y}O$ ceramics, polished-ceramic samples sintered at 1200 °C, can be characterized by the impedance spectroscopy. It is proved that the $Li_xTi_yNi_{1-x-y}O$ ceramics are electrically heterogeneous consisting of semiconducting grains and insulating grain boundaries. Two semicircles of impedance spectra with relative small and large diameters are observed in the high-frequency and low-frequency ranges, respectively. The small and large diameters can be suggested to two parts in the polycrystalline $Li_xTi_yNi_{1-x-y}O$ ceramics that have a low and high resistance, respectively. Due to the semiconducting properties of the Li-doped NiO grains, the small semicircle can be assigned as the electrical response of grain. Thus, the large semicircle should be referred to the grain boundary effect. In many cases, there exist three semicircles exhibited in the impedance spectra in the frequency range of 10^0-10^7 Hz for materials such as $CaCu_3Ti_4O_{12}$ ceramics (Shao et al., 2006; Fang et al., 2009). The added semicircle at the lowest-frequency range is usually suggested to the electrode effect (Fang et al., 2009), the surface-layer effect (Morrison et al., 2001), or domain boundary effect (Shao et al., 2006). The use of suitable electrodes, the applying dc bias, or the removing of the outmost surface layers is usually a method that can prove the existence of these three effects.

To clarify the outmost surface-layer effect, the impedance spectrum of a polished-sample is therefore compared to that of an as-sample with identical concentrations of Li and Ti doping. Figure 5.33 demonstrates the complex impedance plane plot at 30 °C for the $Li_xTi_yNi_{1-x-y}O$ ceramics before and after polishing. The inset of each figure shows an expanded view of high frequency data close to the origin, showing a non-zero intercept. First of all, it is worth noting that the impedance spectra at a high-frequency range of both as- and polished-samples are similar. At the highest frequency, the impedance spectrum of the as-sample coincides completely with the spectrum of the polished-sample. This observation indicates that the surface layers do not have an influence on the high-frequency electrical response of the $Li_xTi_yNi_{1-x-y}O$ ceramics. This electrical response corresponds to the dielectric response in this high-frequency range—both of the high-frequency relaxation and the high-frequency electrical response do not change with the removing of the surfaces. In these ceramics, therefore, the electrical properties may have a close relationship to the dielectric properties. For the variation in a large semicircle of the $Li_xTi_yNi_{1-x-y}O$ ceramics, the effect of surface layer on the impedance spectra is described and discussed as the follows.

1) Group-I

For the $Li_{0.05}Ti_{0.02}Ni_{0.93}O$ ceramic, the diameter of the large semicircle observed in the dielectric spectrum of the as-sample is larger than that of the polished-sample. After the surface layers of the $Li_{0.05}Ti_{0.02}Ni_{0.93}O$ ceramic are removed, the total resistance decreases. Looking carefully at the loss tangent spectra as a function of frequency (10^2-10^6 Hz) for the as- and polished-samples of the $Li_{0.05}Ti_{0.02}Ni_{0.93}O$ ceramic (Fig. 5.29(a.2)), both of the spectra are not different. These impedance and dielectric results seem to be strange. The total resistance decreases; whereas, the loss tangent remains constant.

With considering the $Li_{0.10}Ti_{0.02}Ni_{0.88}O$ ceramic, it is found that the diameter of the large semicircle observed in the dielectric spectrum of the as-sample is smaller than that of the polished-sample. In the other words, after the surface layers are removed, the total resistance of the $Li_{0.10}Ti_{0.02}Ni_{0.88}O$ ceramic is enhanced. This result is opposite to that observed in the $Li_{0.05}Ti_{0.02}Ni_{0.93}O$ ceramic. The increase in the total resistance corresponds to the decrease in the loss tangent that is due to the dc conductivity effect. The dc conduction of the system can be decreased by increasing the resistance.

The changes in the dielectric properties and the related electrical response in these two $Li_xTi_yNi_{1-x-y}O$ ceramics are difficult to ascribe because there are no other experimental results supported such as the use of other electrode materials. According the SEM and XRD results of these two ceramics, the second phase of $NiTiO_3$ can not be detected on the outmost surface. It is suggested from the microstructure and crystal structure analyses that the Li doping can assist to dissolve the Ti doping into the NiO crystal lattice. Thus, the $NiTiO_3$ phase disappears on the surfaces of these two as-samples. However, this information is still not sufficient to describe these changes in dielectric and electrical properties. On the other ways, the different chemical compositions between the outmost surface layer and the inner part might be responsible for these changes. The oxygen vacancy concentration at the surface layer might be less than that of the inner part (Wang, Zhang, 2006). As a result, the conductivity (and resistivity) of the outmost surface layer should be less (higher) than that of the inner part. Therefore, after the high-resistive surface layer of the $Li_{0.05}Ti_{0.02}Ni_{0.93}O$ ceramic is moved, the total resistance decreases. Another possible mechanism, which is quite more reasonable than the previous one, is the accumulation of the $NiTiO_3$ phase on the surface. As seen in the SEM image of the as-sample for the $Li_{0.05}Ti_{0.02}Ni_{0.93}O$ ceramic, some parts of this phase have accumulated on the surface. Therefore, the total resistance should be decreased by removing the surface layers of the $NiTiO_3$ sub-micron grains. The increase in the dielectric constant of the polished-sample of the $Li_{0.05}Ti_{0.02}Ni_{0.93}O$ ceramic sample might be due to the metal/semiconductor Schottky contact (Ibach, Luth, 2003). This contact can be introduced by applying the suitable metallic contact on the semiconducting surface, forming a thin insulating layer at this contact. Thus, the electrical polarization can be generated at this interface; as a result, the total polarization of the polished-sample of the $Li_{0.05}Ti_{0.02}Ni_{0.93}O$ ceramic should be increased. The giant dielectric constant observed in CuO ceramics was found to be introduced by this way (Li M et al., 2009a). Moreover, it was also proposed that the low-frequency relaxation observed in the $CaCu_3Ti_4O_{12}$ ceramics and single crystal is attributed to the Schottky contact effect (Li M et al., 2009b; Krohns et al., 2007, 2008). It is possible that the different dielectric constants of the as- and polished-samples of the $Li_{0.05}Ti_{0.02}Ni_{0.93}O$ ceramic might be due to the difference of the surface state between them (Kimura et al., 2008). The different concentrations of oxygen vacancies between the surface and the inner part might also result from the surface state of the $Li_{0.05}Ti_{0.02}Ni_{0.93}O$ ceramic. For the polished-sample of the $Li_{0.05}Ti_{0.02}Ni_{0.93}O$ ceramic, surface charged-carriers might be trapped at this Schottky contact; consequently, the capacitance of the contact increases and the loss tangent does not change. For the $Li_{0.10}Ti_{0.02}Ni_{0.88}O$ ceramic, the increase in the total resistance of the polished-sample, which results in the reduction of the loss tangent, might be related to either of Schottky barrier height or the problem of electrode contact.

2) Group-II

For the $Li_{0.02}Ti_{0.05}Ni_{0.93}O$ and $Li_{0.10}Ti_{0.05}Ni_{0.85}O$ ceramics as revealed in figures 5.29(e) and 5.29(f), the values of the dielectric constant of the polished-samples are slightly less than those of the as-samples; whereas, the loss tangents remain constant. As displayed in figures 5.33(e) and 5.33(f), the total resistance of the polished-sample of the $Li_{0.02}Ti_{0.05}Ni_{0.93}O$ ceramic is not significant larger than that of the as-sample. For the $Li_{0.10}Ti_{0.05}Ni_{0.85}O$ ceramic, the total resistances of both as- and polished-samples are nearly constant. These results indicate that the surface layer does not have an effect on the electrical properties and the related dielectric response in these two ceramics. Although the Ti doping concentration in the $Li_{0.10}Ti_{0.05}Ni_{0.85}O$ ceramic is relatively high, the Li doping is high as well. Hence, the Ti doping can be dissolved into the NiO crystal lattice, as discussed in section 5.1.2. Thus, the electrical conductivity of this sample seems to be low comparing to the $Li_{0.05}Ti_{0.02}Ni_{0.93}O$ ceramic due to the effect of the Ti-induced point defects. This might result from the inhibition of the formation of the Schottky barrier at the interface between electrode and surface sample.

3) Group-III

As discussed in the previous section, the low-frequency dielectric constant of the ceramics in this group decreases with removing the surface layers. However, it is also found that the loss tangent in the low-frequency range increases with removing the surface layers. Based on only the variation of dielectric properties due to the surface effect, it is expected that the surface layer, the sub-micron grains of the $NiTiO_3$ phase that cover the surface, may behave as the insulating layer. This insulating layer is between the electrode and the inner part of the bulk ceramics. This expectation is already proved as represented in figures 5.33(b)-5.33(d). These complex impedance plane plots show that surface layers have a great impact on the electrical property—the total resistance—of the $Li_{0.05}Ti_{0.05}Ni_{0.90}O$, $Li_{0.05}Ti_{0.10}Ni_{0.85}O$, and $Li_{0.05}Ti_{0.15}Ni_{0.80}O$ ceramics. The total resistance of the polished-samples is much less than that of the as-samples. This observation indicates that the total resistance of the as-sample can be decreased by removing the surface layers, which are the layers of $NiTiO_3$ sub-micron grains. In the other words, the removed-surface layers are the relative non-conducting layer, the insulating layer. This is the best data supported to the expectation above.

Looking carefully at the impedance spectra of these three as-samples, it is clearly seen that each impedance spectrum contains two overlapping semicircles and a nonzero intercept at high frequencies. This observation indicates that there are at least three electrical responses exhibited in this impedance spectrum. The nonzero intercept can usually be assigned as the electrical response of grains (Sinclair et al., 2002). This is due to the fact that the grain response at 30 °C can be occurred at the frequencies that are higher than the measuring frequency range. Therefore, the semicircle arc corresponding to the grain response can not be observed in the spectrum in the measuring frequency range. The overlapping semicircles consist of a large arc at the relative low-frequency range and a small arc at a high-frequency range. In many cases, if three electrical responses are observed in the impedance spectrum, the first arc at the lowest-frequency range is usually suggested to either of an electrode effect (Li M et al., 2009a,b; Wang et al., 2007) or insulating surface-layer effect (Morrison et al., 2009). Although, the electrode effect is not investigate, it is clear that the large semicircle at the low-frequency range can be assigned as the surface-layer effect. After the surface layers are polished to remove the insulating layers, the large semicircle arc of the impedance spectrum disappears. The remained-small arc and the nonzero intercept can be observed in the polished-samples. As a result, the resistance of the inner part, which is excluded from the insulating surface layers, can roughly be estimated by measuring the diameter of the semicircle arc of the polished-sample. On the other hand, the resistance of the surface layers, which are removed, can be estimated from the difference in the total resistance of the as-sample and the estimated resistance of the inner part. The remained-semicircle arc and the nonzero intercept observed in the polished-sample might be assigned as the grain boundary and the bulk grain responses, respectively.

However, a careful inspection of the impedance spectrum of the polished-sample of the $Li_{0.05}Ti_{0.15}Ni_{0.80}O$ ceramic (Fig. 5.33(d)) demonstrates that there may be two overlapping of semicircle arcs. Thus, the remained-arc observed in the impedance spectrum of the polished-sample can not be assigned as only the grain boundary effect, but also as another unknown effect. This result is consistent with the dielectric properties of this ceramic. As revealed in figure 5.29(d), after the surface layers are removed from both sides of the as-sample, the dielectric constant decreases slightly. However, the low-frequency relaxation (LFR) is still observed in the dielectric spectrum of the polished-sample of the $Li_{0.05}Ti_{0.15}Ni_{0.80}O$ ceramic. These results indicate that there are at least four sources of polarization that can contribute to the total dielectric response in these three samples. The difference of a contribution among these three samples may be related to the different chemical composition of the Li and Ti doping. The electrical responses of overlapping arcs observed in the impedance spectrum of the $Li_{0.05}Ti_{0.15}Ni_{0.80}O$ ceramic can not be characterized now, because there are no experimental data supported. This subject will be briefly discussed in sections 5.1.8 and 5.1.9.

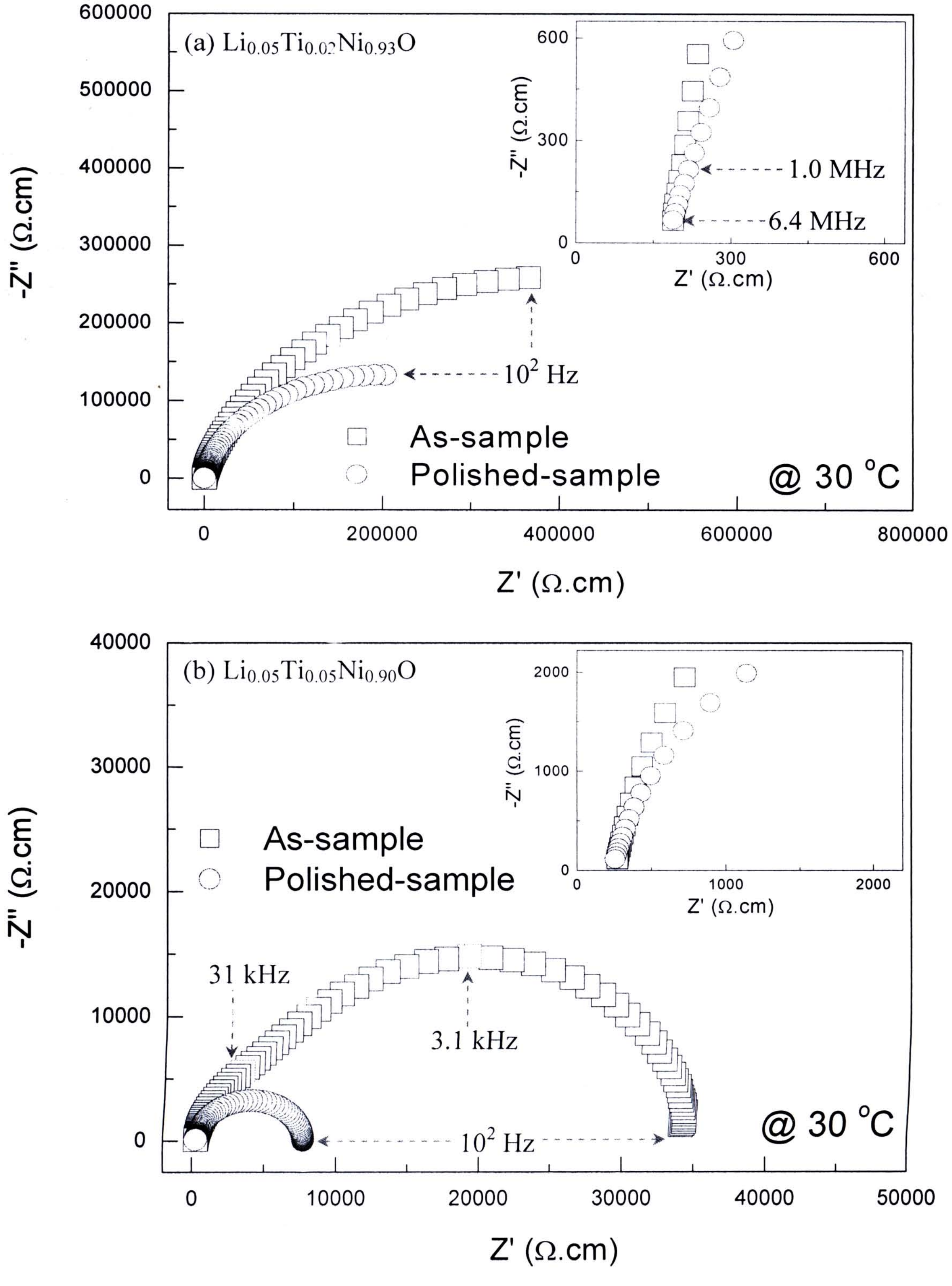

Figure 5.33 Complex impedance plane plot at 30 °C of $Li_xTi_yNi_{1-x-y}O$ ceramics *sintered at 1280 °C for non- (as-) and polished-samples; inset is an* expanded view of high frequency data close to the origin.

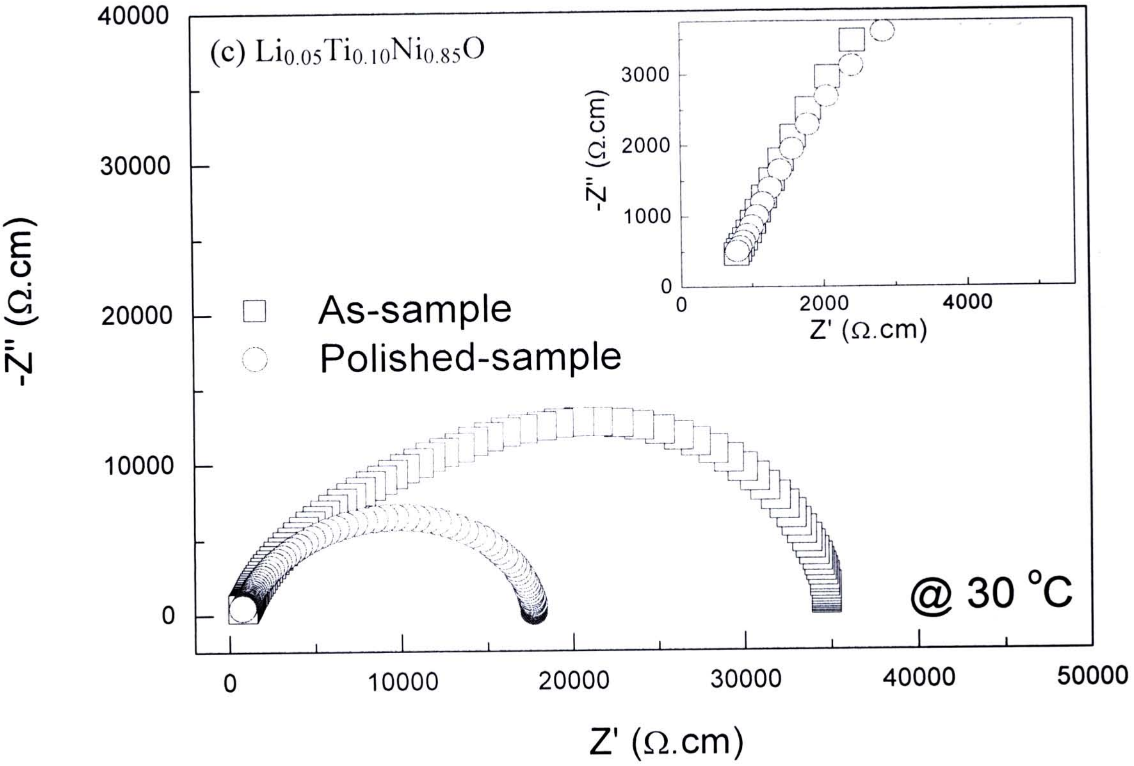

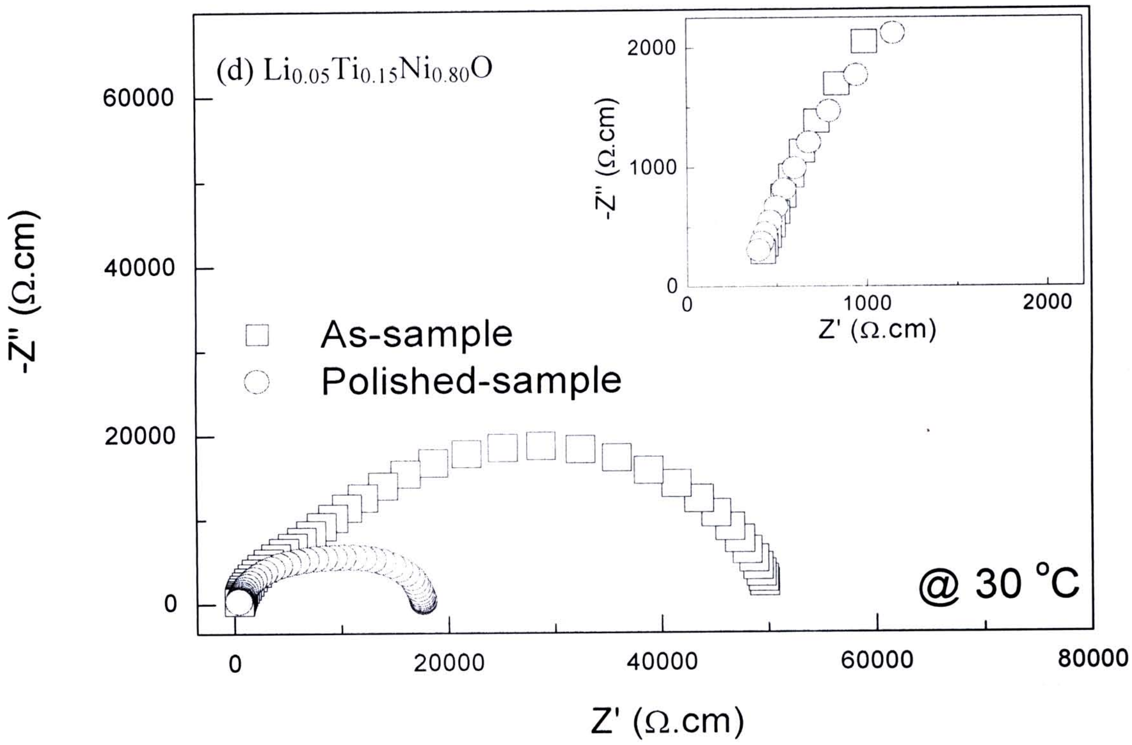

Figure 5.33 Complex impedance plane plot at 30 °C of $Li_xTi_yNi_{1-x-y}O$ ceramics sintered at 1280 °C for non- (as-) and polished-samples; inset is an expanded view of high frequency data close to the origin. (Cont.)

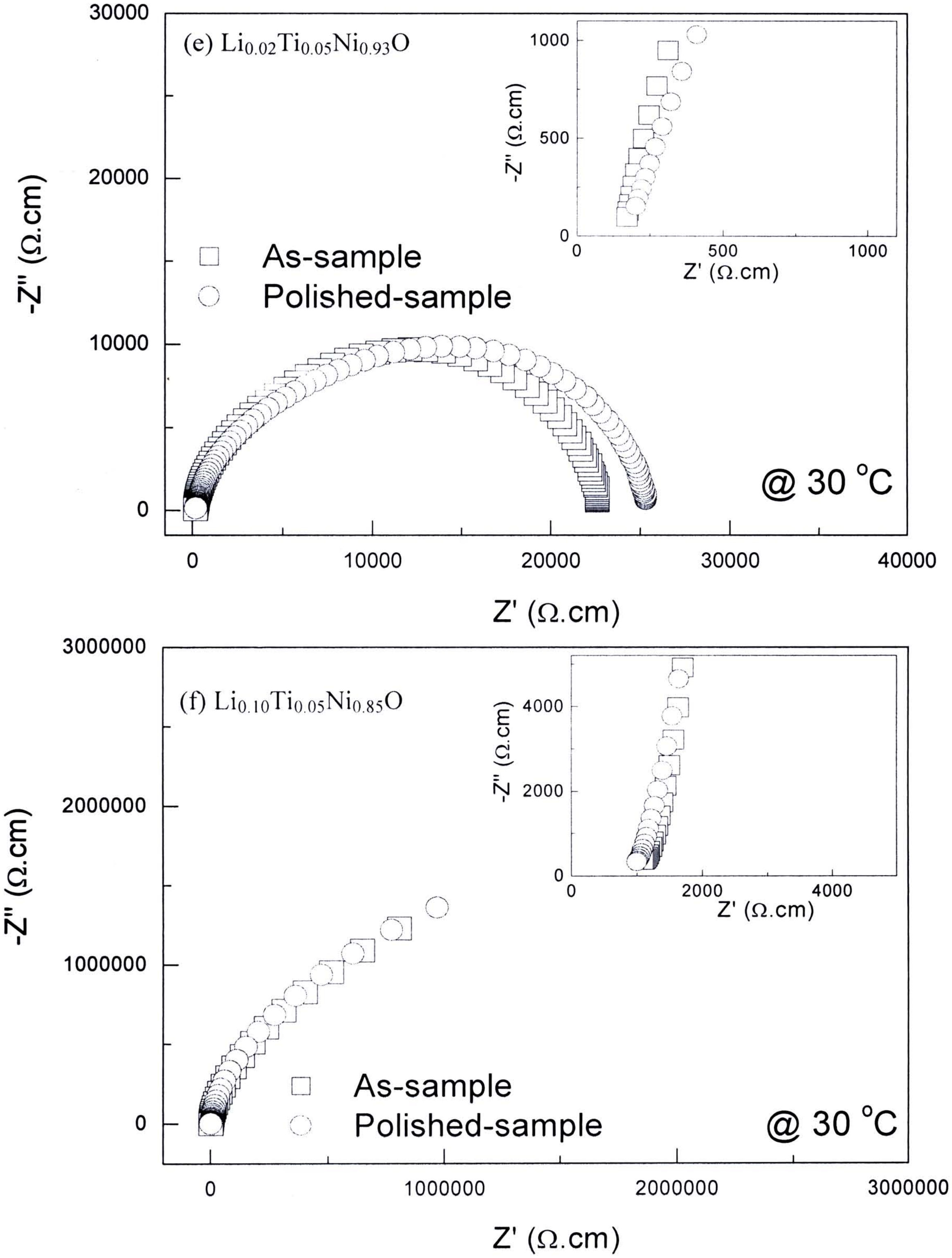

Figure 5.33 Complex impedance plane plot at 30 °C of $Li_xTi_yNi_{1-x-y}O$ ceramics sintered at 1280 °C for non- (as-) and polished-samples; inset is an expanded view of high frequency data close to the origin. (Cont.)

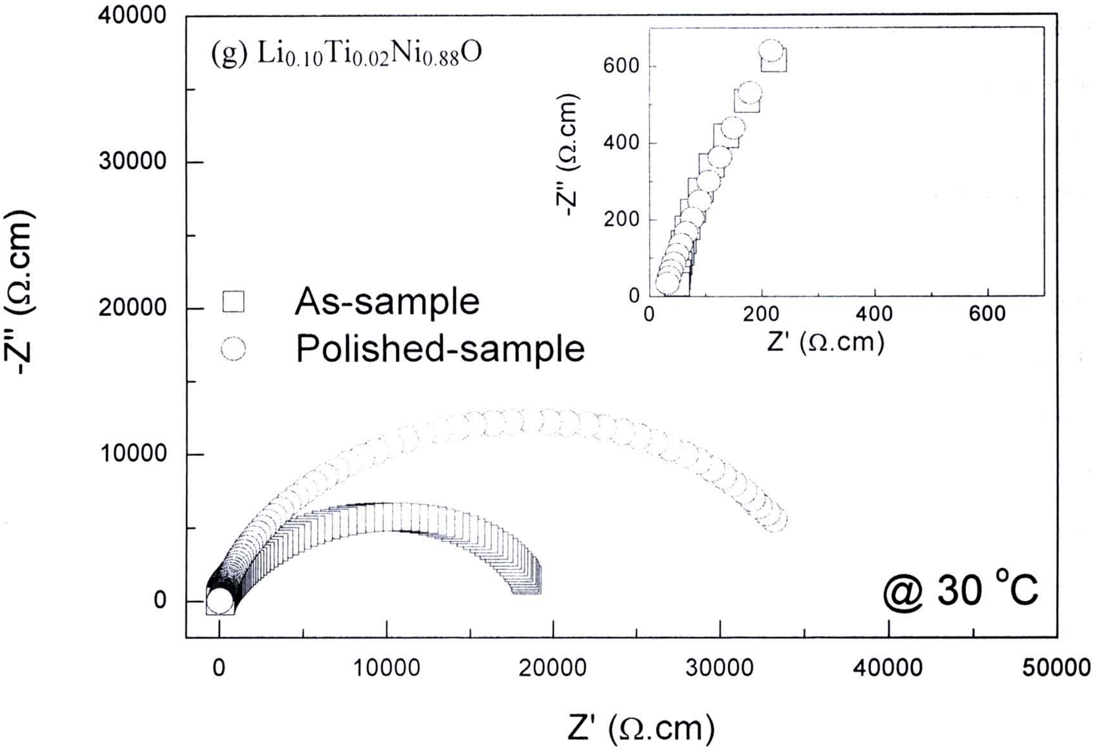

Figure 5.33 Complex impedance plane plot at 30 °C of $Li_xTi_yNi_{1-x-y}O$ ceramics sintered at 1280 °C for non- (as-) and polished-samples; inset is an expanded view of high frequency data close to the origin. (Cont.)

5.1.7.3 Low-frequency relaxation observed in the as-samples for the $Li_xTi_yNi_{1-x-y}O$ ceramics classified in group-III

To understand the mechanism of the low-frequency relaxation (LFR), it is important to carefully characterize the LFR combined with the HFR. Figures 5.34(a) and 5.34(b) demonstrate the frequency dependence of the dielectric constant of the as-samples of the $Li_{0.05}Ti_{0.05}Ni_{0.90}O$ and $Li_{0.05}Ti_{0.15}Ni_{0.80}O$ ceramics, respectively. Two thermally activated dielectric relaxations can be observed in the dielectric spectra. Note that only a set of high-frequency relaxation peaks (loss tangent peak) can be observed. While a set of low-frequency relaxation peaks can not be observed. As shown in figure 5.35 for the evolution of the loss tangent, beside the HFR-peak, a small hump can be observed at the low frequency range, as indicated by the vertical arrow. By using the Cole-Cole relaxation model combined with the dc conductivity term (Eq. (5.10)), the small hump is expected to be the peak of the loss tangent at the low-frequency range, the LFR-peak, as demonstrated by the dots curve. However, it is now unsuitable to believe that this hump is the relaxation peak, until there is a strong indication supported to this expectation. The supported-experimental results will be demonstrated and discussed in section 5.1.8.

Turning to see the dielectric constant relaxation illustrated in figures 5.34(a) and 5.34(b), two sets of the rapid drop of the dielectric constant shift to higher frequency with increasing the measuring temperature. The thermally activated mechanism is suggested to relate to this observation. Certainly, with increasing the measuring temperature, dipoles are activated to a new state with higher energy. The dipoles can relax with a quick rate; thus, the dielectric response can occur at higher frequencies. According to the LFR, relaxation times (τ) can not be achieved by the relationship, as

$$2\pi f_{p(\varepsilon")}\tau = 1, \tag{5.16}$$

and

$$2\pi f_{p(\delta)}\tau = \sqrt{\frac{\varepsilon'_s}{\varepsilon'_0}}, \tag{5.17}$$

where $f_{p(\varepsilon")}$ and $f_{p(\delta)}$ are the frequencies at the relaxation peaks of a dielectric loss and loss tangent, respectively. Unfortunately, the LFR-peaks of the loss tangent ($\tan\delta$) and the dielectric loss (ε'') can not be observed in the dielectric spectra of the as-samples for the $Li_{0.05}Ti_{0.05}Ni_{0.90}O$ and $Li_{0.05}Ti_{0.15}Ni_{0.80}O$ ceramics. As a result, τ can not be calculated because the $f_{p(\varepsilon")}$ and $f_{p(\delta)}$ can not be obtained from the experimental results. Thus, activation energy required for the LFR process can not be calculated by this way due to the disappearance of the relaxation peaks. On the other way, relaxation times at different temperatures can be obtained by fitting the experimental data with a relaxation model such as the Cole-Cole relaxation model (Cole KS, Cole RH, 1941). The Cole-Cole equation is

$$\varepsilon^* = \varepsilon' - j\varepsilon'' = \varepsilon'_\infty + \frac{\varepsilon'_s - \varepsilon'_\infty}{1 + (j\omega\tau)^\alpha}. \tag{5.18}$$

A careful inspection of figure 5.34 demonstrates that both of LFR and HFR can be well fitted with the Cole-Cole relaxation model. The values of τ at various temperatures for the LFR are obtained from the fitted results. Three important results are obtained from the fitting. First, the α value of the fitted LFR data decreases with increasing temperature; whereas, it is constant for the HFR. It is found that α values of the LFR decrease from 0.88 to 0.81 and 0.79 to 0.76 with increasing the temperature from -20 to 70 ^{o}C for the as-samples of the $Li_{0.05}Ti_{0.05}Ni_{0.90}O$ and $Li_{0.05}Ti_{0.15}Ni_{0.80}O$ ceramics, respectively. α values of the HFR are constant to be 0.94 and 0.87 for the as-samples of the $Li_{0.05}Ti_{0.05}Ni_{0.90}O$ and $Li_{0.05}Ti_{0.15}Ni_{0.80}O$ ceramics, respectively.

According to the fitted LFR results, it is found that the fitted τ values at different temperatures obey the Arrhenius law (Eq. (5.7)), as shown in figure 5.36. As demonstrated in figure 5.34, it can indicate that both of the LFR and HFR are typical of Debye-type relaxation. E_a values of the LFR exhibited in the as-samples for the $Li_{0.05}Ti_{0.05}Ni_{0.90}O$ and $Li_{0.05}Ti_{0.15}Ni_{0.80}O$ ceramics can be estimated to be 0.281 and 0.262 eV, respectively. It should be recognized that these values are comparable to 0.291 and 0.278 eV, which are the activation energy for the HFR of the as-samples for the $Li_{0.05}Ti_{0.05}Ni_{0.90}O$ and $Li_{0.05}Ti_{0.15}Ni_{0.80}O$ ceramics. Normally, the relaxation activation energy of a LFR is much higher than that of a HFR. For example, the values of activation energy of the LFR and HFR observed in $CaCu_3Ti_4O_{12}$ ceramics were found to be 0.515-0.678 and 0.084-0.156 eV, respectively (Zhang et al., 2005; Ni, Chen, 2007). In $BiFeO_3$ multiferroic ceramics, the values of activation energy of LFR and HFR were found to be 0.690 and 0.325 eV, respectively (Hunpratub et al., 2009). This is the second important result that is found in the study of the LFR in these two as-samples. Third, τ_0 of the LFR process is found to be two orders of magnitude higher than that of the HFR process. The τ_0 values of the LFR process are found to be 3.09×10^{-10} and 5.92×10^{-10} s for the as-samples of the $Li_{0.05}Ti_{0.05}Ni_{0.90}O$ and $Li_{0.05}Ti_{0.15}Ni_{0.80}O$ ceramics, respectively. τ_0

values of the HFR process are obtained to be 2.81×10^{-12} and 2.62×10^{-12} s for the as-samples of the $Li_{0.05}Ti_{0.05}Ni_{0.90}O$ and $Li_{0.05}Ti_{0.15}Ni_{0.80}O$ ceramics, respectively. These relative high-values of τ_0 for the LFR process strongly suggest to the existence of the Maxwell-Wagner polarization or the interfacial polarization (Hence, West, 1990). This analysis can be used to support the previous discussion, where the $NiTiO_3$ sub-micron grains have acted as the insulating surface layer. The interfacial polarization at the interface between the insulating outmost surface-layer and the semicondicting inner-part can be generated. Note that this LFR may also be related to the interfacial polarization at grain boundaries of these two samples.

The close values of the relaxation activation energies between the LFR and HFR processes can not be certainly suggested now, because the origins of the LFR and HFR are still not unclear. However, it is possible that the LFR and HFR might be associated with the surface-layers and the grain boundary effects, respectively. Based on the microstructural analysis, the second phase of $NiTiO_3$ is more accumulated on the top surfaces of these two as-samples. It is also more observed at the grain boundaries, especially at the corners of the grains. As a result, it possible that both of the relaxations might exhibit at same type of interface, i.e., the interface between the insulating layer of the $NiTiO_3$ phase and the inner part of the semiconducting grains of Li-doped NiO. Therefore, the activation energies of these LFR and HFR process should be nearly the same in value. However, the assumption is needed to further characterization. The variation in α values of the LFR is certainly attributed to the change in the distribution of relaxation times of the dipoles in the bulk ceramics. The decrease in α value with increasing temperature corresponds to the large distribution of the relaxation times. It is highly possible that charge carriers with different types and concentrations as well as ion diffusions can be enhanced with increasing temperature. With increasing the concentration and type of the charge carriers, distribution of the relaxation times of the dipoles at a high temperature should be larger than that of a low temperature. Consequently, α value, a distribution function, should be decreased.

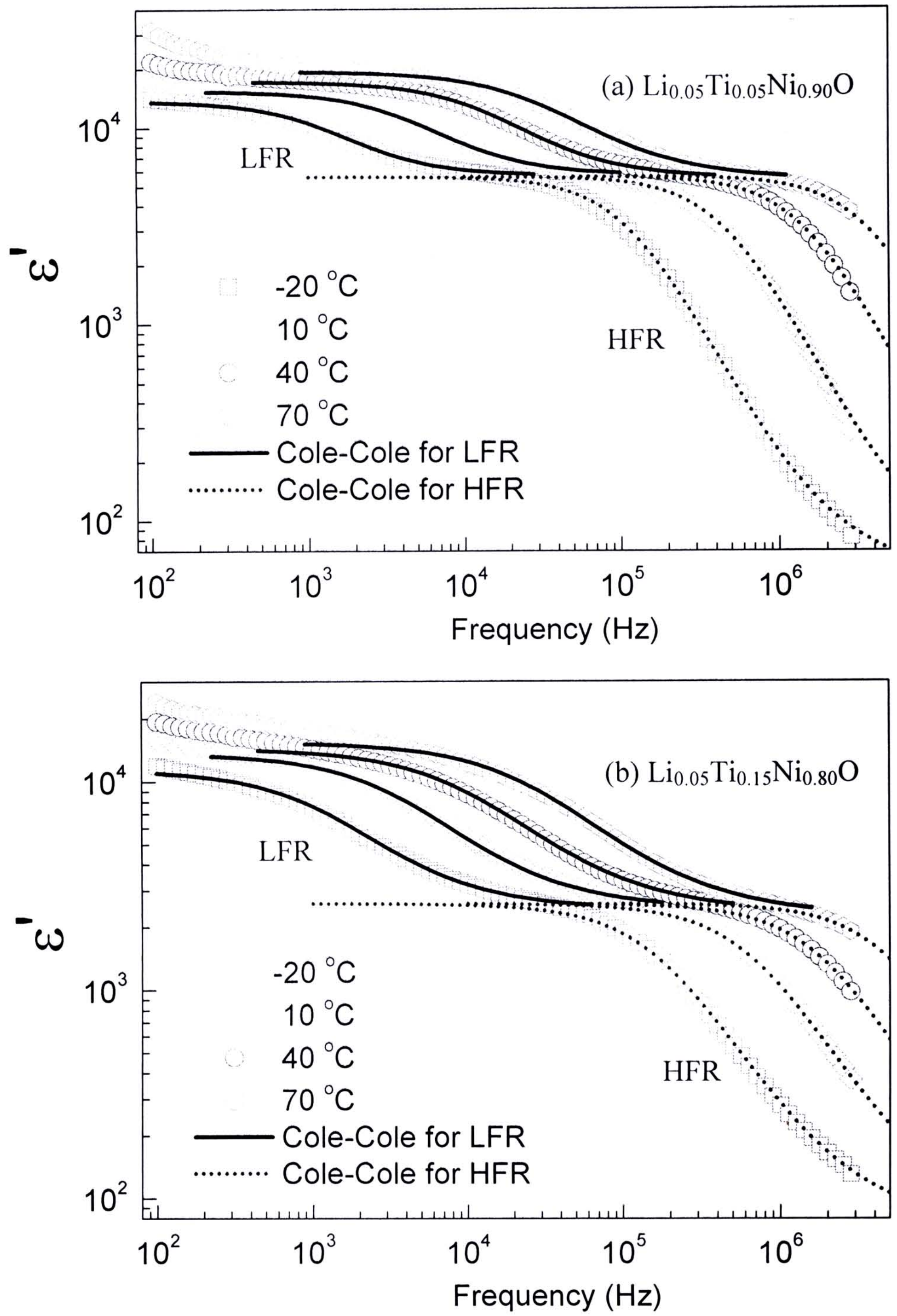

Figure 5.34 Low-frequency relaxation (LFR) and high-frequency relaxation (HFR) of (a) $Li_{0.05}Ti_{0.05}Ni_{0.90}O$ and (b) $Li_{0.05}Ti_{0.15}Ni_{0.80}O$ ceramics sintered at 1280 °C at various temperatures; the solid and dot curves are the best fit to Cole-Cole relaxation model for the LFR and HFR, respectively.

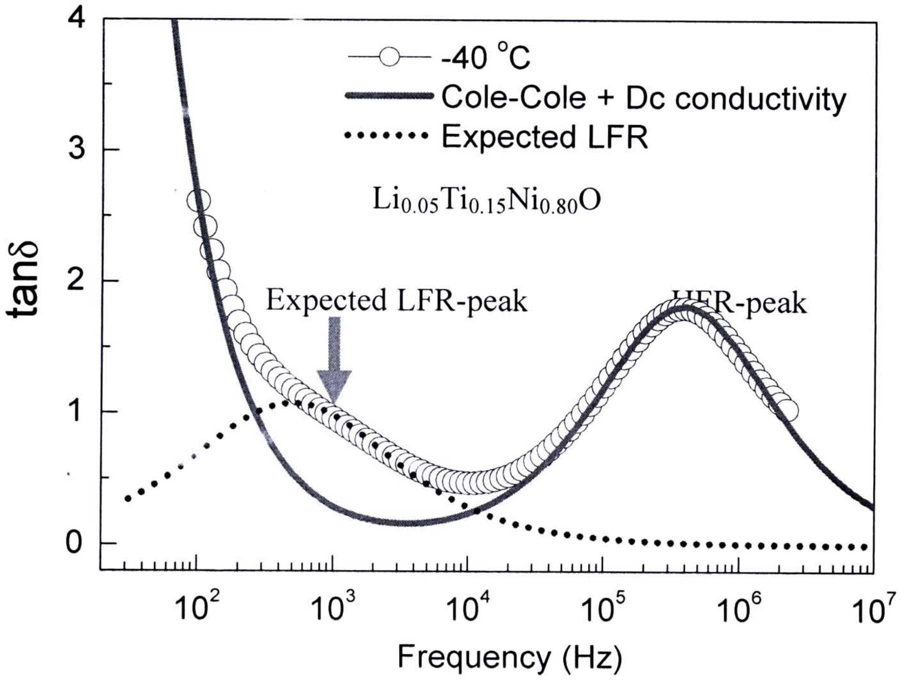

Figure 5.35 The evolution of the relaxation and dc conductivity contributed to the total loss tangent at -40 °C for the as-sample for $Li_{0.05}Ti_{0.15}Ni_{0.80}O$ ceramic sintered at 1280 °C; the red solid curve and the blue dot curve are respectively the best fit to Eq. (5.10) for HFR and the expected LFR estimated by the Cole-Cole relaxation model (Eq. (5.18)).

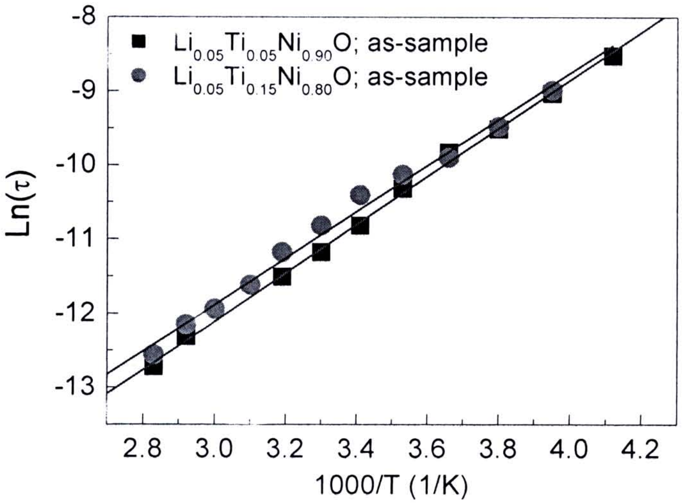

Figure 5.36 Arrhenius plot of the LFR of the as-samples for the $Li_{0.05}Ti_{0.05}Ni_{0.90}O$ $Li_{0.05}Ti_{0.15}Ni_{0.80}O$ ceramics sintered at 1280 °C.

5.1.8 Effect of annealing on dielectric and electrical properties

In order to investigate the effects of annealing on the dielectric and electrical properties, the polished-samples of the $Li_xTi_yNi_{1-x-y}O$ ceramics were annealed in the flowing argon (Ar) (99.9 %). The post-annealing process can be ascribed as following. After the dielectric properties of the polished-samples were conducted, these polished-samples were polished by SiC paper to remove the electrode and some parts of surfaces from both sides of the pellet samples. Then, the samples were annealed in Ar atmosphere at 900 °C for 3 h and allowed cooling to room temperature. Theses samples were denoted as *Ar-samples*. The Ar-samples were electroded by silver paint again. Finally, the dielectric properties of the Ar-samples with silver paint electrodes were conducted. The dielectric and electrical properties of the as-samples, polished-samples, and Ar-samples are represented and discussed together as following.

5.1.8.1 Effect of annealing on dielectric properties

Figures 5.37(a)-5.37(g) show the frequency dependence of the dielectric constant (ε') and the loss tangent ($\tan\delta$) at 30 °C for the $Li_xTi_yNi_{1-x-y}O$ ceramics. The inset of each figure demonstrates the frequency dependence of the dielectric constant at the low temperature of -40 °C. The evolution of the dielectric properties can be observed from these figures. The variation of the dielectric properties is found to be due to both of the insulating surface-layer and the annealing process effects. According to the section 5.7.1.2, it is strongly suggested that the low-frequency dielectric properties, which are in the frequency range of 10^2-10^4 Hz, are affected by the insulating surface-layer. This surface-layer effect is clearly seen in the $Li_{0.05}Ti_yNi_{0.95-y}O$ ceramics. However, high-frequency dielectric properties (10^4-10^6 Hz) do not change with the removing of the insulating surface-layers by polishing. This means that the high-frequency relaxation of the $Li_xTi_yNi_{1-x-y}O$ ceramics is certainly associated with the electrical response in the inner part (a pellet interior). Focusing on the pellet interior, normally, there are several possible sources of polarizations that can occur in dielectric ceramics such as grain boundaries, domain boundaries, defect dipoles, or a small polaron hopping inside gains. Certainly, just polishing process can not affect to these sources of polarizations.

Surprisingly, the annealing in Ar can lead to a chance in the high-frequency relaxation (HFR) of the $Li_xTi_yNi_{1-x-y}O$ ceramics. The rapid decrease in the dielectric constant at the high-frequency range observed in dielectric spectra of the Ar-samples occurs at a relative low frequency, comparing to those of the as-samples and polished-samples. This change in the HFR behavior can be seen clearly in the inset of each figure for the HFR process at -40 °C. This observation indicates that the HFR process is also closely related to the concentration of oxygen vacancies contained in the bulk ceramics and the surfaces. Although the concentration of oxygen vacancies may not directly affect to the HFR process, it may affect to something important that has a great contribution to the HFR mechanism.

For the $Li_{0.05}Ti_yNi_{0.95-y}O$ ceramics (y = 0.05, 0.10, and 0.15), the evolution of the dielectric properties of each sample is similar in every way to each other. After the surfaces were removed by polishing, at a low-frequency range, the dielectric constant decreased, but the loss tangent increased. While high-frequency dielectric properties did not change. With annealing the polished-samples in Ar atmosphere, the low-frequency dielectric constant increases higher than the initial values of the as-samples and the polished-samples. Moreover, the characteristic frequency that relates to the step-like rapid decrease of the LFR is found to be lower than those of the as-samples and polished-samples. The low-frequency loss tangent, which is largely contributed by to the effect of dc conduction, is found to greatly reduce, as revealed in figures 5.37(b.2)-5.37(d.2)—the left hand side of the dashed-lines. The low-frequency loss tangent of the Ar-samples is found to be lowest among these three samples—as-samples, polished-samples, and Ar-samples. In contrast, the high-frequency dielectric constant decreases with the annealing in Ar atmosphere; whereas, the high-frequency loss tangent is found to enhance. This increase in the loss tangent relates to the variation in the HFR process, as demonstrated in figures 5.37(b.2)-5.37(d.2)—the right hand side of the dashed-lines. The exponential-like increase of the loss tangent in a high-frequency range is the part of the HFR-peak, as clearly seen in figure 5.37(c.2). Consequently, the high-frequency loss tangent increases with the shift of the HFR-peak to lower frequency, which is due to the annealing effect. It is worth noting that the changes in the low-frequency dielectric properties due to the annealing effect are opposite to the changes that are due to the polishing. These results indicate that the total resistance of the $Li_{0.05}Ti_yNi_{0.95-y}O$ ceramics may increase with the post-annealing in Ar.

According to the expectation for the existence of the LFR-peak illustrated in Fig. 5.35, the observed small hump in the loss tangent of the as-sample of the $Li_{0.05}Ti_{0.15}Ni_{0.80}O$ ceramic can genuinely be suggested as the LFR-peak, as clearly seen in figure 5.37(d.2). This LFR-peak has occurred in the loss tangent spectrum of the Ar-sample of the $Li_{0.05}Ti_{0.15}Ni_{0.80}O$ ceramic. It is likely that the LFR-peak may occur in the loss tangent spectra of all $Li_{0.05}Ti_yNi_{0.95-y}O$ ceramics. The disappearance of such LFR-peak in the as-samples and polished-samples is due to the large contribution of the dc conduction to the total loss tangent. Therefore, the peak is concealed by the background of the exponential-like increase in the loss tangent with decreasing frequency. Thus, it is believed that the LFR-peaks of the Ar-samples of the other two ceramics can certainly be introduced by decreasing the dc conduction. In many perovskite dielectric materials such as La-doped $BaTiO_3$ and $CaCu_3Ti_4O_{12}$ ceramics, the total resistance can usually be reduced or enhanced by annealing the ceramics in oxidizing atmosphere (i.e., O_2) or in reducing atmosphere (e.g., N_2 or Ar) (Morrison et al., 2001; Adams et al., 2006; Wang, Zhang, 2006; Wang et al., 2007). However, the post-annealing in Ar of the $Li_{0.05}Ti_yNi_{0.95-y}O$ ceramics—a non-perovskite material—can lead to decrease in the loss tangent. This result seems to be strange—the dc conduction in the bulk NiO-based ceramics decreases with increasing the concentration of oxygen vacancies, which are as the electrically charged species. The details of this subject will be discussed in section 5.1.8.3.

For the $Li_{0.05}Ti_{0.02}Ni_{0.93}O$ and $Li_{0.10}Ti_{0.02}Ni_{0.88}O$ ceramics, the dielectric constant decreases with the annealing in Ar atmosphere. For the $Li_{0.02}Ti_{0.05}Ni_{0.93}O$ and $Li_{0.10}Ti_{0.05}Ni_{0.85}O$ ceramics, the dielectric constant does not significantly change with the annealing. Considering the change of the loss tangent by Ar-annealing, the low-frequency loss tangent of the $Li_{0.05}Ti_{0.02}Ni_{0.93}O$ and $Li_{0.02}Ti_{0.05}Ni_{0.93}O$ ceramics is found to be reduced by the annealing. This observation is similar to that observed in the $Li_{0.05}Ti_yNi_{0.95-y}O$ ceramics (y = 0.05, 0.10, and 0.15). The interesting results are observed in the $Li_{0.10}Ti_{0.02}Ni_{0.88}O$ and $Li_{0.10}Ti_{0.05}Ni_{0.85}O$ ceramics—the ceramics that contain the highest concentration of Li doping ions. The low-frequency loss tangent increases with the annealing. This result is opposite to those observed in the other ceramics, which are the ceramics that contain the relative-low Li doping concentrations.

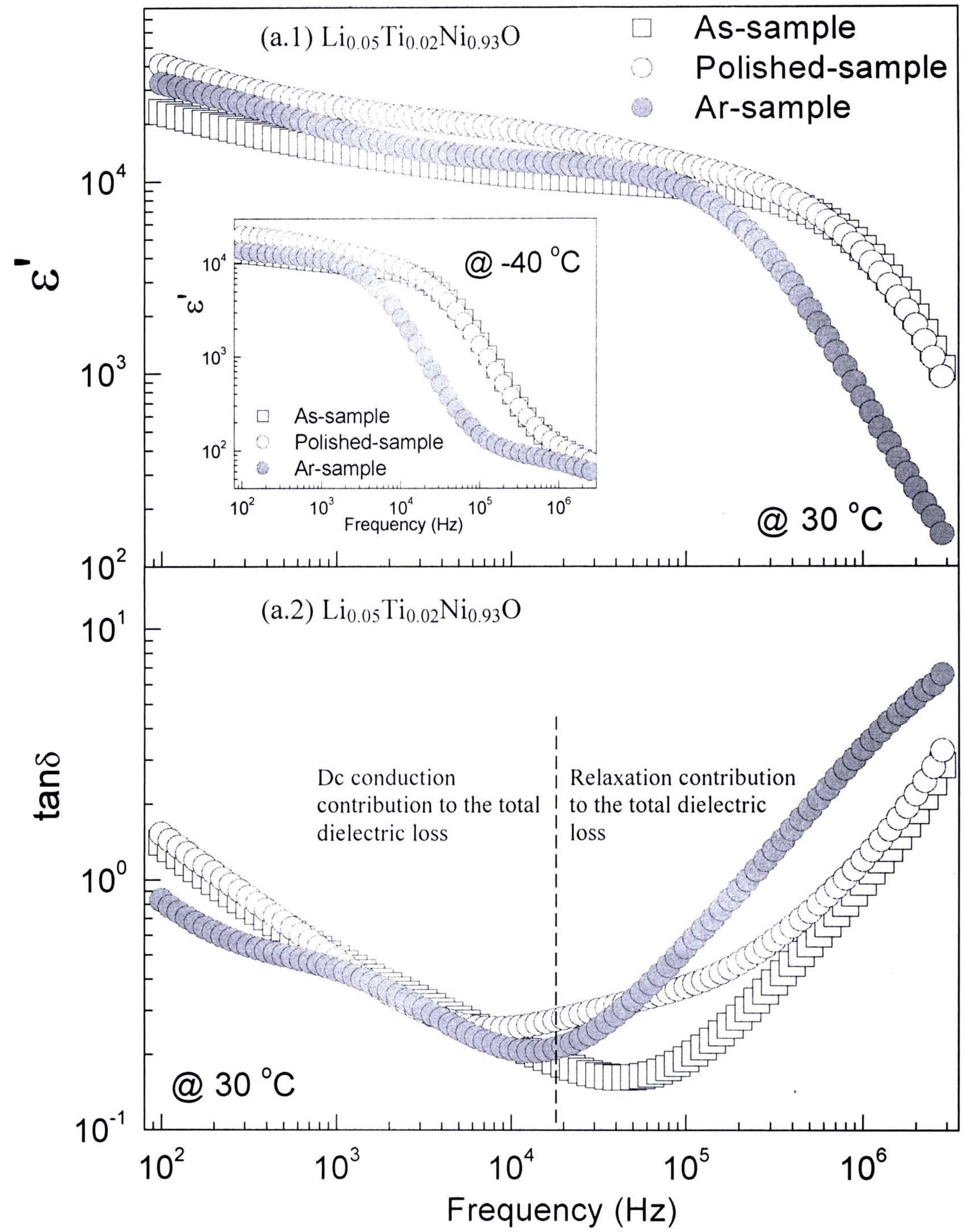

Figure 5.37 Frequency dependence of dielectric properties at 30 °C for as-sample, polished-sample, and Ar-sample of $Li_xTi_yNi_{1-x-y}O$ ceramics sintered at 1280 °C for 4 h; inset shows the frequency dependence of the dielectric constant of these four samples at -40 °C.

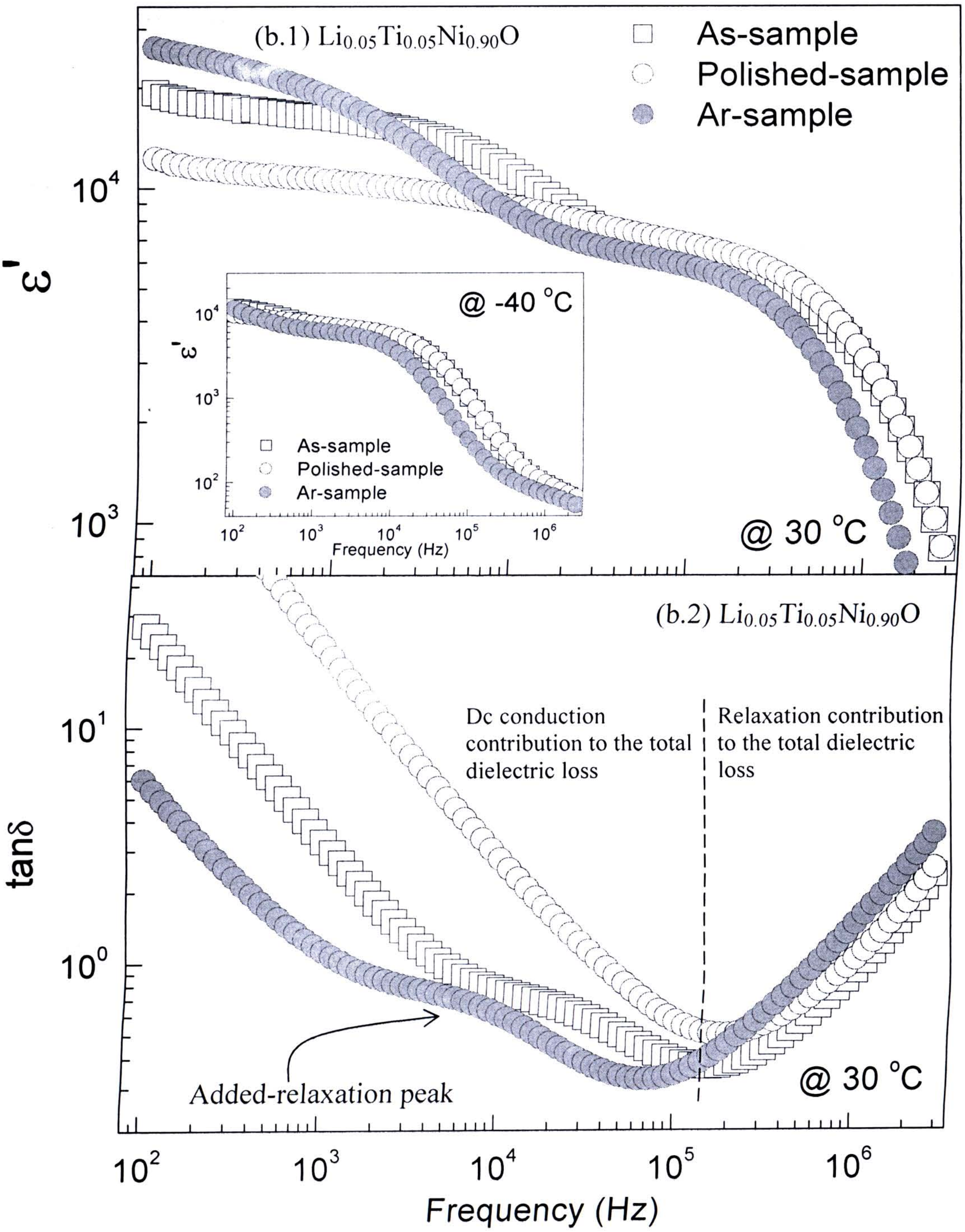

Figure 5.37 Frequency dependence of dielectric properties at 30 °C for as-sample, polished-sample, and Ar-sample of $Li_xTi_yNi_{1-x-y}O$ ceramics sintered at 1280 °C for 4 h; inset shows the frequency dependence of the dielectric constant of these four samples at -40 °C. (Cont.)

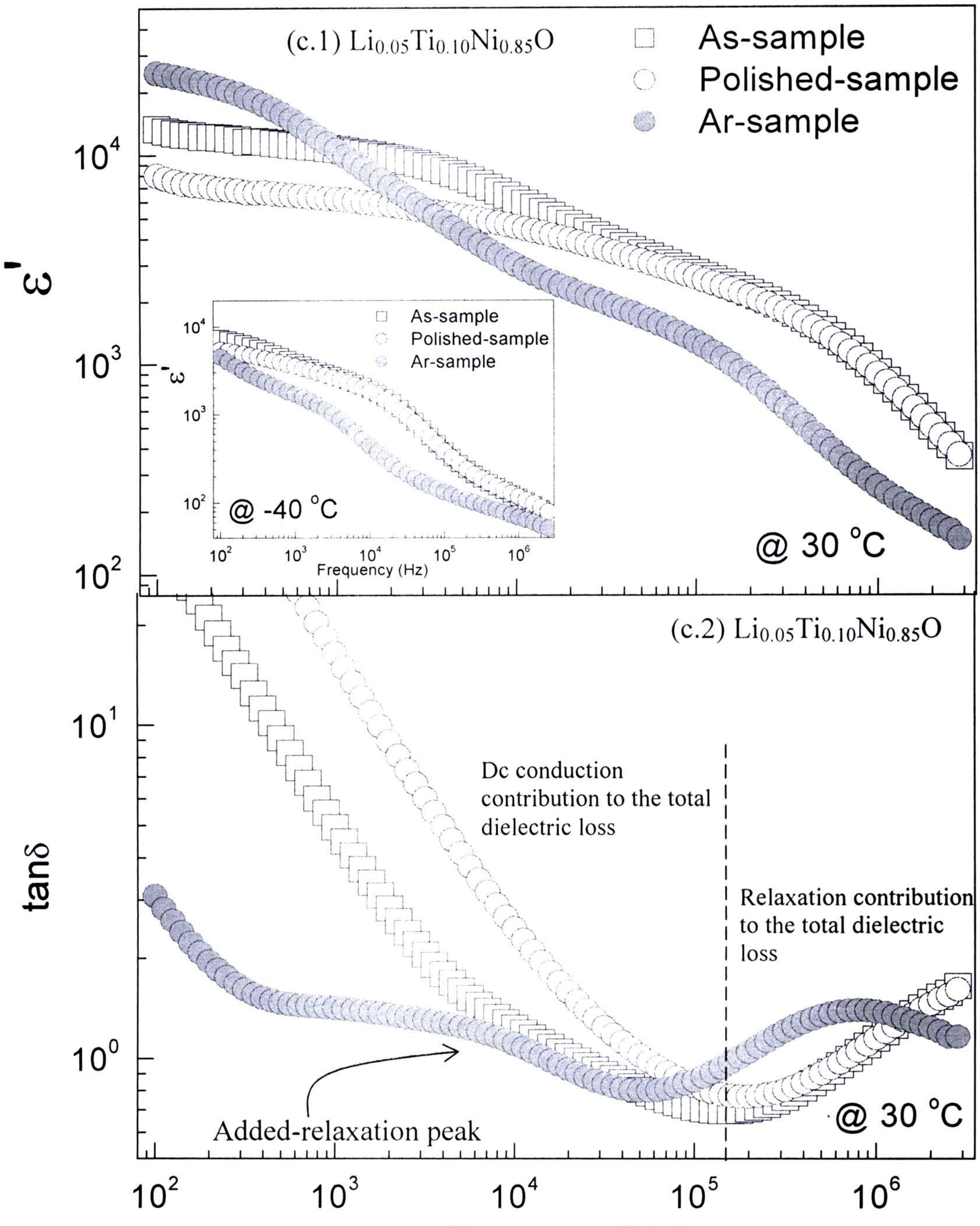

Figure 5.37 Frequency dependence of dielectric properties at 30 °C for as-sample, polished-sample, and Ar-sample of $Li_xTi_yNi_{1-x-y}O$ ceramics sintered at 1280 °C for 4 h; inset shows the frequency dependence of the dielectric constant of these four samples at -40 °C. (Cont.)

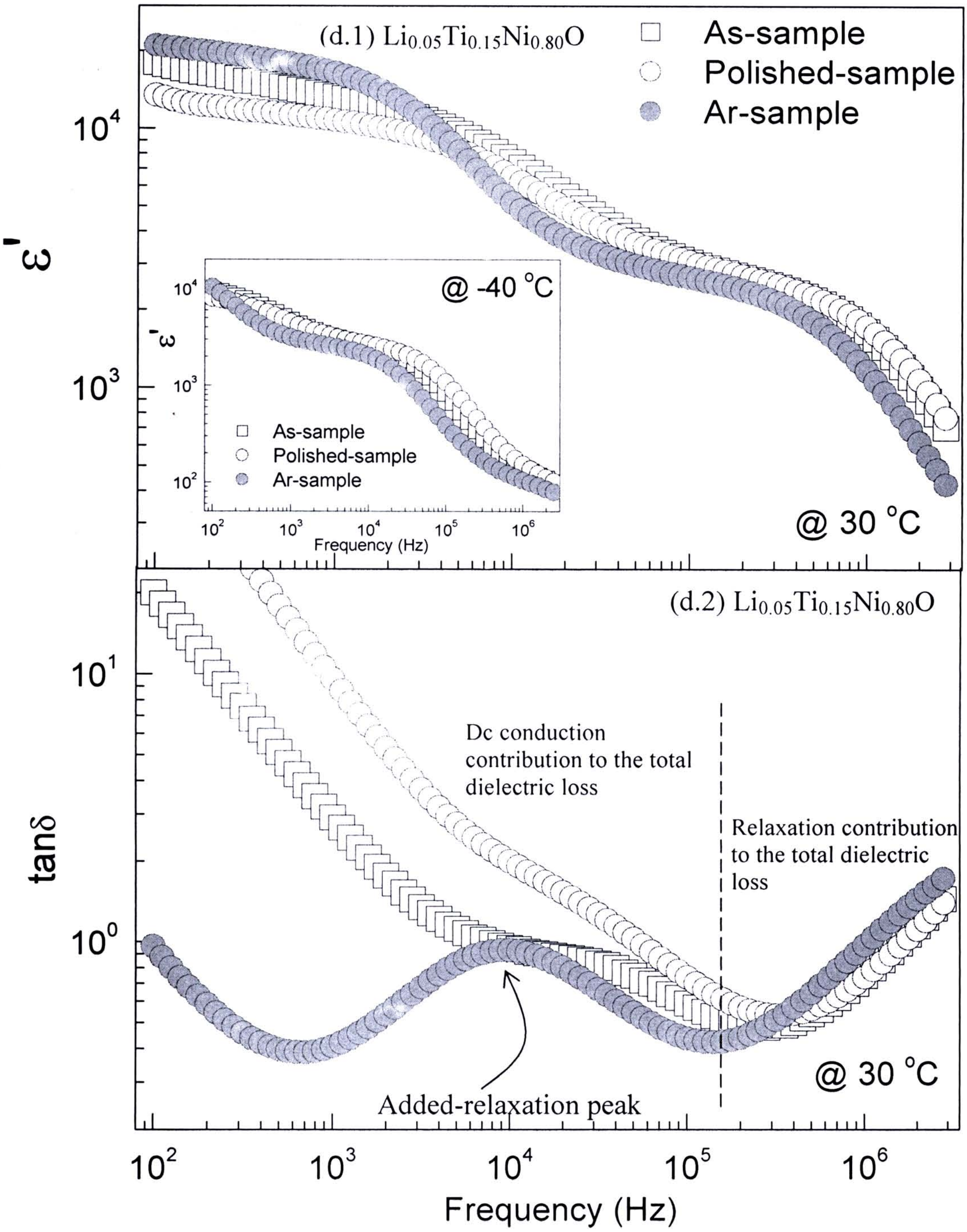

Figure 5.37 Frequency dependence of dielectric properties at 30 °C for as-sample, polished-sample, and Ar-sample of $Li_xTi_yNi_{1-x-y}O$ ceramics sintered at 1280 °C for 4 h; inset shows the frequency dependence of the dielectric constant of these four samples at -40 °C. (Cont.)

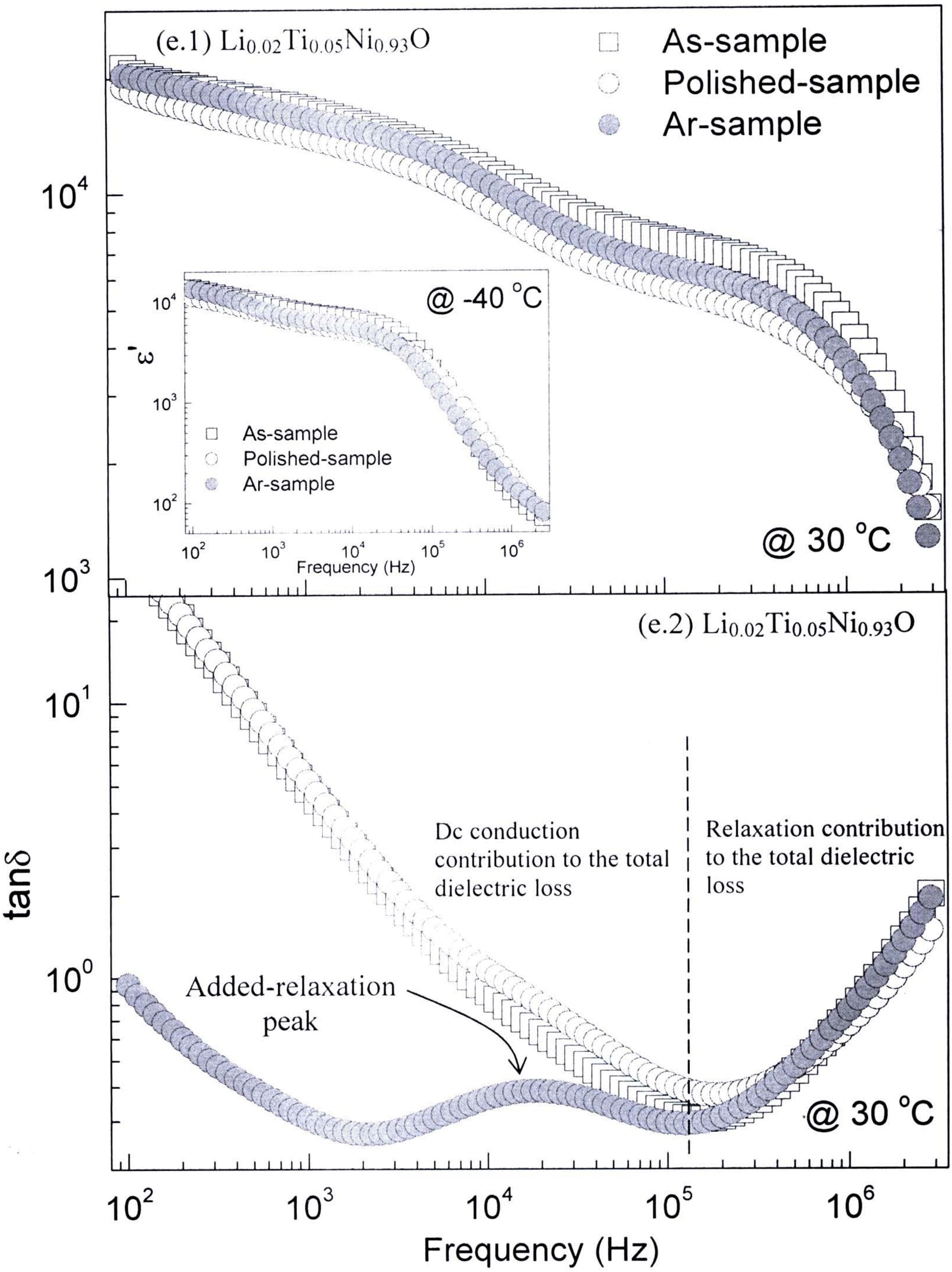

Figure 5.37 Frequency dependence of dielectric properties at 30 °C for as-sample, polished-sample, and Ar-sample of $Li_xTi_yNi_{1-x-y}O$ ceramics sintered at 1280 °C for 4 h; inset shows the frequency dependence of the dielectric constant of these four samples at -40 °C. (Cont.)

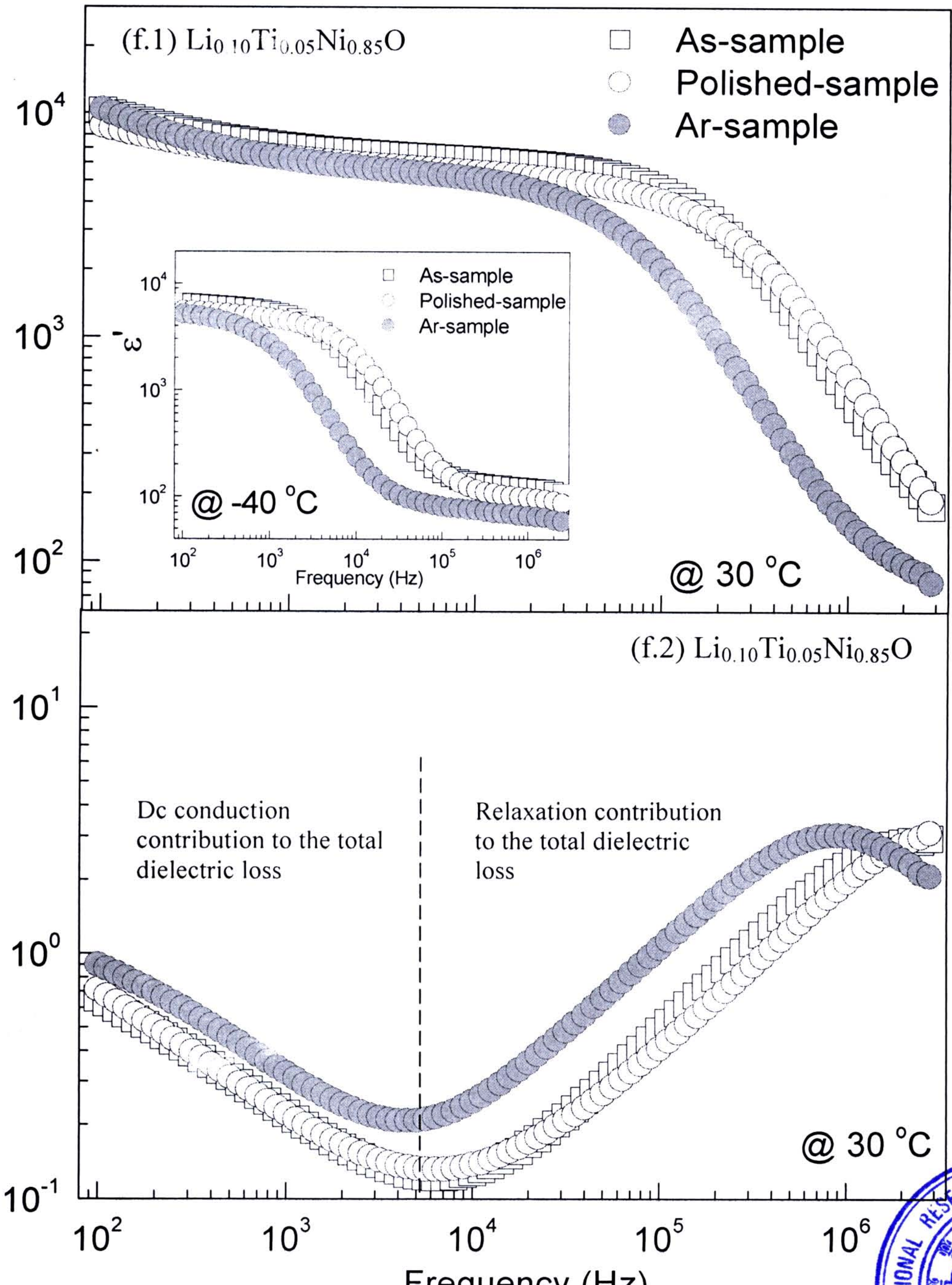

Figure 5.37 Frequency dependence of dielectric properties at 30 °C for as-sample, polished-sample, and Ar-sample of $Li_xTi_yNi_{1-x-y}O$ ceramics sintered at 1280 °C for 4 h; inset shows the frequency dependence of the dielectric constant of these four samples at -40 °C. (Cont.)

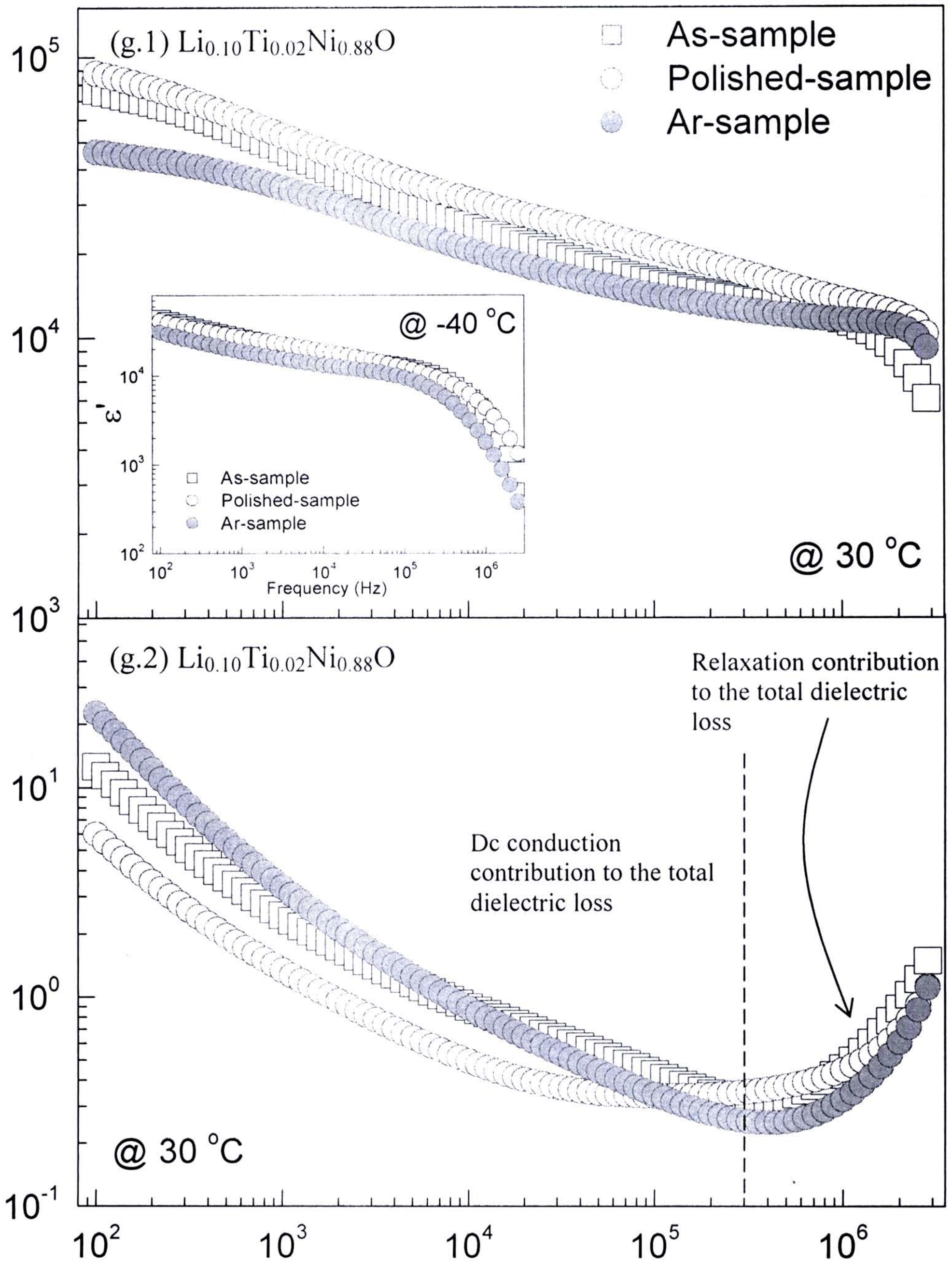

Figure 5.37 Frequency dependence of dielectric properties at 30 °C for as-sample, polished-sample, and Ar-sample of $Li_xTi_yNi_{1-x-y}O$ ceramics sintered at 1280 °C for 4 h; inset shows the frequency dependence of the dielectric constant of these four samples at -40 °C. (Cont.)

5.1.8.2 Impedance spectroscopy of the $Li_xTi_yNi_{1-x-y}O$ ceramics

Figure 5.38 demonstrates the electrical properties of the $Li_xTi_yNi_{1-x-y}O$ ceramics at 30 °C, which are investigated by using the impedance spectroscopy. Certainly, the annealing process has a considerable influence on the electrical properties of the $Li_xTi_yNi_{1-x-y}O$ ceramics. An expanded view of high frequency data close to the origin is showed in the inset of each figures 5.38(a)-5.38(g). It is found that the electrical properties of the pellet interior are affected by the annealing process in Ar atmosphere. The resistance of this inner part increases with the post-annealing in Ar atmosphere. Except for the $Li_{0.10}Ti_{0.02}Ni_{0.88}O$ and $Li_{0.10}Ti_{0.05}Ni_{0.85}O$ ceramics, interestingly, the total resistance of the $Li_xTi_yNi_{1-x-y}O$ ceramics is found to be increased with the post-annealing. This result corresponds to the decrease in the dielectric loss due to the annealing, which indicates that the total resistance of these $Li_xTi_yNi_{1-x-y}O$ ceramics increases with increasing the concentration of oxygen vacancies. It seems to be strange because as well known, the oxygen vacancies are electrically charge carriers. Unlikely, the total resistance of the $CaCu_3Ti_4O_{12}$ ceramics (Sinclair et al., 2002; Adams et al., 2006) and La-doped $BaTiO_3$ ceramics (Morrison et al., 2001) was found to be reduced by annealing in reducing atmosphere of N_2, just like in Ar atmosphere. Thus, the total resistance of the $Li_xTi_yNi_{1-x-y}O$ ceramics—except for the $Li_{0.10}Ti_{0.02}Ni_{0.88}O$ and $Li_{0.10}Ti_{0.05}Ni_{0.85}O$ ceramics—should decrease when the concentration of oxygen vacancies increases. However, only a change in the total resistance on the annealing in reducing atmosphere of $Li_{0.10}Ti_{0.02}Ni_{0.88}O$ and $Li_{0.10}Ti_{0.05}Ni_{0.85}O$ ceramics, the ceramics that contain the highest concentration of Li doping, is found to be similar to those observed in the $CaCu_3Ti_4O_{12}$ and $BaTiO_3$ ceramics. Therefore, the impedance spectroscopy results are as another important clue that can assist to reach the most possible mechanism for the observed giant dielectric properties in NiO-based ceramics.

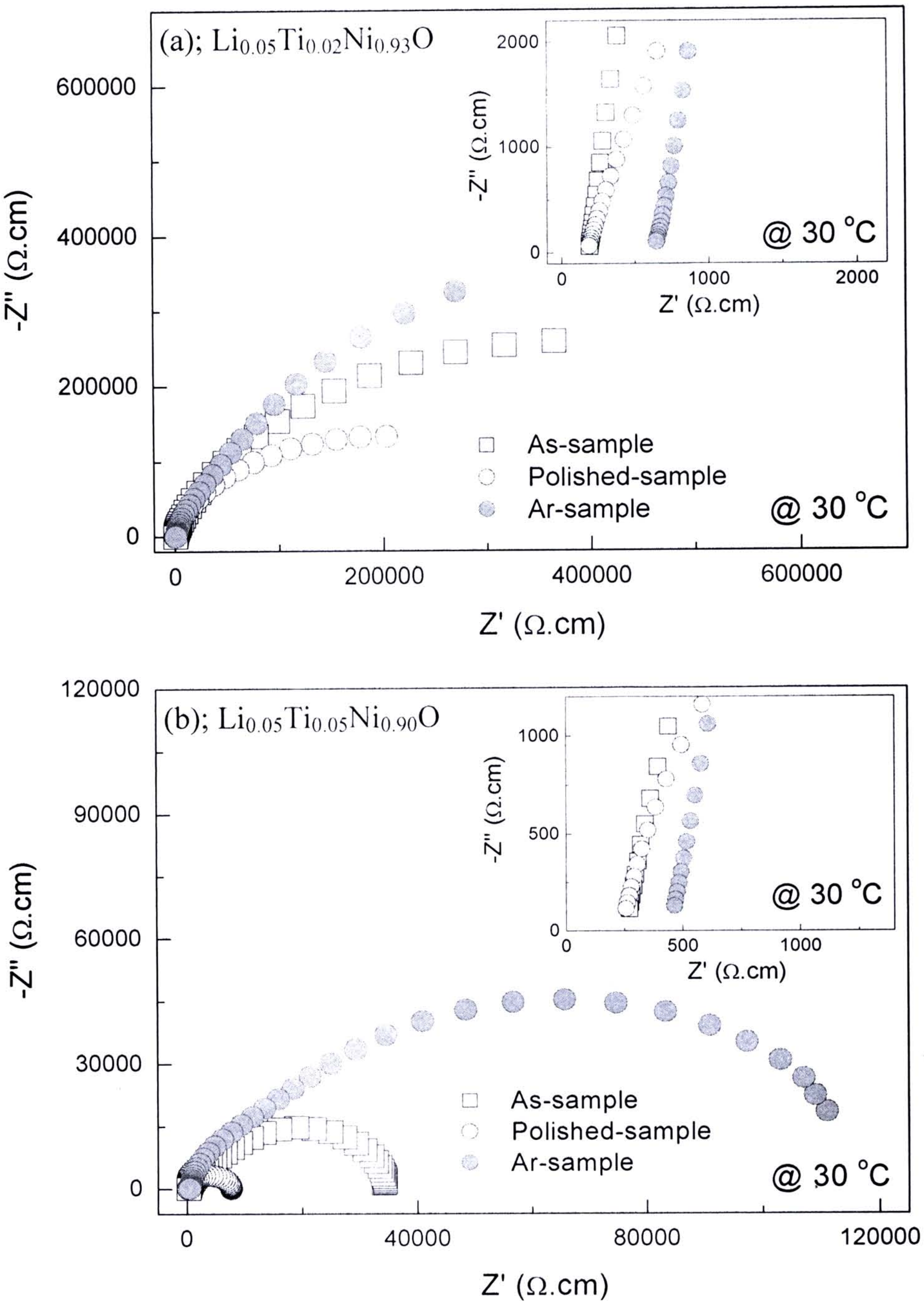

Figure 5.38 Complex impedance plane plot at 30 °C of $Li_xTi_yNi_{1-x-y}O$ ceramics sintered at 1280 °C for as-sample, polished-sample, and Ar-sample; inset is an expanded view of high frequency data close to the origin.

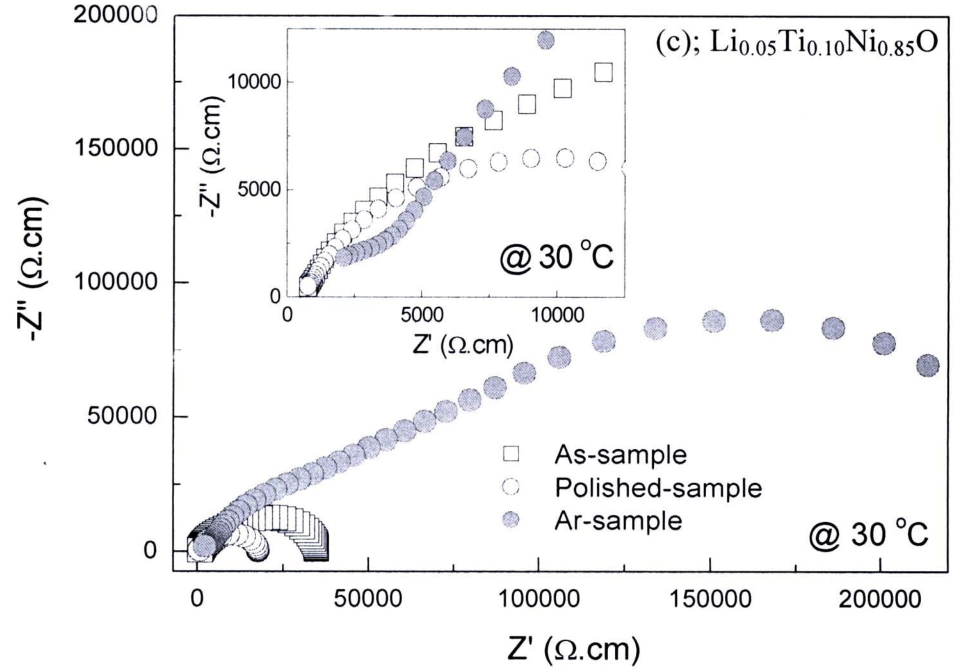

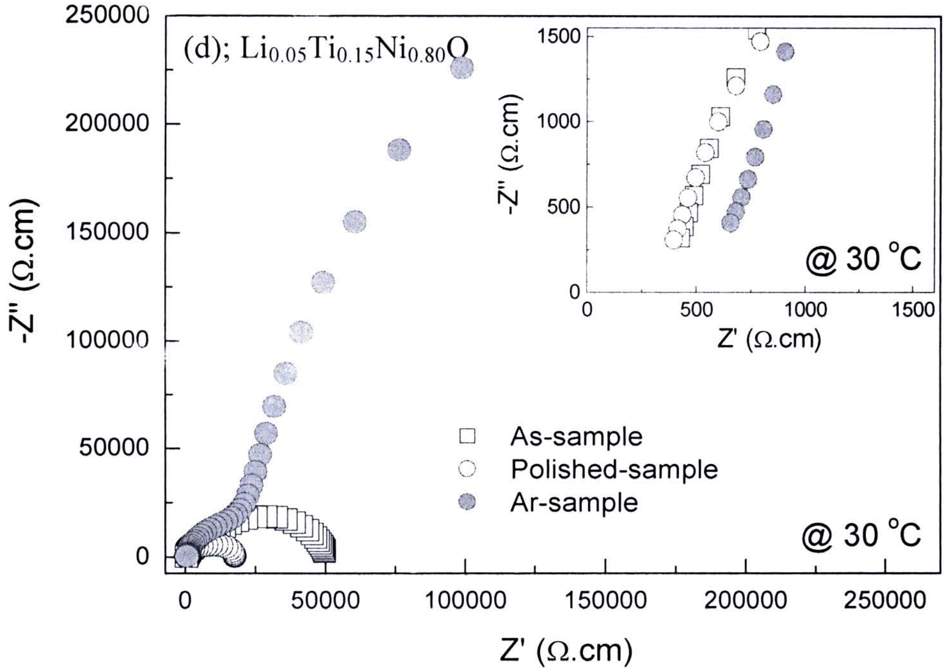

Figure 5.38 Complex impedance plane plot at 30 °C of $Li_xTi_yNi_{1-x-y}O$ ceramics sintered at 1280 °C for as-sample, polished-sample, and Ar-sample; inset is an expanded view of high frequency data close to the origin. (Cont.)

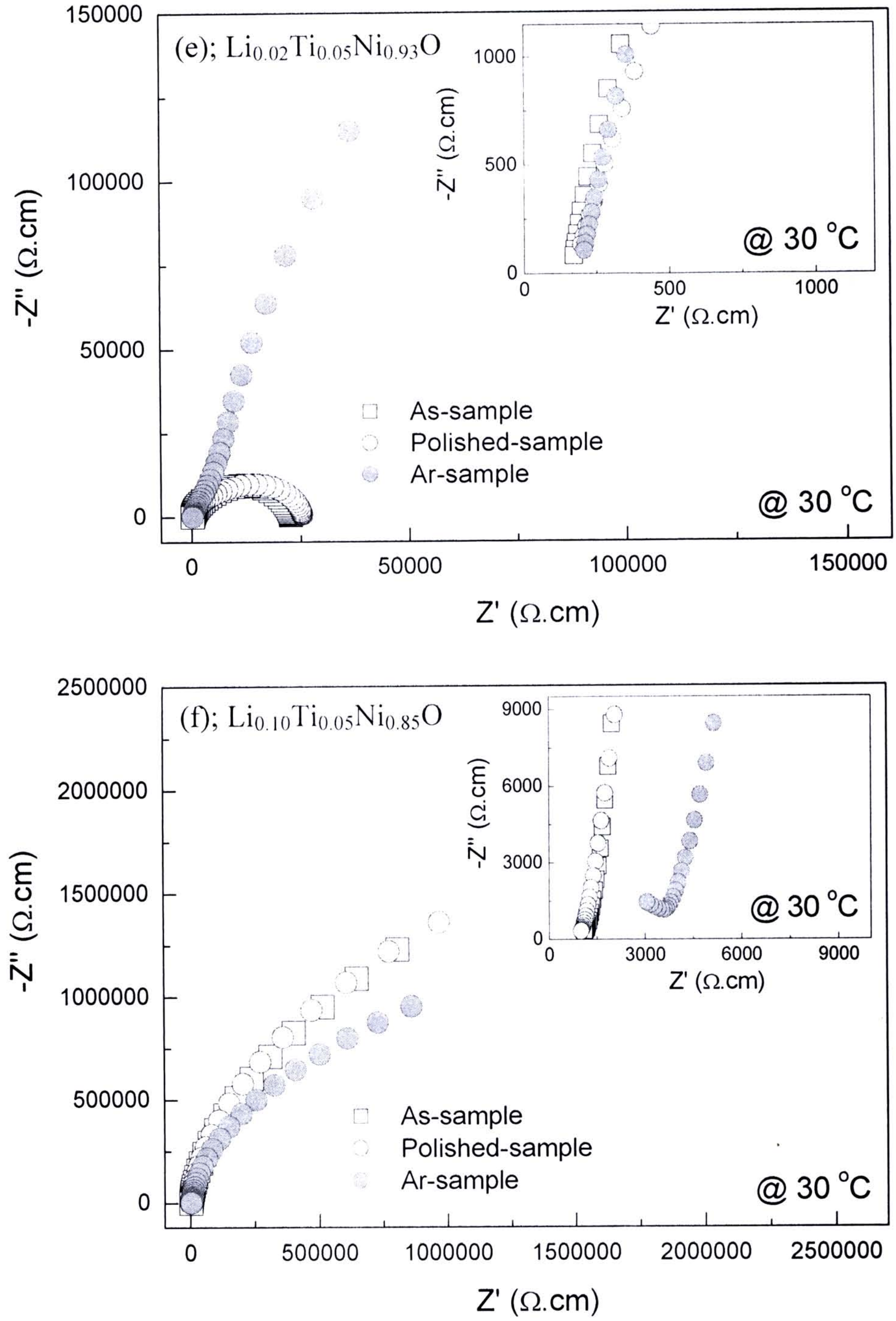

Figure 5.38 Complex impedance plane plot at 30 °C of $Li_xTi_yNi_{1-x-y}O$ ceramics sintered at 1280 °C for as-sample, polished-sample, and Ar-sample; inset is an expanded view of high frequency data close to the origin. (Cont.)

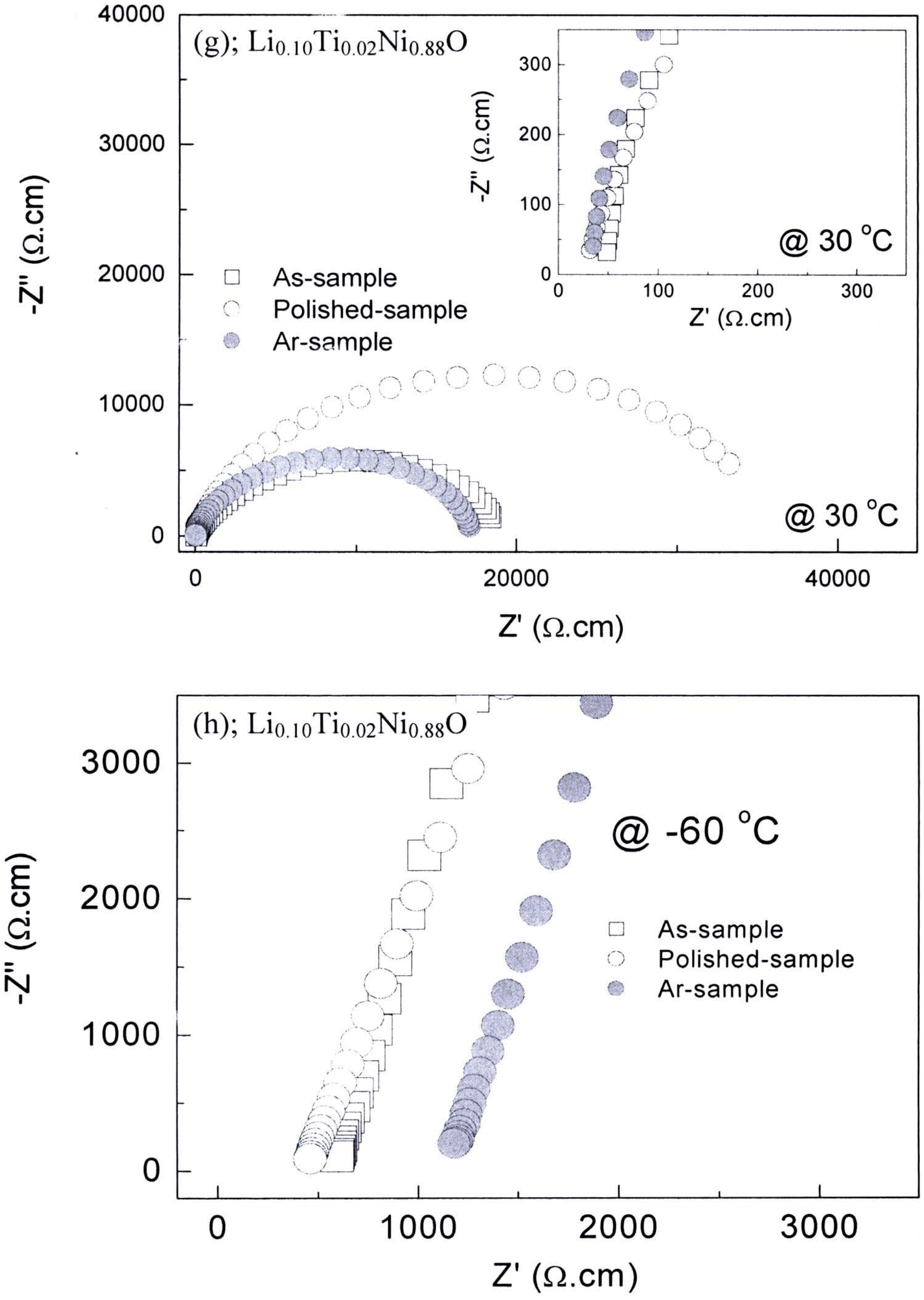

Figure 5.38 Complex impedance plane plot at 30 °C of Li$_x$Ti$_y$Ni$_{1-x-y}$O ceramics sintered at 1280 °C for as-sample, polished-sample, and Ar-sample; inset is an expanded view of high frequency data close to the origin; figure (h) demonstrates complex impedance plane plot at -60 °C for the Li$_{0.10}$Ti$_{0.02}$Ni$_{0.88}$O samples. (Cont.)

5.1.8.3 Dielectric relaxations of $Li_xTi_yNi_{1-x-y}O$ ceramics annealing in argon (Ar)

To understand the physical mechanism of dielectric responses in the Ar-samples and achieve some clues about the annealing effect, the dielectric relaxations are carefully investigated. The thermally activated dielectric relaxation(s) observed in the Ar-samples are revealed in figures 5.39(a)-5.39(f). Note that the dispersion of the HFR observed in these Ar-samples is similar to those observed in $CaCu_3Ti_4O_{12}$ single crystal and ceramics (Homes et al., 2001; Liu et al., 2005; Krohns et al., 2008; Zhang et al., 2005). The most interesting result is the evolution of the LFR, which may be related to the external effects such as the outer surface-layer or electrode. For the Ar-samples of the $Li_{0.05}Ti_yNi_{0.95-y}O$ ceramics (y = 0.05, 0.10, 0.15) and the $Li_{0.02}Ti_{0.05}Ni_{0.93}O$ ceramic, the LFR is more evident compared to those observed in the as-samples, especially for the $Li_{0.05}Ti_{0.15}Ni_{0.80}O$ and $Li_{0.02}Ti_{0.05}Ni_{0.93}O$ ceramics. The sets of LFR-peaks of these two Ar-samples are clearly observed [Figs. 5.38(d.2) and 5.38(e.2)]; whereas, just a small hump can be observed in the loss tangent spectra of the as-samples. Moreover, the LFR-like behavior, the rapid decrease in the dielectric constant, is also introduced in the $Li_{0.05}Ti_{0.02}Ni_{0.93}O$ and $Li_{0.10}Ti_{0.05}Ni_{0.85}O$ ceramics [Figs. 5.38(a.1) and 5.38(f.1)]. This LFR-like behavior has never been observed in the as-samples and polished-samples of these two ceramic compositions. According to the SEM images of these two ceramics both of as-samples [Figs. 5.12(1) and 5.18(c)] and polished-samples [Figs. 5.30(a.2) and 5.31(a.2)], it was revealed that the surface morphologies consist of the smooth grains and grain boundaries. The XRD results also demonstrate that the second phase of $NiTiO_3$ can not be detected in their diffraction patterns. Thus, the observed LFR-like behavior might be attributed to an unknown insulating surface layers, which are related to the presence of oxygen vacancies. The activation energy required for the thermally activated-HFR and -LFR processes calculated from the dielectric loss data (ε'') of the Ar-samples as well as the as-samples and polished-samples are summarized in Table 5.5. The activation energy required for the HFR process of the Ar-samples is significantly higher than those of the as-samples and polished-samples. The activation energy of the HFR process is enhanced by the post-annealing, corresponding to the increase in the concentration of oxygen vacancies. Moreover, activation energy required for the LFR process is found to be enhanced by the post-annealing as well. The activation energies are found to respectively be 0.262 and 0.329 eV for the as-sample and Ar-sample of the $Li_{0.05}Ti_{0.15}Ni_{0.80}O$ ceramic.

According to equation (5.7), $\tau = \tau_0 \exp(E_a / k_B T)$, and the relationship of $f_p = 1/2\pi\tau$, it can be expressed that

$$f_p = f_0 \exp\left(\frac{-E_a}{k_B T}\right), \tag{5.19}$$

where f_p is the frequency at the maxima value of the HFR-peak. Accordingly, the increase in the activation energy can cause a change in the characteristic-f_p. At a fixed temperature, the characteristic-f_p decreases with increasing the activation energy (E_a). This relationship corresponds to the experimental results, as shown in figure 5.40. f_p of the Ar-samples is much lower than those of the as-samples. This means that the average relaxation time of dipoles at any temperature of the system increases with the post-annealing process. At this f_p, it was proved that the peak-height of the loss tangent should be

$$\tan\delta = \frac{\varepsilon'_s - \varepsilon'_\infty}{2\sqrt{\varepsilon'_s \varepsilon'_\infty}}. \tag{5.20}$$

Therefore, the difference in the peak-height is suggested to the different dielectric strengths, $\Delta\varepsilon' = \varepsilon'_s - \varepsilon'_\infty$, between the as-sample and Ar-sample.

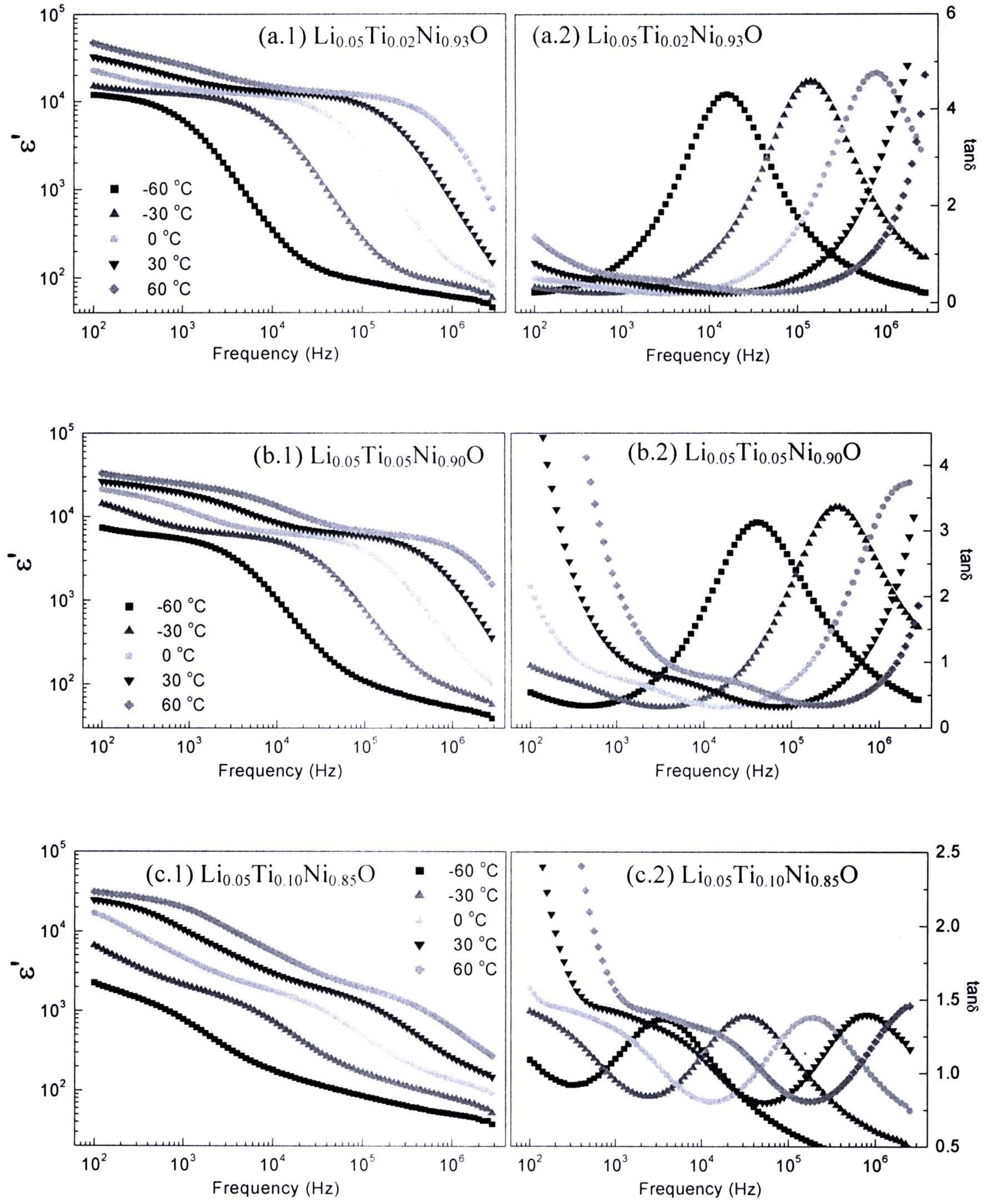

Figure 5.39 Frequency dependence of dielectric properties at various temperatures for Ar-samples of $Li_xTi_yNi_{1-x-y}O$ ceramics sintered at 1280 °C for 4 h.

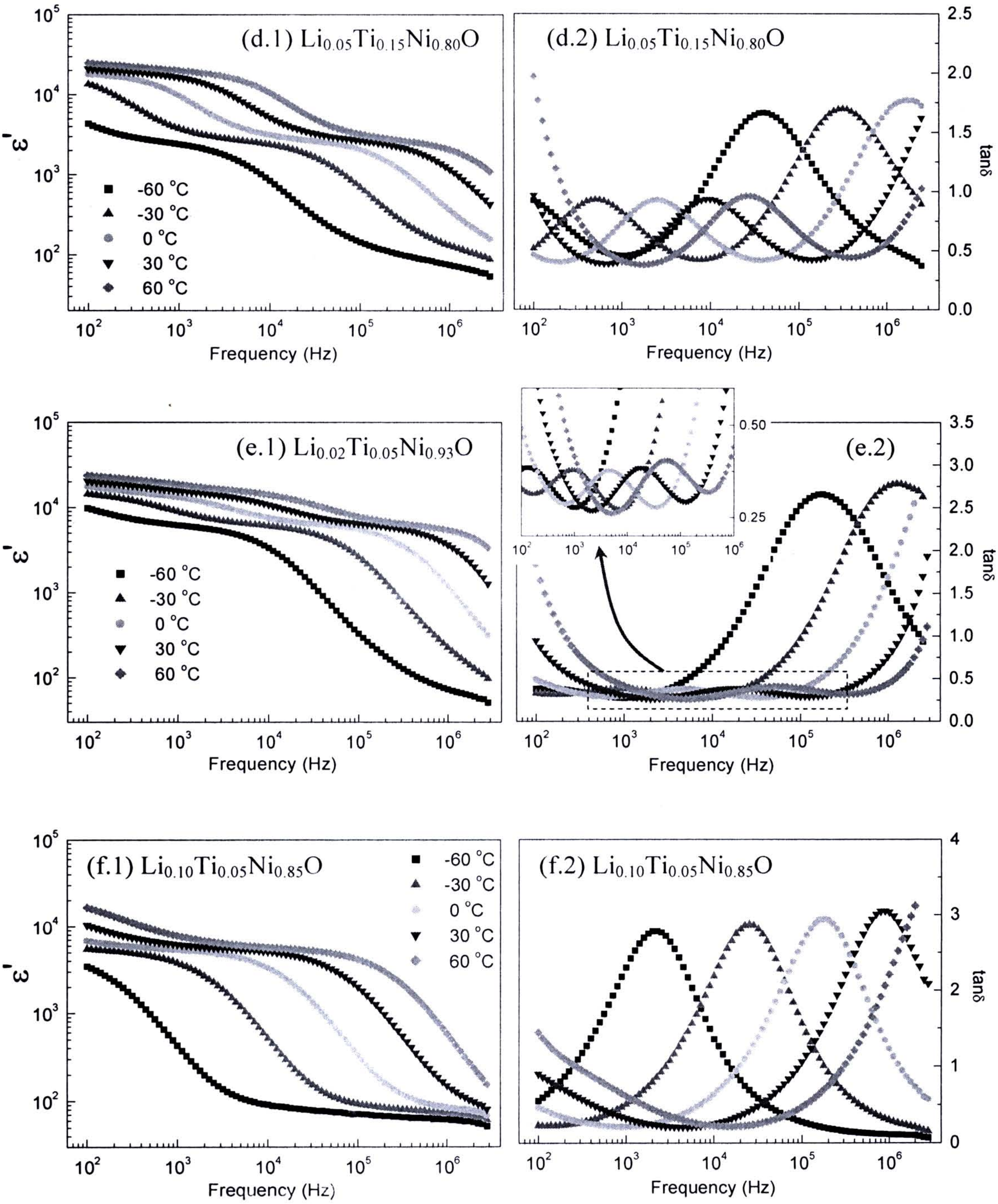

Figure 5.39 Frequency dependence of dielectric properties at various temperatures for Ar-samples of $Li_xTi_yNi_{1-x-y}O$ ceramics sintered at 1280 °C for 4 h; inset of (e.2) shows the enlarged part of the dashed rectangle area. (Cont.)

Table 5.5 Activation energy required for HFR process (E_a) of as-, polished-, air-, and Ar-samples of $Li_xTi_yNi_{1-x-y}O$ ceramics sintered at 1280 °C.

Sample	**Activation energy (eV)**		
	as-sample	**polished-sample**	**Ar-sample**
$Li_{0.05}Ti_{0.02}Ni_{0.93}O$	0.285	0.299	0.333
$Li_{0.05}Ti_{0.05}Ni_{0.90}O$	0.291	0.298	0.320
$Li_{0.05}Ti_{0.10}Ni_{0.85}O$	-	-	-
$Li_{0.05}Ti_{0.15}Ni_{0.80}O$	0.287	0.268	0.317 [0.329]
$Li_{0.02}Ti_{0.05}Ni_{0.93}O$	0.282	0.267	0.300 [0.347]
$Li_{0.10}Ti_{0.05}Ni_{0.85}O$	0.332	0.315	0.374

Note: [0.329] and [0.347] are the LFR activation energies of the Ar-samples of the $Li_{0.05}Ti_{0.15}Ni_{0.80}O$ and $Li_{0.02}Ti_{0.05}Ni_{0.93}O$ ceramics, respectively.

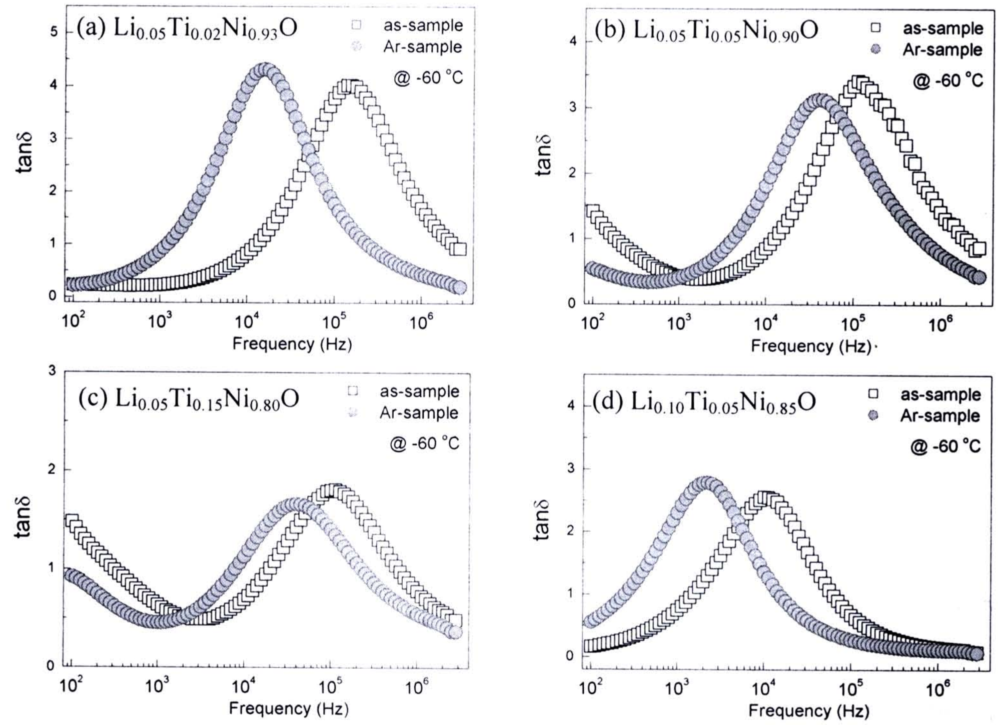

Figure 5.40 Frequency dependence of dielectric properties at -60 °C for Ar-samples of $Li_xTi_yNi_{1-x-y}O$ ceramics sintered at 1280 °C for 4 h.

5.1.9 Possible origin(s) of the observed giant dielectric response in Li and Ti co-doped NiO ceramics

Up to now, it is widely accepted that the giant dielectric properties observed in all of giant-dielectric NiO-based materials are suggested to be the internal barrier layer capacitance (IBLC) effect based on the presence of the Maxwell-Wagner polarization grain boundaries (Wu J et al., 2002; Lin et al., 2005a; Chen K et al., 2007; Hsiao et al., 2007; Chen GJ et al., 2009; Manna et al., 2008; Dakhel, 2009; Manna, De, 20010). This polarization is related to the inhomogeneous microstructure consisting of semiconducting grains and insulating grain boundaries. Under an applied electric field, the accumulation of charge carriers at the insulating boundaries can produce the interfacial polarization, which is referred to as the Maxwell-Wagner polarization. As proved in Chapter II, both of the Maxwell-Wagner polarization and hopping polarization can exhibit the dielectric relaxation. First of all, it must be recognized that one source of either these two polarizations can introduce one set of the dielectric properties spectra, as shown in figure 2.7. The dielectric constant (ε') spectrum consists of two plateaus—low- (a high-dielectric constant range) and high-frequency (a low-dielectric constant range) ranges—and one step-like rapid decrease. A relaxation peak is exhibited in the loss tangent ($\tan\delta$) and the dielectric loss (ε'') spectra. According to all previous reports in literatures, it is important to impress that two thermally activated relaxations (LFR and HFR) exhibited in some ceramic composition of $Li_xTi_yNi_{1-x-y}O$ can be observed in the experimental data of this research, which are the first observation. This observation may give a new important clue to elucidate the origin of the giant dielectric response in these ceramics. Interestingly, the added second relaxation at the low-frequency range can be tuned by surface polishing and the post-annealing in Ar atmosphere. However, the LFR can not be observed in some ceramic compositions. Therefore, for comparison, the term of "*giant dielectric constant*" is referred to only the HFR process.

To reach to most possible mechanism that may be responsible for the abnormally giant dielectric properties, the microstructure and phase formation analyses as well as the investigation of chemical compositions are used to ascribe together with the dielectric and electrical properties. The origin of the giant dielectric response in the (Li, Ti)-doped NiO ceramics is briefly discussed as follows.

5.1.9.1 Microstructure and phase composition analyses

According to the microstructure and phase formation analyses, as represented in section 5.1.2, it can be suggested that the Li doping ions prefer to form the solid solution with the host of NiO. In contrast, the Ti doping ions prefer to form a second phase of $NiTiO_3$. The solubility of Li ions in NiO seems to be higher than that of the Ti ions. However, the solubility of Ti ions in the NiO matrix can be enhanced by increasing the concentration of Li doping, which is used to co-dope together with the Ti doping. The microstructure characteristics and phase compositions of all $Li_xTi_yNi_{1-x-y}O$ ceramics are tabulated in Table 5.6.

Table 5.6 Microstructure characteristics and phase compositions of $Li_xTi_yNi_{1-x-y}O$ ceramics sintered at 1280 °C.

x, y	Microstructure characteristics and phase compositions					
	grain	Grain boundary	$NiTiO_3$	Expected-solubility of Li	Expected-solubility of Ti	Grain size (μm)
0.05, 0.02	Quite smooth	Slightly accumulated of $NiTiO_3$	Did not detect	~ 5 mol %	< 2 mol %	~9.7
0.05, 0.05	Covered with small grains	Accumulated of $NiTiO_3$	Detected	~ 5 mol %	~ 2 mol %	~9.9
0.05, 0.10	Covered with small grains	Accumulated of $NiTiO_3$	Detected	~ 5 mol %	~ 2 mol %	~10.5
0.05, 0.15	Covered with small grains	Highly accumulated of $NiTiO_3$	Detected	~ 5 mol %	~ 2 mol %	~10.7
0.02, 0.05	Quite smooth	Largely accumulated with $NiTiO_3$	Detected	~ 2 mol %	≤ 2 mol %	~9.0
0.10, 0.05	Very smooth	Clean and clear	Did not detect	~ 10 mol %	~ 5 mol %	~6.9
0.10, 0.02	Very smooth	Clean and clear	Did not detect	~ 10 mol %	~ 2 mol %	~5.9

According to Table 5.6, the concentrations of Li and Ti doping have remarkable influences on the microstructure and phase formation of the $Li_xTi_yNi_{1-x-y}O$ ceramics. The Li and Ti doping ions of the $Li_{0.10}Ti_{0.05}Ni_{0.85}O$ and $Li_{0.10}Ti_{0.02}Ni_{0.88}O$ ceramics can completely be dissolved into the NiO matrix, forming solid solutions. It can also be deduced that the Li doping of all ceramics can totally be dissolved into the NiO matrix without the evaporation of Li ions during the sintering process. Although, the second phase of $NiTiO_3$ can not be detected in the XRD pattern of the $Li_{0.05}Ti_{0.02}Ni_{0.93}O$ ceramic, a few parts of this phase are found along the grain boundaries, as revealed in the SEM-EDS results (Fig. 5.13). Thus, it can be deduced that all concentrations of Ti doping ions in the starting mixtures of $Li_{0.05}Ti_yNi_{0.95-y}O$ (y = 0.02, 0.05, 0.10, and 0.15) ceramics can dissolve into the NiO matrix with nearly the same in concentration, i.e., the solubility of the Ti doping ions (Li doping = 5 mol %) is roughly estimated to be about 2 mol %.

The radius of Ni^{2+} ions (~0.69 Å) is nearly equivalent to those of Li^+ (~0.76 Å) and Ti^{4+} (~0.605 Å) (Shannon, 2005b), and there are small crystallographic distortions when Ni^{2+} sites are replaced with Li^+ and Ti^{4+}. Some electrically defects can therefore be introduced due to the different valences of the doped ions. The formation of the defects can usually be ascribed by the Kröger-Vink notation, i.e.,

$$Li_2O \xrightarrow{NiO} 2Li'_{Ni} + V_O^{\bullet\bullet} + O_O^x, \tag{5.21}$$

$$TiO_2 \xrightarrow{NiO} Ti_{Ni}^{\bullet\bullet} + V''_{Ni} + 2O_O^x. \tag{5.22}$$

Equations (5.21) and (5.33) mean that two Li^+ ions can promote one oxygen vacancy, and one Ti ion can promote one titanium vacancy in the NiO crystal structure. The 2-dimensional crystal structures of the NiO, Li-doped NiO, and Ti-doped are respectively demonstrated in figures 5.41(a)-5.41(c). The ideally NiO crystal structure demonstrated illustrated in figure 5.41(a) consist of 10 ions of Ni^{2+} and 10 ions of O^{2-} ions, the total charge is neutral. Therefore, when Ni^{2+} ions are replaced by two Li^+ (Fig. 5.41(b)) and one Ti^{4+} (Fig. 5.41(c)) ions, one oxygen vacancy and two titanium vacancies are compensated to maintain the electroneutrality. As results, the total positive and negative charges are still equal to +20 and -20, respectively.

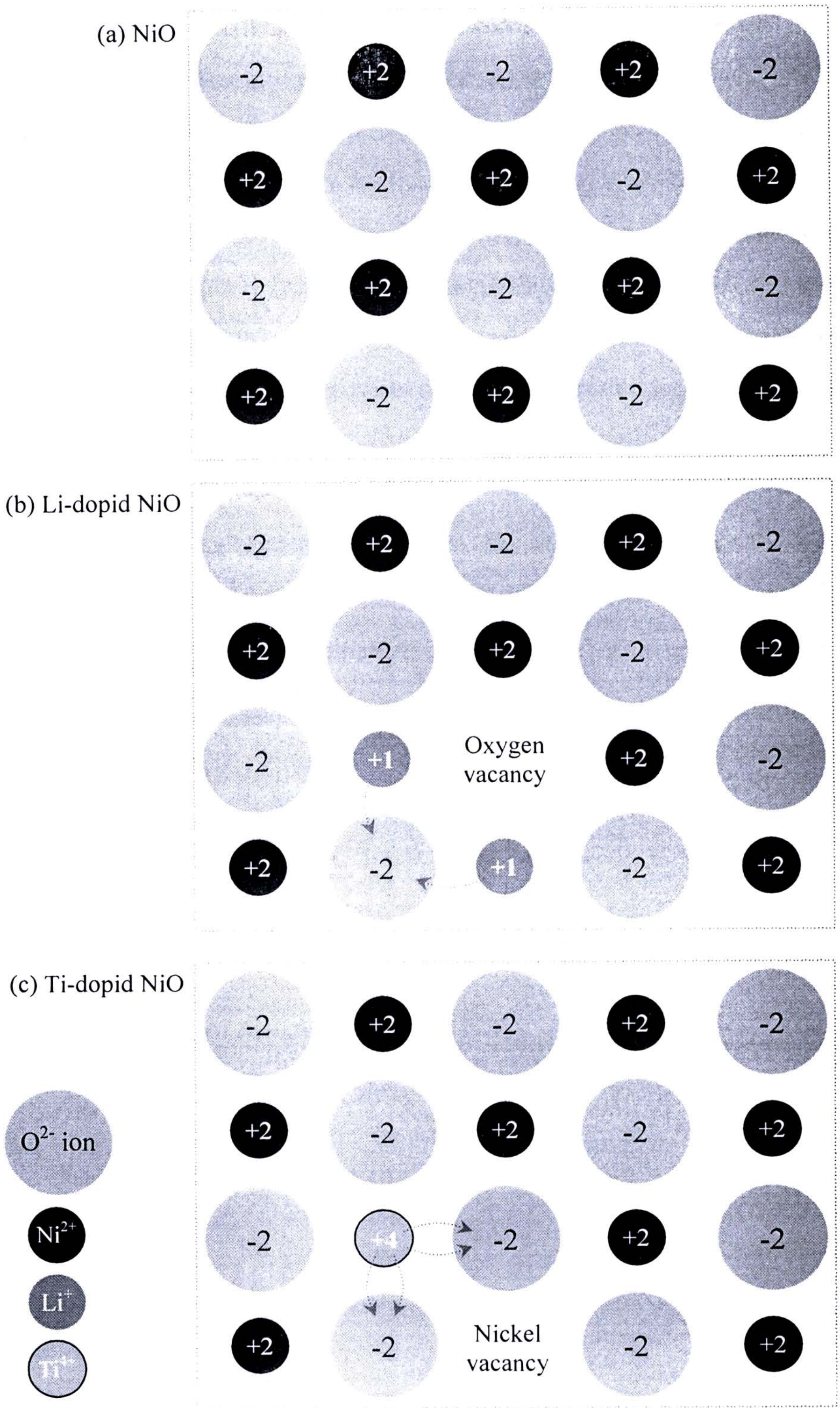

Figure 5.41 Schematics of (a) NiO, (b) Li-doped NiO, and (c) Ti-doped NiO, showing the formation of defect.

5.1.9.2 Internal barrier layer capacitance (IBLC) effect

According to the previous works reported in the several literatures, the giant dielectric response of all NiO-based ceramics was suggested to associate with the internal barrier layer capacitance (IBLC) effect based on the Maxwell-Wagner polarization of grain boundaries (Wu J et al., 2002; Lin et al., 2005a; Chen K et al., 2007; Hsiao et al., 2007; Chen GJ et al., 2009; Manna et al., 2008; Dakhel, 2009; Manna, De, 20010). The Li doping can cause a change in the electrical property of grains; whereas, the Ti doping (or other aliovalent dopants) is associated to .the grain boundary properties. The inhomogeneous microstructure resulting to the introduction of the electrically microstructure in the (Li, Ti)-doped NiO ceramics was proposed (Wu J et al., 2002). In general, the dielectric constant of NiO ceramics is about 30 at room temperature (Lin et al., 2005a). The NiO ceramic is classified as an insulating ceramic material with dc conductivity less than 10^{-13} S/cm (Terakura et al., 1984; Mckay, Henrich, 1984). However, it can be enhanced by 15 orders of magnitude through doping of monovalent ions such as Li^+ (Shin, Murayama, 2000; Biju, Khadar, 2001); as a result, the insulating property of the bulk NiO ceramic can be changed to the semiconducting property. It was shown that the Ti doping is more accumulated along grain boundaries of $Li_xTi_yNi_{1-x-y}O$ ceramics, forming a second phase of $NiTiO_3$ (Lin et al., 2006a). By using impedance spectroscopy, it was suggested that this second phase may act as insulating boundaries. Consequently, the microstructure of the $Li_xTi_yNi_{1-x-y}O$ ceramics can suitably be proposed as the brick-well like structure, as demonstrated in figure 5.42(a). With applying an electric field, the polarization can be generated at the insulating grain boundaries, producing the Maxwell-Wagner polarization. Charge carriers in the semiconducting grains of Li-doped NiO particles are restricted at the insulating grain boundary regions. This is the complete model of IBLC, which has been used to describe the observed giant dielectric response in the NiO-based ceramics.

According to the experimental results in this thesis, the second phase of $NiTiO_3$ is found to highly accumulate at the grain boundaries of some ceramic compositions such as $Li_{0.05}Ti_{0.15}Ni_{0.80}O$ and $Li_{0.02}Ti_{0.05}Ni_{0.93}O$. However, this accumulation can not be observed in some ceramic compositions, e.g., $Li_{0.05}Ti_{0.15}Ni_{0.80}O$ and $Li_{0.02}Ti_{0.05}Ni_{0.93}O$. It is interesting that the giant dielectric constant can also be exhibited in these ceramics with no second phase of $NiTiO_3$. In this case, it is possible that the insulating property of grain boundaries might be due to the Ti doping effect (such as related-defects) that does not relate to the $NiTiO_3$ phase. Moreover, it is also possible that this giant dielectric response does not relate to the Maxwell-Wagner polarization, but might be due to a small polaron hopping on the dopant levels (Wu P et al., 2009). The complex impedance (Z^*) of the equivalent circuit (Fig. 5.42(b)) corresponding to the microstructure model (Fig. 5.42(a)) can be determined, as demonstrated in section 5.1.6 for equations (5.12)-(5.15). Note that the electrode effect, which might be induced by formation of Schottky contact, in this model is negligible. The impedance spectra of the $Li_{0.05}Ti_{0.02}Ni_{0.93}O$ ceramic can be well fitted by the impedance calculated by the IBLC model, as shown in figure 5.28. To strongly confirm the fitted result, the impedance data of the $Li_{0.10}Ti_{0.05}Ni_{0.85}O$ ceramic—the ceramic that its grains and grain boundaries are clearly smooth—are used to be fitted by complex impedance calculated from the microstructure model (Eq. (5.15)). As shown in figure 5.43, the experimental data are well fitted by the model. This fitted results imply that the $Li_{0.10}Ti_{0.05}Ni_{0.85}O$ ceramic might be electrically heterogeneous that consists of semiconducting grains and insulating grain boundaries, as modeled in figure 5.42. If this assumption is true, the insulating property of the grain boundaries should be related to the defects that are produced by the Ti doping. Moreover, the Ti ions sitting on the Ni^{2+} sites should be located at the outer surface of the grains.

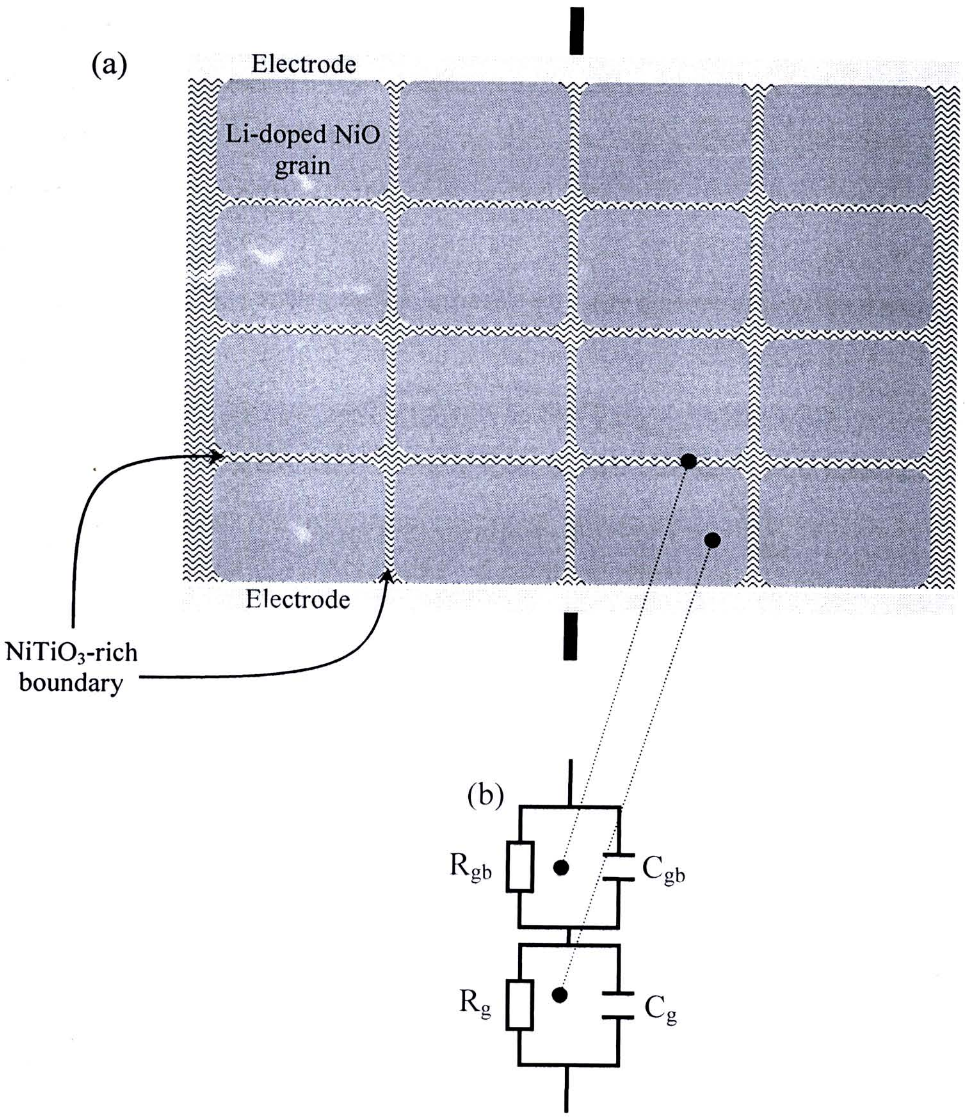

Figure 5.42 (a) Idealized ceramic microstructure of the brick-wall model or IBLC structure model, and (b) Equivalent circuit corresponding to the microstructure model.

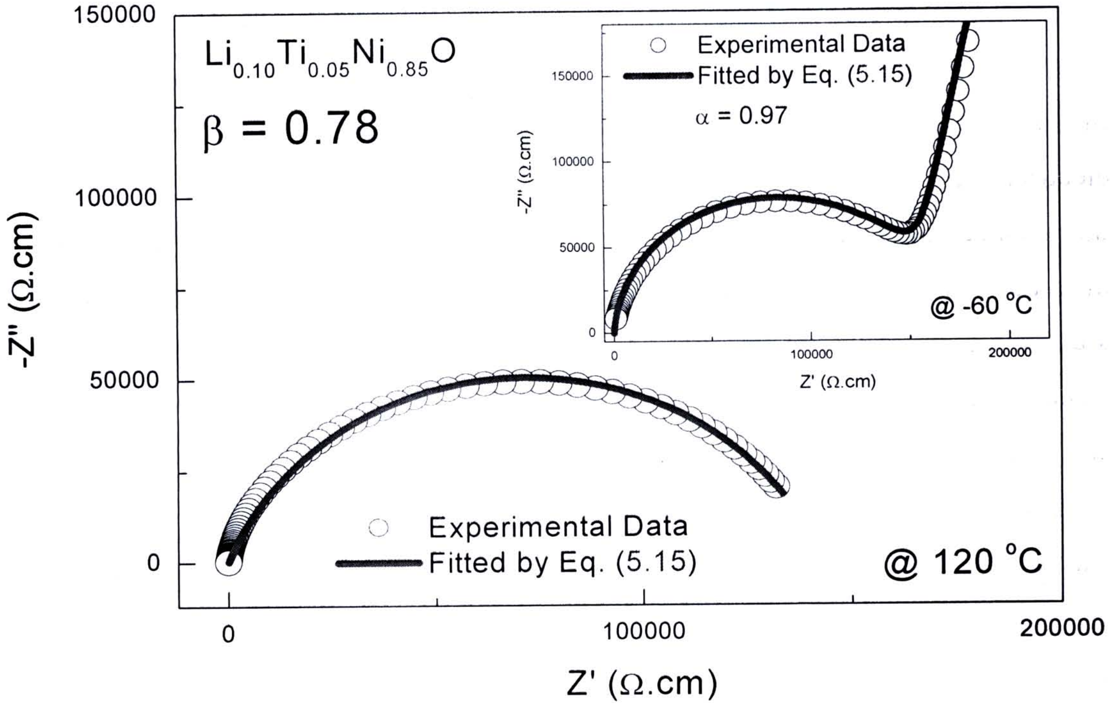

Figure 5.43 Impedance spectrum at 120 °C for the $Li_{0.10}Ti_{0.05}Ni_{0.85}O$ ceramic (polished-sample) sintered at 1280 °C fitted by equation (5.15); inset shows the fitted result at -60 °C.

5.1.9.3 Surface barrier layer capacitance (SBLC) effect

According to section 5.1.7, it is found that the surface layers of the $Li_{0.05}Ti_yNi_{0.95-y}O$ ceramics have considerable influences on the dielectric and electrical properties. By using the impedance spectroscopy, the insulating character of the surface layers can be suggested. The interfacial polarization can therefore be introduced at the interface between the surface and the inner part, contributing to the total polarization of the ceramics. This polarization may be related to the LFR process observed in the dielectric spectra, as demonstrated in figures 5.29(b)-5.29(b). To describe and confirm the existence of the insulating surface-layers contributed to both of the dielectric properties and electrical response, microstructure model as well as the related equivalent circuit is represented, as shown in figure 5.44. The complex impedance (Z^*) of the equivalent circuit presented in figure 5.44(b) can be expressed as

$$Z^* = \frac{1}{R_g^{-1} + j\omega C_g} + \frac{1}{R_{gb}^{-1} + j\omega C_{gb}} + \frac{1}{R_s^{-1} + j\omega C_s}, \tag{5.23}$$

where C_s and R_s are represented as the capacitance and resistance of surface layer. Usually, $-Z''$ vs. Z' plot is better ascribed by using the Cole-Cole equation, as

$$Z^* = \frac{1}{R_g^{-1} + (j\omega C_g)^{\alpha}} + \frac{1}{R_{gb}^{-1} + (j\omega C_{gb})^{\beta}} + \frac{1}{R_s^{-1} + (j\omega C_s)^{\gamma}}, \tag{5.24}$$

where α, β, and γ are constant values and $0 < \alpha, \beta, \gamma \leq 1$. As clearly seen in figure 5.45, the experimental results of the as-samples for the $Li_{0.05}Ti_{0.05}Ni_{0.90}O$ and $Li_{0.05}Ti_{0.15}Ni_{0.80}O$ ceramics can be well fitted by equation (5.24). The insets show expanded views of high frequency data close to the origin. The model can also be used to predict the high-frequency data that are over the limitation of the measuring frequency range. The various values obtained from the fitted results are summarized in Table 5.7. According to the fitted results, it is observed that both of the resistance and capacitance of the expected surface-layer are larger than those of the part that is expected to be the grain boundary effect. Based on this model, the fitted results indicate that besides the internal barrier layer capacitor (IBLC) effect, the surface barrier layer capacitor (SBLC) effect can also contribute to the total dielectric response in the $Li_xTi_yNi_{1-x-y}O$ ceramics. The contribution of SBLC to the total dielectric response can also be observed in the giant-dielectric $CaCu_3Ti_4O_{12}$ ceramics (Krohns et al., 2007, 2008; Lunkenheimer et al., 2002, 2004). However, the source of the SBLC effect between the $Li_xTi_yNi_{1-x-y}O$ and $CaCu_3Ti_4O_{12}$ ceramics is different.

Although the IBLC/SBLC model, as proposed in figure 5.44, can be used to ascribed the experimental results of the as-samples very well, it is necessary to test this model with the experimental results of the polished-samples. To verify the model, the value of R_s must be zero, and the other parameters should be remained to the same values as the fitting of the as-samples. For the fitting of equation (5.24) to the impedance spectra of the polished-samples, except for the values of R_s that are assigned to be zero, all of the values in Table 5.7 are remained. The fitted results are demonstrated in figures 5.46(a) and 5.46(b). It is surprise that the R_{gb} values obtained from the fitted results are less than the total resistance of the polished-samples, which is expected to be the resistance of grain boundary. This discrepancy is more evident in the fitted result of the $Li_{0.05}Ti_{0.15}Ni_{0.80}O$ ceramic, as illustrated in figure 5.46(b). The resistance values obtained from the fitting and the experimental data are about 8,130 and 17,500 Ω.cm, respectively. Looking carefully at the impedance spectrum of the $Li_{0.05}Ti_{0.15}Ni_{0.80}O$ ceramic (Fig. 5.46(b)), it seems that the spectrum may contain two semicircle arcs. Turning to see the surface-layer effect on the dielectric properties of the $Li_{0.05}Ti_{0.05}Ni_{0.90}O$ and $Li_{0.05}Ti_{0.15}Ni_{0.80}O$ ceramics (Figs. 5.29(a) and 5.29(d)), the LFR of the first one can be erased completely, but it remains for the another one when the surfaces of both were polished. These results correspond to the results fitted by the equation (5.25) for the IBLC/SBLC model. Certainly, it can be suggested that there are at least two sources of polarization that are related to the LFR process. Another source of polarization will be briefly discussed in the next section.

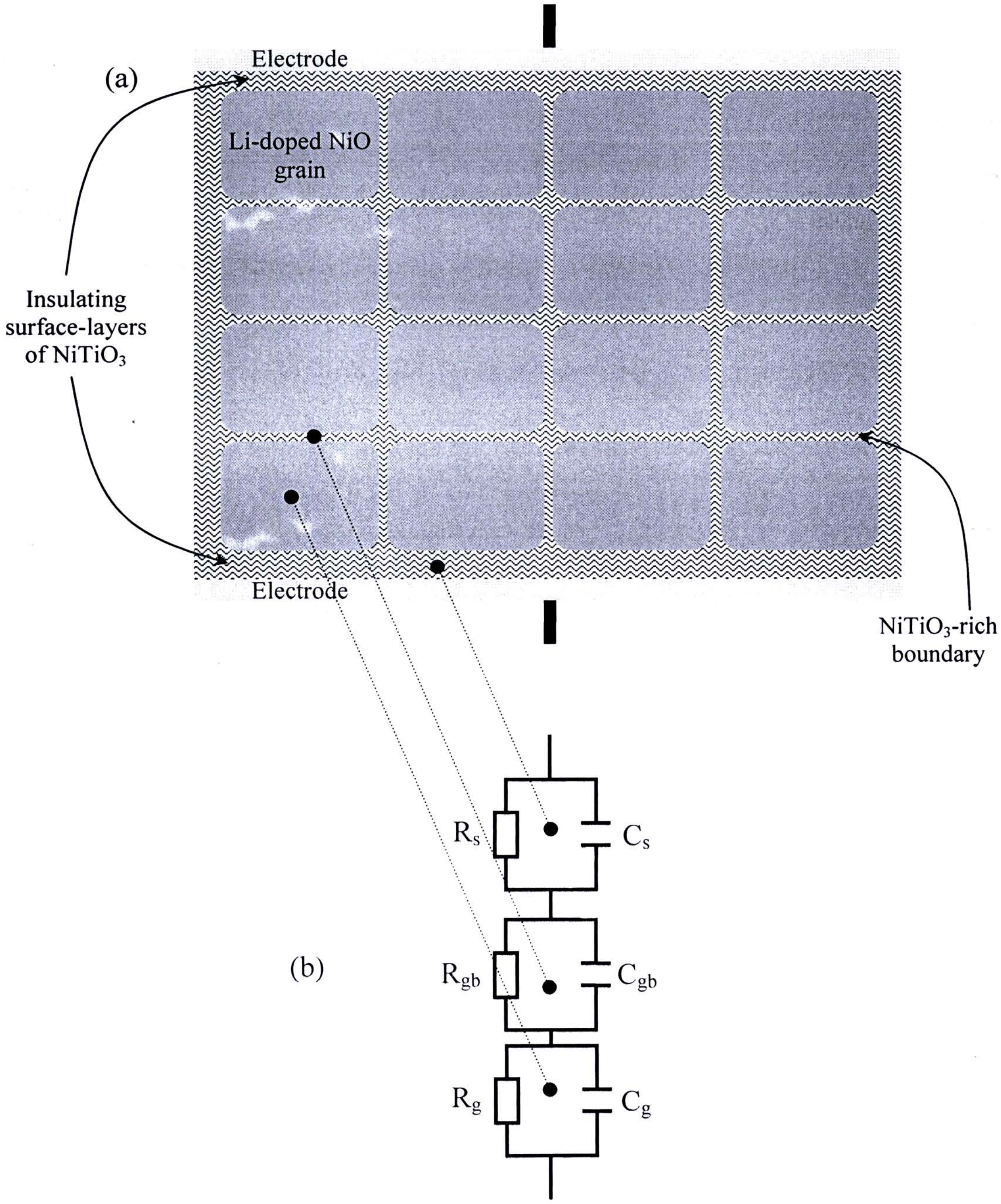

Figure 5.44 (a) Idealized ceramic microstructure of the IBLC/SBLC structure model, and (b) Equivalent circuit corresponding to the microstructure model.

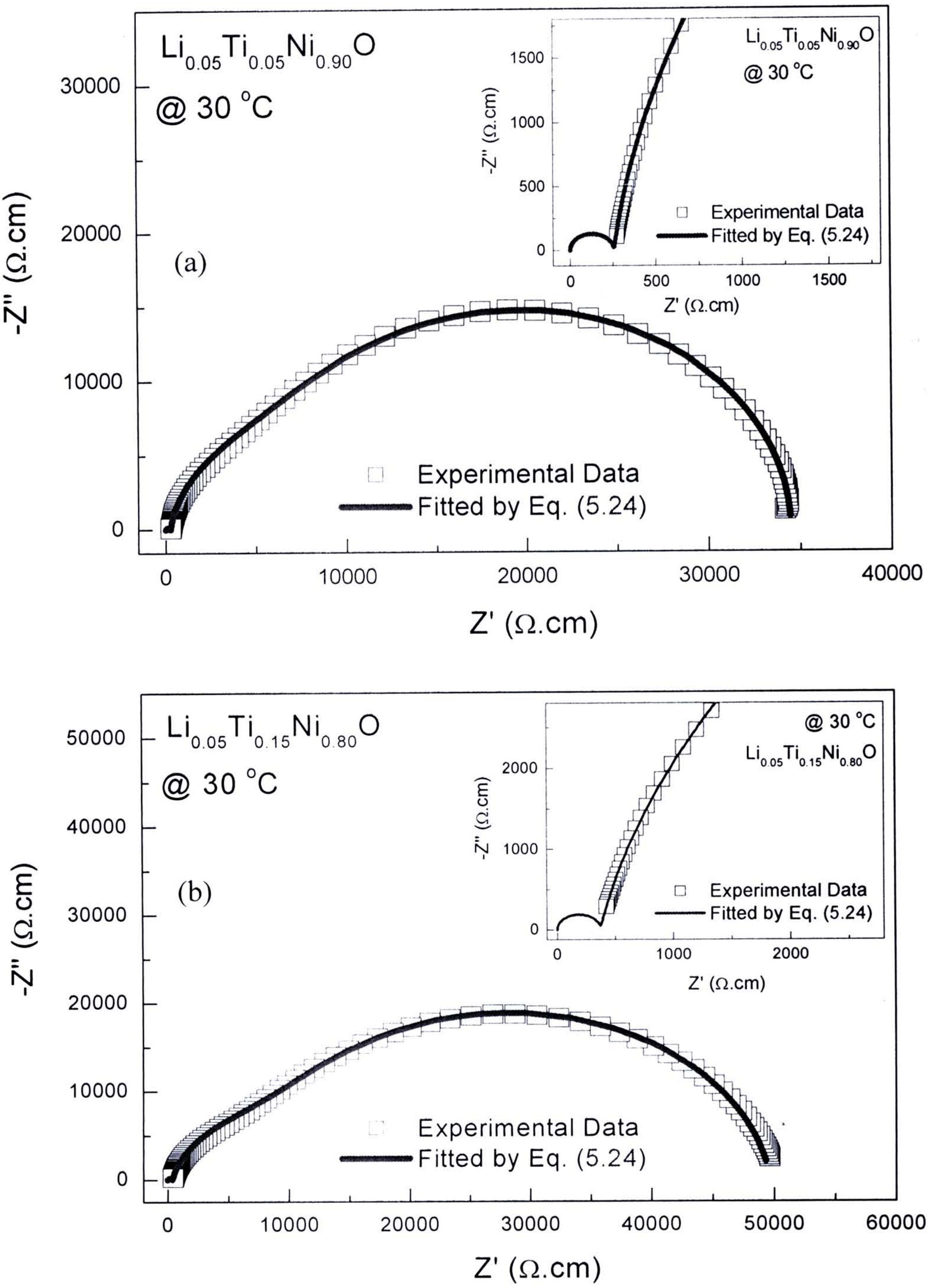

Figure 5.45 Impedance spectra at 30 °C of (a) $Li_{0.05}Ti_{0.05}Ni_{0.90}O$ and (b) $Li_{0.05}Ti_{0.15}Ni_{0.80}O$ ceramics (as-samples) sintered at 1280 °C fitted by equation (5.24); inset shows an expanded view of high frequency data close to the origin.

Table 5.7 Resistances, capacitances, constant parameters obtained from the fitted results in figure 5.45 for the as-samples.

Sample	Fitted result						
	R_g (Ω.cm)	R_{gb} (Ω.cm)	R_s (Ω.cm)	C_{gb} (nF/cm)	C_s (nF/cm)	β	γ
$Li_{0.05}Ti_{0.05}Ni_{0.90}O$	225	6,545	20,345	0.87	1.60	0.91	1.0
$Li_{0.05}Ti_{0.15}Ni_{0.80}O$	370	8,130	31,930	0.54	1.50	0.88	0.92

Note: Cg and α can not be achieved from the fitted results because the semicircle arc corresponding to the electrical response of the grain disappears in the impedance spectra of both samples.

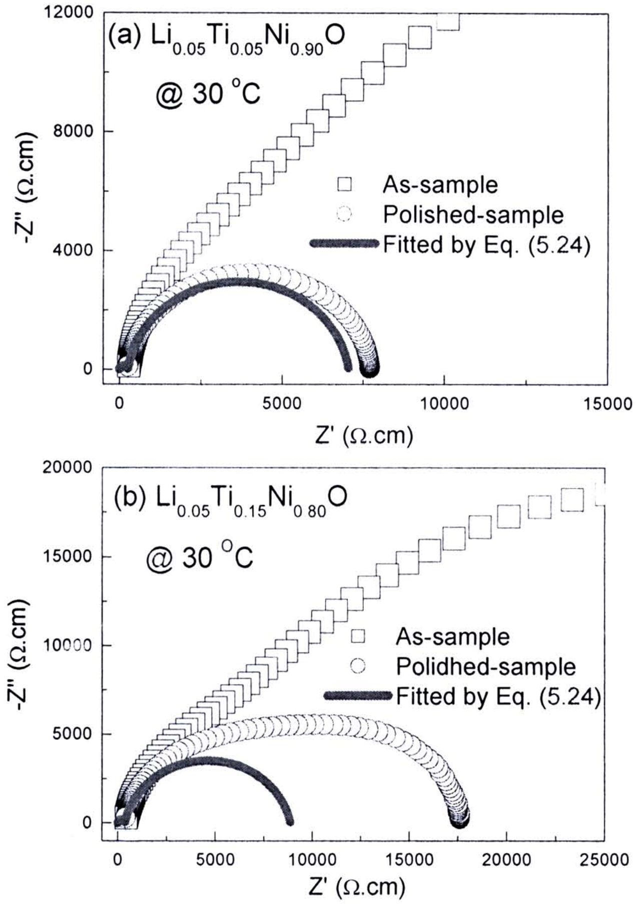

Figure 5.46 Impedance spectra of (a) $Li_{0.05}Ti_{0.05}Ni_{0.90}O$ and (b) $Li_{0.05}Ti_{0.15}Ni_{0.80}O$ ceramics (as- and polished-samples) fitted by equation (5.24) using the same parameters as revealed in Table 5.7, but given R_s=0.

5.1.9.4 Characterization of the LFR process.

If only the dielectric and electrical properties of the as- and polished-samples of the $Li_{0.05}Ti_{0.05}Ni_{0.90}O$ ceramic are investigated, the discussion of these dielectric and electrical properties is certainly incorrect. Fortunately, there are more data that are enough to support the better discussion. As discussed previously, the LFR of the $Li_{0.05}Ti_{0.15}Ni_{0.80}O$ ceramic can be still observed although the surfaces have been removed. The remained LFR is suggested to another source of polarization that occurs at the low-frequency range. Throughout this research, there are four ceramics that can exhibit the LFR process: the $Li_{0.05}Ti_{0.05}Ni_{0.90}O$, $Li_{0.05}Ti_{0.10}Ni_{0.85}O$, $Li_{0.05}Ti_{0.15}Ni_{0.80}O$, and $Li_{0.02}Ti_{0.05}Ni_{0.93}O$ ceramics. The microstructural evolution and a change in the dielectric constant on the polishing are revealed in figures 5.47(a)-5.47(d). The difference in value of the low-frequency dielectric constant between the as- and polished-samples (fixed Li doping concentration) seems to be decreased with increasing the Ti doping concentration. These different values of the dielectric constant of these four ceramics are found to be 7045, 5352, 4569, and 2426, respectively. On the other hand, the LFR of the polished-samples is more evident as the Ti doping concentration increases, as demonstrated in figures 5.47(a)-5.47(c).

According to the microstructure and phase formation analyses, as concluded in Table 5.6, the solubility of the Ti doping dissolved in the solid solution can be roughly estimated to be equal. The remained Ti doping should enhance with the increase in the Ti doping; thus, the amount of the $NiTiO_3$ phase in the microstructure increases. As a result, the remained LFR in the polished-samples may be related to the accumulation of the $NiTiO_3$ phase at the grain boundaries that are enhanced by the increase in Ti doping. Thus, the LFR may be attributed to both of the insulating surface-layer and the grain boundary regions. This assumption is supported by the dielectric and structure properties of the $Li_{0.02}Ti_{0.05}Ni_{0.93}O$ ceramic, as displayed in figure 5.47(d). The grain-surface of this ceramic is quite clear and smooth; whereas, the $NiTiO_3$ phase is found to be more at the grain boundaries. Although the sub-micron grains do not appear on the surface of this sample, just like the first three ceramics, the LFR can also be observed in the dielectric spectrum for both of as- and polished samples. Note that the LFR does not be exhibited in the dielectric properties of the $Li_{0.05}Ti_{0.02}Ni_{0.93}O$, $Li_{0.10}Ti_{0.02}Ni_{0.88}O$, and $Li_{0.10}Ti_{0.05}Ni_{0.85}O$

ceramics, which are the ceramics that their grains and grain boundaries are more clear and smooth. Another supported result is due to the fact that the polishing surface does not relate to the existence of grain boundaries, which are in the pellet interior. This result strongly indicates that there are at least two sources of polarizations—surface layers and grain boundaries—that contribute to the dielectric response in the low-frequency range. It is important to note that the IBLC/SBLC structural model, as demonstrated in figure 5.44, fails to describe the electrical response and dielectric properties of these four ceramics. Exactly, there are at least four electrical responses in these four ceramics—surface layer, grain boundary, an unknown source, and bulk grain. The LFR is attributed to the surface layer and grain boundary effects; while, the non-zero intercept of observed in the impedance spectra at high frequencies can be suggested as the effect of the bulk grain (Sinclair et al., 2002; Shao et al., 2006; Li M et al., 2009a,b). The unknown source of polarization related to the HFR process is briefly discussed based on the effect of the post-annealing in section 5.1.9.5.

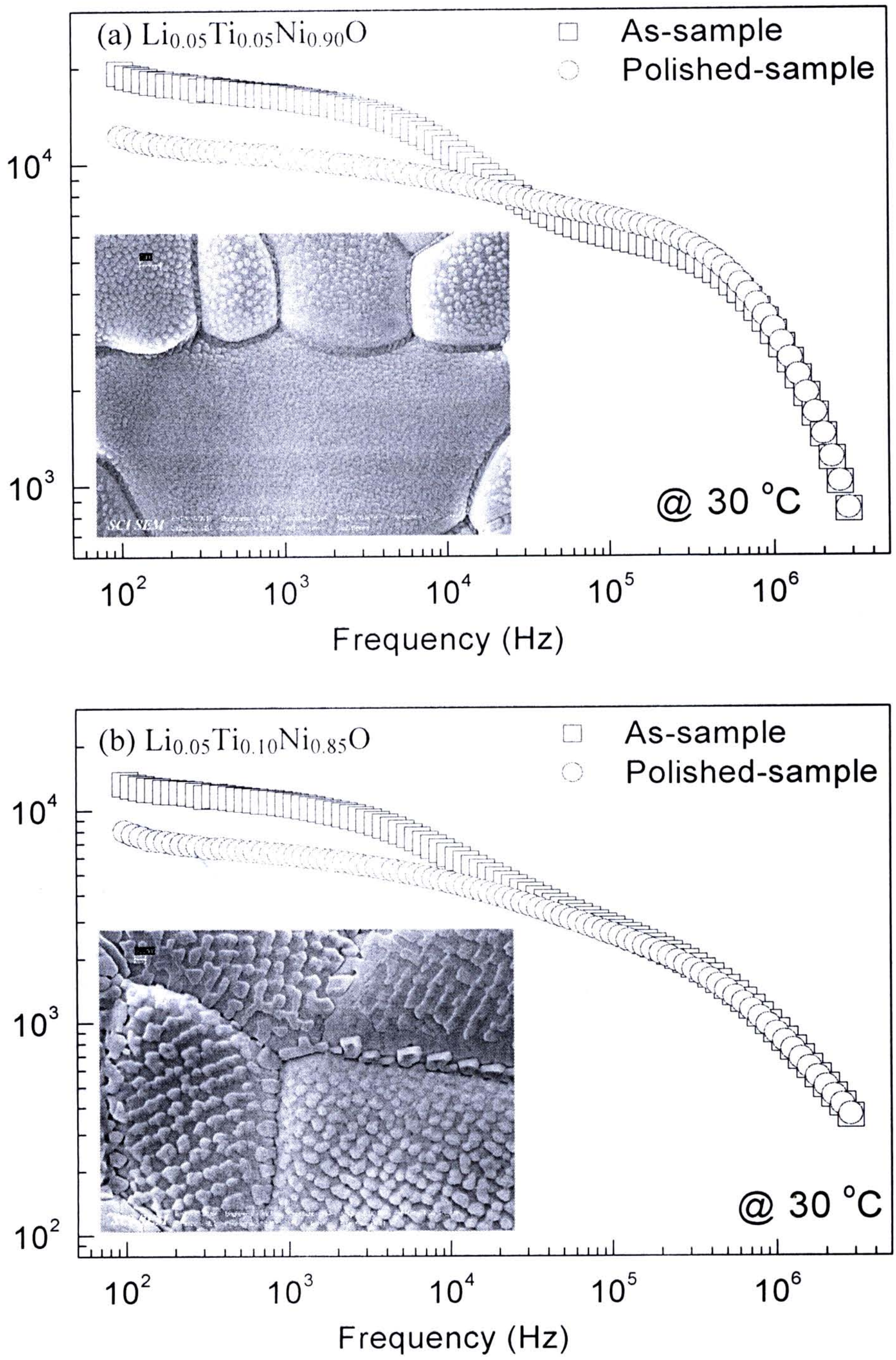

Figure 5.47 Frequency dependence of dielectric constant (ε′) of $Li_xTi_yNi_{1-x-y}O$ ceramics sintered at 1280 °C for as- and polished-samples; inset shows surface morphology.

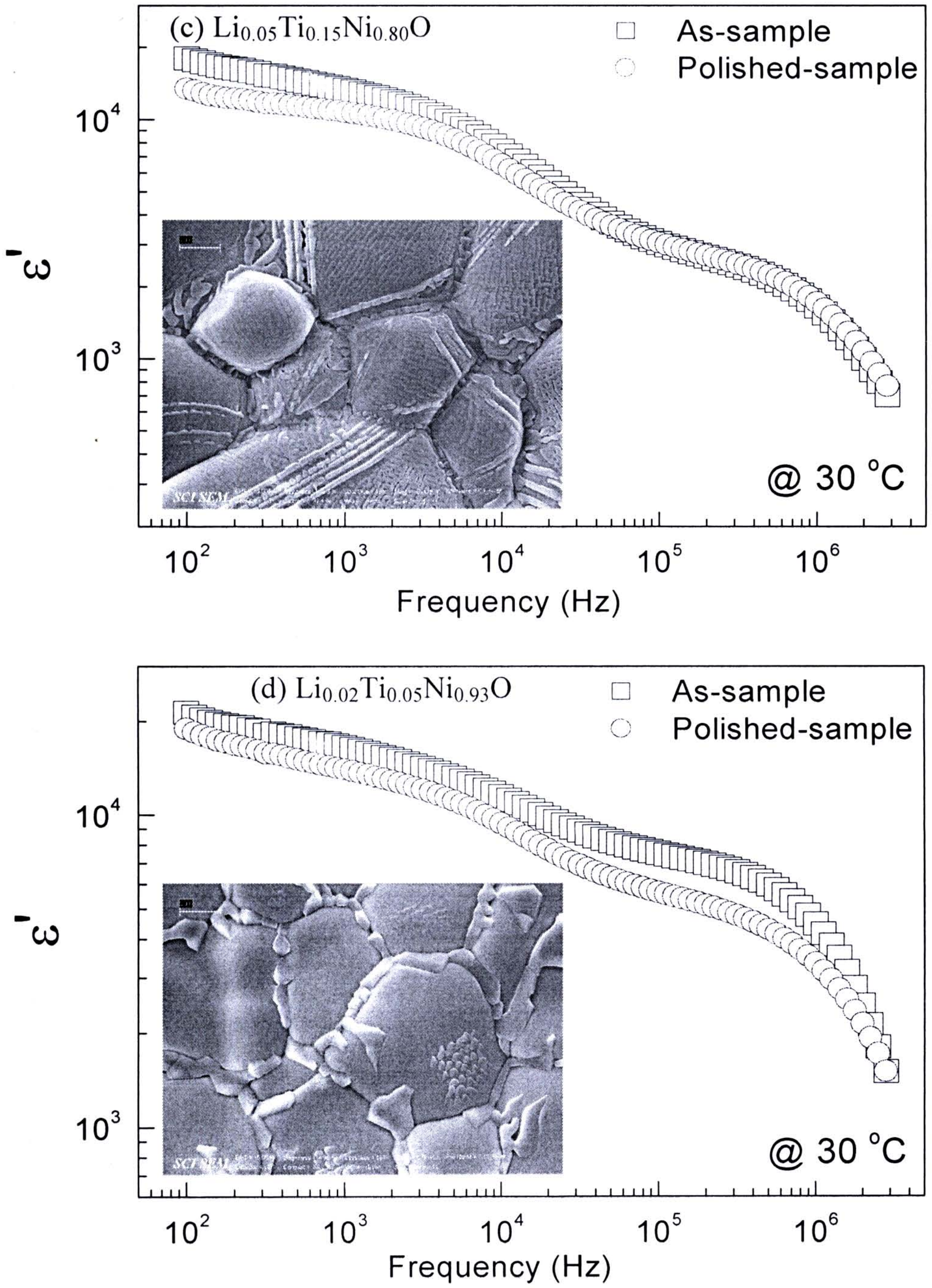

Figure 5.47 Frequency dependence of dielectric constant (ε′) of $Li_xTi_yNi_{1-x-y}O$ ceramics sintered at 1280 °C for as- and polished-samples; inset shows surface morphology. (Cont.)

5.1.9.5 Characterization of the HFR process: Based on the effect of annealing on the dielectric and electrical properties

As outlined earlier, the term of "*giant dielectric constant*" in these $Li_xTi_yNi_{1-x-y}O$ ceramics is referred to the dielectric constant value of the HFR process. The study of the origin of the giant dielectric response in NiO-based ceramics is therefore to investigate the HFR process. As discussed previously, the unknown source of polarization related to the HFR process must be briefly discussed to obtain the most possible mechanism that relates to the HFR. The investigation of a change in dielectric and electrical properties on the post-annealing may provide important information about the HFR process. To brief, a least of changes, qualitative changes, in dielectric and the related electrical properties is summarized in Table 5.8.

Table 5.8 Least of changes, qualitative changes, in dielectric properties

x, *y*	Dielectric and electrical parameter						
	LF-ε′	LF-tanδ	HF-ε′	LF/HF-τ	R-total	R-grain	E_a
$Li_{0.05}Ti_{0.02}Ni_{0.93}O$	-	Dec.	Dec.	Inc.	Inc.	Inc.	Inc.
$Li_{0.05}Ti_{0.05}Ni_{0.90}O$	Inc.	Dec.	Dec.	Inc.	Inc.	Inc.	Inc.
$Li_{0.05}Ti_{0.10}Ni_{0.85}O$	Inc.	Dec.	Dec.	Inc.	Inc.	Inc.	-
$Li_{0.05}Ti_{0.15}Ni_{0.80}O$	Inc.	Dec.	Dec.	Inc.	Inc.	Inc.	Inc.
$Li_{0.02}Ti_{0.052}Ni_{0.93}O$	Inc.	Dec.	Inc.	Un.	Inc.	Inc.	Inc.
$Li_{0.10}Ti_{0.05}Ni_{0.85}O$	-	Inc.	Un.	Inc.	Dec.	Inc.	Inc.
$Li_{0.10}Ti_{0.02}Ni_{0.88}O$	-	Inc.	Dec.	Inc.	Dec.	Inc.	Inc.

Note: LF and HF are denoted as Low-frequency and High-frequency, respectively. Inc. and Dec. are denoted as the increase and decrease in parameters. Un. is denoted as an unchanged of properties.

As well known, point defects in ceramics can possess an effective charge, but cannot for metals. Types of point defects, which can introduce in the ceramics, are vacancies and interstitials of catios or anions. It is interesting that the composition of the ceramic may become or can be induced to nonstoichiometric by annealing in a suitable gaseous atmosphere. Thus, the compound must seek to equilibrate itself with the partial pressure of one of its components in the surrounding atmosphere. This new equilibrium can cause a change in the composition and a change in the type and concentration of the defects (Ramaman, 2003). In this research, the $Li_xTi_yNi_{1-x-y}O$ ceramics were annealed in argon (Ar) atmosphere, which is a low oxygen partial pressure. This post-annealing may lead to an oxygen-deficient oxide, $Li_xTi_yNi_{1-x-y}O_{1-z}$, producing relative-high concentration of oxygen vacancies in the ceramics. It can be proved that the concentration of oxygen vacancies ($[V_O^{\bullet\bullet}]$) is related to the oxygen partial pressure (p_{O_2}), as

$$[V_O^{\bullet\bullet}] = \left(\frac{K}{4}\right)^{1/3} p_{O_2}^{-1/6}, \tag{5.25}$$

where K is the equilibrium constant. This equation means that the concentration of oxygen vacancies increases with decreasing the oxygen partial pressure. As a result, it is possible to indicate that the concentration of oxygen vacancies in the Ar-samples should be higher than that of the polished-samples.

Generally, Li-doped NiO ceramic is well known as the semiconducting ceramic material. In the case on elemental semiconductor such as Si or Ge and in the case of covalently-bounded compound semiconductors such as GaAs and GaP, the features of the band model are usually correct. However, in the oxide semiconductor, it is difficult to achieve the correct band structures. This is due to the fact that sufficiently precise physical and chemical characterization of the materials is often extremely difficult. Although several models have been proposed to explain the hole state that is introduced by the Li doping ions (van Elp et al., 1992; Kuiper et al., 1989; Kunes et al., 2007a,b; Bengone et al., 2000; Taguchi et al., 2008; Takahashi et al., 2007; Schuler et al., 2005), it is convenient to describe by using the presence of Ni^{3+} as the species charge compensating for the Li^+ doping ions rather that of the band model (Moulson, Herbert, 2003). The schematics of charge compensation following to either of the Kröger-Vink notation for the presences of oxygen vacancy or the presence of Ni^{3+} are illustrated in figure 5.48. As demonstrated in figure 5.48(c), for every added Li^+, one Ni^{2+} is induced to the Ni^{3+} state; thus, the lattice now contains Ni^{2+} and Ni^{3+} ions. This is the model situation for conduction by 'polaron hopping'.

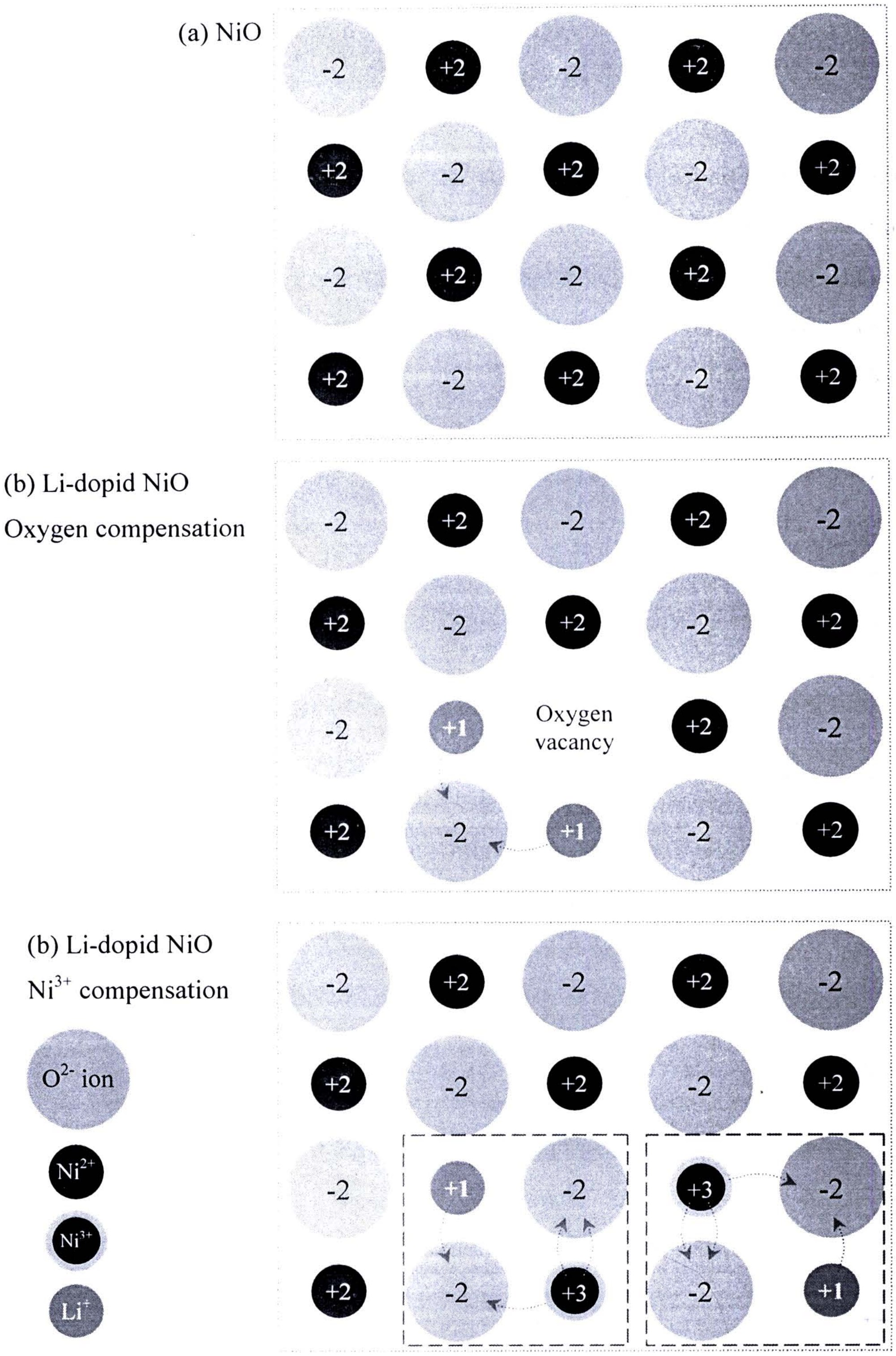

Figure 5.48 Schematics of (a) NiO and Li-doped NiO structure with different types of charge compensation: (b) oxygen vacancy and (c) Ni^{3+}, respectively.

1) Possible mechanisms of the changes in the conduction in the $Li_xTi_yNi_{1-x-y}O$ ceramics

As demonstrated in Table 5.8, when the polished-samples were annealed in Ar atmosphere, the resistance of the grain (R_g) of all ceramic samples is found to increase. While the total resistance (R_{total}) of the $Li_{0.05}Ti_{0.02}Ni_{0.93}O$, $Li_{0.05}Ti_{0.05}Ni_{0.90}O$, $Li_{0.05}Ti_{0.10}Ni_{0.85}O$, $Li_{0.05}Ti_{0.15}Ni_{0.80}O$, and $Li_{0.02}Ti_{0.05}Ni_{0.93}O$ ceramics increases. In these five samples, both of R_g and R_{total} are enhanced with the post-annealing process. In contrast, R_{total} of the $Li_{0.10}Ti_{0.02}Ni_{0.88}O$ and $Li_{0.10}Ti_{0.05}Ni_{0.85}O$ ceramics, which are the ceramics that contain the highest concentration of Li ions among these seven samples, is found to decrease. As suggested above, the post-annealing in Ar atmosphere leads to the reduction in the oxygen vacancies, and the composition of $Li_xTi_yNi_{1-x-y}O$ is changed to $Li_xTi_yNi_{1-x-y}O_{1-z}$, producing relative-high concentration of oxygen vacancies in the ceramics. This seems strange, because the oxygen vacancy is classified as charge carriers; therefore, the R_{total} must be increased with annealing in Ar. On the other way, the increase in the oxygen vacancies in the $Li_xTi_yNi_{1-x-y}O$ ceramics—oxygen vacancies have already been introduced in the ceramics due to the effect of Ti doping (Fig. 5.41(c))—the post-annealing may have some effects on the charged compensations, as demonstrated in figures 5.48(b) and 5.48(c).

In the case of oxygen compensation (Fig. 5.48(b)), R_{total} will enhance as the concentration of the oxygen vacancies increases due to the introduction of donor state in the band structure of the ceramics, as illustrated in figure 5.49. One induced-oxygen vacancy can induce $2e^-$, which are trapped electrons that contribute electrons to the conduction band (Hence, West, 1990). This case is consistent with the decrease in the R_{total} of the highest-concentration samples of the $Li_{0.10}Ti_{0.02}Ni_{0.88}O$ and $Li_{0.10}Ti_{0.05}Ni_{0.85}O$ ceramics, but is not with to the increase in the R_{total} of the $Li_{0.05}Ti_{0.02}Ni_{0.93}O$, $Li_{0.05}Ti_{0.05}Ni_{0.90}O$, $Li_{0.05}Ti_{0.10}Ni_{0.85}O$, $Li_{0.05}Ti_{0.15}Ni_{0.80}O$, and $Li_{0.02}Ti_{0.05}Ni_{0.93}O$ ceramics. Moreover, this case is also not consistent with the increase in the R_g of the $Li_{0.10}Ti_{0.02}Ni_{0.88}O$ and $Li_{0.10}Ti_{0.05}Ni_{0.85}O$ ceramics. This indicates that the band structure model may be unsuitable for the explanation of the annealing effect on the dielectric and electrical properties of the $Li_xTi_yNi_{1-x-y}O$ ceramics.

In the case of Ni^{3+} compensation (Fig. 5.48(c)), R_{total} will decrease as the concentration of the oxygen vacancies increases due to the reduction of valent state of the Ni^{3+} to Ni^{2+}, as illustrated in figure 5.50. This result is due to the fact that the ceramics must seek to equilibrate itself. This new equilibrium can cause a change in the type and concentration of the defects. For every induced-oxygen vacancy (one lost oxygen), two Ni^{3+} are reversed to two Ni^{2+} state; thus, the concentration of Ni^{3+} ions decrease with increasing the concentration of the oxygen vacancies. As a result, the conduction due to the polaron hopping in the $Li_xTi_yNi_{1-x-y}O$ ceramics will decrease when the samples are annealed in Ar atmosphere. Therefore, it can be suggested that the conductivity of the $Li_xTi_yNi_{1-x-y}O$ ceramics can be decreased by increasing the concentration of oxygen vacancies in the ceramics. This case is consistent with the increase in both of the R_{total} and R_g of the $Li_{0.05}Ti_{0.02}Ni_{0.93}O$, $Li_{0.05}Ti_{0.05}Ni_{0.90}O$, $Li_{0.05}Ti_{0.10}Ni_{0.85}O$, $Li_{0.05}Ti_{0.15}Ni_{0.80}O$, and $Li_{0.02}Ti_{0.05}Ni_{0.93}O$ ceramics. Moreover, it is consistent with the increase in the R_g of the $Li_{0.10}Ti_{0.02}Ni_{0.88}O$ and $Li_{0.10}Ti_{0.05}Ni_{0.85}O$ ceramics.

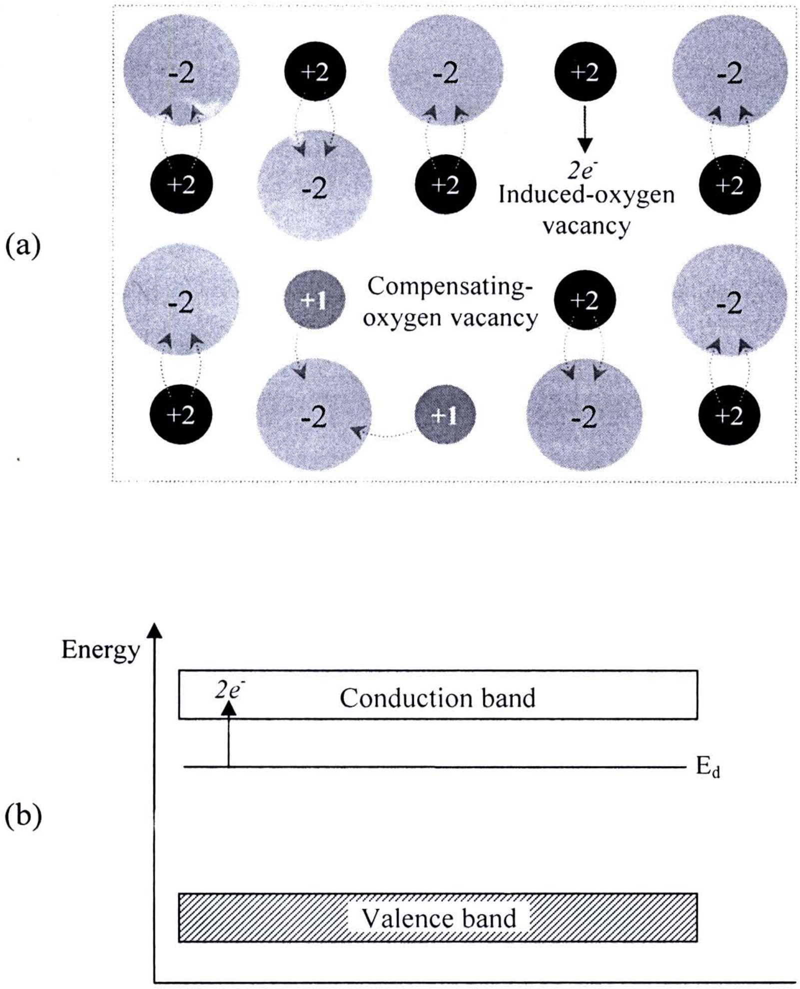

Figure 5.49 (a) Schematics of Li-doped NiO structure with oxygen compensation and (b) the related band structure.

(a) Before annealing

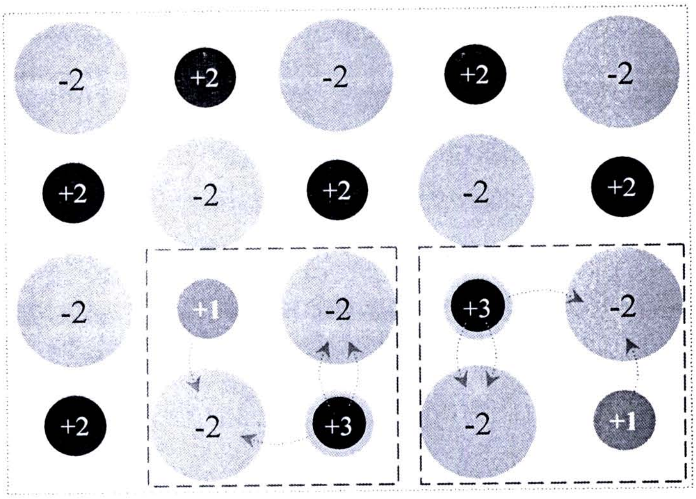

(b) After annealing

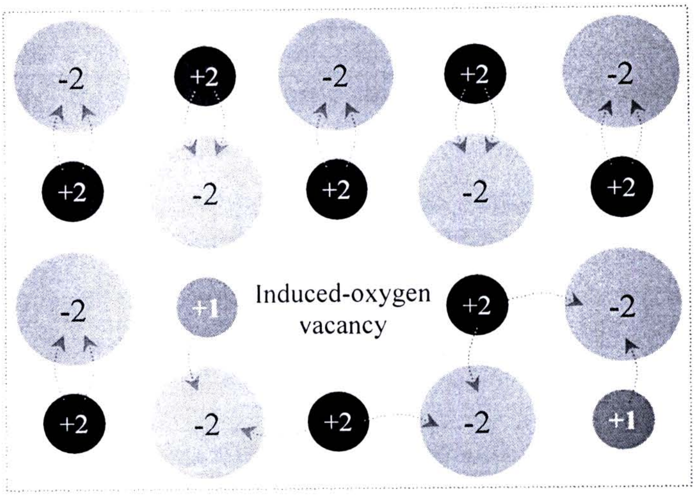

Figure 5.50 Schematics of Li-doped NiO structure with Ni^{3+} compensation: (a) before annealing and (b) after annealing.

2) The distribution of additives of Li and Ti doping ions

Before consideration the effect of annealing, effect of oxygen vacancy concentration on the dielectric properties, the strange result—the decrease in the R_{total} of the $Li_{0.10}Ti_{0.02}Ni_{0.88}O$ and $Li_{0.10}Ti_{0.05}Ni_{0.85}O$ ceramics should be clarified. It is likely that the presence of Ni^{3+} compensation is more suitable than the oxygen vacancy compensation. It should be recognized that the LFR process can not be observed in dielectric spectra of these two samples, suggesting that the giant dielectric response in the ceramics is not related to the second phase of $NiTiO_3$ just like in the other ceramics. Thus, the distribution of the Li and Ti doping ions in the microstructure may be related to this result. The distribution might be associated with the *electrostatic interaction for space charge concept* (Rahaman, 2003). In general, the bulk of the crystal in ionic ceramics must be electrically neutral; thus, the defects concentration in the bulk will be determined by the principle of electroneutrality. The defect concentration in the bulk will be different from that at the grain boundary. The difference in potential between the bulk and the grain boundary can cause segregation of charged doping ions at the grain boundary.

According to the intrinsic defects that produce in ceramics during sintering process, Frenkel defect—point defects can usually be observed in binary oxides such as FeO, CoO, and NiO ceramics (Hence, West, 1990). The creation of the Frenkel defect in NiO may be written as,

$$Ni_{Ni} \leftrightarrow Ni_i^{\bullet\bullet} + V_{Ni}'', \qquad (5.26)$$

where $Ni_i^{\bullet\bullet}$ is the Ni ion in the interstitial lattice site. Normally, the defect concentration produced by dopants is higher than that of the thermally induced defects. By consider equation (5.22), it indicates that the concentration of Ni vacancies ($[V_{Ni}'']$) increases with increasing the concentration of the Ti doping. This in turn leads to a decrease in the concentration of Ni^{2+} ions at the boundary. Consequently, the boundary will be negatively charged; hence, the negatively electrostatic potential is exhibited at the boundary. It is also expected that this electrostatic potential will vary with the distance from the grain boundary, as revealed in figure 5.51 (Rahaman, 2003). The negatively charged boundary can pull the Ti doping ions that are the positive effective charge at the grain boundary as a space charge to maintain bulk of the crystal electrically neutral. These variations in of the electrostatic potential and the defect concentration for Ti-doped NiO are illustrated in figure 5.51. According to the schematics of Li-doped NiO structure with Ni^{3+} compensation (Fig. 5.48(c)) and the presence of the negatively electrostatic potential at boundary, the effective negative charge of Li'_{Ni} is therefore driven into the bulk grain. Thus, $[Li'_{Ni}]$ should be large in the grain interior, but should be small at grain boundary region.

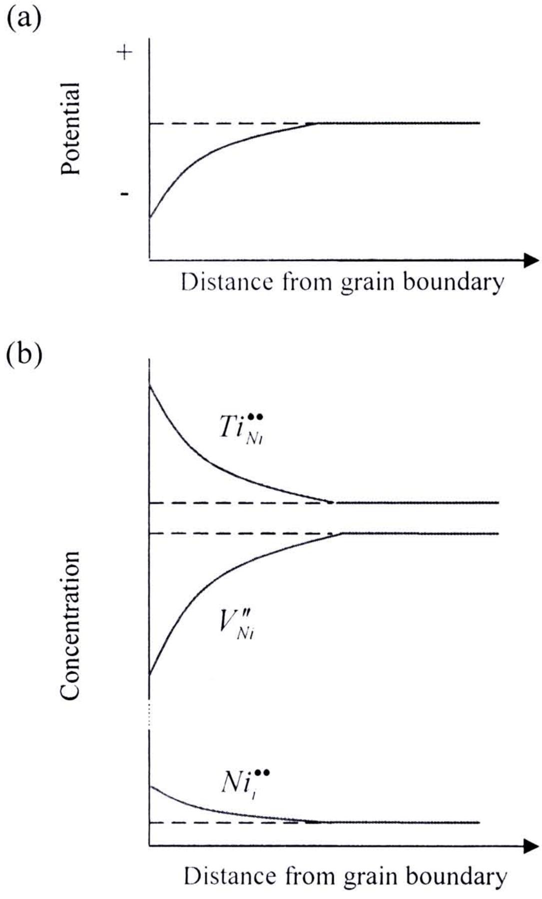

Figure 5.51 Schematics of the changes in (a) electrostatic potential and (b) defect concentrations as a function of distance from grain boundary for the segregation of the Ti doping ions in $Li_xTi_yNi_{1-x-y}O$ ceramics.

3) Microstructural models of the $Li_xTi_yNi_{1-x-y}O$ ceramics

According to the IBLC/SBLC structural model, as illustrated in figure 5.44(a), this model can be used quite well to ascribe the dielectric and electrical properties of the $Li_xTi_yNi_{1-x-y}O$ ceramics that exhibit the LFR—the $Li_{0.05}Ti_{0.05}Ni_{0.90}O$, $Li_{0.05}Ti_{0.10}Ni_{0.85}O$, $Li_{0.05}Ti_{0.15}Ni_{0.80}O$, and $Li_{0.02}Ti_{0.05}Ni_{0.93}O$ ceramics. However, it can not be used to prove the electrical and dielectric properties of the polished-samples of these ceramics. It contrast, it is suitable for only the as-samples (nonpolished-samples). Moreover, this microstructural model can not be used to describe the dielectric and electrical properties of the $Li_{0.05}Ti_{0.02}Ni_{0.93}O$, $Li_{0.10}Ti_{0.02}Ni_{0.88}O$ and $Li_{0.10}Ti_{0.05}Ni_{0.85}O$ ceramics—the ceramics that have only the HFR and clean grains and grain boundaries. Accordingly, it is proposed that most of Ti doping ions that can dissolve into the solid solution are segregated near the grain boundary region, whereas the Li doping ions are expected to be in the grain interior. Thus, the outer grain is Ti-rich region; while, the interior is semiconducting particle of Li-doped NiO. As well known, the institution of Ti ions on the Ni site can not change remarkable the insulating character of the NiO ceramics (van Elp et al., 1992; Kuiper et al., 1989; Wu J et al., 2002). Therefore, the grains of the $Li_xTi_yNi_{1-x-y}O$ ceramics can be considered as the core/shell particle, consisting of semiconducting particle of Li-doped NiO and insulating layer of the outer grains. The possible microstructural models corresponding to these ceramics are demonstrated in figure 5.52. The double-IBLC/SBLC model (Fig. 5.52(a)) may be suitable for the ceramics that exhibit the LFR—the $Li_{0.05}Ti_{0.05}Ni_{0.90}O$, $Li_{0.05}Ti_{0.10}Ni_{0.85}O$, $Li_{0.05}Ti_{0.15}Ni_{0.80}O$, and $Li_{0.02}Ti_{0.05}Ni_{0.93}O$ ceramics and may be for the $Li_{0.05}Ti_{0.02}Ni_{0.93}O$ ceramic. On the other hand, the original IBLC model (Fig. 5.52(b)) may be suitable for the $Li_{0.10}Ti_{0.02}Ni_{0.88}O$ and $Li_{0.10}Ti_{0.05}Ni_{0.85}O$ ceramics—the clear and smooth microstructure-ceramics.

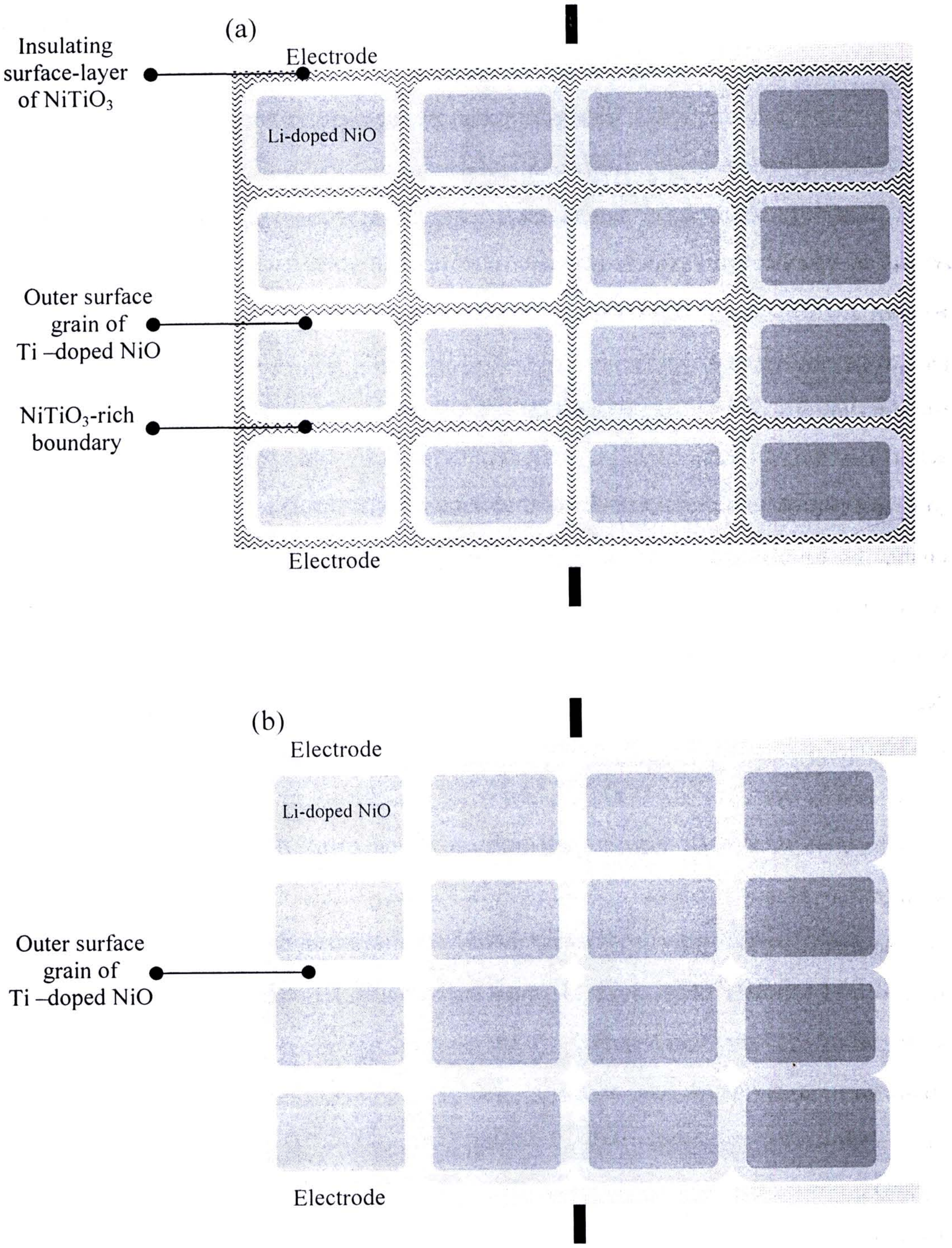

Figure 5.52 Microstructural models proposed for $Li_xTi_yNi_{1-x-y}O$ ceramics; (a) double-IBLC/SBLC model and (b) IBLC model.

4) The mechanism of the changes in the total resistance, grain resistance, and dielectric properties on the annealing process: Based on the compensated Ni^{3+} and the microstructural models

As recognized to Table 5.8, it is found that the resistance of the grains (R_g) of all ceramic samples increases with the annealing in Ar process. Except for the $Li_{0.10}Ti_{0.02}Ni_{0.88}O$ and $Li_{0.10}Ti_{0.05}Ni_{0.85}O$ ceramics, the total resistance (R_{total}) of all samples increases with this annealing as well. As discussed previously, the conduction due to the polaron hopping in the $Li_xTi_yNi_{1-x-y}O$ ceramics will decrease when the polished-samples were annealed in Ar atmosphere. This is due to the fact that the removing oxygen can be compensated by the reduction of Ni^{3+} to Ni^{2+}, as easily demonstrated in figure 5.50(b). Therefore, the increase in the resistance is due to the decrease in the Ni^{3+} ions. The charge transport in the $Li_xTi_yNi_{1-x-y}O$ ceramics can be inhibited by increasing the concentration of oxygen vacancies—decreasing the Ni^{3+} ions. As demonstrated in figure 5.53, on the annealing process, oxygen ions at the outmost surfaces and some parts inside the grains are reduced from the microstructure. As a result, the concentration of the oxygen vacancies in these regions is enhanced, especially at the outer surfaces. Thus, the induced oxygen vacancies should be highest at the out most surfaces, producing the insulating surfaces. Moreover, the increase in the values of R_g of all samples is therefore due to the slight increase in the oxygen vacancies inside grains. Hence, the semiconducting character-surfaces of the polished-samples can be tuned to the insulating layers again just as the insulating surfaces of the second phase of $NiTiO_3$ do. These induced insulating surface-layers can reduce the low-frequency loss tangent ($\tan\delta$) of the $Li_{0.05}Ti_{0.02}Ni_{0.93}O$, $Li_{0.05}Ti_{0.05}Ni_{0.90}O$, $Li_{0.05}Ti_{0.10}Ni_{0.85}O$, $Li_{0.05}Ti_{0.15}Ni_{0.80}O$, and $Li_{0.02}Ti_{0.05}Ni_{0.93}O$ ceramics [Figs. 5.37(a.1)-5.37(e.1)]. For the annealing effect on the dielectric constant, the LFR of the dielectric constant for the $Li_{0.05}Ti_{0.05}Ni_{0.90}O$ ceramic appears again—the LFR of the as-sample is erased completely by the polishing, and then it returned by the annealing (Fig. 5.37(b)). While the LFR of the other ceramics is more dominant, especially for the $Li_{0.05}Ti_{0.15}Ni_{0.80}O$ ceramic, the related LFR-peak can be observed clearly in the loss tangent (Fig. 5.37(d)). This result strongly indicates that the LFR-peaks of the as- and polished-samples are concealed by the large contribution of dc conduction to the total loss tangent, as suggested in sections 5.1.5 and *5.7.1.3* (Fig. 5.35). With decreasing the dc conduction by the annealing, the exponentially background of the dc conductivity will decrease, resulting to the appearance of the LFR-peak. To understand the annealing effect on the dielectric properties through the change in the dc conductivity, a modified-double Cole-Cole model combined with the dc conductivity term is adapted as

$$\varepsilon^{*}=\varepsilon'_{\infty}+\left(\frac{\varepsilon'_{s}-\varepsilon'_{\infty}}{1+j\omega\tau^{\alpha}}\right)_{LFR}+\left(\frac{\varepsilon'_{s}-\varepsilon'_{\infty}}{1+j\omega\tau^{\beta}}\right)_{HFR}-\left(j\frac{\sigma_{dc}}{\omega\varepsilon_{0}}\right). \tag{5.27}$$

The second and the third terms are the LFR and HFR, respectively. As shown in figure 5.54, that the dielectric properties of the polished- and Ar-samples of the $Li_{0.05}Ti_{0.15}Ni_{0.80}O$ ceramic can be very well fitted by equation (5.27). It is clear that that the annealing has great effects on the dielectric properties. If σ_{dc} (5×10^{-3} S/m) of the polished-sample is used to fit the data of the Ar-sample, it is clear that the LFR-peak becomes disappearance; whereas, the HFR-peak does not change.

In the case of the $Li_{0.10}Ti_{0.02}Ni_{0.88}O$ and $Li_{0.10}Ti_{0.05}Ni_{0.85}O$ ceramics, the original IBLC structural model is suggested to be related to the dielectric and electrical properties of these two ceramics. As shown in figure 5.52(b), there is no expected second phase of $NiTiO_3$ accumulated along the grain boundaries. The outer grain is designed as an insulating thin layer of Ti-doped NiO, while the core of the grain is designed as a semiconducting particle of Li-doped NiO. This means that the there is much concentration of Ni^{3+} ions inside the grains, but it is indigent at the outer layers. With annealing these two samples in Ar atmosphere, the O^{2-} ions in the outer grain layers are therefore removed as well as the O^{2-} ions inside the core grains. This results in an increase in the concentration of oxygen vacancies in the grain boundaries, which are as the Li^{+}-poor regions—few Ni^{3+} ions. Thus, the charge compensation in the grain boundaries should be followed to the mechanism that is expressed in figure 5.49. As a result, the conductivity increases due to the introduction of donor state in the band structure under the conduction band. According to the IBLC model (Fig. 5.52(b)), R_{total} is mainly depended on the resistance of the grain boundary

(R_{gb}). R_{total} of these two samples should be decreased with decreasing the value of R_{gb}. Turning to the increase in R_g, on the annealing process, some Ni^{3+} ions inside the grains are reduced to Ni^{2+} state; as a result, R_g of these two samples is found to increase just like the other samples.

From these points of view, it is most likely that the HFR observed in all samples may be related to the outer surface of the grain, as expressed in figure 5.52. The decrease in the high-frequency dielectric constant can be ascribed based on the polarization at the interface between the outer grains—grain boundaries induced by the Ti doping, which is not the grain boundaries of the accumulated $NiTiO_3$—and the core grains. When the polished-samples have been annealed in Ar atmosphere, R_g increases, resulting from the decrease in the concentration of charge carriers. Thus, under applied electric field, the accumulated charges at this interface should be decreased. Certainly, the intensity of polarization is decreased, resulting in the decrease in the dielectric constant.

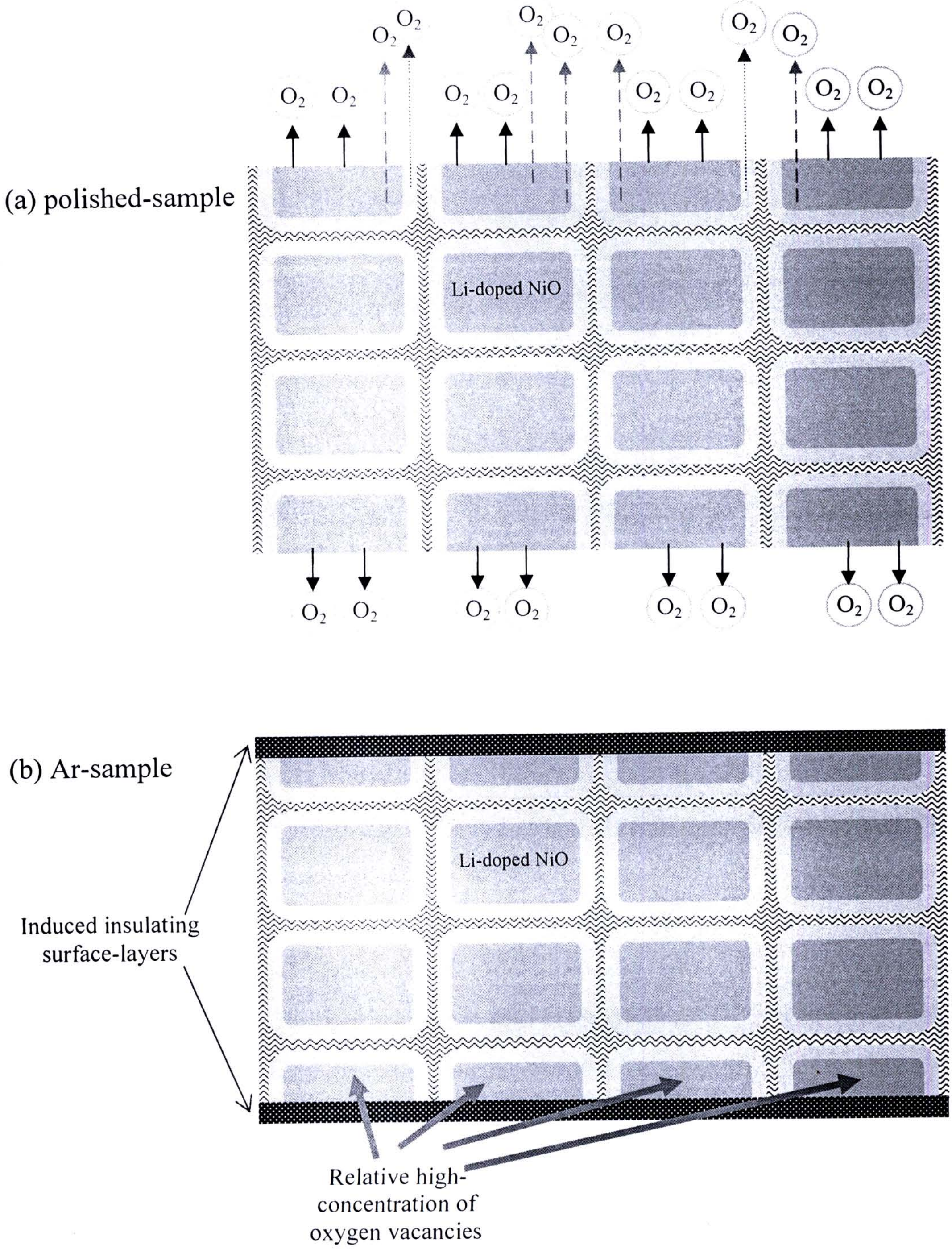

Figure 5.53 Effect of annealing on the microstructure the double-IBLC/SBLC model for the polished-samples.

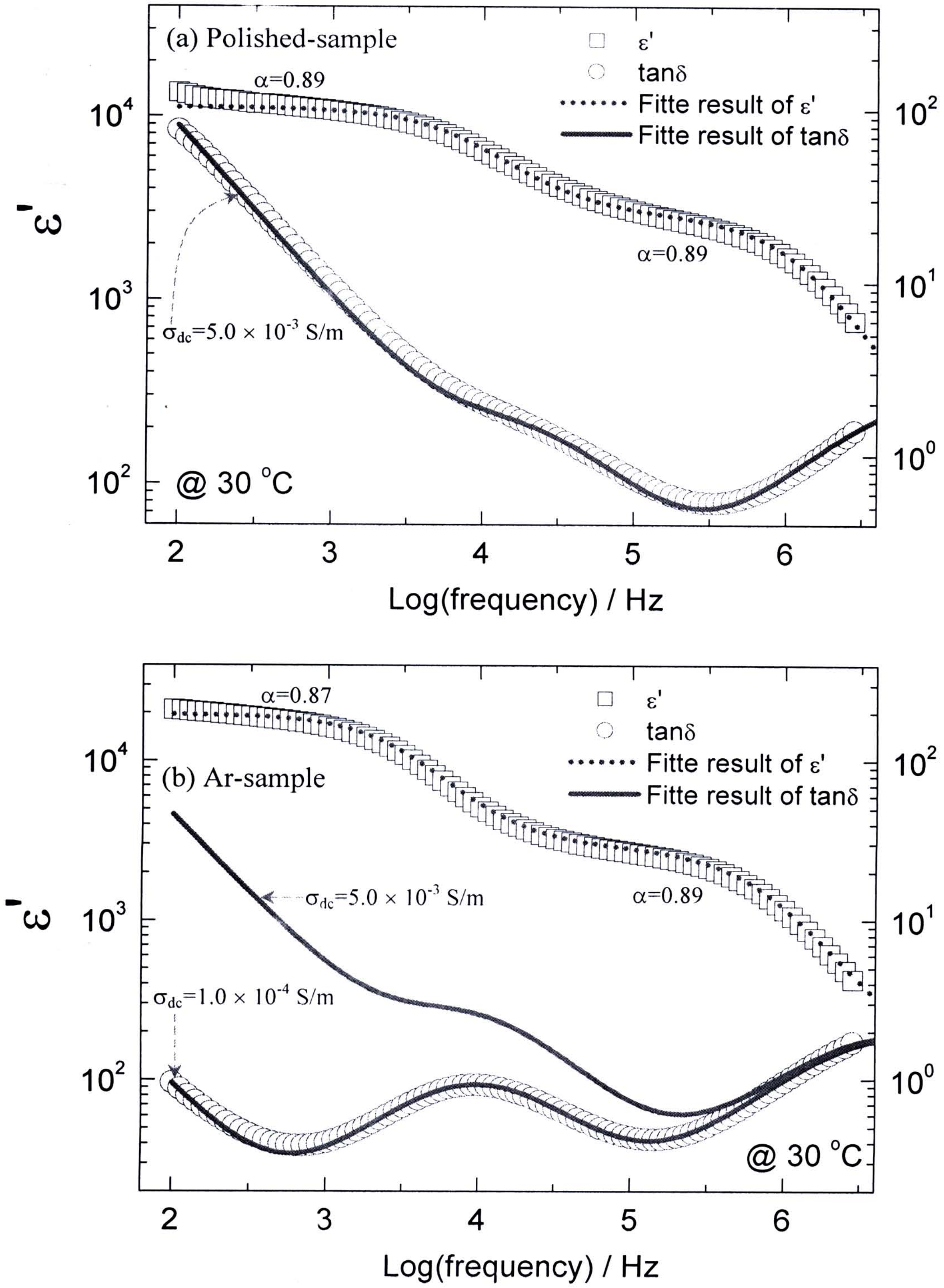

Figure 5.54 Dielectric constant and loss tangent of the $Li_{0.05}Ti_{0.15}Ni_{0.80}O$ ceramic fitted by equation (5.27); (a) polished-sample and (b) Ar-sample.

5.1.9.6 Effect of Ti and Li doping concentrations on the dielectric and properties

As reported in the literature (Wu et al., 2002), it was found that the dielectric constant of the $Li_xTi_yNi_{1-x-y}O$ ceramics increased as the Li doping concentration increased (fixed Ti(y) =0.02). On the other hand, it decreased with the increase in the Ti doping ions (fixed Li(x) = 0.05). In the former case, the increase in the dielectric constant was suggested to an increase in the charge carriers inside grains, which are induced by the substitution of Li ions. The later case, the decrease in the dielectric constant was ascribed based on a series layer model—the decrease was attributed to the increase in the thickness of grain boundaries due to the accumulation of $NiTiO_3$ phase. Interestingly, the experimental results in this research are consistent with the literature, as illustrated in figures 5.55(a) and 5.55(b). It is important to note that the dielectric constants are selected at the high-frequency of 10^5 Hz to eliminate the contribution of LFR. With increasing the fixed-Li doping concentration up to 10 mol % ($x = 0.10$), the decrease in the dielectric constant due to the effect of Ti doping concentration can still be observed, as shown in figure 5.55(d). The interesting results can be observed in figure 5.55(c)—with fixed Ti doping at 5 mol % ($y = 0.05$), the increase in the dielectric constant with the Li doping concentration is exhibited in only the range of Li = 2 – 5 mol % (x = 0.02-0.05). With further increasing the Li doping concentration up to 10 mol % ($x = 0.10$), however, the dielectric constant decreases. This result means that the explanation for the decrease in the dielectric constant due to the effect of Ti doping concentration may be failed. On the other hand, the explanation for the increase in the dielectric constant with the increase in the Li doping concentration is likely reasonable. The decrease in the dielectric constant that is related to the Ti doping may be associated with the solubility of Ti ions in the solid solution of the $Li_xTi_yNi_{1-x-y}O$ ceramics. In the conditions of $x = 0.10$ and $y = 0.05$, the Ti doping ions can substitute into the NiO crystal very well. Thus this decrease in the dielectric constant is most likely due to the decrease in the grain conductivity, which is affected by the incorporation of Ti ions in the grain interior. In addition, it is clear that the Li doping ions have a great effect on the high-frequency dielectric constant. The dielectric constant of the $Ti_xNi_{1-y}O$ ceramics increases with increasing the Li doping, as demonstrated in figure 5.55(e).

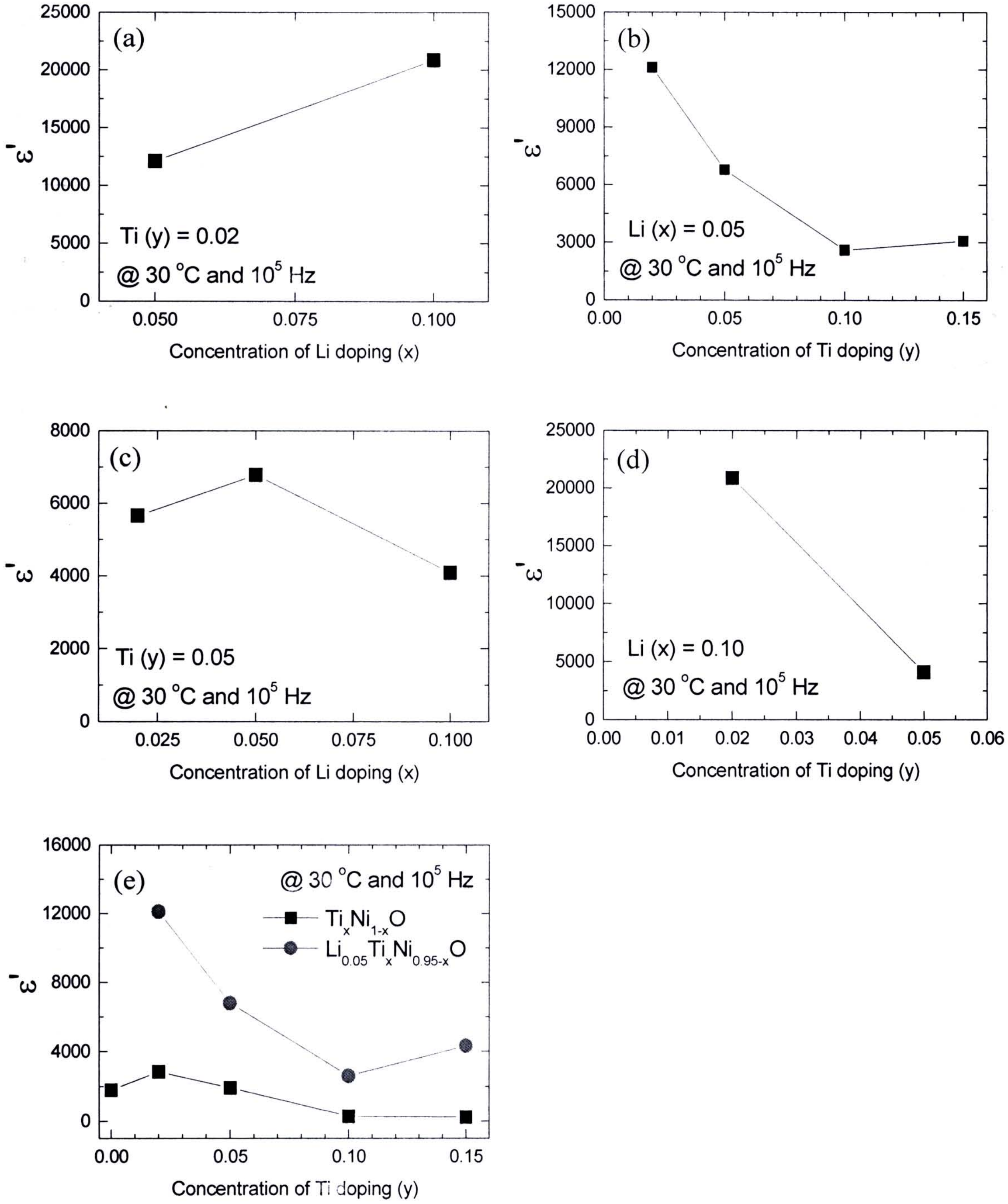

Figure 5.55 The dependence of the dielectric constant at 30 °C and 10^5 Hz on the concentration of Li and Ti doped in $Li_xTi_yNi_{1-x-y}O$ ceramics (polished-samples).

5.2 Li and Fe co-doped NiO system

It is generally believed that the presence of insulating layers in polycrystalline ceramics has remarkable effects on their electrical properties, and they are usually used to design ceramic properties for practical applications. The effects of insulating layers, e.g., surface layers, grain boundaries, and internal domains within the bulk grain, on high dielectric properties of materials are often observed. For example, the existence of these three insulating layers in $CaCu_3Ti_4O_{12}$ ceramics has an influence on the giant dielectric constant of the $CaCu_3Ti_4O_{12}$ (Sinclair et al., 2002; Chung et al., 2004; Wang, Zhang., 2006). The Maxwell–Wagner polarization (interfacial polarization) at these insulating layers has, therefore, been used to ascribe the giant dielectric response in this material. For (***A***, ***B***)–doped NiO ceramics (***A***=Li, Na, K and ***B***=Ti, Si, Al, Ta, V, Fe) (Wu J et al., 2002; Lin et al., 2004; Lin et al., 2005a; Hsiao et al., 2007; Jana et al., 2008; Chen GJ et al., 2009), it is widely accepted that the giant dielectric response in these ceramics is associated with their heterogeneous microstructure, consisting of semiconducting grains (***A***–doped NiO) and insulating grain boundaries (***B***–rich insulating boundaries). It is interesting that the dielectric properties and the related electrical response of these NiO–based systems can be modified by varying the composition via additions of ***A*** and ***B*** (Wu J et al., 2002; Lin et al., 2006a). The presence of oxygen vacancies and the existence of internal domains might be responsible for these observations. These results imply that both DS and bulk grain effects may have impacts on the electrical and dielectric properties of these NiO-based ceramics. However, the experimental results supported these are still missing.

In this section for the Li and Fe co-doped NiO ceramics, the effects of insulating layers on the electrical properties of high-permittivity $Li_{0.05}Fe_xNi_{0.95-x}O$ (LFNO) ceramics are investigated. The results reveal that the electrical responses in the surface layers, grain boundaries, and grains have significant effects on the electrical properties of the LFNO ceramics. The evident surface-layer effect is proved by removing the sample surface layer, while the bulk grain effect is identified by applying dc bias. The close relationship between the relaxation mechanism and the electrical transport inside the grains is observed.

To brief, throughout this section, the symbols of LFNO-1Be and LFNO–2Be are assigned for the as-samples for $Li_{0.05}Fe_{0.05}Ni_{0.90}O$ and $Li_{0.05}Fe_{0.10}Ni_{0.85}O$ ceramics, and LFNO–1Af and LFNO–2Af for the sintered samples with surface polishing of $Li_{0.05}Fe_{0.05}Ni_{0.90}O$ and $Li_{0.05}Fe_{0.10}Ni_{0.85}O$ ceramics.

Figure 5.56(a) demonstrates the fractured surface of the $Li_{0.05}Fe_{0.10}Ni_{0.85}O$ ceramic sample, showing obvious structure consisting of grains and grain boundaries. Interestingly, the EDS analysis, as shown in figure 5.56(b), shows that the lower relative intensity of Fe atom is detected at the white core regions (points 2 and 5), but it is high at the hilly dark regions (points 1, 3, and 6). According to the XRD (did not shown) and ESD analyses, it is reasonable to suggest the existence of the core/shell structure in the LFNO ceramics, consisting of semiconducting core grains (e.g., Li–doped NiO) and Fe–rich insulating grain boundaries (e.g., $NiFe_2O_4$). The existent core/shell structure in the NiO–based ceramics was also be observed in the (Li, Si)–, (Li, V)–, and (Li, Ti)–doped NiO ceramic systems (Lin et al., 2005a, 2006). It is worth noting that the Fe–dopant is also rich on the outmost sample surfaces, as *displayed in the inset of Figure 5.56(a).*

It is clearly seen from figure 5.57 that the surface layer has a significant influence on the high dielectric properties of the LFNO ceramics. As illustrated in figure 5.57, after the LFNO–1Be sample was polished evenly from both sides, the decrease in dielectric constant and the exponential increase in the loss tangent (tanδ) were observed in the polished–LFNO–1Be sample (LFNO–1Af sample). Under an applied electric field, some mobile charges in the inner part of the bulk LFNO ceramics may be blocked by the surface layers. Thus, the Maxwell-Wagner polarization is produced by the accumulated charges at the interface between the insulating surface layers and the inner part. After the surface layers were removed, these accumulated charges are free and they become mobile charge carriers. Consequently, the polarization at the surface layer does not response, which causes decrease in the total polarization. On the other hand, the observed exponential increase in the loss tangent is suitably attributed to the dc conductivity effect. It is interesting that the LFNO–1Af sample still exhibits the high dielectric response, implying that there may be other polarizations contributing to the dielectric responses in the LFNO−1Af sample.

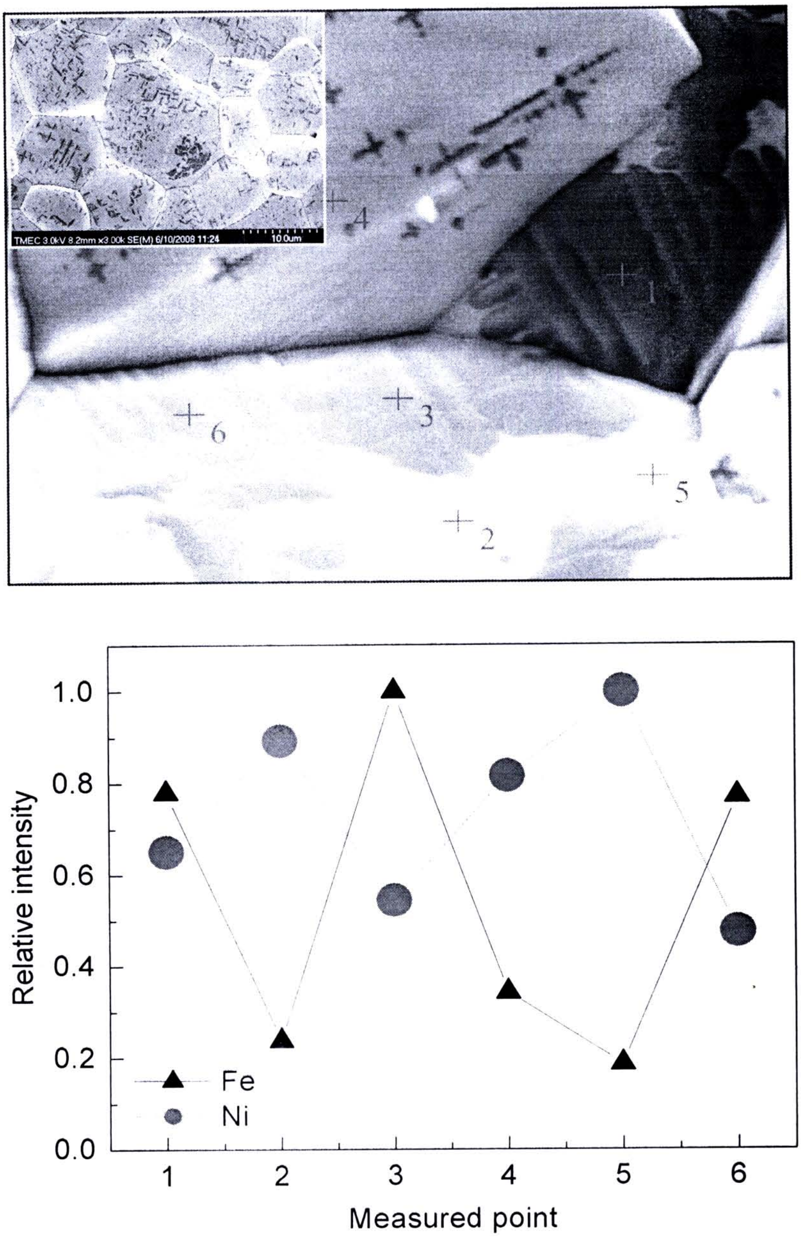

Figure 5.56 (a) Fractured surface of the $Li_{0.05}Fe_{0.10}Ni_{0.85}O$ sample and (b) shows Ni and Fe element profiles obtained from the EDS spectra at different points; inset shows SEM image of surface morphology.

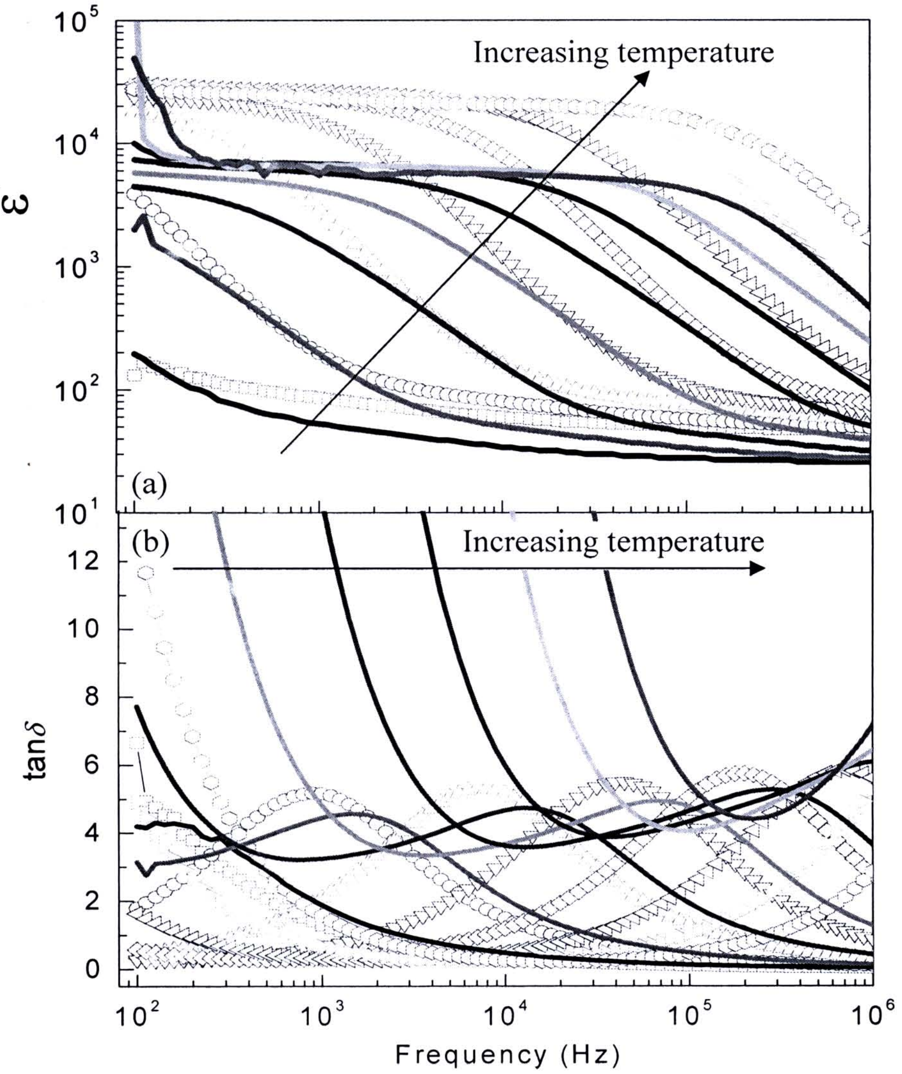

Figure 5.57 Frequency dependence of (a) dielectric constant and loss tangent for LFNO-1Be (symbols) and LFNO-1Af (solid lines) samples at various temperatures from -40 to 200 °C with the step increase in temperature is 30 °C.

Although the surface layers were removed, the relaxation peaks of the loss tangent still appear and the activation energy for relaxation process (E_a) remains almost constant, i.e., E_a = 0.483 eV (0.419 eV) and 0.468 eV (0.411 eV) for the LFNO–1Be (LFNO–2Be) and LFNO–1Af (LFNO–2Af) samples, respectively. Therefore, the E_a values of the LFNO ceramics may actually be affected by the relaxation in the inner part of the LFNO ceramics. This is similar to that observed in the CCTO ceramic (Wang, Zhang, 2006), which was clearly explained based on the different electrical conductivities between the surface layer and inner part due to the difference in oxygen concentration between them. This might be responsible for the formation of the insulating surface-layer in the LFNO ceramics. Moreover, the surface-layer effect may also be attributed to the fact that the shells of the grains are the $NiFe_2O_4$ phase, which is rich on the outmost surface layers of the LFNO ceramic samples (inset of Fig. 5.56).

Figure 5.58(a) shows the impedance spectra of the as–sintered LFNO and polished–LFNO ceramic samples, proving the surface-layer effect on their electrical properties. It is clear that, after the surface layers of the as–sintered samples were removed, the arcs of the polished–LFNO samples (LFNO-1Af and LFNO-2Af samples) at lower frequencies decreased, whereas the arcs at higher frequencies remained constant. These results strongly indicate that the enhanced arcs in the low frequency range contain two overlapped arcs, and thus the surface-layer and grain boundary effects are roughly separated. Consequently, it is reasonable to suggest that there are three sets of electrical responses in the LFNO ceramics, i.e., surface-layer, grain boundary and bulk grain responses. Based on the above analysis, it is clearly proved from figure 5.58(b) that the interfacial polarizations of the surface layers and grain boundaries are suppressed by applying dc bias, whereas the bulk polarization is independent of the biases.

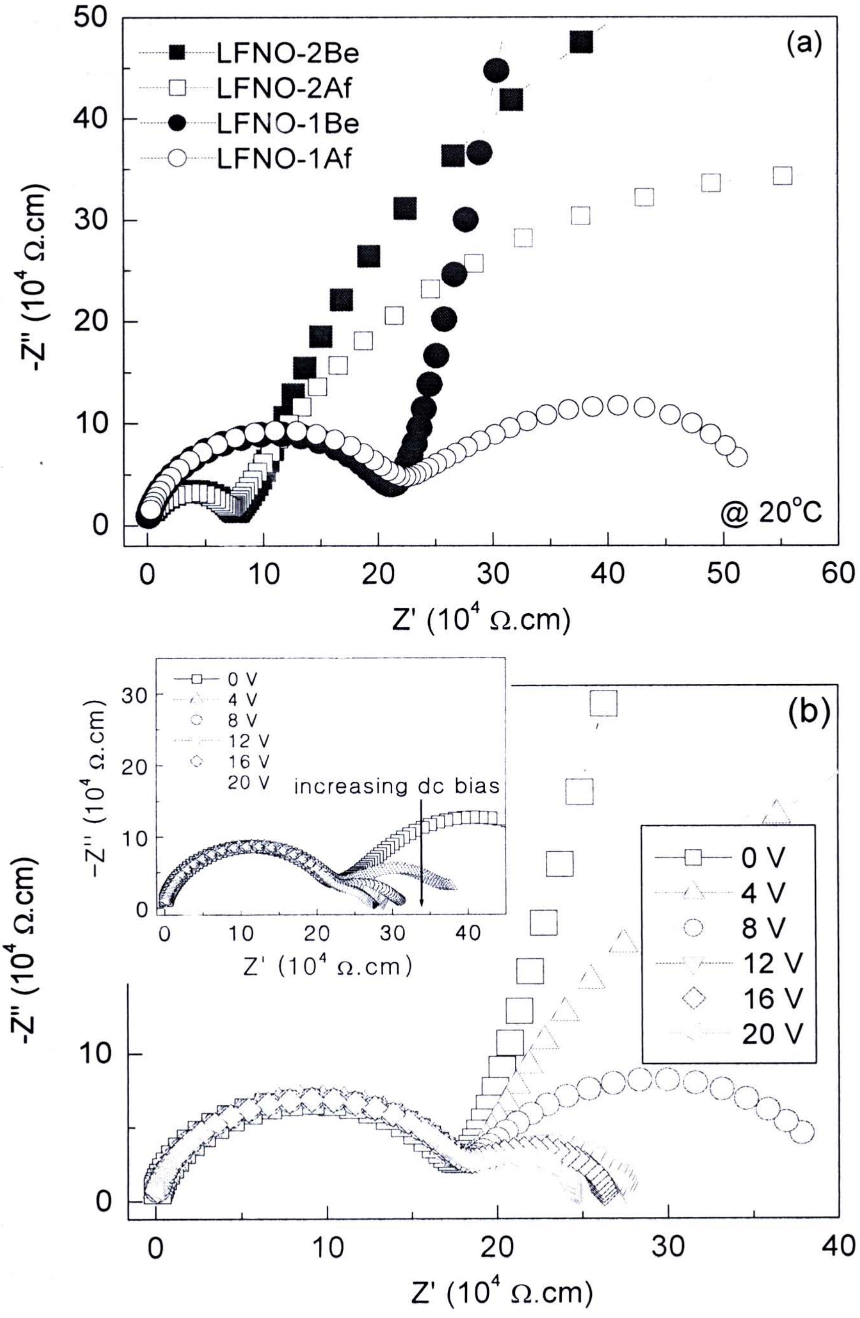

Figure 5.58 (a) Impedance spectra of LFNO samples before and after surface polishing at 20 °C. (b) Impedance spectra as a function of dc bias of LFNO-1Be; inset shows impedance spectra of LFNO-1Af.

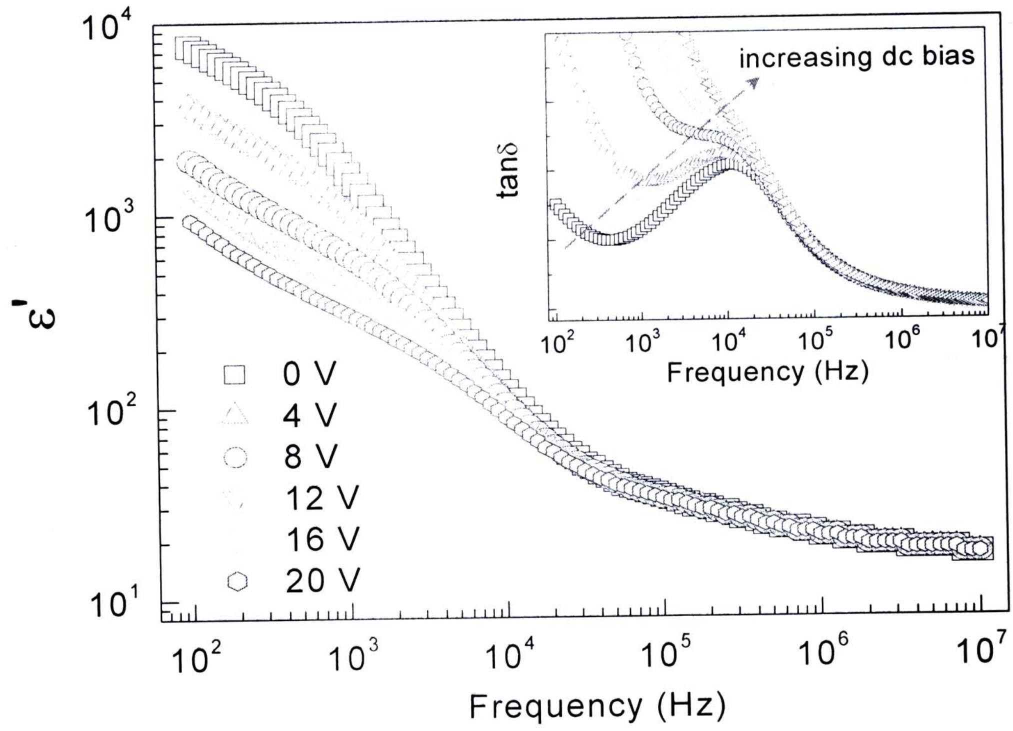

Figure 5.59 Frequency dependence of dielectric constant at various applied voltages at room temperature for LFNO-1Af sample; inset shows its frequency dependence of loss tangent at different applied voltages.

Figure 5.59 demonstrates the effect of dc bias on the frequency dependence of ε' for the LFNO-1Af sample at room temperature. It is found that, the dielectric constant values below 10^4 Hz decrease with the increase of applied voltage, corresponding to the decrease in the capacitance of grain boundaries (Guo et al., 2006), which is being accompanied by the decrease in R_{GB} (inset of Fig. 5.59(b)). These results suggest that, with increasing the applied voltage, the accumulated charge carriers are becoming more and more overcome the potential barrier at the grain boundaries, implying that these accumulated charge carriers become mobile charges. Consequently, the intensity of the space charge polarization at this region is decreased by the increase in the applied voltage, while the conductivity increases due to the increase in the mobile charge. This is confirmed by the observed exponential increase in loss tangent $\tan\delta$ at the highest applied voltage, as shown in the inset of figure 5.59. When the applied voltage increases over 20 V, the dc bias is over limit balance (over 20 V) due to the large leakage current, which results from the large conductivity in the bulk ceramics.

Figure 5.60 shows the frequency dependence of the imaginary parts Z'' of complex impedance at selected temperatures, in which Z'' plots usually highlight phenomena characterized by the large resistance. Two thermally activated electrical responses are observed at lower and higher frequencies—both shift to higher frequency with increasing the temperature. To identify these electrical responses, the frequency dependence of Z'' has been studied as a function of dc bias. As illustrated in the inset of figure 5.60, both the peak height and frequency of the Z'' peak of the electrical response at the lower frequency are strongly dependent of the applied voltage, but not for the higher–frequency electrical response. As a result, the lower– and higher–frequency electrical responses are suitably identified to the grain boundary and bulk effects, respectively. Moreover, it was found that the plots of $(Z'')_{\max}$ frequency and versus $1000/T$ follow the Arrhenius law, (does not present). The estimated activation energies of the LFNO-1Af (LFNO-2Af) were found to be 0.454 (0.408) and 0.444 (0.506) eV for the bulk grains and grain boundaries, respectively. The two activation energies of the electrical responses in the LFNO-1Af sample are similar to its relaxation activation energy. However, the activation energies of the grain electrical response in the LFNO-2Af and its relaxation are almost the same in value, while its activation energy of the grain boundary is larger than that of the relaxation activation energy. Therefore, it is appropriate to suggest that the relaxation mechanism in the LFNO ceramics has a close relation to the conductivity inside the grains. Lin *et al.*, (Lin et al., 2006b) reported that the dc conduction activation energy of pure–NiO ceramics could be increased by doping with Fe ions, which was attributed to the effects of $Fe_{Ni}^{\bullet}$ defects and the nickel vacancies. This might be responsible for the observed large relaxation activation energy in the LFNO ceramics comparing to the other NiO–based ceramics systems (Lin et al., 2005b, 2006a). With the larger conduction activation energy, the dielectric relaxation of the LFNO ceramics is hardly activated by thermal. Thus, the polarization should fully be responded at higher temperatures. From these points of view, it is believed that the relaxation behavior of the NiO–based ceramics can be adjusted by varying the semiconductivity of grains. Note that the increase of grain boundary conduction activation energy of the LFNO-2AF sample might be associated with the accumulation of $NiFe_2O_4$ phase at the grain boundary, as revealed in figure 5.56.

Finally, the high dielectric permittivity LFNO ceramics were investigated as functions of frequency, temperature, and dc bias. Three thermally activated electrical responses were observed at the surface layers, grain boundaries, and bulk grains. The effects of the surface layer and grain boundary were separated by removing the surface samples, whereas the applied dc bias was used to identify the electrical response of the bulk grain. It was found that the interfacial polarizations of the surface layers and grain boundaries could be suppressed by the applied voltage, but not for the bulk polarization.

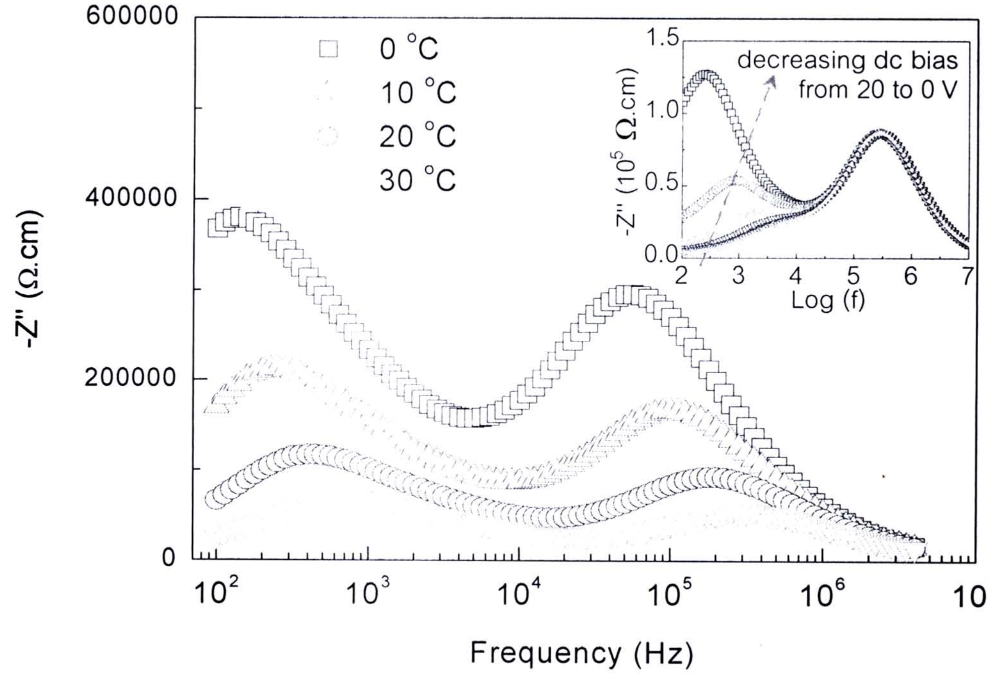

Figure 5.60 Frequency dependence of Z'' at various temperatures for LFNO-1Af sample. Inset shows the frequency dependence of Z'' at different applied voltages for LFNO-1Af sample.

5.3 Li and V co-doped NiO system

Figures 5.61(a)-5.61(c) show the XRD patterns of the $Li_{0.05}V_{y}Ni_{0.95-y}O$ (y = 0.02, 0.05, and 0.10) (LVNO) powders and the as-sintered ceramic samples with different concentrations V doping ions, confirming a main phase of NiO in all the samples. The second phase of NiV_2O_6 was only observed in the LVNO powder samples, but it was not detected in the as-sintered LVNO samples. However, after the as-sample for the $Li_{0.05}V_{0.10}Ni_{0.85}O$ was polished, the second phase of NiV_2O_6 could be observed (Fig. 5.61(d)). This might be due to the outmost layer surface of the sintered samples is V-phase deficient. Similar observation was reported for $CaCu_3Ti_4O_{12}$ (CCTO)/Ag composites having the Ag deficient in outmost layer and Ag rich in the inner part of the composites (Wang et al., 2006). From the SEM-EDS measurements, as revealed in figure 5.62, of the grains and grain boundary, however, it was found that the V dopant is rich at the grain boundary, but is indigent in the grain. Therefore, the LVNO samples have a heterogeneous structure consisting of the shell of grain and the core grain, regarding to an insulating V-rich boundary layer (i.e., NiV_2O_6) and Li-doped NiO particles, respectively

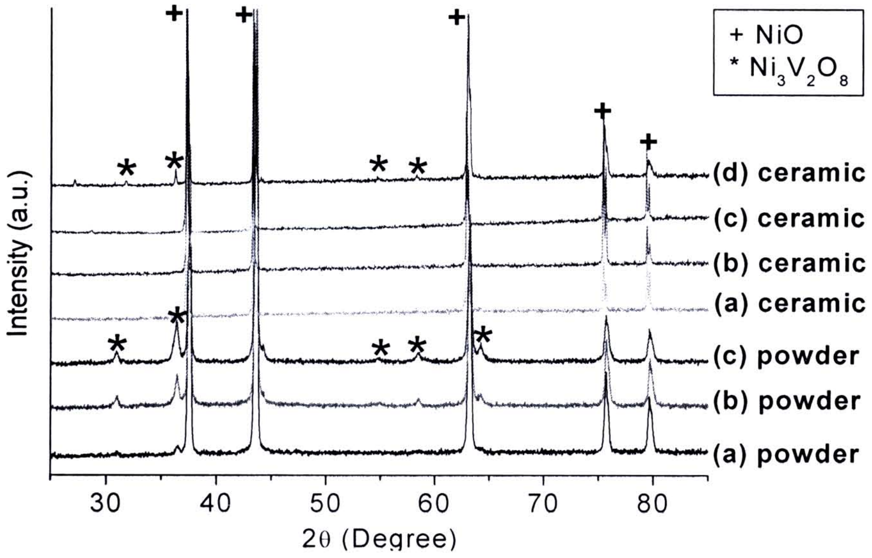

Figure 5.61 XRD patterns of the LVNO powders and sintered ceramics; (a) $Li_{0.05}V_{0.02}Ni_{0.93}O$ (b), $Li_{0.05}V_{0.05}Ni_{0.90}O$, and (c) $Li_{0.05}V_{0.10}Ni_{0.85}O$; (d) is XRD pattern of $Li_{0.05}V_{0.10}Ni_{0.85}O$ with polished surface.

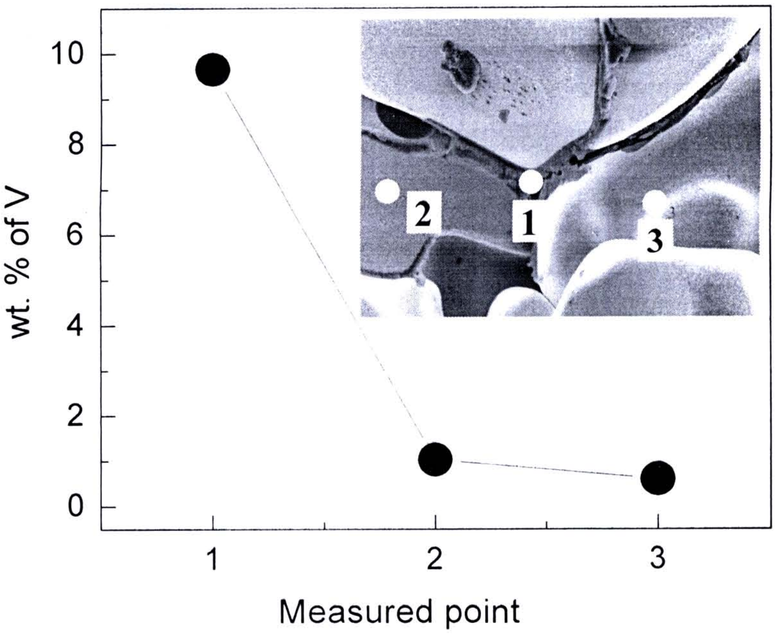

Figure 5.62 The element profile obtained from EDS spectra.

The dielectric properties of the LVNO samples were measured over wide ranges of temperature and frequency. The dielectric constant values at 1 kHz and room temperature for the $Li_{0.05}V_{0.02}Ni_{0.93}O$, $Li_{0.05}V_{0.05}Ni_{0.90}O$, and $Li_{0.05}V_{0.10}Ni_{0.85}O$ ceramics are 61,907, 34,854, and 30,503, respectively. It is seen that all of the LVNO samples exhibit the high-dielectric constant values. The dielectric constant decreases with increasing V doping ions concentration, which can be attributed to the increase in the thickness of the grain boundary layer (t_{gb}). Similar result was reported for $Li_xTi_yNi_{1-x-y}O$ (LTNO) system, and the giant ε' of this LTNO system was explained by the simple series-layer model for the boundary-layer capacitors (BLC) (Wu J et al., 2002). Figure 5.63 demonstrates the frequency dependence of dielectric permittivity (ε') and dielectric loss (ε'') of the $Li_{0.05}V_{0.05}Ni_{0.90}O$ ceramic at different temperatures. The dielectric constant shows the high values at low frequencies, and it rapidly decreases if the frequency is sufficiently high. This step decrease shifts to higher frequency with increasing the temperature, corresponding to the movement of the ε'' peaks. This behavior is similar to that observed in the other NiO-based ceramic systems (Wu J et al., 2002; Lin et al., 2004) and the other giant dielectric systems such as $CaCu_3Ti_4O_{12}$ (Homes et al., 2001; Thongbai et al., 2007) and CuO ceramics

(Sarkar et al., 2006). Such behavior is typical for the Maxwell-Wagner relaxation, which is generally employed to describe the observed high-dielectric constant in electrically inhomogeneous materials (Lin et al., 2006a). Thus, the observed core/shell structure in the LVNO samples is responsible for their apparent giant dielectric response. According to the fitted curve using equation (5.9), as shown in figure 5.64 for the LVNO samples with different V contents, the E_a values can be obtained to be 0.221, 0.250, and 0.261 eV for the $Li_{0.05}V_{0.02}Ni_{0.93}O$, $Li_{0.05}V_{0.05}Ni_{0.90}O$, and $Li_{0.05}V_{0.10}Ni_{0.85}O$ ceramics, respectively.

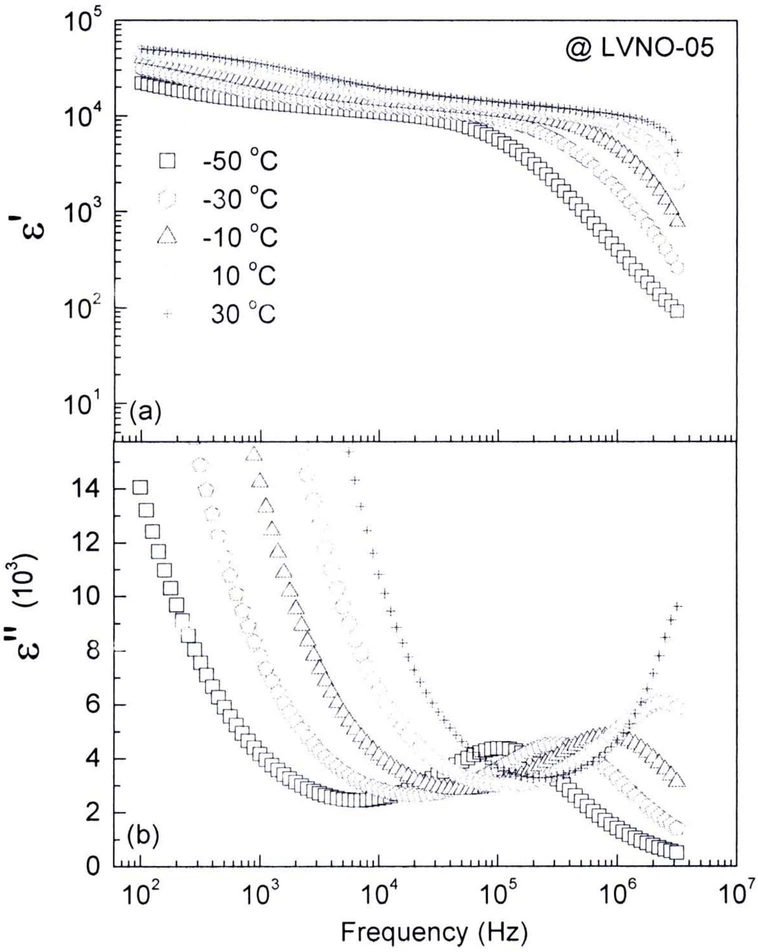

Figure 5.63 Frequency dependence of (a) the dielectric constant (ε') and (b) dielectric loss (ε'') at different temperatures. Inset is the temperature dependence of the relaxation time for the different LVNO samples.

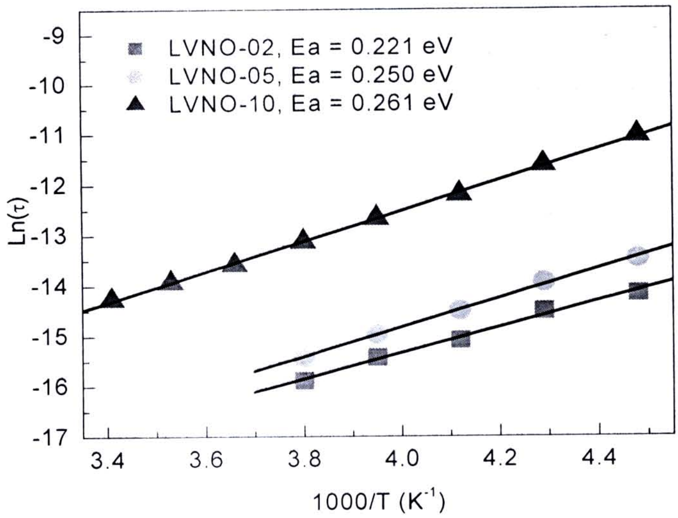

Figure 5.64 Temperature dependence of relaxation times of LVNO ceramics.

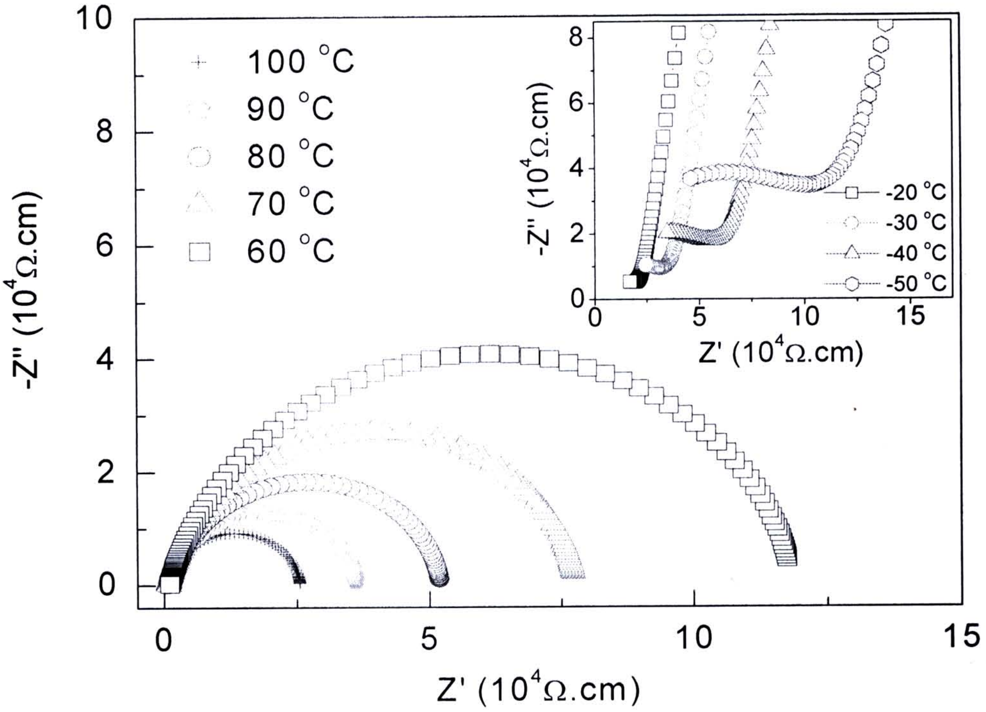

Figure 5.65 Impedance spectra as a function of temperature for the $Li_{0.05}V_{0.10}Ni_{0.85}O$ ceramic; inset shows impedance spectra at a low-temperature range.

To characterize the electrical properties of the core/shell structure in the LVNO ceramics, impedance spectroscopy (Sinclair et al., 2002) which is a powerful tool in separating out the bulk and the grain boundary effects was carried out. As illustrated in figure 5.65, the impedance semicircle spectra of the $Li_{0.05}V_{0.10}Ni_{0.85}O$ ceramic become larger with decreasing temperature. When the temperature is sufficiently low, other impedance semicircles can be observed (inset of Fig. 5.65). The observation of the two semicircles suggests that the LVNO ceramics are electrically heterogeneous, and thus a core/shell model is appropriated for further analysis. Accordingly, the observed semicircles at higher and lower temperatures can be assigned to the effects of charge transport within the grain and grain boundary, respectively. Note that, the impedance spectra of the $Li_{0.05}V_{0.02}Ni_{0.93}O$ and $Li_{0.05}V_{0.05}Ni_{0.90}O$ ceramics are similar to that of the $Li_{0.05}V_{0.10}Ni_{0.85}O$ ceramic, but their impedance semicircles at low temperature can not be detected (does not present). This might be attributed to that the electrical responses of grain of these samples shift out of the measured frequency range.

As known, the conduction mechanism of the Li-doped NiO system can be well explained by the polaron hopping theory (Lin et al., 2005b, 2006a). In polaronic scenario, the temperature dependence of the conductivity (σ) is, with a temperature dependence prefactor, ascribed as,

$$\sigma \propto T^{-1} \exp\left(-E / k_B T\right), \tag{5.28}$$

where E, is the conduction activation energy. Normally, the GB effect on electric conductivity may originate from a grain boundary potential barrier (Lin et al., 2006a), which should be ascribed by the V-rich boundary for the LVNO system. From the intercepts of each semicircular arc with the real axis, the resistance of the grain (R_g) and the resistance of the grain boundary (R_{gb}) can be calculated. As a result, conductivity data were obtained for the grain (σ_g) and grain boundary (σ_{gb}) components. Interestingly, the temperature dependence of σ_g and σ_{gb} follows equation (5.28), as respectively shown in figure 5.66(a) and figure 5.66(b). As a result, the conduction activation energies inside the grain (E_g) and at the grain boundary (E_{gb})

can be obtained—the values of E_g are 0.202, 0.246, and 0.274 eV, while the values of E_{gb} are 0.323, 0.414, and 0.413 eV for the $Li_{0.05}V_{0.02}Ni_{0.93}O$, $Li_{0.05}V_{0.05}Ni_{0.90}O$, and $Li_{0.05}V_{0.10}Ni_{0.85}O$ ceramics, respectively. These results strongly indicate that the grain and grain boundary have different characteristics of electrical transport.

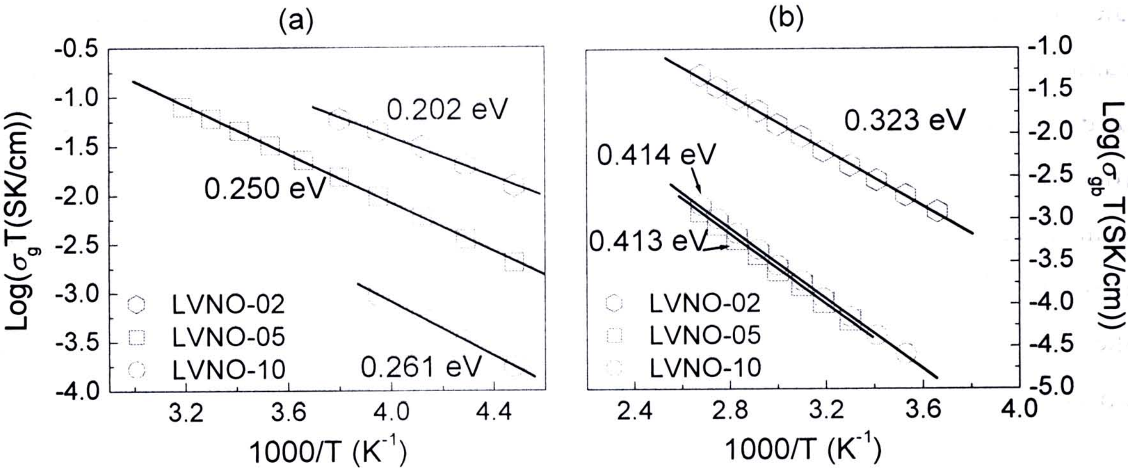

Figure 5.66 Temperature dependence of grain (a) and (b) grain boundary conductivity.

It is important to note that the values of E_g and E_a of each sample are almost the same in value. Similar result was observed in the LTNO system as reported by Lin *et al.* (Lin et al., 2006a) The authors explained that the natures of charge carriers responsible for dielectric relaxation peaks and dc conduction belonged to the same category, which indicated that the polarization relaxation had a close relation to the conductivity in the grain interior, and the polarization process depended on the conducting of the charge in the grain interior. Moreover, it is interesting that both of E_g and E_a in the LVNO samples increase with increasing the V content, but E_{gb} slightly changes as the V-dopant is more than 5 mol %. These results suggest that the NiV_2O_6 phase only changes the t_{gb} value which has an influence on the dielectric constant, but not the intrinsic properties of the LVNO ceramics. Furthermore, it can be seen that the concentration of the V dopant has a strong effect on the electrical transport characteristic inside the grain and the related dielectric behavior of the

LVNO ceramics. This is due to the fact that some part of V have entered into the NiO crystal lattice (indicated by the EDS analysis in inset of Fig. 5.62) leading to the variation of E_g. Obviously, the $Li_{0.05}V_{0.02}Ni_{0.93}O$ ceramic with the smaller E_g value shows a higher dielectric constant among these three samples. This is possibly due to the following two reasons. First, the polarization process is closely related to the conduction of the charge carriers in the grain interiors (Cheng B et al., 2008); second, the t_{gb} of the $Li_{0.05}V_{0.02}Ni_{0.93}O$ ceramic sample is smaller than those of the other two samples (Wu J et al., 2002). Additionally, it is found that the temperature at loss peak at the fixed frequency shifts to the low temperature with decreasing V concentration (does not show), corresponding to the decrease in E_g. This is because the electrical charge carriers in the grain interiors of the sample with the lowest E_g can easily be thermally activated. Therefore, the discrepancy in E_g and t_{gb} of each sample caused by the different concentrations of V doping results in the various dielectric behavior observed in the LVNO system.

Finally, the giant dielectric constant and related electrical properties of LVNO ceramics have been characterized as functions of frequency and temperature. EDS results reveal that the V dopant is rich at grain boundary and exists as the insulating NiV_2O_6 phase. The concentration of the V has a remarkable effect on the dielectric properties of the LVNO ceramics due to the difference in the values of E_g and t_{gb}. The giant dielectric behavior of the LVNO ceramics can be explained based on the Maxwell-Wagner polarization (i.e., interfacial polarization) and thermally activated mechanisms

5.4 Effects of various valent states of doping ions on the microstructure and electrical properties of giant dielectric NiO-based ceramics

Generally, the relationship between the structure of materials and their properties is studied at two different levels of length scale: microscopic level and microstructural level. Thus, the inhomogeneities within macroscopically homogeneous ceramic materials can be classified as microscopic and microstructural inhomogeneities. Lattice defects and the grain growth are possible causes for these two inhomoheneities, respectively (Nan, 1993).

In recent years, high permittivity Bi/Pb-free dielectric materials with good thermal stability have particularly attracted ever-increasing attention for their practical applications in microelectronics such as capacitors and memory devices. High-permittivity $\boldsymbol{A}_x\boldsymbol{B}_y\mathrm{Ni}_{1\text{-}x\text{-}y}\mathrm{O}$ ceramic system (where $\boldsymbol{A}$ = Li, Na, K and $\boldsymbol{B}$ = Ti, Al, Ta, Si) is one of the most important high-permittivity materials that has been intensively researched in the recent years (Wu J et al., 2002; Maensiri et al., 2007; Lin et al., 2004, 2005a; Jana eet al., 2006, 2008; Hsiao et al., 2008). It is widely accepted that a high dielectric constant of these materials is attributed to the Maxwell-Wagner polarization mechanism based on the existence of the inhomogeneities of grain, grain boundary and defects within the materials. Interestingly, the dielectric properties and related electrical response of these NiO-based systems can be tuned by changing the composition of the additives of A and $\boldsymbol{B}$ (Wu J et al., 2002), which normally have the effects on the grain and grain boundary properties, respectively. However, it has been reported that the Ti content in the $\mathrm{Li}_x\mathrm{Ti}_y\mathrm{Ni}_{1\text{-}x\text{-}y}\mathrm{O}$ system also has a strong effect on the transport properties inside the grain, which should be attributed to the fact that some part of Ti has entered into the NiO crystal lattice.

In this section, the effects of the microstructure, grain and grain boundary modifications on the giant dielectric properties of the $\mathrm{Li}_{0.05}\boldsymbol{B}_{0.02}\mathrm{Ni}_{0.93}\mathrm{O}$ ($\boldsymbol{B}$ = Fe, Ti, and V) ceramics are discussed. The results suggest that Fe, Ti, and V doping has great impacts on the microstructure and the electrical transports of the grains and grain boundaries, which are major contributions on the giant dielectric response in these materials.

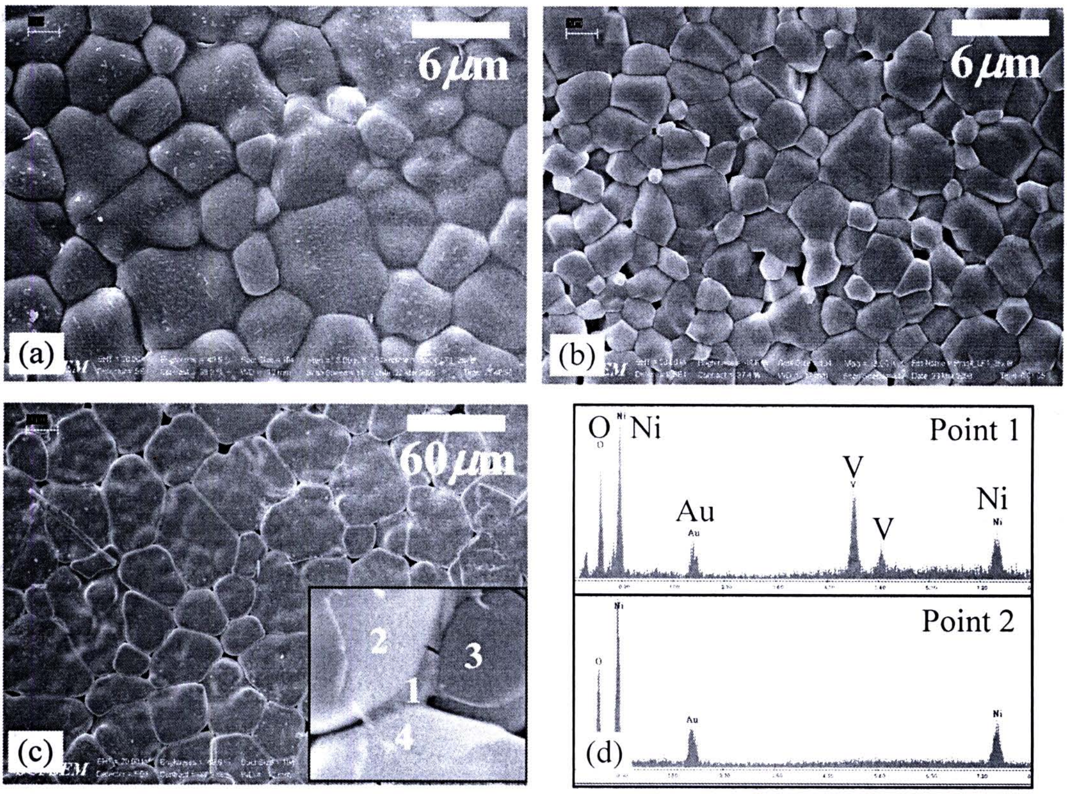

Figure 5.67 SEM images of the surfaces for the (a) $Li_{0.05}Ti_{0.02}Ni_{0.93}O$, (b) $Li_{0.05}Fe_{0.02}Ni_{0.93}O$, and (c) $Li_{0.05}V_{0.02}Ni_{0.93}O$ ceramics; inset of Fig. 5.67(c) shows the fractured surface of the LVNO sample. (d) EDS spectra of the grains and grain boundary for $Li_{0.05}V_{0.02}Ni_{0.93}O$ ceramic.

Figures 5.67(a)-5.67(c) show surface morphologies of the $Li_{0.05}Ti_{0.02}Ni_{0.93}O$, $Li_{0.05}Fe_{0.02}Ni_{0.93}O$, and $Li_{0.05}V_{0.02}Ni_{0.93}O$ ceramic samples, indicating that Fe, Ti, and V doping ions have a remarkable effect on their microstructures. The mean grain sizes of the $Li_{0.05}Ti_{0.02}Ni_{0.93}O$, $Li_{0.05}Fe_{0.02}Ni_{0.93}O$, and $Li_{0.05}V_{0.02}Ni_{0.93}O$ ceramic samples are 3.34, 4.8, and 45.79 μm, respectively. The observed abnormal grain growth in the LVNO sample is attributed to a typical liquid phase of their microstructure, which usually contribute to form the grain-to-grain bridges and to eliminate of the inter-grain pores. The effect of V-dopant on the microstructure of ceramics has also been observed in V-doped ZnO system. It was caused by the relatively low melting points of V and the related second phase (Tsai, Wu, 1994).

Inset of figures 5.67(c) illustrates the fracture surface of the $Li_{0.05}V_{0.02}Ni_{0.93}O$ ceramic sample, showing the obvious grain and grain boundary structures. The EDS measurements of the grain (point 2) and grain boundary (point 1) of the $Li_{0.05}V_{0.02}Ni_{0.93}O$ ceramic sample, as shown in figures 5.67(d), reveal the V-rich at the grain boundary but not in the grain. The EDS spectra at point 3 and point 4 (not shown) are similar to that detected at point 2, i.e., no corresponding peak of V observed. Therefore, the shells of the grains of these three samples could be regarded as Fe-, Ti-, and V-rich boundaries, while the core of the grains is part of Li-doped NiO particles. Thus, dielectric properties of these ceramics might be ascribed by the Maxwell-Wagner polarization.

Figure 5.67(a) demonstrates the frequency dependence of dielectric constant and loss tangent of the samples of the $Li_{0.05}Ti_{0.02}Ni_{0.93}O$, $Li_{0.05}Fe_{0.02}Ni_{0.93}O$, and $Li_{0.05}V_{0.02}Ni_{0.93}O$ ceramics at 30 ^{o}C, showing the giant dielectric constant (10^4-10^5) response in all ceramic samples. The $Li_{0.05}Ti_{0.02}Ni_{0.93}O$ sample has the lowest dielectric constant among these three samples over the measured frequency range, corresponding to the observed lowest value of the loss tangent. The dielectric constant of the $Li_{0.05}V_{0.02}Ni_{0.93}O$ ceramic is slightly higher than that of the $Li_{0.05}Fe_{0.02}Ni_{0.93}O$ ceramic sample, and interestingly its loss tangent is lower than that of the $Li_{0.05}Fe_{0.02}Ni_{0.93}O$ ceramic sample at below and above frequency 10^4 Hz. The small step decrease of the $Li_{0.05}V_{0.02}Ni_{0.93}O$ ceramic sample at the frequency about 10^4 Hz might be attributed to the heterogeneous relaxation such as defect-induced polarization (Jana et al., 2008). Figure 5.67(b) illustrates the temperature dependence of the dielectric constant of the $Li_{0.05}V_{0.02}Ni_{0.93}O$ ceramic sample at the selected frequencies. The temperature independence of the dielectric constant can be observed at frequency below 100 kHz. However, with increasing the frequency, the dielectric constant drops dramatically to the low values at low temperatures, and such step decrease moves to the higher temperature range with increasing the frequency. This is a suggestion of the thermally excited relaxation process. The overall dielectric behavior is similar to those observed in other NiO-based ceramics (Wu J et al., 2002), which is in marked contrast to the well-known ferroelectric one resulting from the structure distortion due to the soft-mode condensation.

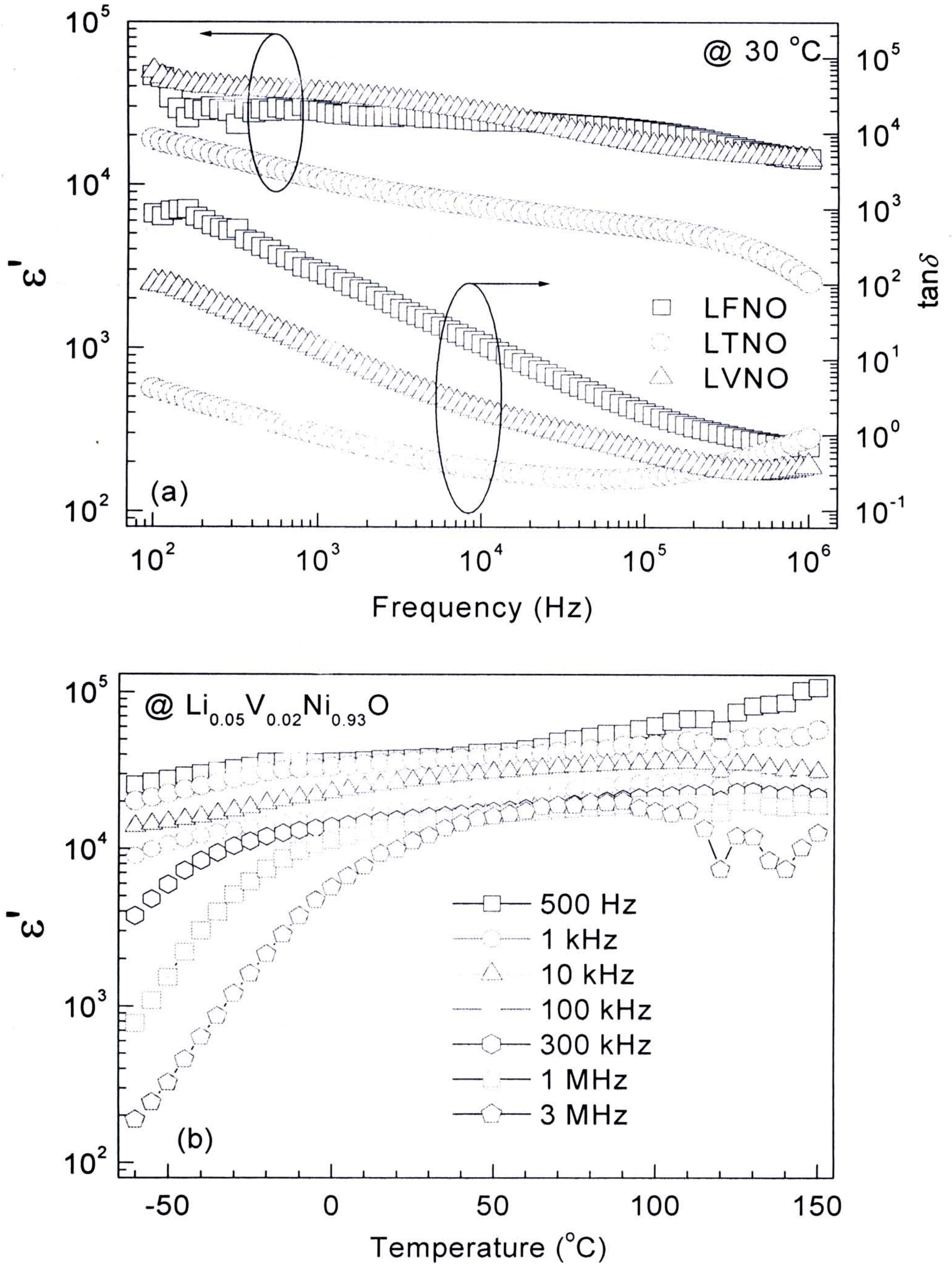

Figure 5.68 Frequency dependence of dielectric constant and loss tangent at 30 °C for the $Li_{0.05}Ti_{0.02}Ni_{0.93}O$, $Li_{0.05}Fe_{0.02}Ni_{0.93}O$, and $Li_{0.05}V_{0.02}Ni_{0.93}O$ ceramics. (b) The temperature dependence of dielectric constant at selected frequencies for the $Li_{0.05}V_{0.02}Ni_{0.93}O$ ceramic.

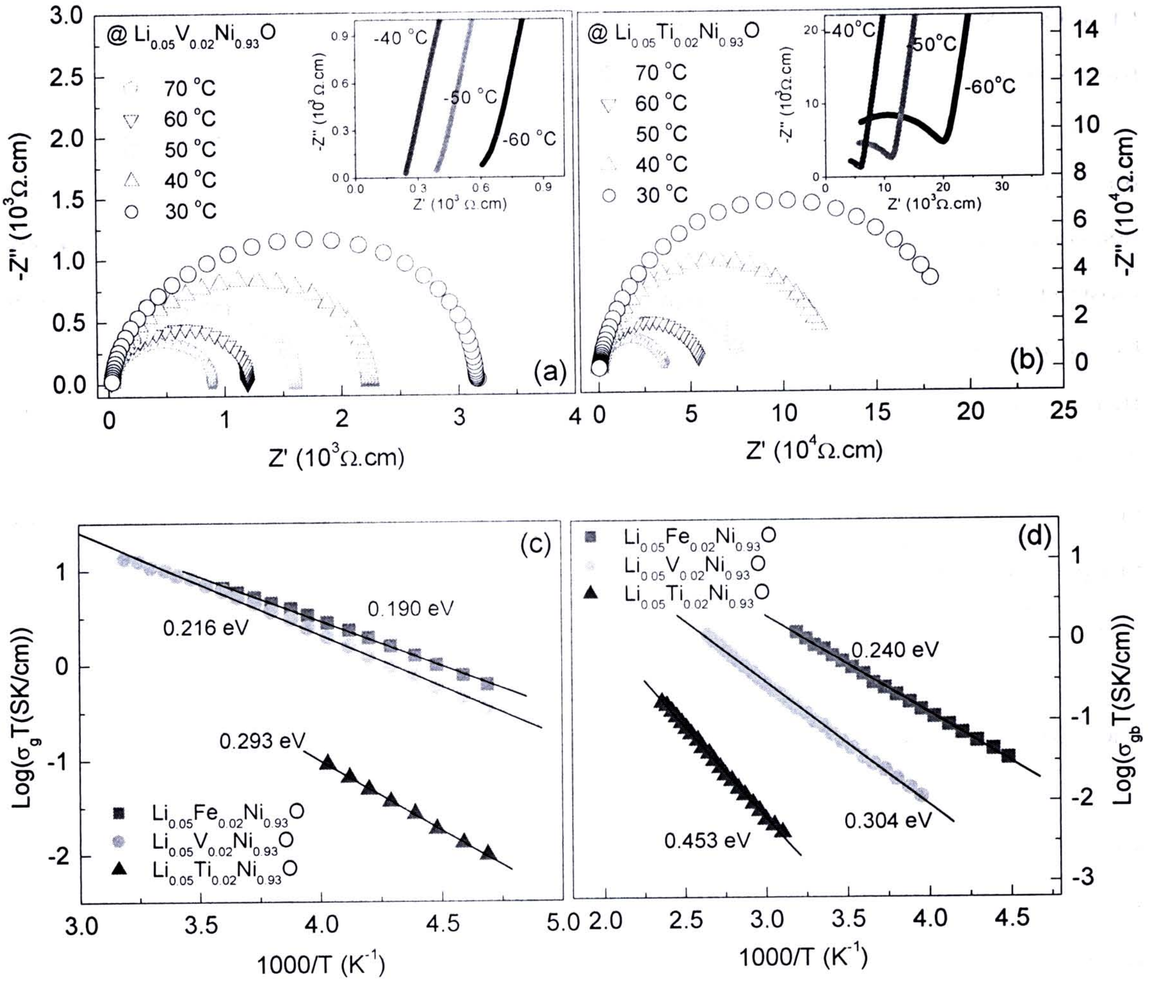

Figure 5.69 The complex impedance plane plots for the (a) $Li_{0.05}V_{0.02}Ni_{0.93}O$ and (b) $Li_{0.05}Ti_{0.02}Ni_{0.93}O$ ceramics at various temperatures; insets show the corresponding impedance spectra at low temperatures. (c) and (d) are the Arrhenius plots of the conductivities of the grains and grain boundaries, respectively.

Figures 5.69(a) and 5.69(b) demonstrate the complex impedance plain plots of the $Li_{0.05}V_{0.02}Ni_{0.93}O$ and $Li_{0.05}Ti_{0.02}Ni_{0.93}O$ ceramics, respectively. The impedance semicircles become larger with decrease in temperature, and when the temperature is sufficiently low, the other impedance semicircles of the $Li_{0.05}Ti_{0.02}Ni_{0.93}O$ ceramic sample can be observed (inset of Fig. 5.69(b)). The observed two semicircles suggest the existence of the electrical inhomogeneities in the $Li_{0.05}Ti_{0.02}Ni_{0.93}O$ ceramic. Accordingly, the observed semicircles at lower and higher temperatures in the

$Li_{0.05}Ti_{0.02}Ni_{0.93}O$ ceramic sample can be assigned to the effects of the charge transport within the grain and grain boundaries. Note that, the impedance semicircles at low temperature can not be observed in the $Li_{0.05}V_{0.02}Ni_{0.93}O$ ceramic sample and the $Li_{0.05}Fe_{0.02}Ni_{0.93}O$ ceramic sample (not shown). This is because the electrical responses of grains in both samples shift out of the measured frequency range. However, the nonzero intercepts at low temperatures can be assigned to the effects of the grains (Sinclair et al., 2002). Consequently, the core/shell model is appropriate for further analysis. Generally, the GB effect on electric conductivity may originate from a GB potential barrier,[9] which should be ascribed by the Fe-, Ti-, and V-rich boundaries for the NiO-based systems. Based on the RC model, the resistances of the grain and grain boundary can be obtained at various measuring temperatures. According to the fitted curves using equation (5.28) for the $Li_{0.05}Fe_{0.02}Ni_{0.93}O$, $Li_{0.05}V_{0.02}Ni_{0.93}O$, and $Li_{0.05}Ti_{0.02}Ni_{0.93}O$ ceramic samples shown in Figures 5.69(c) and 5.69(d), the conduction activation energies inside the grain (E_g) and at the GB (E_{gb}) can be estimated—the values of E_g are 0.190, 0.216, and 0.293 eV, while the values of E_{gb} are 0.240, 0.304, and 0.453 eV for the samples of $Li_{0.05}Fe_{0.02}Ni_{0.93}O$, $Li_{0.05}V_{0.02}Ni_{0.93}O$, and $Li_{0.05}Ti_{0.02}Ni_{0.93}O$ ceramic samples, respectively. These results indicate that the grain and grain boundary of these materials have different characteristics of electrical transport.

As previously reported (Cheng et al., 2008), the different valence states of ***A*** in the $\boldsymbol{A}_{0.03}Ti_{0.10}Ni_{0.87}O$ (A = K^{+}, Mg^{2+} and Y^{3+}) materials had a remarkable effect on the dielectric properties of NiO-based ceramics, which should be mainly attributed to the large variation of E_g values. In the present work, the different observed values of E_g and E_{gb} of these three NiO-based ceramics imply that the Fe, Ti, and V doping have the remarkable effects on both grain and grain boundary conductivities. Such various E_g values observed in the $Li_{0.05}Ti_{0.02}Ni_{0.93}O$ and $Li_{0.05}Fe_{0.02}Ni_{0.93}O$ ceeramic samples may be caused by the substitution of some parts of Ti^{4+} (0.68 Å) and Fe^{3+} (0.64 Å) ions into the Ni^{2+} (0.69 Å) ion sites in the NiO crystal lattice, which induces the different defects (i.e., $Fe_{Ni}^{\bullet}$ and $Ti_{Ni}^{\bullet\bullet}$) in the grain interiors (Lin et al., 2006a,b). The different electrical properties of these two samples can suitably be referred to as the microscopic inhomogeneity effect. On the other hand, the V-doping is most likely to present only at grain boundaries to form a second liquid phase, as clearly seen in figures 5.67(c) and 5.67(d). Sub-grains usually develop inside larger grains and affect the mobility of charge carriers and the dielectric response at different frequencies (Fang, Liu, 2005). This would be responsible for the observed highest low-frequency dielectric constant of the $Li_{0.05}V_{0.02}Ni_{0.93}O$ ceramic among these three samples. These results indicate that the microstructural inhomogeneity has a strong effect on the electrical properties of the NiO-based ceramics. Additionally, the relaxation activation energies (E_a) of the $Li_{0.05}V_{0.02}Ni_{0.93}O$ (0.224 eV) and $Li_{0.05}Ti_{0.02}Ni_{0.93}O$ (0.287 eV) samples are almost the same as their E_g values (data not shown). E_a of the $Li_{0.05}Fe_{0.02}Ni_{0.93}O$ ceramic with the smallest E_g cannot be obtained because its dielectric relaxation peak shifts out of the measured temperature range. Therefore, it is suggested that the observed lowest dielectric constant of the $Li_{0.05}Ti_{0.02}Ni_{0.93}O$ ceramic sample among these three samples and such disappeared relaxation peak of the $Li_{0.05}Fe_{0.02}Ni_{0.93}O$ ceramic sample are due to the fact that the polarization relaxation in these three samples has a close relation to the conductivity inside the grains. Therefore, it is reasonable to suggest that the Fe, Ti, and V dopants have significant effects on both the microstructure and the electrical transports inside the grain and at the grain boundaries, which leads to the different dielectric responses in these NiO-based ceramics. These different ceramic properties can be ascribed to both microscopic and microstructural inhomogeneities, which should be due to the differences in the valence state and the melting point of the dopants, respectively.

Turning to see the effects of Fe, Ti, and V doping on the grain boundary conductivity in the NiO-based ceramics, it is reported the positive values of the Seebeck coefficient of Fe-doped NiO samples, indicating that holes are major carriers in these samples (Lin et al., 2006b). In the case of $Li_{0.05}Fe_{0.02}Ni_{0.93}O$ ceramic sample, it is believed that the different concentrations of the holes at the grains and grain boundaries might be attributed to the effects of Li- doped NiO and Fe-doped NiO, respectively. This is responsible for the slight difference between E_g and E_{gb} in the LFNO sample. Thus, the different values of E_{gb} in the NiO-based ceramic samples could be attributed to the difference in the intrinsic properties of the grain boundaries, which are affected by the dopants.

In conclusion of this section, the giant dielectric $Li_{0.05}\boldsymbol{B}_{0.02}Ni_{0.93}O$ ($\boldsymbol{B}$ = Fe, Ti, and V) ceramics have been investigated. The giant dielectric response and related electrical properties of these materials are studied as functions of frequency and temperature. The results demonstrate that Fe, Ti, and V doping ions have great effects on both microstructure and electrical properties of the grains and grain boundaries, resulting in the giant dielectric response in these materials. The giant dielectric behavior of these NiO-based ceramics can be explained based on the Maxwell-Wagner polarization and thermally activated mechanisms.

5.5 Dielectric and electrical properties of NiO-based ceramic systems prepared by a direct thermal decomposition method

5.5.1 Li and Ti co-doped NiO ceramics: Effect of sintering temperature on dielectric properties

Dielectric oxide ceramics with high dielectric constant have raised considerable research attentions in recent years because these oxides play an important role in microelectronics, and have numerous technological applications such as capacitors and memory devices (Homes et al., 2001). Generally, high-permittivity dielectric materials are ferroelectric and relaxor oxides. However, both kinds of materials have dielectric constants that strongly depend on temperature and their structures contain lead, which it pollutes the environment. Therefore, lead-free materials with high dielectric constant and good thermal stability are becoming increasingly attractive. For non-perovskite NiO-based ceramic materials, it is now widely accepted that the high dielectric constant at radio frequencies is associated with internal barrier layer capacitance (IBLC) effect arising from core/shell structure, which induces Maxwell-Wagner polarization at the interfaces between grains and grain boundaries. The relative high-valent cation doping is rich on the grain boundaries (indigent within the grains) and forms a second phase which acts as an insulator enclosing the core of the grain which is semiconductive Li-doped NiO particles, and the polarization relaxation is closely related with the conductivity in the grain interior. Moreover, it was found that the dielectric response of $Li_xTi_yNi_{1-x-y}O$ system could be also enhanced by the polarization of defect dipoles such as oxygen vacancies (Lin et al., 2005b). Normally, such defect is easily induced by processing conditions (e.g., sintering temperature and duration of sintering) (Sinclair et al., 2002; Adams et al., 2006) and the concentration of defect depend on the microstructure of ceramics such as grain size (Fang, Liu, 2005). Therefore, the processing conditions should have a strongly influence on the polycrystalline ceramics properties (e.g., electric conductivity and optical and dielectric properties).

Unfortunately, only a few studies have focused on the effect of sintering conditions on the dielectric properties of NiO-based ceramics. The study of the influence of sintering conditions (effects of grain size) on the electrical properties of (Li, Ti)-doped NiO ceramics have not been reported. Generally, the sintering conditions are often used to tune the microstructure of ceramics, leading to dramatic changes in its electrical properties. Thus, investigation of the effects of sintering conditions may not only be useful to optimize the preparing conditions for the future applications, but also be able to provide the important clues about the underlying mechanism governing the intriguing dielectric behavior of ceramics.

In this section, the effects of grain size on dielectric and electrical properties of the $Li_{0.05}Ti_{0.02}Ni_{0.93}O$ ceramics synthesized by a simple thermal decomposition method is investigated. The results demonstrate that high dielectric constant increases with an increase in grain size. Impedance spectroscopy result shows that the $Li_{0.05}Ti_{0.02}Ni_{0.93}O$ ceramics has an electrically heterogeneous structure. The high dielectric constant behavior and dielectric relaxation of the $Li_{0.05}Ti_{0.02}Ni_{0.93}O$ ceramics are also investigated and it is suggested that such a dielectric response can be enhanced by the IBLC mechanism through Maxwell-Wagner relaxation. Interestingly, the activation energy required for relaxation and related conduction activation energy inside the grain decreases with grain size increasing, which may be attributed to the effect of oxygen vacancies in ceramics.

Figure 5.70 shows the XRD patterns of the prepared $Li_{0.05}Ti_{0.02}Ni_{0.93}O$ powder and sintered ceramics with different sintering temperatures, confirming a single phase of NiO in the powder and ceramic samples. All of the main peaks are comparable to that of powder diffraction pattern of NiO in JCPDS card No. 78-0429. The values of lattice parameter calculated from XRD spectra are shown in Table 5.9. These values are close to value reported in JCPDS card No. 78-0429. Additionally, it is also important to notice that a normal insulating phase $NiTiO_3$ does not detected in the XRD patterns. This is not surprising given that the typical detection limit of the technique when the Ti content is less than 0.05 and/or it might be attributed to the Ti-dopant content which is not over the solid solution limitation of Ti-Ni-O system, forming a single solid solution.

The surface morphology of $Li_{0.05}Ti_{0.02}Ni_{0.93}O$ ceramics is revealed by scanning electron microscopy as shown in figures 5.71(a) and 5.71 (b). It is clear that the grain size increases with increasing the sintering temperature. The mean grain sizes are about 2.67 and 6.02 μm for the ceramics sintered at 1200 and 1280 °C. Note that, large portion of porosity is observed in the microstructure of the ceramic sintered at 1200 °C, but the ceramic sintered at 1280 °C is dense ceramic.

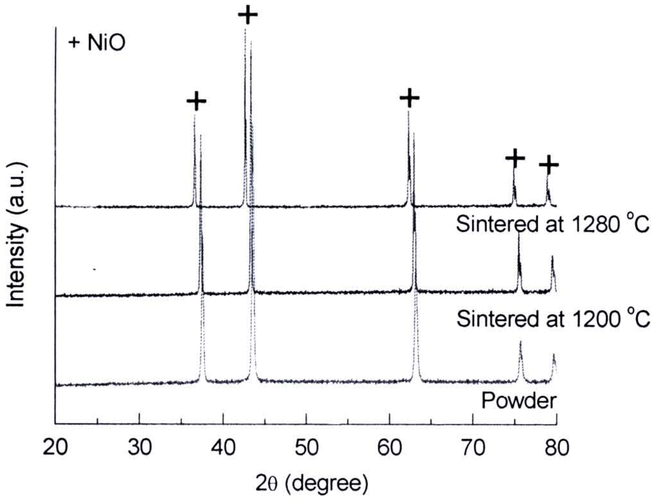

Figure 5.70 XRD patterns of $Li_{0.05}Ti_{0.02}Ni_{0.93}O$ powder and ceramics sintered at 1200 and 1280 °C.

Table 5.9 Lattice parameter (*a*), grain size (GS), dielectric constant (ε') at 30 °C and 1 kHz, and activation energy for $Li_{0.05}Ti_{0.02}Ni_{0.93}O$ ceramics sintered at 1200 and 1280 °C.

Sintering temperature	***a* (Å)**	**GS (μm)**	ε'	**Activation energy (eV)**		
				E_a	E_g	E_{gb}
1200 °C	4.173	2.67	5,534	0.320	0.324	0.562
1280 °C	4.175	6.02	11,187	0.303	0.315	0.483

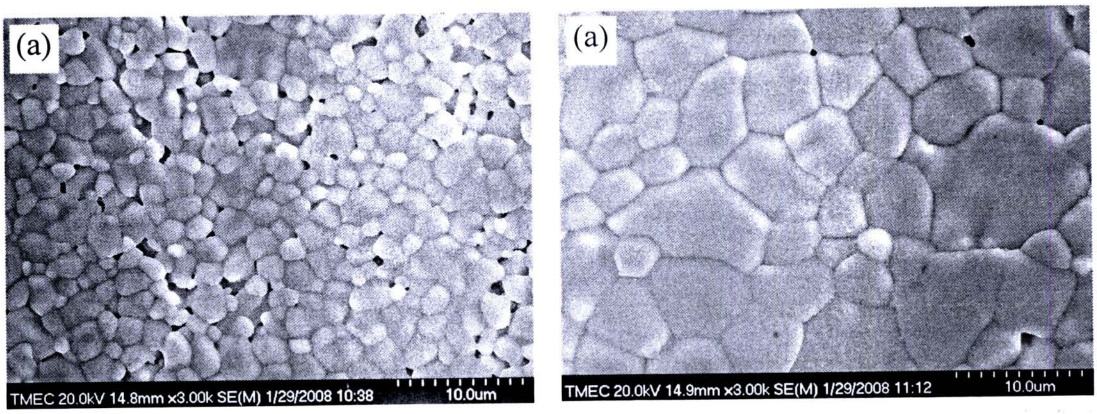

Figure 5.71 SEM images of surface morphologies of $Li_{0.05}Ti_{0.02}Ni_{0.93}O$ ceramics sintered at (a) 1200 and (b) 1280 ^{o}C.

To confirm the existence of electrically inhomogeneous in the LTNO samples, impedance spectroscopy which is a powerful tool in separating out the bulk and the grain boundary effects was carried out. In general, figure 5.72(a) shows the impedance spectra of the ceramic sintered at 1280 ^{o}C as a function of temperature. The impedance semicircles became larger with decreasing temperature. When the temperature was sufficiently low, other impedance semicircles were observed (inset of Fig. 5.72(a)). Note that the ceramic sintered at 1200 ^{o}C also show a similar spectra (does not present). The observation of two semicircles suggests that the $Li_{0.05}Ti_{0.02}Ni_{0.93}O$ ceramics are electrically heterogeneous and the core/shell model could be appropriated for further analysis. These results are similar to the other report in literature (Lin et al., 2006a). Accordingly, the observed semicircles at high and low temperatures can be assigned to the effect of charge transport within the grain and grain boundary, respectively. The charge transport inside the grain is mainly affected by the addition of Li ions in NiO, leading to an increase of conductivity and some electrically defects can be introduced due to different valences of doped ions (0.69 Å for Ni^{2+} and 0.68 Å for Li^{+}) (Lin et al., 2004). For every added Li^{+}, one Ni^{2+} is promoted to the Ni^{3+} state, which is the lost electron filling a state in the oxygen *2p* valence band. The lattice now contains Ni^{2+} and Ni^{3+} ions on equivalent sites and is the model situation for conduction by polaron hopping (Moulson, Herbert, 2003). From the intercepts of each semicircular arc with the real axis, the resistance of the grain R_g and the resistance of the grain boundary R_{gb} can be obtained. As a result, conductivity data were obtained for the grain (σ_g) and GB (σ_{gb}) components. According to polaronic scenario, the temperature dependence of the conductivity is, with a temperature dependence prefactor, ascribed as equation (5.28). It is found from 5.72(b) that both σ_g and σ_{gb} values at different temperatures follow equation (5.28). Accordingly, in the ceramic sintered at 1280 °C, the conduction activation energies inside the grain and at the GB, were obtained to be $E_g = 0.315$ eV and $E_{gb} = 0.483$ eV, respectively. These results strongly indicate that the grain and grain boundary have different characters of electrical transport, forming an electrically heterogeneous structure. This difference was also observed in the ceramic sintered at 1200 °C, the summary of activation energies and related parameters are also tabulated in Table 5.9. From this point of view, it is appropriate to make the assumption that such the appearance of electrically heterogeneous should be a key factor of affecting the dielectric behavior in the $Li_{0.05}Ti_{0.02}Ni_{0.93}O$ ceramic samples synthesized by the direct thermal decomposition method.

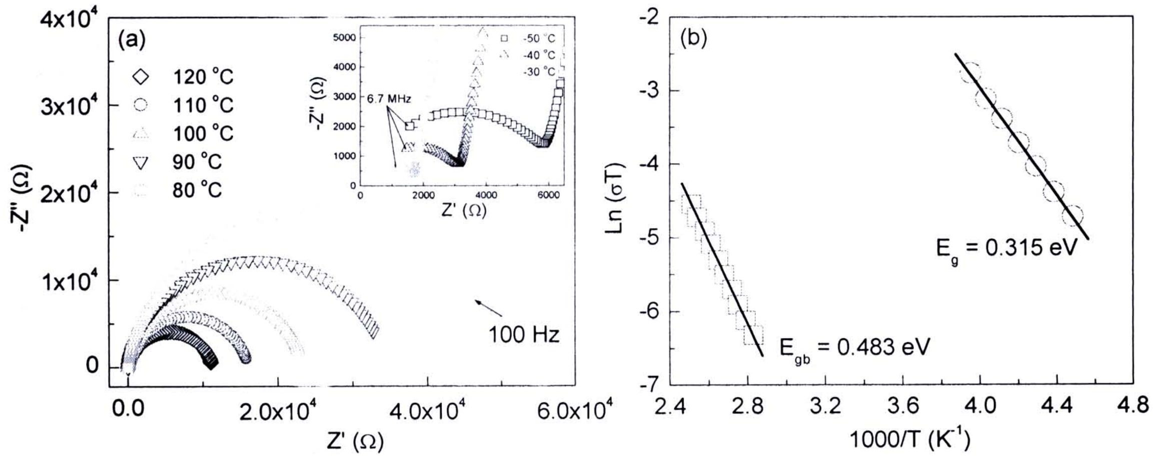

Figure 5.72 SEM images of surface morphologies of $Li_{0.05}Ti_{0.02}Ni_{0.93}O$ ceramics sintered at (a) 1200 and (b) 1280 °C.

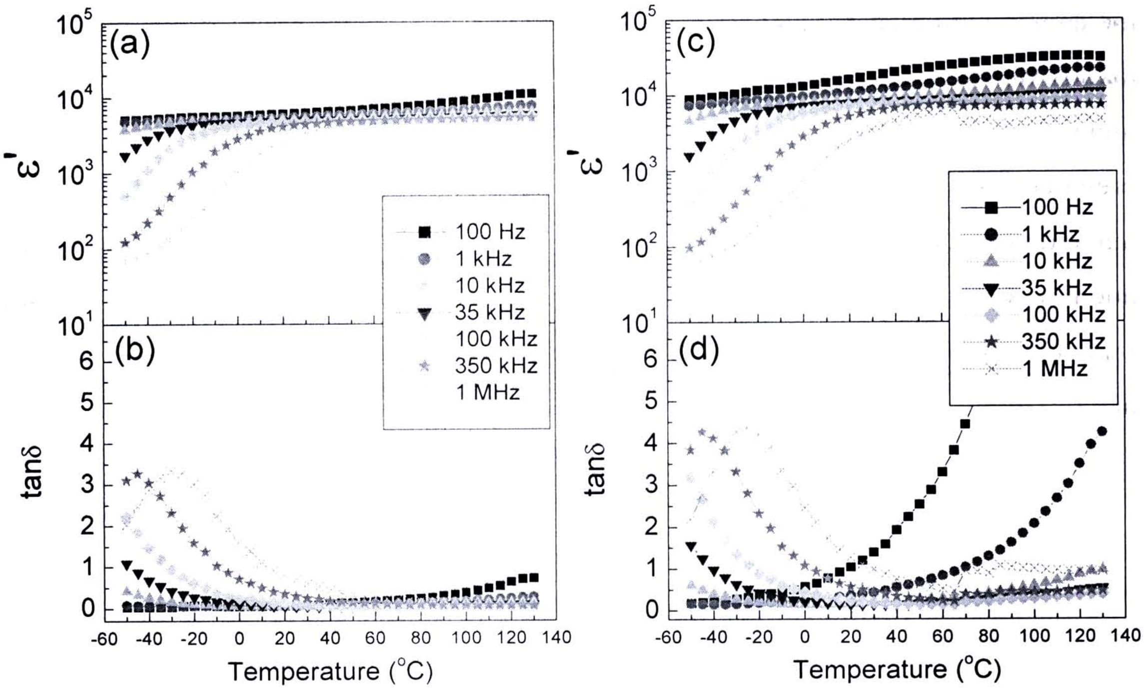

Figure 5.73 (a) and (c) Temperature dependence of ε' for the LTNO-1 and LTNO-2, respectively. (b) and (d) Temperature dependence of $\tan\delta$ for the LTNO-1 and LTNO-2, respectively.

To clarify the assumption above, the temperature dependence of the dielectric constant and the loss tangent for the $Li_{0.05}Ti_{0.02}Ni_{0.93}O$ ceramics is therefore studied at various frequencies, as shown in figure 5.73. It is clearly seen from figure 5.73(a) and figure 5.73(c) that both samples exhibit high dielectric constant of 5,534 and 11,187 at 30 °C and 1 kHz for the ceramics sintered at 1200 and 1280 °C, and each sample has a similar dielectric behavior. Below 10 kHz, the dielectric constant is nearly temperature independence over the measured temperature range. However, with increasing the frequency, the dielectric constant dramatically drops to the low values at low temperatures, being accompanied by the appearance of corresponding peaks in the loss tangent (Figs. 5.73(b) and 5.73(d)). Moreover, the loss tangent-peak moves to higher temperature range with increasing frequency, which is a suggestion of the thermally excited relaxation process. With decreasing the temperature, the electric dipoles freeze through relaxation process and then the rate of polarization is decreased, resulting in the dramatical decrease in the dielectric constant. According to the ceramic sintered at 1280 °C, the increase in the loss tangent at high temperature is mainly due to the effect of dc conductivity (Wu J et al., 2002). Note that, the overall dielectric behavior in the reported samples is similar to that observed in the other prepared $Li_{0.05}Ti_{0.02}Ni_{0.93}O$ methods (Wu J et al., 2002; Lin et al., 2005b), which is in marked contrast to the well-known ferroelectric one resulting from structure distortion due to a soft-mode condensation. Therefore, the high dielectric response in these two $Li_{0.05}Ti_{0.02}Ni_{0.93}O$ ceramics might be attributed to the apparent electrically heterogeneous structure in the ceramics.

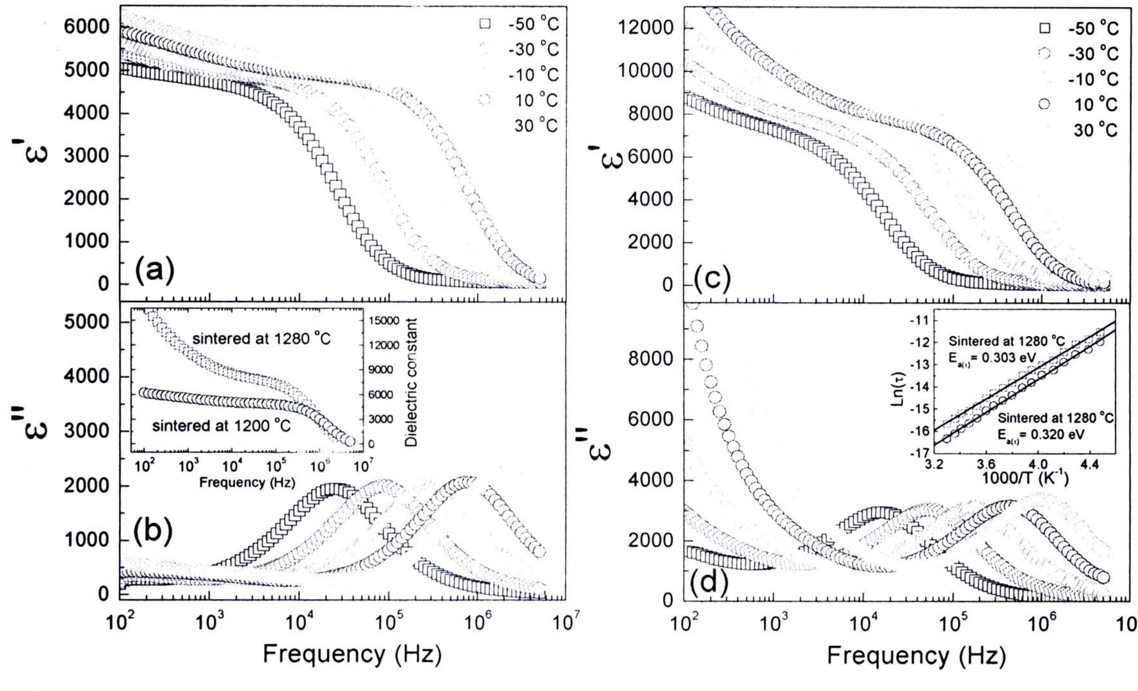

Figure 5.74 (a), (c) Frequency dependence of dielectric constant for the ceramics sintered at 1200 and 1280 °C, respectively. (b), (d) Frequency dependence of dielectric loss (ε'') for the ceramics sintered at 1200 and 1280 °C, respectively. Inset of Fig. 5.74(b) shows the comparison of dielectric constant at 30 °C over the measured frequencies. Inset of figure 5.74(d) demonstrates the Arrhenius plots of the relaxation process.

The frequency dependence of the dielectric constant (ε') and the dielectric loss (ε'') at various temperatures in order to obtain the underlying mechanism of high dielectric response in the $Li_{0.05}Ti_{0.02}Ni_{0.93}O$ ceramics, the results are shown in figure 5.74. As demonstrated in figure 5.74(a) and 5.745(c), the dielectric constant shows the high values at low frequencies, and it rapidly decreases if the frequency is sufficiently high. This step decrease shifts to higher frequency with increasing the temperature, corresponding to the movement of the dielectric loss peaks. Such a behavior is typical for the Dabye-like relaxation, which for the present work can be attributed to the Maxwell-Wagner polarization relaxation. This polarization relaxation model was usually employed to explain the observed high dielectric constant in electrically inhomogeneous materials. Thus, this may be the most appropriate one to elucidate the origin of the high dielectric constant in the $Li_{0.05}Ti_{0.02}Ni_{0.93}O$ prepared by the direct thermal decomposition method due to the different electrical transport between the grain and the grain boundary, as confirmed by the impedance spectroscopy study (Fig. 5.72).

To describe the dielectric relaxation behavior of the $Li_{0.05}Ti_{0.02}Ni_{0.93}O$ samples, the plot of ln(τ) vs $1/T$ is introduced, as shown in the inset of figure 5.74(d). According to the fitted curve using equations (5.7) and (5.9) for the $Li_{0.05}Ti_{0.02}Ni_{0.93}O$ ceramics with different grain sizes, the activation energy (E_a) for relaxation process can be obtained. The values of E_a are 0.320 and 0.303 eV for the ceramics sintered at 1200 and 1280 °C, respectively. From Table 5.9, the activation energies of the conductivity in the grain interiors of the ceramics sintered at 1200 °C ($E_g \sim 0.324$ eV) and 1280 °C ($E_g \sim 0.315$ eV) obtained from figure 5.72(b) are very close to the activation energies required for relaxations. These results imply that the nature of charge carriers responsible for dielectric relaxation peaks and dc conduction belongs to the same category, indicating that the polarization relaxation has a close relation to the conductivity in the grain interior. Consequentially, E_a and E_g are almost the same in value and the polarization process depends on the conductivity of the charge inside the grain. This behavior is consistent with the literature report for LTNO prepared by sol-gel method (Lin et al., 2006a). According to the impedance spectroscopy and dielectric results, it is believed that the high dielectric response in the $Li_{0.05}Ti_{0.02}Ni_{0.93}O$ ceramics is mainly due to the Maxwell-Wagner polarization relaxation caused by the existent of electrically inhomogeneous in microstructure. Such structure is referred to as a core/shell structure, i.e., the LTNO samples consist of semiconducting grains enclosed by insulating boundaries, so the grains and their boundaries give rise to the different electrical response in the impedance formalism.

It is of interest to note that E_a decreases from 0.320 to 0.303 eV with increasing the grain size from 2.67 to 6.02 μm, corresponding to the increase in the dielectric constant, as shown in Table 5.9. As shown in the inset of figure 5.74(b), the dielectric constant of the ceramics sintered at 1280 °C is higher than that of the ceramics sintered at 1200 °C over frequency range of 100 Hz to 1 MHz. However, the dielectric constant of both ceramics is almost the same in value at the frequencies higher that 1 MHz, this is possibly due to the bulk effect. Obviously, the dielectric constant increases with the sintering temperature, and is accordingly closely related to the polycrystalline microstructure, particularly to the grain size. Thus, the differences in the values of the dielectric constant and E_a for the these two ceramics are strongly affected by their microstructures. All these facts indicate that microstructures play a crucial role in changing the electrical properties and related dielectric behavior. Such the observed microstructure dependence of dielectric properties is similar to that observed in CCTO ceramics (Shao et al., 2006).

According to the impedance spectroscopy results, grain and grain boundary in the $Li_{0.05}Ti_{0.02}Ni_{0.93}O$ ceramics have different values of conductivities (σ_g and σ_{gb}) and dielectric permittivities (ε'_g and ε'_{gb}). Therefore, the complex permittivity in the $Li_{0.05}Ti_{0.02}Ni_{0.93}O$ system can be described as

$$\varepsilon_g^* = \varepsilon_g - j\sigma_g / \omega , \tag{5.29}$$

$$\varepsilon_{gb}^* = \varepsilon_{gb} - j\sigma_{gb} / \omega . \tag{5.30}$$

The total complex permittivity (ε^*) can be quantitatively approximated by (Raevski et al., 2003):

$$\varepsilon^* = L\left(\frac{t_g}{\varepsilon_g^*} + \frac{t_{gb}}{\varepsilon_{gb}^*}\right)^{-1}, \tag{5.31}$$

where t_g is the particle size of the conducting grain, t_{gb} is the thickness of boundary layer, and $L = t_g + t_{gb}$. Since $L >> t_{gb}$ and $\sigma_g >> \sigma_{gb}$, Eq. (5) can be simplified as

$$\varepsilon^* = \frac{\varepsilon_g}{a} + \left(\frac{\varepsilon_{gb}}{a\delta}\right)\left(\frac{1}{1 + j\omega\tau}\right), \tag{5.32}$$

where $a = 1 + \delta\varepsilon_g / \varepsilon_{gb}$, $\tau = a\varepsilon_{gb} / \delta\sigma_g$, $\delta = t_{gb} / L$. At zero or very low frequency, the Eq. (6) can be further simplified as,

$$\varepsilon' = \frac{L\varepsilon_{gb}}{t_{gb}}. \tag{5.33}$$

From the relation in equation (5.33), it is reasonable to propose that the different dielectric constants in the ceramics sintered at 1200 and 1280 $^{\circ}$C are affected by the grain size. Note that, t_{gb} are about the same in value because it depends on the Ti-dopant concentration. It is important to note that the lower in dielectric constant in the ceramic sintered at 1200 $^{\circ}$C may also be affected by the observed porosity, as shown in the SEM image of figure 5.72. However, it is believed that the grain size is still the main effect on the dielectric properties of these two ceramics. To support this conclusion, the dielectric constant of the ceramics sintered at 1200 (ε_{LTNO-1}= 5,534) and 1280 $^{\circ}$C (ε_{LTNO-2}= 11,187) at 30 $^{\circ}$C and 1 kHz and evaluate the ratio of the dielectric constant of the ceramics sintered at 1280 and 1200 $^{\circ}$C based on the dimensions of the grain observed in SEM images. Since both ceramics have the same amount of Ti, the thickness of grain boundary t_{gb} of these two samples may be assumed to be the same. From equation (5.33) and by assuming t_{gb} and ε_{gb} to be the same for both ceramics, the ratio of the dielectric constant of $Li_{0.05}Ti_{0.02}Ni_{0.93}O$ ceramics sintered at 1200 and 1280 °C becomes

$$\frac{\varepsilon'_{1280}}{\varepsilon'_{1200}} = \frac{L_{1280}}{L_{1280}}. \tag{5.34}$$

By substituting L_{1200}=2.67 μm and L_{1280}=6.02 μm into equation (5.34), $\varepsilon'_{1280}/\varepsilon'_{1200}$ was obtained to be 2.25. This result agrees with the experimental result (i.e. $\varepsilon'_{1280}/\varepsilon'_{1200}$ = 11,187/5,534 =2.02).

For the present work, it is speculated that the high dielectric constant of $Li_{0.05}Ti_{0.02}Ni_{0.93}O$ ceramics prepared by the direct thermal decomposition method is attributed to their electrically inhomogeneous structures. When the alternative electric field is applied through the samples, the charge carriers are restricted by the Ti-rich boundary, and thus the opposite charges accumulate at the two edges of the grain boundaries. Consequentially, the polarization formation primarily depends on the accumulation of the charge via conducting in the grain interiors. This provides an extended description for the physical explanation for the underlying polarization. Therefore, the difference in the dielectric constant of these two samples of $Li_{0.05}Ti_{0.02}Ni_{0.93}O$ ceramics with different grain size is attributed to the different amount of the accumulated charges at grain boundaries. As well known, these accumulated charges in the $Li_{0.05}Ti_{0.02}Ni_{0.93}O$ ceramics depend on the concentration of monovalent impurities like Li^+ ions (Wu J et al., 2002). For both of ceramic samples, however, they have the same chemical composition, but different sintering temperature. Hence, the increase in the dielectric constant in the $Li_{0.05}Ti_{0.02}Ni_{0.93}O$ ceramic sintered at 1280 °C with higher sintering temperature may be attributed to the other free charge carriers but does not related to the affect of the dopant concentration. One may deduce from this assumption that grains made by different sintering conditions could have very different electrical properties. The fact that the higher conduction activation energy of 0.324 eV for the grains in the $Li_{0.05}Ti_{0.02}Ni_{0.93}O$ ceramic sintered at 1200 °C than that of 0.315 eV for the ceramic sintered at 1280 °C may imply that there are lower oxygen vacancies concentration in the grains of the ceramic sintered at 1200 °C than in the grain of the ceramic sintered at 1280 °C. This is reasonable because the ceramic sintered at 1280 °C was fabricated using temperature higher than that of the ceramic sintered at 1200 °C. Based on the explanation above, it is possible that the oxygen vacancies have the influence on the electrical properties of the $Li_{0.05}Ti_{0.02}Ni_{0.93}O$ ceramics and the contribution to the total dielectric response in a $Li_xTi_yNi_{1-x-y}O$ system. It is worth to noting that the lower τ_0 values of the ceramic sintered at 1200 °C than those of the ceramic sintered at 1280 °C over the measured temperature is attributed to the shorter distance between the nearest grain boundaries in the ceramic sintered at 1200 °C compared to the larger grain for the ceramic sintered at 1280 °C. Thus, the polarization of the ceramic sintered at 1200 °C is fully developed at higher frequency than that of the ceramic sintered at 1280 °C at the same temperature, as shown in figure 5.74. Additionally, E_{gb} also decreases with increasing the sintering temperature (Table 5.9). This is associated to the ceramic microstructure of $Li_{0.05}Ti_{0.02}Ni_{0.93}O$ samples. The higher E_{gb} observed in the ceramic sintered at 1200 °C compared to that of the ceramic sintered at 1280 °C is attributed to the observed porosity in the first one sample. Some of the grain boundary regions are replaced by the porosities (air gaps) in the ceramic sintered at 1200 °C, and thus the total potential barrier at the grain boundary regions increases. Another possible of such observation is that the defect equilibium at the grain boundary regions may be modified by the increase of grain size, affecting on the electrical transport at the regions.

Finally, the high dielectric constants of $Li_{0.05}Ti_{0.02}Ni_{0.93}O$ ceramics have been synthesized by a simple thermal decomposition method. The complex impedance spectroscopy indicates that the electrically heterogeneous structures exist in the $Li_{0.05}Ti_{0.02}Ni_{0.93}O$ ceramics consisting of semiconducting grain and insulating grain boundary. The dielectric constant of the $Li_{0.05}Ti_{0.02}Ni_{0.93}O$ ceramics increases with the increase in grain size, and the dielectric response can be well explained by the Maxwell-Wagner relaxation polarization. The experimental results indicate that the polarization relaxation has a close relation to the conductivity inside the grain. These results also reveal that E_a and related E_g and E_{gb} decrease with the increase in grain size. It can be proposed that the different microstructures lead to the chemical change (e.g., oxygen vacancies) inside the grains and at the grain boundaries.

5.5.2 Li and Al co-doped NiO ceramics

In this section, the dielectric properties and electrical response in $Li_xAl_yNi_{1-x-y}O$ (LANO) ceramics prepared by a simple direct thermal decomposition method are investigated. It is suggested that the Al-dopant has remarkable influences on the grain size and the electrical conductivity in the grain interiors of the LANO ceramics. This work has also confirmed that LANO ceramics have electrically heterogeneous structure consisting of semiconducting grain and insulating grain boundary, which is responsible for such a high apparent dielectric constant. First of all, the polycrystalline LANO ceramic samples with different addition contents of Al, i.e., $Li_{0.05}Al_{0.04}Ni_{0.91}O$ (LANO-04), $Li_{0.05}Al_{0.06}Ni_{0.89}O$ (LANO-06), and $Li_{0.05}Al_{0.10}Ni_{0.85}O$ (LANO-10) are designed.

The phase formation of LANO materials was characterized by X-ray diffraction. As shown in figures 5.75(a) and 5.75(b), all of LANO powders and sintered samples with different Al-doped contents exhibit a main phase of NiO. The main peaks are comparable to that of the powder diffraction pattern of NiO in JCPDS card No. 78-0429. The values of lattice parameter calculated from XRD spectra are close to the value of 0.4177 nm reported in JCPDS card No. 78-0429, as shown in Table 1. It is important to note that the second phase of Ni (JCPDS card No. 04-0850) is still detected in all XRD patterns of LANO powders, and the relative intensity of Ni phase tends to increase with increasing Al-dopant content. This implies that the Al-dopant inhibits the formation of NiO phase. Additionally, a second phase $NiAl_2O_4$ can only be observed from XRD pattern of LANO-10 sintered sample. The relative amounts of the $NiAl_2O_4$ second phase and NiO phase can be estimated from the XRD pattern of the LANO-10 sample by following relation (Hsiao et al., 2007),

$$NiAl_2O_4\,phase(\%) = \frac{I_{NiAl_2O_4}(311)}{I_{NiAl_2O_4}(311) + I_{NiO}(200)} \times 100 \qquad (5.35)$$

where $I_{NiAl_2O_4}(311)$ and $I_{NiO}(200)$ are the major peak intensities for the $NiAl_2O_4$ (311)

and NiO (200) phases, respectively. The calculated relative amount of the observed $NiAl_2O_4$ second phase in the LANO-10 ceramic is 7.1 %. This can be deduced that just 2.9 % of Al-doping can substitute the Ni site in the NiO crystal lattice. Disappearance of such second phase in the XRD patterns of the other two samples might be attributed to the small amount of this phase.

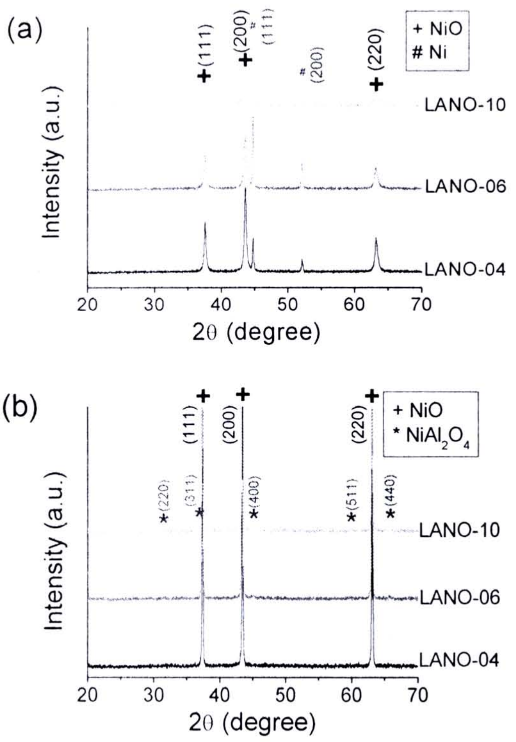

Figure 5.75 XRD patterns of (a) LANO powders and (b) LANO sintered samples.

Table 5.10 Lattice constants (*a*), dielectric constant (ε') at room temperature and 1 kHz, and activation energies for LANO samples.

Sample	***a* (Å)**	ε'	**Activation energy (eV)**		
			E_a	E_g	E_{gb}
LTNO-04	4.167	8.468	0.340	0.354	0.369
LTNO-06	4.168	7,396	0.354	0.362	0.374
LTNO-10	4.162	6,566	0.373	0.367	0.377

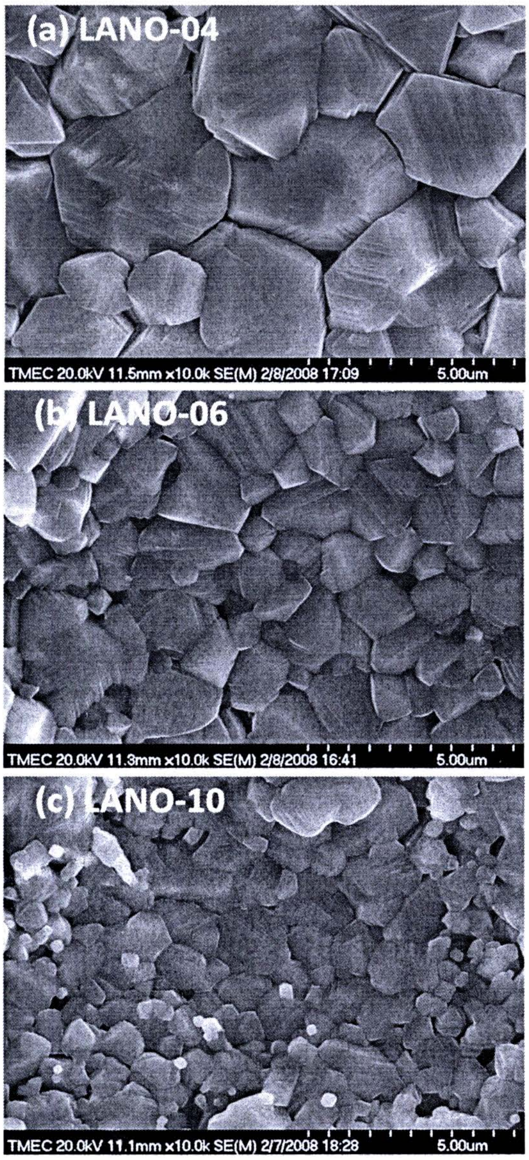

Figure 5.76 SEM images of surface morphologies for (a) LANO-04, (b) LANO-06, and (c) LANO-10 sintered samples.

Figure 5.76 shows the surface morphologies of the LANO ceramic samples. It is clear that grain size significantly decreases with increasing the Al-doped content. As previously discussed, the phase formation of NiO is suppressed by the Al-dopant. Thus, it is strongly believed that the grain growth mechanism of LANO ceramics system is affected by the Al-dopant.

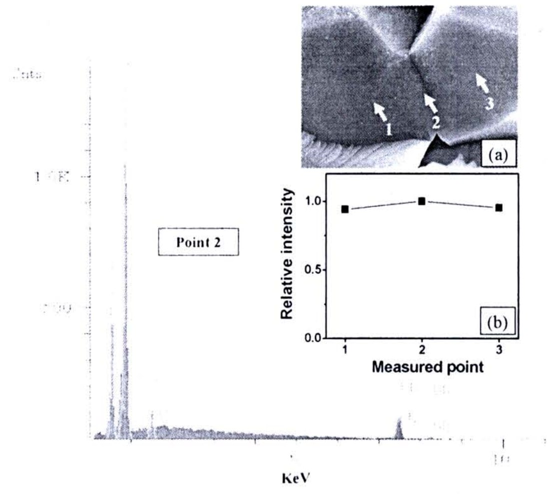

Figure 5.77 EDS spectrum of grain boundary (point 2) for LANO-06 ceramic sample; inset (a) is the fractured surface of the LANO-06 sample; inset (b) is the Al element profile obtained from the EDS spectrum at different measured locations as displayed in the inset (a).

The microstructures of the LANO ceramics are analyzed by energy-dispersive x-ray spectroscopy (EDS), as showed in figure 5.77, revealing the distribution of Al-dopant at the grain and grain boundary of the LANO-06 ceramic sample. It is clearly seen from the EDS analysis at different regions for the LANO-06 ceramic sample (inset (a) of Fig. 5.77) that Al-dopant appears in both the grain and grain boundary which is in agreement with the XRD results. This confirms that some parts of the Al-dopant have entered into the grain interiors and other parts have formed the second phase of $NiAl_2O_4$ at the grain boundaries.

The temperature dependence of dielectric properties of the LANO samples is measured between -60 to 130 °C at the frequency range of 100 Hz to 10 MHz. The values of the dielectric constant at 1 kHz for the LANO-04, LANO-06, and LANO-10 samples are about 8468, 7396, and 6566, respectively. These results are consistent with the work reported by Lin *et al* (Lin et al., 2004). Figure 5.78 demonstrates the temperature dependence of the dielectric constant and loss tangent ($\tan\delta$) of LANO-04 ceramic sample. At low frequency, the dielectric constant is nearly temperature independent over the measured temperature range. With increasing the frequency, however, the dielectric constant decreases rapidly at the low temperature. This characteristic temperature shifts to the higher temperatures with increasing the frequencies, corresponding to the movement of tanδ-peak. Such behavior suggests that the Maxwell-Wagner polarization relaxation mechanism possibly play an important role in the high dielectric response of the LANO ceramics. This dielectric behavior may be ascribed to the migration of excited electrical particles at high temperatures, which has also been observed in the $Ca(Fe_{1/2}Nb_{1/2})O_3$ system (Liu YY et al., 2007b) and $Y_{0.03}Ti_{0.10}Ni_{0.87}O$ (Cheng et al., 2008).

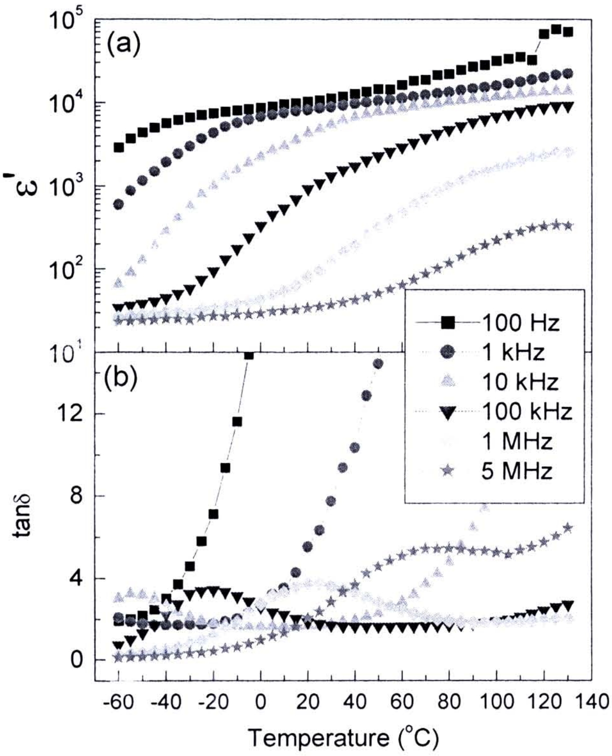

Figure 5.78 Temperature dependence of (a) dielectric constant and (b) loss tangent of LANO-04 sample at frequency range of 100 Hz to 5 MHz

The frequency dependence of ε' and $\tan\delta$ for the LANO ceramic samples has further studied. As shown in figure 5.79, a frequency dependent plateau region of the dielectric constant is observed at low frequencies for LANO-04 sample, followed by a rapid decrease of the dielectric constant at higher frequencies. The plateau region expands over a wider frequency range as the temperature increases.

The movement of the rapid decrease at high frequencies coincides with the translation of $\tan\delta$-peak, which it shifts to higher frequency with increasing temperature. According to the fitted curve using equation (5.7), as shown in the inset of figure 5.79, for LANO-04 sample, the activation energy of relaxation process (E_a) can be obtained to be 0.340 eV. The frequency dependence of the dielectric response for the samples of LANO-06 and LANO-10 (does not present) is similar to that of LANO-04 sample, but the frequency at the loss peak at the fixed temperature shifts to low frequency range with increasing Al concentration. The E_a values of the samples of LANO-06 and LANO-10 are respectively obtained to be 0.354 and 0.373 eV, as summarized in Table 5.10.

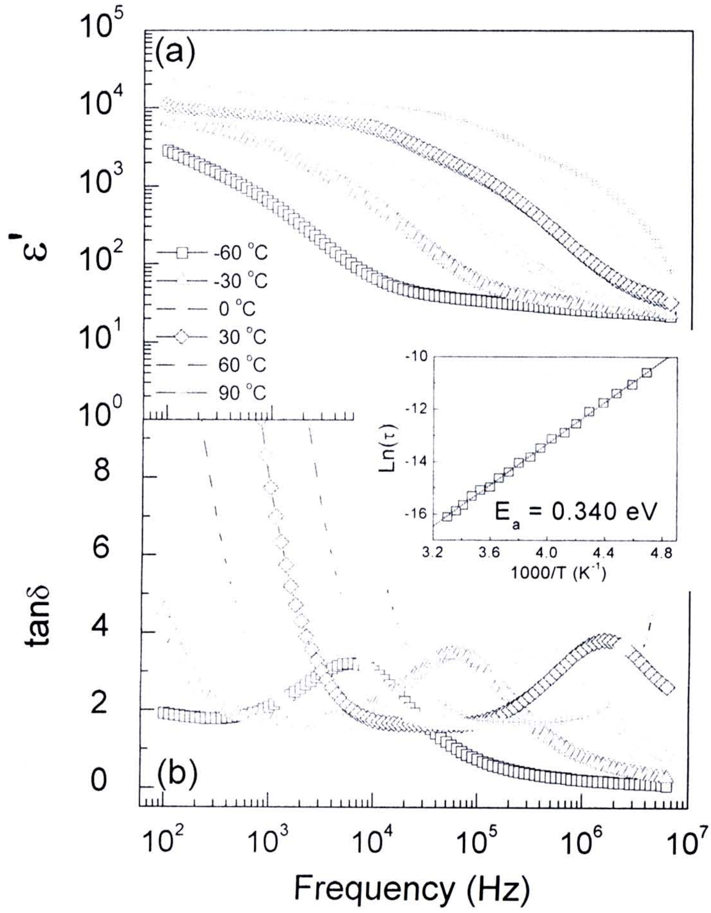

Figure 5.79 Frequency dependence of (a) dielectric permittivity and (b) dissipation factor of LANO-04 sample at various temperatures; inset shows the Arrhenius plots of the relaxation process.

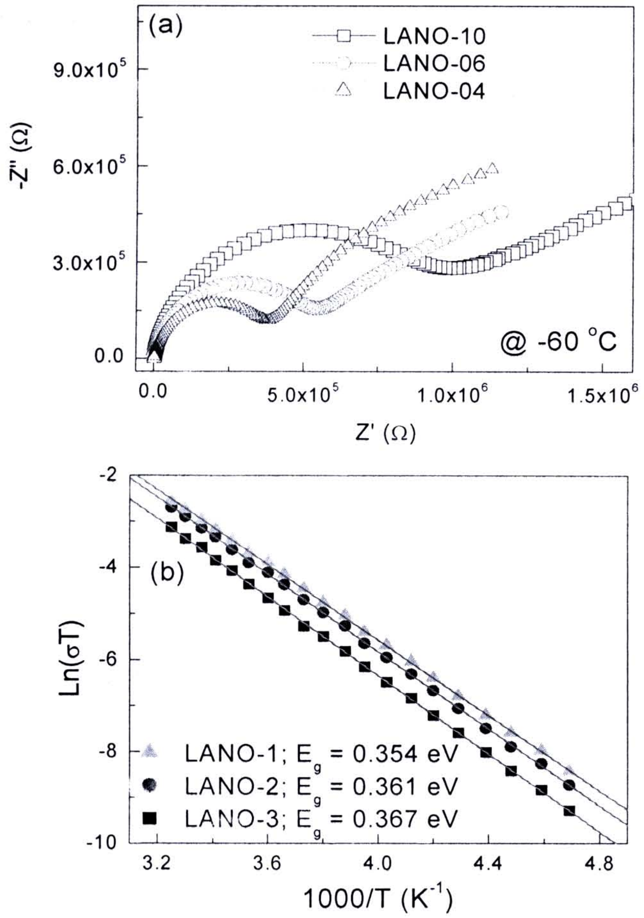

Figure 5.80 (a) Comparison of impedance spectra for LANO samples at -60 °C and (b) the Arrhenius plots of the grain conduction of LANO samples.

Let us now consider the complex impedance spectroscopy which is a powerful tool in separating out the bulk and GB effects. Data collected from this technique can often be modeled on an ideal equivalent circuit consisting of two parallel *RC* elements connected in series, one *RC* element for the bulk and the other for the grain boundary response (Sinclair et al., 2002). Figure 5.80(a) shows the complex impedance (Z^*) plot of all the LANO samples at -60 °C. Two impedance semicircles corresponding to the grain and grain boundary are clearly observed in all of the samples. The observation of two semicircles suggests that the electrically heterogeneous structure exists in the LANO samples and the core/shell model is appropriate for further analysis. Thus, it is strongly indicated that such a presence of electrically inhomogeneous structure is responsible for the high dielectric constant in the LANO ceramics. From this result, it is proposed that for the LANO ceramic samples the grain boundary layers are nonconducting or less conducting, while the bulk grains are semiconductive. Under the applied electric field, the carrier-conducting access is blocked by the insulating grain boundary layer; thus, the opposite charges accumulate at the two edges of the insulator layer to form many microcapacitors, which result in the large dielectric constant in these LANO ceramics. This behavior is similar to that of LTNO system (Lin et al., 2004).

According to the complex impedance spectra shown in figure 5.80(a), the resistance of grain (R_g) and grain boundary (R_{gb}) can be obtained. From figure 5.80(b), it is found that both σ_g and σ_{gb} values at different temperatures follow equation (5.28). Accordingly, the calculated values of the conduction activation energy inside the grain (E_g) are obtained to be 0.354, 0.361 and 0.367 eV for the LANO-04, LANO-06, and LANO-10, respectively. The estimated values of the grain boundary activation energy (E_{gb}) are obtained to be 0.369, 0.374, and 0.377 eV for LANO-04, LANO-06, and LANO-10, respectively. The observation of the small increase in E_g with increasing the Al content may be because the parts of Al that have entered into the NiO crystal lattice (as clearly seen in Fig. 5.77) have small different amounts. Because of the difference in valence states of Al^{3+} and Ni^{2+}, the electrically defects can be introduced inside the grains of the LANO ceramics, i.e.,

$$Al_2O_3 \xrightarrow{NiO} 2Al^{\bullet}_{Ni} + V''_{Ni} + 3O_o . \tag{5.36}$$

This has an influence of the electric conductivity of the grains, which induces the variation of the E_a values. This behavior was also observed in $Li_xTi_yNi_{1-x-y}O$ ceramics system (Lin et al., 2006b).

Generally, for $A_xB_yNi_{1-x-y}O$ systems, *B*-dopants (Ti, Al, Si, Ta) normally form a second phase at grain boundary enclosing the semiconducting core grain of *A*-doped NiO. Thus, the electrical characters at grain boundary should be modified by the *B*-dopant. For this work, it is clear that some parts of Al-dopant accumulated at the grain boundaries and formed the second phase of $NiAl_2O_4$, as evidenced in figures 5.75 and 5.77. Moreover, it was found that the $NiAl_2O_4$ ceramic is a good insulator with the value of resistance of more than 100 MΩ.cm (does not show), and as a result the grain boundary potential barrier can be ascribed to the appearance of such second phase of $NiAl_2O_4$ at grain boundaries. Therefore, the observed high dielectric constant in the samples of LANO ceramic is due to the Maxwell-Wagner polarization mechanism, i.e., charge carriers in the semicondicting grain are accumulated at the insulating grain boundary layer under the influence of electric field. Interestingly, the *B*-dopant (Al) in the LANO system has also a remarkable effect on the electrical properties in the grain interiors, where the resistance of the grain decreases with increasing the Al content, as evidenced in figure 5.80. This result implies that the Al-dopant may not only be able to improve the electrical character at grain boundaries, but also strongly affect on the electrical properties inside the grains. Moreover, the effect of Al-dopant on microstructure was also clearly observed. The reason for this is that most of Al-dopant in the LANO ceramics has entered into the grains, while the concentration of Al at the grain boundary of each sample does not significant difference in composition. This leads to the little change in the dielectric constant. It is worth nothing that all of the *B*-dopants in NiO-based ceramics have remarkable impact on the electrical properties inside grain due to the different physical nature of *B*-doped and the different synthesis method. As well known, the strategy for reducing the dielectric loss in high dielectric ceramics is an increase in the grain boundary resistance. For the LANO ceramics, however, the $\tan\delta$ values do not significant change with the concentrations of Al-dopant. This suggests that the electrical properties of grain boundary for all the LANO samples are not significant difference. This observation may be attributed to the synthesis method used in the present work and/or the physical nature of Al-dopant. However, it is beyond the scope of this work and further work is needed to make a more detailed explanation. Of great interest, it is very important to seek for the preparation method that provides a good distribution of *B*-dopant only at grain boundaries and to explore the suitable *B*-dopant which can modify the defect equilibrium at grain boundary, leading to the higher resistance of grain boundary.

In conclusion of this section, high dielectric LANO ceramics have been successfully prepared by a simple thermal decomposition method. The microstructure and phase formation of the prepared LANO powders and ceramics were characterized by XRD and FE-SEM. The phase formation of NiO-based ceramics and the grain growth mechanism was suppressed by the Al-popant. This work demonstrates that the high dielectric constant of the LANO decreases with increasing the Al-dopant content. Giant dielectric response in such ceramics was attributed to the appearance of electrically heterogeneous structure, responsible for the observed high dielectric constant in the LANO ceramics. The results also showed that the Al-dopant has a strong effect on electrical transport in the grain interiors.

5.6 Dielectric and electrical properties of NiO-based ceramic systems prepared by a PVA method

5.6.1 Li and Fe co-doped NiO ceramics

In this section, the dielectric properties of (Li, Fe)–doped NiO (LFNO) ceramics are studied. The polycrystalline LFNO ceramic samples with different addition contents of Li and Fe, i.e., $Fe_{0.02}Ni_{0.98}O$, $Li_{0.02}Fe_{0.02}Ni_{0.96}O$, $Li_{0.05}Fe_{0.02}Ni_{0.93}O$, $Li_{0.10}Fe_{0.02}Ni_{0.88}O$, $Li_{0.05}Fe_{0.05}Ni_{0.90}O$, and $Li_{0.05}Fe_{0.10}Ni_{0.85}O$, were synthesized from powders prepared by the PVA method. The results indicate that both Li and Fe doping have strong influences on the microstructure and electrical properties of the LFNO ceramics. The dielectric polarization relaxations in this material system might be associated with both the electrical transport (hopping motion) inside the semiconducting grains and/or the space charge polarization.

Figure 5.81 shows the XRD patterns of the LFNO ceramics with different addition contents of Li and Fe ions, confirming a main phase of NiO in all samples. All of the main peaks are comparable to that of the powder diffraction pattern of NiO in JCPDS card no. 78–0429. The second phase of $NiFe_2O_4$ (JCPDS card no. 74–2081) is only detected in the XRD pattern of the $Li_{0.05}Fe_{0.10}Ni_{0.85}O$ sample with highest Fe concentration. Since the difference in ionic radius between Ni^{2+} (0.69 Å), Fe^{2+} (0.74 Å), and Fe^{3+} (0.64 Å) ions is small, Fe ions can substitute the Ni^{2+} ions in the NiO crystal lattice. The observed $NiFe_2O_4$ should be attributed to the Fe-dopant content which is over the solid solution limitation of Fe–Ni–O system.

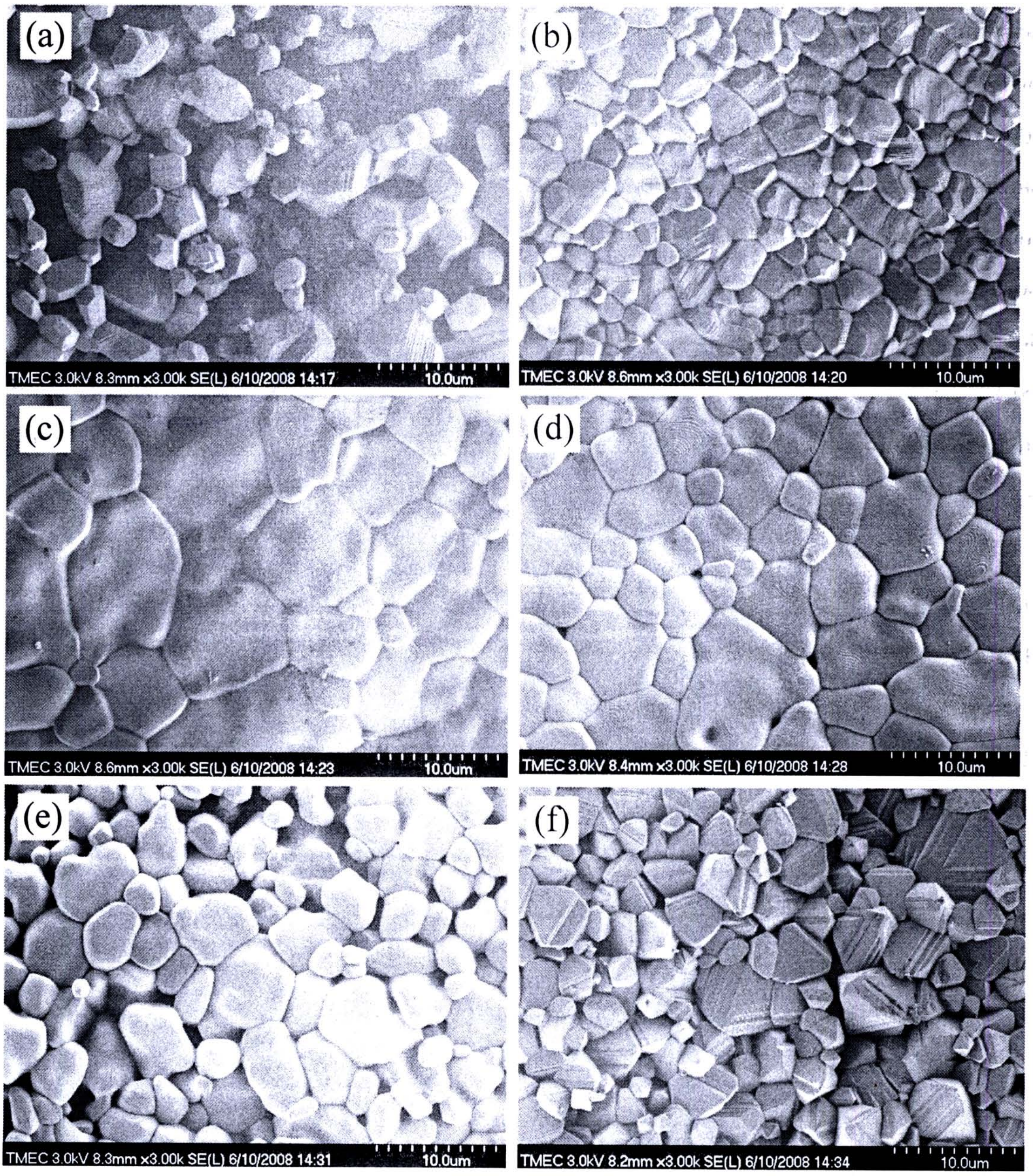

Figure 5.82 SEM images of surface morphologies for (a) $Fe_{0.02}Ni_{0.98}O$, (b) $Li_{0.02}Fe_{0.02}Ni_{0.96}O$, (c) $Li_{0.05}Fe_{0.02}Ni_{0.93}O$, (d) $Li_{0.10}Fe_{0.02}Ni_{0.88}O$, (e) $Li_{0.05}Fe_{0.05}Ni_{0.90}O$, and (f) $Li_{0.05}Fe_{0.10}Ni_{0.85}O$.

Figure 5.82 shows the surface morphologies of the LFNO ceramics, showing obvious grain and grain boundary structure. The microstructural evolution is observed. The SEM image of the $Fe_{0.02}Ni_{0.98}O$ sample, figure 5.82(a), shows hillock-like morphology and large portion of porosity. However, after the $Fe_{0.02}Ni_{0.98}O$ sample was increasingly added by Li ions, the ceramic density tended to increase with increasing Li content and the hillock-like morphology became disappeared and it was completely disappeared after the Li concentration was increased up to 5 %mol, as shown in figure 5.82(c). Interestingly, this special morphology appeared in the Li-Fe-Ni-O system again, when the Fe concentration was increased up to 10 %mol, as seen in figure 5.82(f). These results indicate that both the Li– and Fe–dopants affect the microstructure, i.e., grain size and feature, of the LFNO ceramics.

Figure 5.83 illustrates the influence of Li doping on the dielectric properties of the LFNO ceramics at room temperature. It is clear that the high dielectric response in the LFNO ceramics depends on the Li concentration. Both the dielectric constant and loss tangent of the LFNO samples increase with an increase in the Li content over the measured frequency range. These results are similar to that observed in the (Li, Ti)–doped NiO (LTNO) ceramics system (Wu J et al., 2002). A plateau can be observed in all the dielectric spectra, as displayed in figure 5.83(a). However, the steplike decrease in ε' is only detected in the dielectric spectrum of the $Li_{0.02}Fe_{0.02}Ni_{0.96}O$ sample. This is accompanied by the appearance of the corresponding peak-tanδ in figure 5.83(b). The disappearance of the steplike decrease in the $Li_{0.05}Fe_{0.02}Ni_{0.93}O$ and $Li_{0.10}Fe_{0.02}Ni_{0.88}O$ samples is due to the fact that it shifts out of the measuring frequency range.

The effect of Fe doping on the dielectric behavior of the LFNO ceramics has also been investigated, as illustrated in figure 5.84. Clearly, the concentration of Fe affects on both the value of the dielectric constant and dielectric relaxation behavior of the LFNO ceramics. With increasing the Fe concentration, the dielectric constant decreases and the steplike decrease at the characteristic frequency shifts to lower frequencies. Looking carefully at figure 5.84(a), the dielectric spectrum of the $Li_{0.05}Fe_{0.10}Ni_{0.85}O$ sample with highest Fe concentration exhibits two steplike decreases, corresponding to the two respective peaks in tanδ. This suggests that there exist two sets of thermally activated relaxations, i.e., low– and high–frequency relaxations (abbreviated as LFR and HFR, respectively). It is worth noting that the exponential increase in tanδ, which is usually attributed to the dc conductivity effect, decreases with the increase in the Fe concentration, and disappears in the $Li_{0.05}Ti_{0.10}Ni_{0.85}O$ sample. These might be because the long–range motions of the charge carriers inside the grains of this sample are blocked by the apparent second phase of $NiFe_2O_4$.

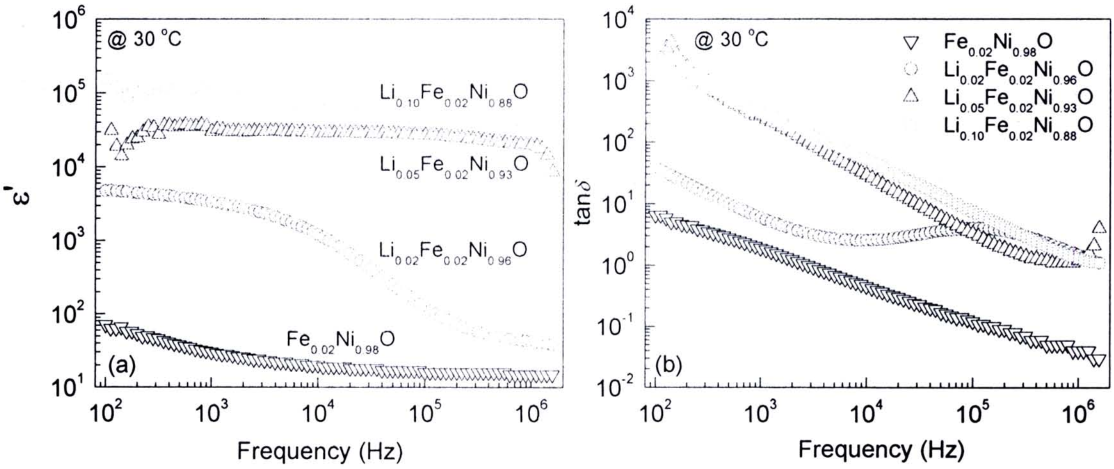

Figure 5.83 The effect of Li concentration on frequency dependence of (a) dielectric constant and (b) loss tangent for the LFNO ceramics at room temperature.

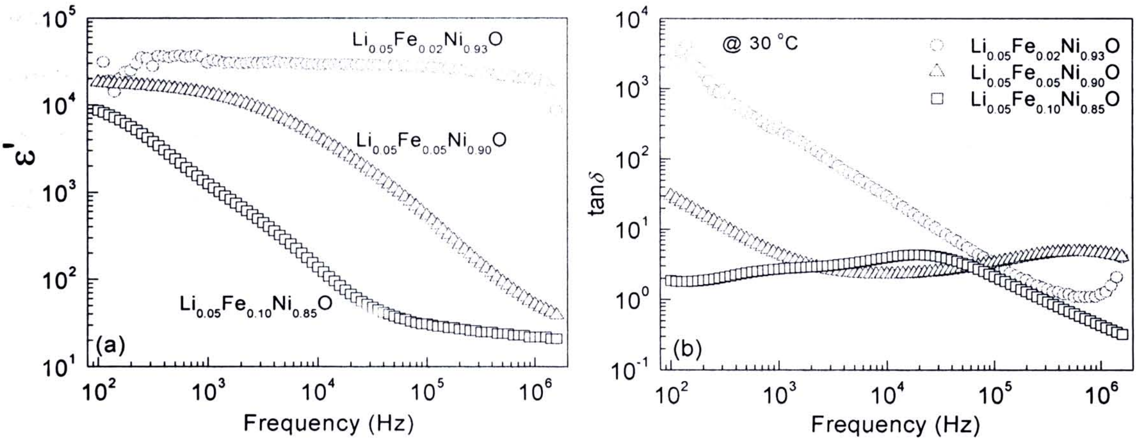

Figure 5.84 The effect of Fe concentration on the frequency dependence of (a) dielectric constant and loss tangent of the LFNO ceramics at room temperature.

It has been reported that pure NiO is a Mott-Hubbard insulator with the conductivity at room temperature less than 10^{-13} S/cm (Wu et al., 2002). However, this low conductivity can greatly be increased by doping with monovalent ions such as Li^+. For every added Li^+, one Ni^{2+} is promoted to the Ni^{3+} state, which is the lost electron filling a state in the oxygen 2*p* valence band. The lattice now contains Ni^{2+} and Ni^{3+} ions on equivalent sites and is the model situation for conduction by polaron hopping (Moulson, Herbert, 2003). Therefore, the carrier concentration in the bulk LFNO ceramics raises with increasing the Li concentration, and thus the accumulated charges at insulating layers (e.g., grain boundary, contact, impurity phase, and internal domain) in the bulk ceramics should increase. This may be responsible for the observed increase in ε' with increasing the content of Li ions, as shown in figure 5.83(a). Moreover, it has been proposed that dipolar effects in semiconducting materials can be induced by the hopping of localized charge carriers between spatially fluctuating lattice potentials (Wang et al., 2007), which usually causes an increase in electrical conductivity. Therefore, it is possible that the dipolar effects in the semiconducting grains of the LFNO ceramics are induced, and it should be increased by increasing the Li doping ions.

It was reported that the high dielectric response in the LTNO ceramics system could be ascribed by a simple series-layer model ($\varepsilon' \sim \varepsilon_{gb}A/t$, where ε_{gb}, A, and t are the dielectric permittivity of the grain boundary, the mean grain size, and the thickness of grain boundary, respectively). The decrease in ε' of the LTNO ceramics was attributed to the increase in t, resulting from the Ti-rich boundaries (second phase of $NiTiO_3$) (Wu j et al., 2002). For the LFNO ceramics, the second phase of $NiFe_2O_4$ can not be detected from the XRD patterns of the LFNO samples with the Fe concentration of less than 10 % mol. Thus, it seems that the simple series-layer model fails to explain the decrease in the dielectric constant because the different values of the dielectric constant between the $Li_{0.05}Fe_{0.02}Ni_{0.93}O$ and $Li_{0.05}Fe_{0.05}Ni_{0.90}O$ samples do not relate to the second phase of $NiFe_2O_4$.

To deepen the understanding on the high dielectric response mechanism in the LFNO ceramics, the dielectric relaxation behavior, which usually provides important clues about the dielectric response mechanisms, has further studied. Therefore, the frequency dependences of the dielectric constant and loss tangent are investigated at various temperatures. As seen in figure 5.85, the step-like decreases and the corresponding $\tan\delta$-peaks of the LFNO samples move to higher frequencies as the temperature increases, indicating the thermally excited relaxation process. This behavior is similar to those observed in the other NiO-based ceramic systems such as (Li, Ti)–, (Li, Si)–, (Na, Ti)–, (Li, V)–, and (Li, Al)–doped NiO systems (Wu J et al., 2002; Lin et al., 2004,2005a; Jana et al., 2008; Chen GJ et al., 2009). Note that, the movements of the LFR and HFR in $Li_{0.05}Fe_{0.10}Ni_{0.85}O$ sample are clearly seen in figure 5.85(d). According to the observed thermally activated relaxations in the LFNO ceramics, the activation energies required for these relaxations can be calculated by using the Arrhenius law (Eq. (5.7)) combined with the extreme value relation,

$$\omega\tau = \sqrt{\varepsilon_S / \varepsilon_\infty}\,, \tag{5.37}$$

Equation (5.7) can be expressed as

$$\ln(2\pi f_p) = -E_a / k_B T + \ln\left(\sqrt{\varepsilon_S / \varepsilon_\infty} / \tau_0\right). \qquad (5.38)$$

According to the fitted curves in figure 5.86, the activation energy (E_a) for the relaxation processes can be calculated by using the relation in equation (5.38), and are summarized in Table 5.11. Note that the characteristic peaks of the LFR, figure 5.85(d), can not be estimated accurately from the experimental data. Thus, two Gaussian peaks were used to fit the experimental data of tanδ, as shown in the inset of figure 5.85(d). The E_a values of the $Li_{0.05}Fe_{0.02}Ni_{0.93}O$ and $Li_{0.10}Fe_{0.02}Ni_{0.88}O$ samples can not be obtained because their relaxation peaks shift out of the measured frequency range, as clearly seen in figure 5.83. It is interesting that, with increasing the Fe concentration from 5 to 10 % mol, E_a increases from 0.353 to 0.448 eV for the HFR. This implies that the Fe-dopant has an influence on the polarization relaxation properties of the LFNO ceramics. It is worth noting that, the dielectric relaxation behavior of the $Fe_{0.02}Ni_{0.98}O$ sample can also be observed at high temperature range, i.e., 50 – 200 °C, as shown in the inset of figure 5.85(a), with E_a ~ 0.855 eV. This value is almost the same to the value of 0.850 eV for the dc conduction as reported in the literature for Fe-doped NiO polycrystalline ceramics (Lin et al., 2006b). The *p*-type semiconductivity of these ceramics was proved by using the Seebeck coefficient measurements technique, indicating that holes were major carriers in this material. As a result, the dielectric response in the $Fe_{0.02}Ni_{0.98}O$ sample should be related to the hopping motions of these holes, which might be ascribed based on the fact that the polarization relaxation in NiO-based ceramics has a close relation to their conductivity inside the grains.

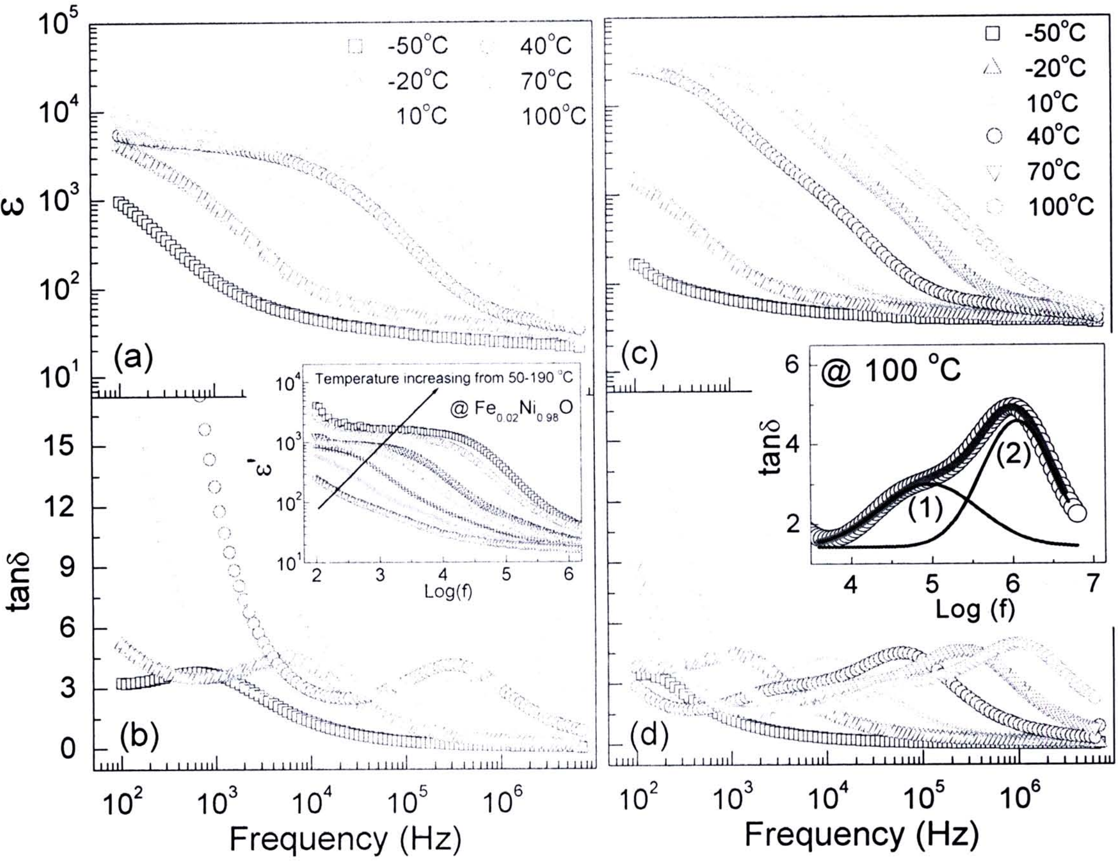

Figure 5.85 Frequency dependence of dielectric constant and loss tangent for $Li_{0.02}Fe_{0.02}Ni_{0.96}O$ [(a) and (b)] and $Li_{0.05}Fe_{0.10}Ni_{0.85}O$ [(c) and (d)] samples at the selected temperatures. The inset of figure (a) and (b) shows frequency dependence of the dielectric constant of $Fe_{0.02}Ni_{0.98}O$ sample at temperature range of 50–190 °C. The inset of figure (c) and (d) shows two Gaussian peaks (blue lines) which are least-squares fitting of experimental data at 100 °C; the red line is fitted result; (1) and (2) are the LFR and HFR, respectively.

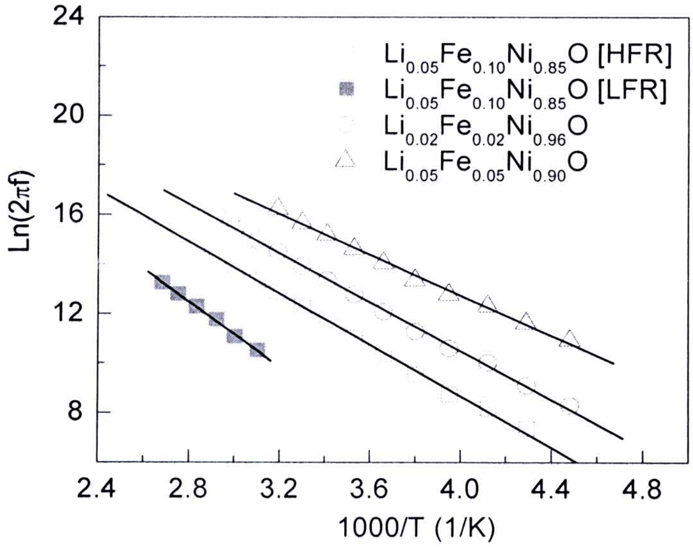

Figure 5.86 Arrhenius plots of the relaxations of the LFNO ceramics.

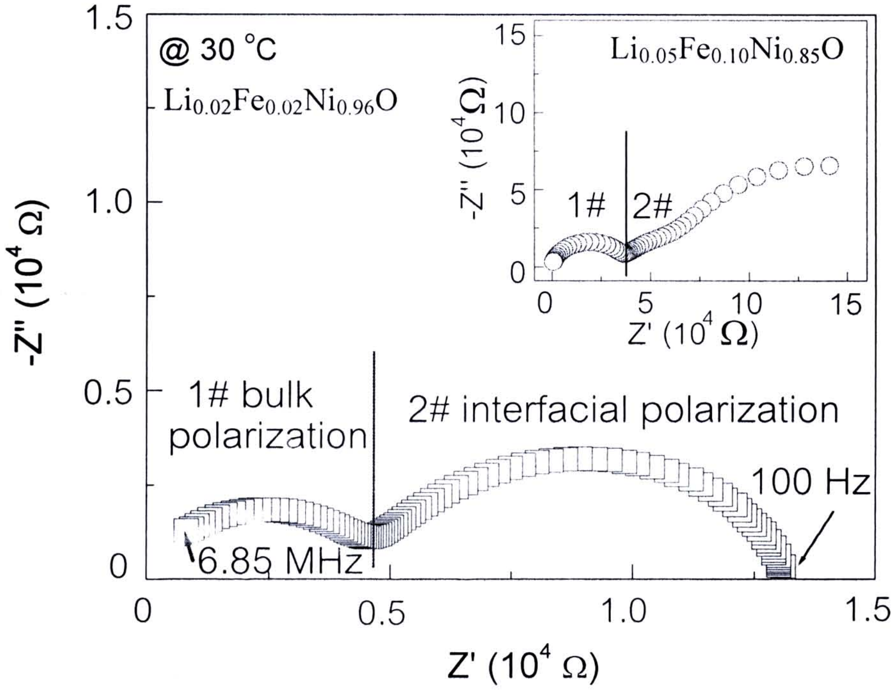

Figure 5.87 Impedance spectrum of $Li_{0.02}Fe_{0.02}Ni_{0.96}O$ sample at room temperature; inset shows the impedance spectrum of $Li_{0.05}Fe_{0.10}Ni_{0.85}O$ sample at room temperature. The vertical lines are used to separate the bulk polarization (1#) and interfacial polarization (2#).

It is now generally accepted that the giant dielectric response in NiO-based ceramics is associated with their core/shell microstructures, which produce an electrically inhomogeneous structure confirming by the complex impedance and microstructure analyses. The large difference in the conductivity between the semiconducting grains and insulating grain boundaries of these materials (more than one order of magnitude) is often detected (Wu J et al., 2003; Lin et al., 2006a). Therefore, it is suitable to associate such apparent giant dielectric response with the Maxwell-Wagner polarization at grain boundaries. However, the observed two electrical responses in the $Li_{0.02}Fe_{0.02}Ni_{0.96}O$ sample show a small difference in the conductivities, as displayed in figure 5.87. This indicates that the explanation of the giant dielectric response in the LFNO ceramics based on the Maxwell-Wagner polarization at the grain boundaries may still incomplete. Moreover, a careful inspection reveals that the enhanced arc in the low-frequency range may contain two overlapping arcs. These overlapping arcs are clearly seen in the impedance spectrum of the $Li_{0.05}Fe_{0.10}Ni_{0.85}O$ sample (the inset of figure 5.87), and the separated small hump (2-2# region) can be observed. The three sets of electrical responses in the LFNO ceramics are the suitable ascriptions for the dielectric relaxation behavior. These electrical responses might be assigned to the electrodes (2-1# region), grain boundaries (2-2# region) and bulk (1# region) effects. According to this analysis, in the present work, the dielectric responses associated with the electrodes and grain boundaries would be termed as an interfacial polarization (2# region), which is separated from the bulk polarization (1# region) by the vertical line, as shown in figure 5.87.

Consider the observation of two dielectric responses in the $Li_{0.05}Fe_{0.10}Ni_{0.85}O$ sample. According to the impedance analysis, the resistance of grains can be estimated at various temperatures, but not for the grain boundaries which is due to the fact that the impedance spectra of electrodes and grain boundaries are overlap and they can not be separated accurately. However, the conduction activation energy inside the grain (E_g) of each sample can be calculated by using the polaron theory (Eq. (5.28)), i.e., $\sigma \propto T^{-1}\exp(-E/k_BT)$, where E is the conduction activation energy. The calculated values of the grain conduction activation energy are summarized in Table 5.11. The grain conduction activation energies (E_g) are almost the same to the E_a values for the $Li_{0.02}Fe_{0.02}Ni_{0.96}O$ and $Li_{0.05}Fe_{0.05}Ni_{0.90}O$ samples. These strongly indicate a close relationship between the polarization relaxation and the conductivity inside the grains. Hence, it is reasonable to mention that the HFR (with E_a~0.448 eV) of the $Li_{0.05}Fe_{0.10}Ni_{0.85}O$ sample is related to the electrical response of the bulk grains (with E_g~0.455 eV), while the LFR (with E_a~0.574 eV) should be associated with the electrical response at the grain boundaries. The disappearance of the dielectric relaxation related to the electrode effect in the lowest frequency range might be due to two possible reasons: (1) It is concealed by the high loss tangent associated with the dc conductivity at high temperature, as revealed in the dielectric loss spectrum at 100 °C in figure 5.85(d). (2) With decreasing temperature, the electrode relaxation peak may appear because charge carriers are frozen, but it moves out of the measured frequency range.

It is important to note that the increases in E_g and related E_a with the increase of the addition of Fe might be related to the point defects in the grains, which could be introduced into NiO by doping Fe ions, i.e.,

$$Fe_2O_3 \xrightarrow{NiO} 2Fe_{Ni}^{\bullet} + V_{Ni}'' + 3O_o, \tag{5.39}$$

$$Fe_{Ni}^{\bullet} \leftrightarrow Fe_{Ni}^{\times} + h. \tag{5.40}$$

Accordingly, the observed decrease in the dielectric constant might be due to the effect of these defects, rather than the increase in the thickness of grain boundaries, based on the simple layer model. As previously discussed, it has been suggested that the HFR is associated with the conduction mechanism inside the grains. Therefore, the difference in the dielectric relaxation of the LFNO ceramics, as demonstrated in figure 5.84, should be attributed to the increase in E_g, i.e., the dielectric relaxation in a ceramic with high E_a is hardly activated by thermal due to its high E_g. Consequently, at a given temperature, the relaxation time of this ceramic should has the longest time, and then its relaxation behavior occurs at the lowest frequency.

The frequency and temperature dependences of the dielectric constant and tanδ of the (Li, Fe)-doped NiO (LFNO) ceramics were studied. The variation of the Li and Fe concentrations had effects on the microstructure and electrical properties of these LFNO ceramics. It was suggested that the dielectric relaxation behavior and high dielectric response in this material system might be associated with both the hopping motions inside the grains and the Maxwell-Wagner polarization at the grain boundaries.

5.6.2 Li and Ti co-doped NiO ceramics

In this section, Li and Ti co-doped NiO with different contents of Li, i.e., $Li_{0.05}Ti_{0.02}Ni_{0.93}O$ (LTNO-05), $Li_{0.10}Ti_{0.02}Ni_{0.88}O$ (LTNO-10), and $Li_{0.20}Ti_{0.02}Ni_{0.78}O$ (LTNO-20), are successfully synthesized by a simple polyvinyl alcohol (PVA) sol-gel method. The PVA sol-gel method is a chemical solution process, which has received considerable attention due to its relative simplicity and usefulness for obtaining a homogeneous and fine powder precursor (Yamamoto et al., 2000). The synthesized fine LTNO powders and ceramics are characterized by X-ray diffraction (XRD), and scanning electron microscopy (SEM). The high dielectric constant and its relaxation were investigated on the LTNO ceramics. It is suggested that such a high dielectric response of LTNO could be partially enhanced by the IBLC mechanism through Maxwell-Wagner relaxation at low frequency (< 1 kHz), and partially associated with the polarization of defect dipoles above 1 kHz. Both contributing factors are thermally activated mechanisms.

5.6.2.1 Ceramic characterization

Figure 5.88 shows the XRD patterns of the LTNO powders and the sintered ceramics with different Li contents, confirming a possibility to produce $Li_xTi_yNi_{1-x-y}O$ phase at a much lower reaction temperature compared to those prepared by sol-gel route (Wu J et al., 2002) and PC method (Maensiri et al., 2007). All of the main peaks are comparable to those of powder diffraction pattern of NiO in JCPDS card No. 78-0429 and those reported in literatures for cubic NiO (Lin et al., 2005b; Wu J et al., 2003). However, the second phase of $LiTiO_2$ is observed in the sintered LTNO-20 sample (JCPDS card No. 74-2257). The SEM micrographs, shown in figure 5.89, reveal that the $Li_xTi_yNi_{1-x-y}O$ ceramics are dense and have obvious grain and grain boundary structure. The mean grain sizes are about 6.29, 4.8, and 6.99 μm for the samples of LTNO-05, LTNO-10, and LTNO-20, respectively. Figure 5.90(a) shows a typical SEM image of the fracture surface of the LTNO-05 sample; the labeled with numeral 1-3 are the EDS measurement points. The EDS spectrum at the point 2 is shown in figure 5.90(b), confirming the presence of Ti-dopant in microstructure of the synthesized LTNO-05 sample. The results of the EDS measurements at the grain and grain boundary regions, shown in figure 5.90(c), indicate that the Ti component can be found in both the grain and grain boundary layer. However, the concentration of Ti-content at grain boundary (point 2) was higher than that at the grain (points 1 and 3).

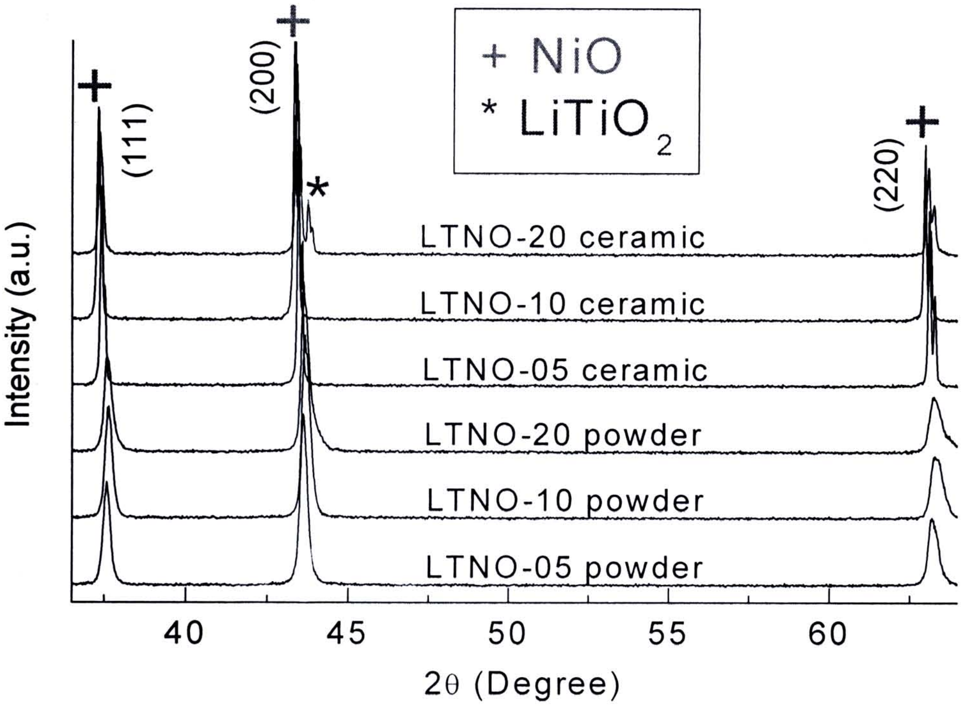

Figure 5.88 XRD patterns of $Li_xTi_yNi_{1-x-y}O$ powders and ceramic samples prepared by a PVA method.

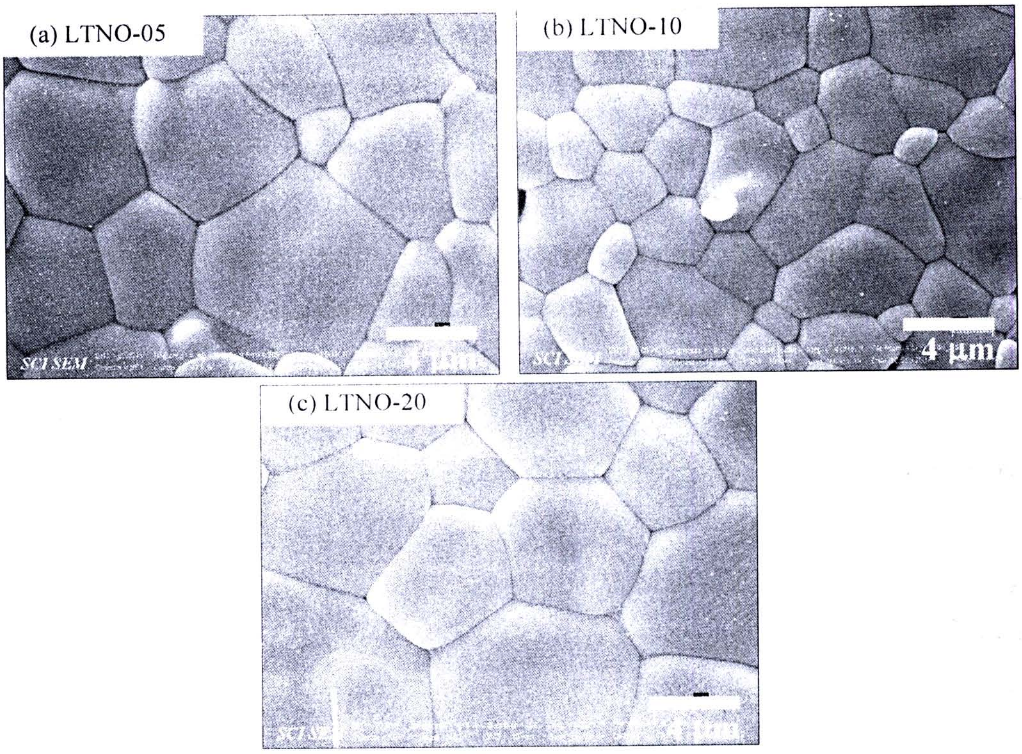

Figure 5.89 SEM micrographs of $Li_xTi_yNi_{1-x-y}O$ ceramics for the samples of (a) LTNO-05, (b) LTNO-10, and (c) LTNO-20.

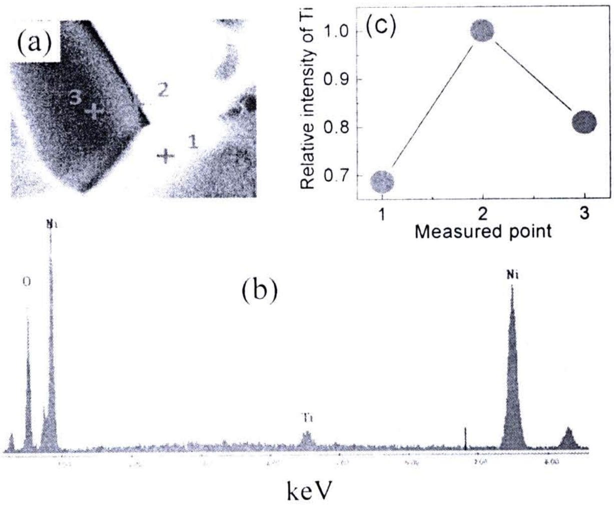

Figure 5.90 (a) SEM micrograph of the fractured surface of LTNO-05 sample, (b) EDS spectra at point 2 in (a), and (c) Ti element profile obtained from the EDS spectra.

5.6.2.2 Effect of Li doping concentration on dielectric properties

The temperature dependence of the dielectric constant (ε') and loss tangent ($\tan\delta = \varepsilon''/\varepsilon'$) of LTNO-05 is demonstrated in figure 5.91(a) at selected frequencies between 0.5-500 kHz. The dielectric constant is nearly independent of temperature above a characteristic temperature, increasing with frequency increase. It attains a high value of the dielectric constant ~10^4, which is close to the value reported in (Wu J et al., 2002) and much larger than that of pure NiO of ~30 (at 1 kHz). The high dielectric constant for $Li_xTi_yNi_{1-x-y}O$ ceramics is not related to the intrinsic nature of ferroelectricity (a thermally driven phase transition). Below the characteristic temperature, a rapid decrease of the dielectric constant by about two orders of magnitude is observed, being accompanied by the appearance of corresponding relaxation peaks in the loss tangent. The peak shifts to lower temperature as the frequency decreases. This confirms the thermally activated behavior which is typical for the Maxwell-Wagner relaxation. At high temperature and low frequency, the increase in the loss tangent may be attributed to the migration of excited electrical particles.

Figure 5.91(b) shows the temperature dependence of the dielectric constant and loss tangent for the samples of LTNO-05, LTNO-10, and LTNO-20 at 1 kHz. The dielectric constant values at room temperature for the LTNO-05, LTNO-10, and LTNO-20 samples are 9,063, 74,499, and 128,236, respectively. The dielectric constant of the LTNO-20 sample is nearly 14 times larger than that for the LTNO-05 sample. It is well known that NiO is a Mott–Hubbard insulator at room temperature (Taguchi et al., 2008). However, introduction of Ni^{2+} vacancies (V_{Ni}'') and/or doping with monovalent cations impurities like Li^+ can dramatically increase the conductivity of NiO and thus NiO becomes semiconducting due to these defects (Wu J et al., 2002). Earlier works (Lin et al., 2006a) have shown that Ti-dopant is rich on the grain boundaries but indigent within the grains in $Li_xTi_yNi_{1-x-y}O$ ceramics. Thus the interiors of the grains for $Li_xTi_yNi_{1-x-y}O$ are semiconducting (i.e., Li-doped NiO), while the shells of the grains are Ti-rich insulating boundaries (e.g., $NiTiO_3$). The giant dielectric permittivity observed in the synthesized $Li_xTi_yNi_{1-x-y}O$ ceramics is therefore caused by its microstructure, because of the creation of an effective circuit of parallel capacitors, as found in boundary-layer capacitors (BLC) (Nan, 1993).

According to the BLC structure and Maxwell–Wagner models, under an applied electric field the carrier conducting access is blocked by the Ti-rich boundary layer and thus the opposite charges will accumulate at the two edges of the insulator layer, creating a macroscopic electric dipole, which can be considered as a micro-parallel capacitor. As a result, the polarization formation primarily depends on the accumulation of charge via conducting in the grain interior. Therefore, a $Li_xTi_yNi_{1-x-y}O$ ceramic with higher Li concentration will possibly process more polarization and ascribe to the boundary layer capacitance effects. The highest dielectric permittivity seen in the LTNO-20 sample is therefore due to its higher Li concentration compared to those of the LTNO-10 and LTNO-05 samples. Note that, because the doping concentration of Ti is kept constant, the difference of dielectric behavior of LTNO samples can only be attributed to the effect of Li. As shown in figure 5.91(b), with increase the temperature, the dielectric constant values of the LTNO-10 and LTNO-20 samples drop rapidly. This corresponds to the strong increases in their tanδ values at the same temperature range. Such electrical responses of the LTNO-10 and LTNO-20 samples in the high temperature region may be attributed to the migration of excited electrical particles at high temperatures. However, the detailed description of the associated conduction behavior goes beyond the theme of this paper.

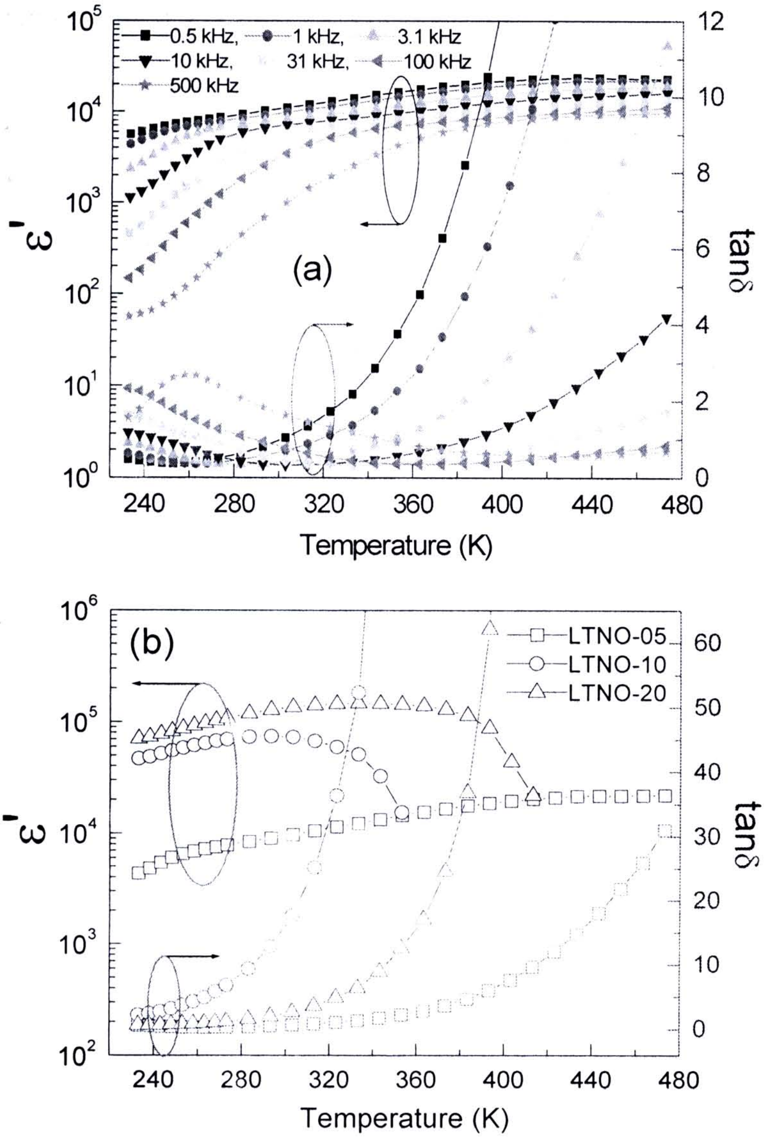

Figure 5.91 (a) Temperature dependences of dielectric constant (ε′) and loss tangent (tanδ) for LTNO-05 at selected frequencies and (b) the temperature dependence of dielectric constant and loss tangent for LTNO-05, LTNO-10, and LTNO-20 at 1 kHz.

5.6.2.3 Characterization of dielectric relaxation behavior

To understand the possible mechanism for high dielectric response in LTNO-05, the dielectric constant (ε') and the dielectric loss (ε'') are plotted as a function of frequency over temperature range of 233 and 313 K, as shown in figures 5.92(a) and 5.92(b). It is clear that the dielectric constant and the dielectric loss show a Debye-like relaxation, namely the dielectric constant displaying a step decrease at the frequency and the relaxation peak shifting to higher frequency with increasing temperature. At high temperature, the dielectric constant increases in the low frequency range (< 1 kHz), and with increasing frequency up to 10^4-10^5 Hz, a sharp decrease in the dielectric constant is observed. Normally, space charge (interfacial) polarization occurs when mobile charge carriers are impeded by a physical barrier (i.e., grain boundary) that inhibits charge migration. The charges then pile up at the barrier producing a localized polarization within grains (Hence, West, 1990). With increased temperature, the density of charges contributing to the space charge polarization is sufficiently large. The frequency range of sensitivity for such polarization may extend from 10^{-3} Hz into the kilocycle range, producing a very large dielectric constant in this region. Therefore, the increase in the dielectric constant at low frequency is possibly due to space charge polarization. For the step-like decrease in the dielectric constant at the frequency range of 10^3-10^5 Hz (corresponding to the respective relaxation peaks in ε'') as shown in figure 5.92(b), dielectric relaxation in this region may be ascribed to the defect-dipole polarization effect, which appears at radio frequency ranges. In general, there are two main effects responsible for the mechanism of polarization: the frequency of applied electric field and temperature. According to the effect of frequency, at fixed temperature, if an alternating field is applied then the polarization may fully develop at sufficiently low applied frequencies (the polarization and the field are in phase) but if the frequency of the applied field is too high then the field is reversed before the polarization has responded and no response will be the result of net effect. The magnitude of the polarization thus drops off as the frequency is increased. For the effect of temperature (Lin et al., 2005b), at low temperature, the electric dipoles freeze through the relaxation process, and there exists decay in polarization with respect to the applied electric field, which results in the sharp decrease in the dielectric constant. When the temperature is high, the rate of polarization formed is quick, and thus the relaxation occurs in high frequency as shown in figure 5.92(a).

In general, the frequency dependent behavior of the dielectric constant and the dielectric loss of high dielectric constant can be well described by the simple Cole-Cole relaxation equation, which ignores the effect of the electrical conduction.

$$\varepsilon^* = \varepsilon'_\infty + \frac{\varepsilon'_s - \varepsilon'_\infty}{1+(j\omega\tau)^{1-\alpha}}, \tag{5.40}$$

where α is Cole-Cole parameter with values between 0 and 1. Note that equation (5.40) is the same as equation (5.18). When the electrical conductivity is dominated at low frequency range as shown in figures 5.92(a) and 5.92(b), a contribution term by the electrical conduction is generally added to the relaxation equation. The modified Cole-Cole equation that incorporates the conductivity term is given by (Abdelkafi et al., 2006),

$$\varepsilon^* = \varepsilon'_\infty + \frac{\varepsilon'_s - \varepsilon'_\infty}{1+(j\omega\tau)^{1-\alpha}} + j\frac{\sigma^*}{\varepsilon_0\omega^s}, \tag{5.41}$$

where $\sigma^*(\sigma^* = \sigma_1 + j\sigma_2)$ is the complex conductivity. Here σ_1 is the conductivity due to the free charge carrier (dc conductivity) and σ_2 is the conductivity due to the space charges (localized charges), and s is a dimensionless exponent $(0 < s < 1)$. For an ideal complex conductivity, $s = 1$. If $s < 1$, it implies that the polarization has a distribution of the carrier polarization mechanisms. From this relation, the complex permittivity can be decomposed into the real and imaginary parts. i.e.,

$$\varepsilon' = \varepsilon'_\infty + \frac{(\varepsilon'_s - \varepsilon'_\infty)\{1+(\omega\tau)^{1-\alpha}\sin(\alpha\pi/2)\}}{1+2(\omega\tau)^{1-\alpha}\sin(\alpha\pi/2)+(\omega\tau)^{2-2\alpha}} + \frac{\sigma_2}{\varepsilon_0\omega^s}, \tag{5.42}$$

$$\varepsilon'' = \frac{(\varepsilon'_s - \varepsilon'_\infty)(\omega\tau)^{1-\alpha}\cos(\alpha\pi/2)}{1 + 2(\omega\tau)^{1-\alpha}\sin(\alpha\pi/2) + (\omega\tau)^{2-2\alpha}} + \frac{\sigma_1}{\varepsilon_0\omega^s}. \tag{5.43}$$

It is clearly seen from equations (5.42) and (5.43) that the conductivity may have contributions to the dielectric permittivity (ε') and dielectric loss (ε''). The first term of equations (5.43) is the part of the losses associated with the dielectric relaxation due to permanent dipole orientation or other motions which do not involve long-range displacement of mobile charge carriers, whereas the second term is the part of the losses associated with long-range migration of carrier response. From the above equations, the charge carrier localization at defect sites and interfaces (σ_2) can make large contribution to the dielectric permittivity, while free charge carrier (σ_1) contributes to the dielectric loss.

Analysis of the experimental data was carried out on the basis of equations (5.42) and (5.43). Typical fitting results are shown in figures 5.92(a) and 5.92(b), the solid lines are the fitted curves of experimental results. As clearly seen from figure 5.92(a) and 5.92(b), the excellent agreement between experimental data and calculated data over the entire range of frequencies and temperatures for both the dielectric constant and the dielectric loss is consistent with equations (5.42) and (5.43) for the LTNO-05 ceramic. A disagreement between the measured and calculated values for the dielectric constant at low frequencies (< 1 kHz) at temperature above 273 K. This may be due to the fact that some parts of Ti-dopant have entered into the NiO crystal lattice, and have an influence on the space charge localized inside the grain. Additionally, figure 5.92(c) shows the evolution of the relaxation and dc conductivity contributing on dielectric loss at 293 K. It is clearly seen that there are two main factors responsible for the dielectric relaxation of LTNO: dipole and conduction relaxation. A complete list of parameters used in the calculation ($\Delta\varepsilon(\varepsilon_s - \varepsilon_\infty)$, τ, α, s, σ_1 and σ_2) for LTNO-05 is shown in Table 5.12. It is also important to mention that the s values tend to increase ($s \rightarrow 1$) with increasing temperature (does not present), indicating that the carrier polarization mechanism is weakly dispersive at higher temperature, which might be attributed to some barrier height extracted. For the value of α, a relatively lower value of $1 - \alpha$ corresponds to a more disorder system. Hence it can be inferred from the $1-\alpha$ values of LTNO-05 (0.66) and $CaCu_3Ti_4O_{12}$ (0.91) (Thongbai et al., 2007) at 233 K that a relatively higher disorder is present in LTNO-05 compared to that of the CCTO system.

In order to elucidate the dielectric relaxation response in LTNO-05, it is important to estimate the activation energy of relaxations. Figure 5.92(d) shows the plot of log τ with $1/T$, in which the solid line is the fitted result obeying the Arrhenius law as expressed in equation (5.7) As shown in Table 5.12 and figure 5.92(d), the rapid decrease in relaxation times (τ) with increasing temperature is suggestive of an increase dipole density and faster polarization process (Wu J et al., 2002). According to the fitted curve for the LTNO-05 sample, the activation energy $E_{a(\tau)}$ value of the relaxation process is 0.391 eV and $\tau_0 = 6.35\times10^{-13}$ s. Additionally, the value of $E_{a(\tau)}$ is higher than that of 0.313 eV as reported by Wu *et al.*, for $Li_{0.05}Ti_{0.02}Ni_{0.93}O$. It is important to note that, with increasing the Li concentration, the relaxation peak moves out of the measured frequency range, which is similar to that reported by Wu *et al.* (Wu J et al., 2002). Thus, the $E_{a(\tau)}$ values of the LTNO-10 and LTNO-20 samples could not be obtained.

Table 5.12 Fitted results of $\Delta\varepsilon'$, τ, α, s, σ_1 and σ_2 using the experimental results with equations (5.42) and (5.43) in different temperature range for the LTNO-05.

T (K)	$\Delta\varepsilon=(\varepsilon_s-\varepsilon_\infty)$	α	s	τ (μs)	σ_1 (10^{-4} Sm^{-1})	σ_2 (10^{-4} Sm^{-1})
233	8700	0.340	-	170	-	-
253	8250	0.320	0.8	38	0.080	0.021
273	7800	0.300	0.8	10	0.210	0.053
293	7500	0.280	0.8	3.1	0.460	0.180
313	7000	0.275	0.85	1.2	1.350	0.640

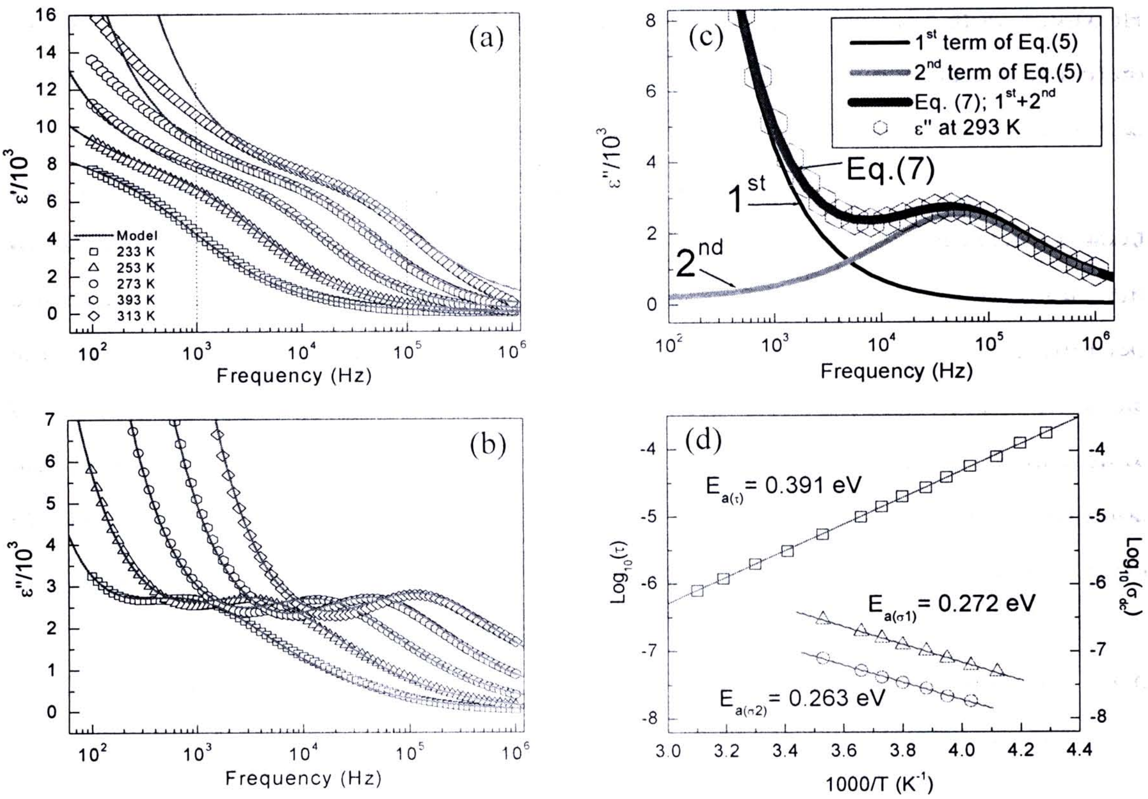

Figure 5.92 Frequency dependences of (a) ε' and (b) ε'' of LTNO-05 at various temperatures. The solid curves are the best fits to equations (5.42) and (5.43) for ε' and ε'', respectively, which include both a Cole–Cole relaxation and a complex conductivity contribution. (c) The evolution of the relaxation and dc conductivity contribute to the dielectric loss. (d) Arrhenius plots of the relaxation time and dc conductivities.

As shown in figure 5.92(d), it is found that the fitted σ_1 and σ_2 values at different temperatures follow the Arrhenius-like law, in which the solid line is the fitted result. Accordingly, in the LTNO-05 sample, both of the conduction activation energies for the localized charge and free charge carrier, $E_{a(\sigma 2)} = 0.263$ eV and $E_{a(\sigma 1)} = 0.272$ eV, were obtained, respectively. As previously reported (Abdelkafi et al., 2006), the polarization relaxation has a close relation to the conductivity in the grain interior, because the value of $E_{a(\sigma)}$ is almost the same as the value for $E_{a(\tau)}$.

However, both values are different from the experimental results, indicating that the dielectric relaxation response in LTNO-05 ceramic does not correspond to the conductivity in the grain interior.

Finally, the high dielectric permittivity LTNO ceramics have been successfully synthesized by a simple PVA-sol-gel method. XRD results show the single phase of NiO. The temperature and frequency dependence of dielectric permittivity and dielectric loss were investigated. An excellent fit between the experimental and simulated data has been obtained over a wide frequency and temperature using the modified Cole-Cole model with the consideration of the conductivity contribution. The high dielectric permittivity response can be ascribed to the Maxwell-Wagner polarization mechanism and defect-dipoles polarization.

5.7 Comparison of giant dielectric properties of NiO-based and pure-CuO ceramics: Dielectric relaxation behavior

As all previous presents, the giant dielectric properties can be observed in NiO-based ceramics. The values of the giant dielectric constant are found to be about 10^3-10^5 at low-frequency range. According to the first report (Wu et al., 2002), it was suggested that the giant dielectric response in the $Li_xTi_yNi_{1-x-y}O$ ceramics could be explained based on the IBLC model according to a core/shell structure. It was proposed that Li doping ions caused a change in electrical conductivity of the core grains—the insulating grains can be transformed to semiconducting grains. The Ti doping ions preferred to form the second phase of $NiTiO_3$ accumulated along grain boundaries, which acted as the shell. Under an applied electric field, free charges can not move through a bulk ceramic because they are inhibited by the insulating layers of $NiTiO_3$ phase. This is responsible for the observed giant dielectric constant in the $Li_xTi_yNi_{1-x-y}O$ ceramics.

Recently, there has been considerable interest in giant dielectric materials because they might offer the opportunity to increase the performance and/or decrease the dimensional size of these devices. Most recently, the giant dielectric properties of CuO are of great interest because it is a low cost lead free environmental friendly material and is simple compound which is easy to prepare in the pure form and available commercially in large scale. So far, only a few studies reported on the dielectric properties of CuO ceramics (Sarkar et al., 2006, 2008a,b) and it still have to pass through extensive compatibility test before available for commercial applications in devices. In the work reported by Sarkar et al., (Sarkar et al., 2006) the purity of starting CuO powder for fabrication of CuO ceramic is 99% and so 1% of impurities would possibly affect the giant dielectric response in the CuO ceramic. It has been reported that only 2.5 at.% Mn doping ($CaCu_3Mn_{0.1}Ti_{3.9}O_{12}$) can suppress the dielectric constant in CCTO by up to two orders of magnitude and the nonlinear varistor characteristics disappear completely (Cai et al., 2007). Therefore, it is important to prepare the CuO ceramics using high purity CuO powder. This will rule out the impurity effects on the high dielectric constant in this CuO system, and thus the origin of giant dielectric response can be proposed.

In this section for the investigation of the dielectric properties of pure-CuO ceramics, high purity CuO (99.999%, Cerac) powder was used to fabricate the CuO polycrystalline ceramics. The CuO powder was pressed into disks and then sintered at 920 and 980 °C for 10 h to obtain bulk CuO ceramics with different grain sizes, hereafter referred to as CuO-1 and CuO-2, respectively.

As demonstrated in figures 5.93(a) and 5.93(b), the frequency dependence of the $Li_{0.05}Ti_{0.02}Ni_{0.93}O$ ceramic (sintered at 1280 °C) and that of the CuO ceramic are quite similar. They demonstrate the high-frequency dielectric relaxation—the step-like decrease in the dielectric constant at the high-frequency range. The dielectric constants at -60 °C and 1 kHz for the $Li_{0.05}Ti_{0.02}Ni_{0.93}O$ and the CuO ceramics are respectively about 11,361 and 19,636—the dielectric constant of the $Li_{0.05}Ti_{0.02}Ni_{0.93}O$ ceramic is found to be lower than that of the CuO ceramic. However, these values are in the same order of 10^4, which is the giant dielectric constant value. The frequency dependence of the dielectric constant of the CuO ceramic seems to be smaller than that of the $Li_{0.05}Ti_{0.02}Ni_{0.93}O$ ceramic. It is interesting that the CuO ceramic can exhibit the giant dielectric constant value without any dopants.

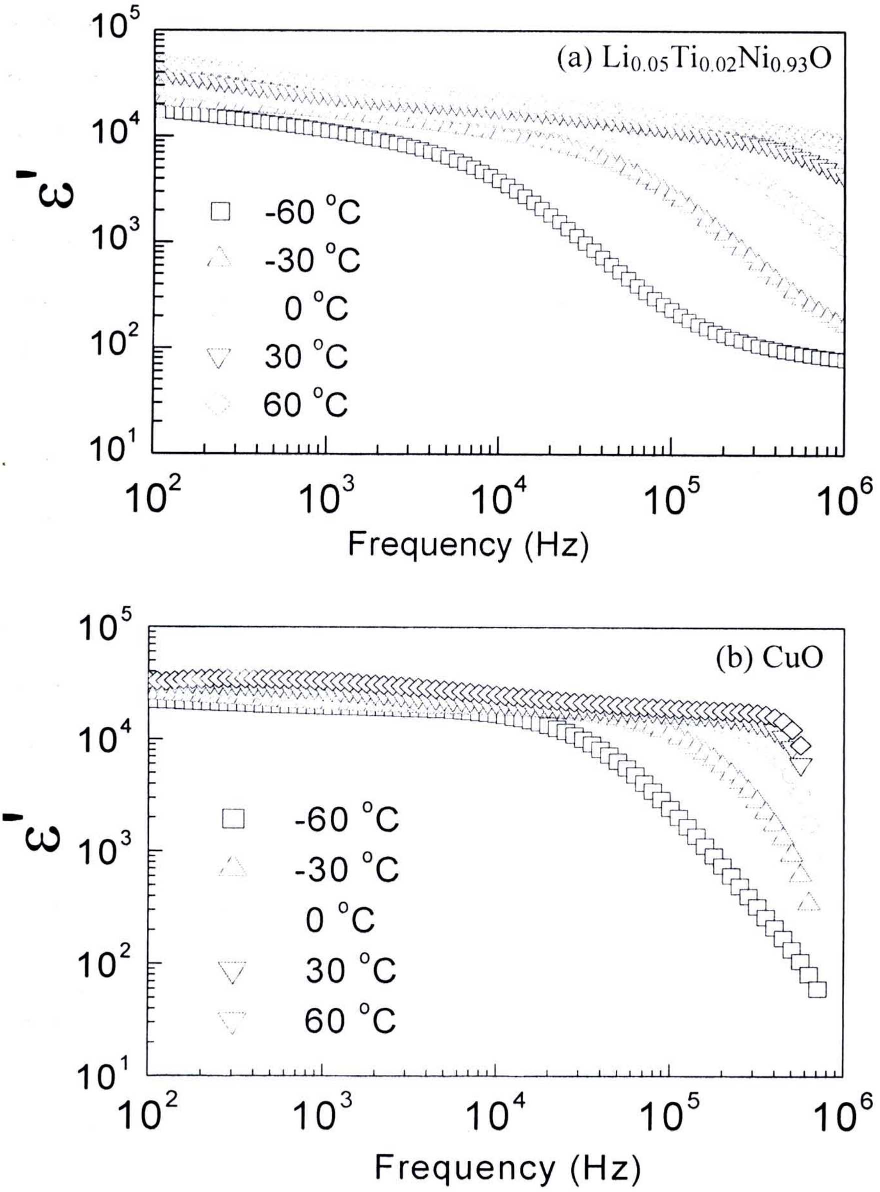

Figure 5.93 Dielectric constant of (a) $Li_{0.05}Ti_{0.02}Ni_{0.93}O$ and (b) CuO (CuO-1 sample) ceramics

The investigations of the CuO ceramics are as the follows. Figure 5.94 shows the surface morphologies of the sintered CuO ceramics. As can be seen, the morphologies change with the sintering temperature, and the grain size increases with increasing sintering temperature. The mean grain sizes of CuO-1 and CuO-2 are 4.57±1.71 and 9.57±3.01 μm, respectively.

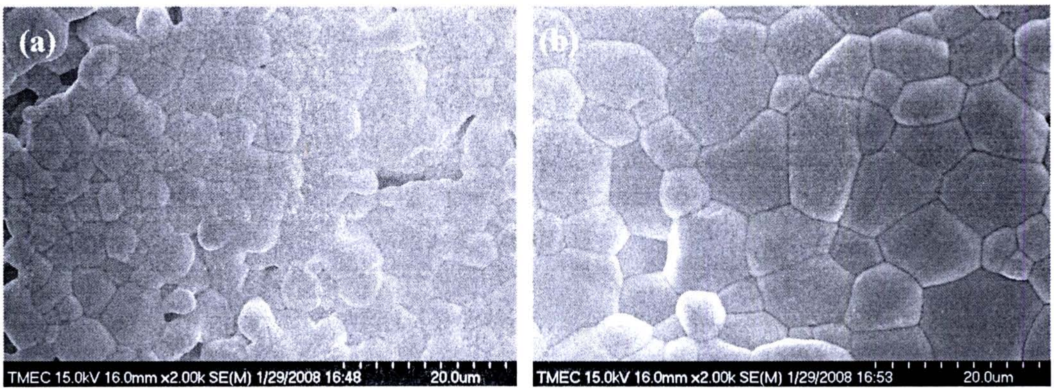

Figure 5.94 SEM images of CuO ceramics: (a) CuO-1 sintered at 920 °C and (b) CuO-2 sintered at 980 °C.

The frequency dependence of the dielectric constant for CuO-1 at various temperatures is demonstrated in figure 5.95(a). It is clear from figure 5.95 that both samples exhibit the giant dielectric constant values of ~2.8×10^4 for CuO-1 and ~3.7×10^4 for CuO-2 (inset (2) of Fig. 5.95(a)) at low frequencies and 263 K. Each sample exhibits similar dielectric behavior, where the dielectric constant shows a step decrease at high frequency and shifts to higher frequency at higher temperature, accompanied by the appearance of corresponding peaks in the imaginary parts of dielectric spectra. This overall dielectric response observed in the CuO ceramics is similar to that observed in $CaCu_3Ti_4O_{12}$ (Zhang et al., 2005; Shao et al., 2006). It is worth noting that that the giant dielectric response in high purity CuO ceramics in this section of the thesis does not arise from the effects of any impurities as observed in the case of CuO ceramic prepared using a 99% CuO starting powder reported in the literature (Sarkar et al., 2006).

Sarkar et al., (Sarkar et al., 2008a) reported the detection of the microscopic amount of Cu^{3+} in CuO polycrystalline ceramics by using x-ray photoelectron and transmission electron microscopies. They also proposed that the concentration of Cu^{3+} is lower in grain boundaries than in grains. Therefore, the conduction mechanism in CuO is mainly governed by hole hopping between Cu^{2+} and Cu^{3+} which produces a *p*-type semiconducting grains. Since the grain boundaries consist of only Cu^{2+}, it behaves as an insulating wall. From these results, an array of boundaries and grains is formed, and high dielectric constant is achieved for CuO ceramics. Therefore, the authors concluded that the giant dielectric response in CuO ceramics is attributed to the IBLCs effect. From the experimental results, it is found that the dielectric constant increases with an increase in the grain size. This implies that the high dielectric response in the CuO ceramics has a close relation to the IBLCs mechanism. According to the simple series-layer model for the IBLCs, the dielectric constant of ceramics can be simply expressed as $\varepsilon' \approx \varepsilon_{gb} d/t$, where ε_{gb} is the dielectric constant of the boundary layer, d is the grain size, and t is the boundary-layer thickness. Hence, dielectric constant of the ceramics would increase with an increase in the grain size, which is in good agreement with the results observed in the CuO ceramics. The activation energy (E_a) of relaxation process of CuO-1 and CuO-2 can be calculated from the fitted curves following equation (5.7), as shown in figure 5.95(b). The results show that E_a increases from 0.195 eV to 0.230 eV with an increase in grain size from 4.57±1.71 to 9.57±3.01 μm. Therefore, the values of activation energy of CuO-1 and CuO-2 are close to the reported value of 0.248 eV for the CuO (99%) ceramic.

As shown in figure 5.96, from the fitted result, the dielectric relaxation in the present ceramic can be concluded as a nearly Debye relaxation, which it is attributed to the dipole relaxation related to the defects in the grain interiors or other motions which do not involve long-range displacement of mobile charge carriers. Note that, the experimental curves are quite well fitted by equation (5.18) at low temperature. However, with increase the temperature, a disagreement between them can be observed at low frequencies. This attributed to the grain boundary effect, which can be responsible for up to 30% (at 1 kHz and 293 K) of the total dielectric constant of CuO ceramic.

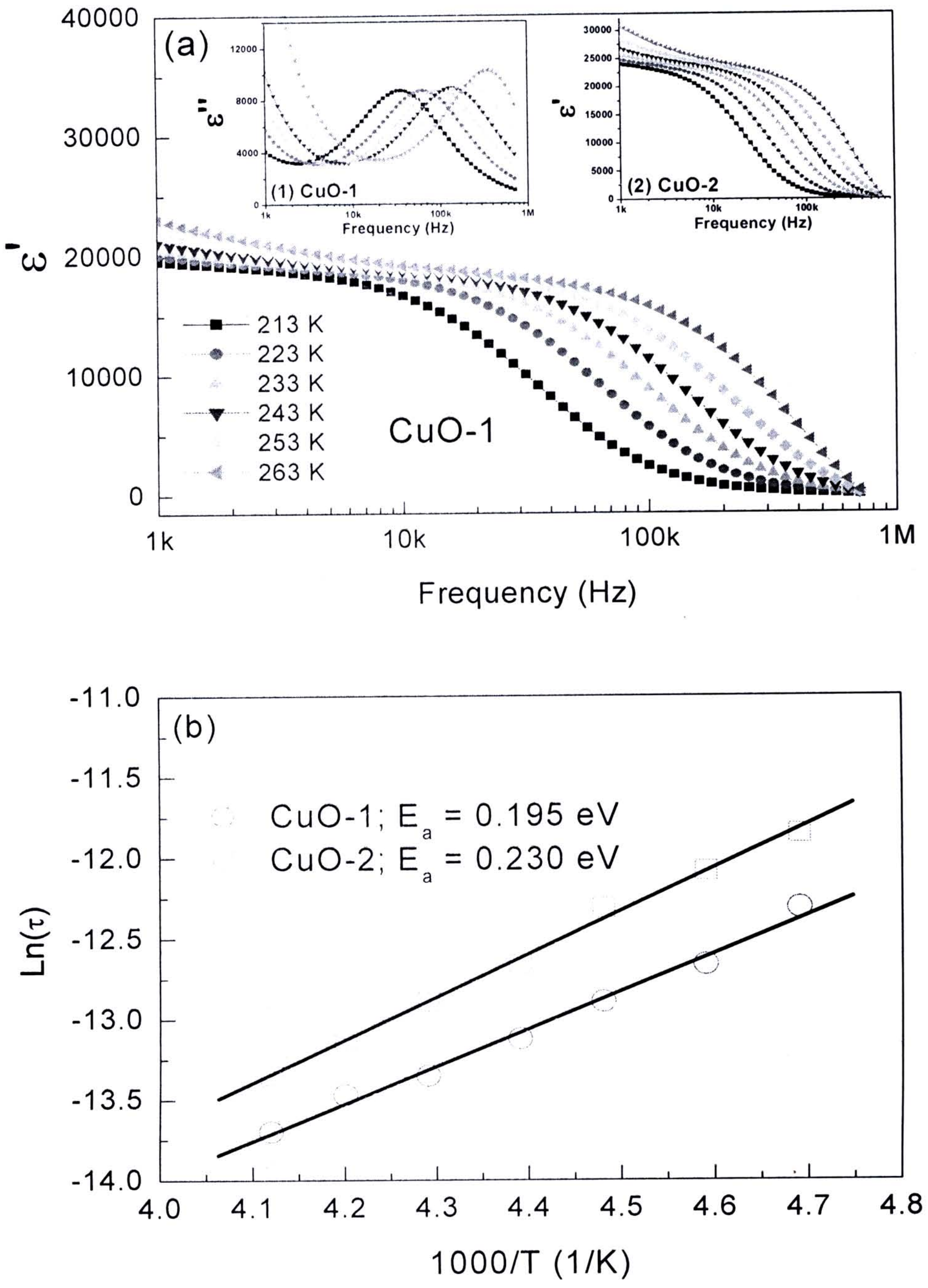

Figure 5.95 (a) The frequency dependence of dielectric constant for CuO-1 at various temperatures; inset (1) shows the frequency dependence of dielectric loss for CuO-1 and inset (2) displays the frequency dependence of dielectric constant for CuO-2. (b) The Arrhenius plot of the dielectric relaxation time for the CuO-1 and CuO-2.

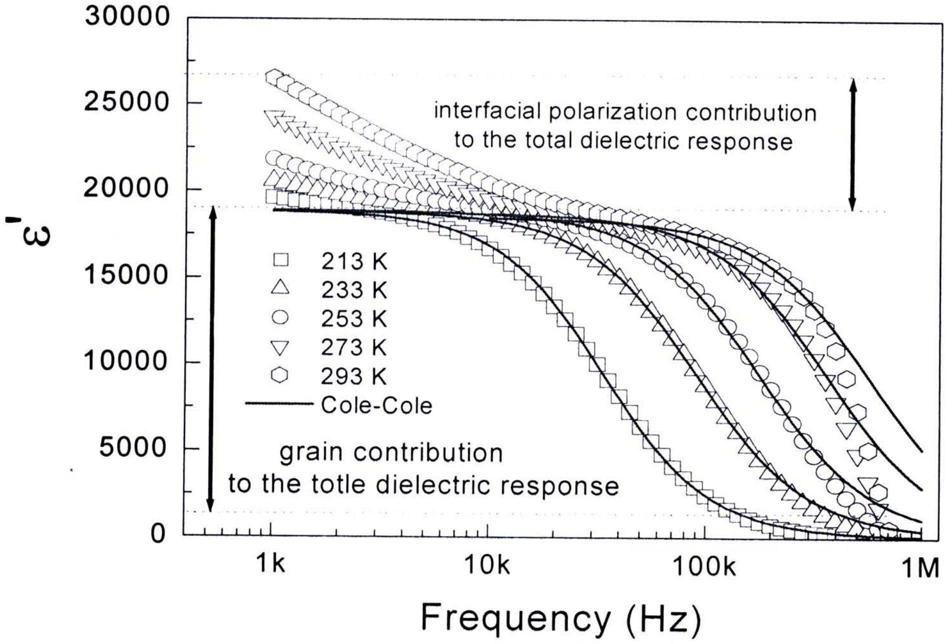

Figure 5.96 The frequency dependence of dielectric constant for CuO ceramic at various temperatures; the solid lines represent calculated values of equation (5.18) for a Cole-Cole model.